



# **Scanning Near-Field Optical Spectroscopy with an Inline Interferometer for Probing Local Absorption**

Von der Fakultät für Mathematik und Naturwissenschaften der Carl von Ossietzky Universität Oldenburg zur Erlangung des Grades und Titels eines Doktors der Naturwissenschaften (Dr. rer. nat.) im Fach Physik angenommene Dissertation

von  
Herrn Jens Brauer  
geboren am 16.03.1989 in Emden

Gutachter: Prof. Dr. Christoph Lienau  
Carl von Ossietzky Universität Oldenburg

Zweitgutachter: Prof. Dr. Erich Runge  
Technische Universität Ilmenau

Tag der Disputation: 20.10.2020

# Contents

---

<b>1</b>	<b>Introduction</b>	<b>5</b>
<b>2</b>	<b>Optical Near-field Microscopy and Spectroscopy</b>	<b>11</b>
2.1	Introduction - The Status Quo . . . . .	12
2.2	Detection Schemes in Scanning Near-Field Microscopy . . . . .	19
2.2.1	Homodyne detection . . . . .	19
2.2.2	Heterodyne detection . . . . .	21
2.2.3	Pseudoheterodyne detection and phase-shifting interferometry . . . . .	22
2.2.4	Synthetic optical holography . . . . .	25
<b>3</b>	<b>Experimental Setup</b>	<b>27</b>
3.1	AFM and optical setup . . . . .	29
3.2	Demodulated near-field signals and spectra . . . . .	35
3.3	Background signal in SNOM measurements . . . . .	39
3.4	Improved separation of background and reference fields in a side-illumination setup . . . . .	44
<b>4</b>	<b>Theoretical Background</b>	<b>49</b>
4.1	Focusing through layered systems with anisotropic thin films . . . . .	50
4.1.1	Microscopic model of the refractive index . . . . .	50
4.1.1.1	Electronic states . . . . .	50
4.1.1.2	Vibrational modes in a two level system . . . . .	54
4.1.2	Transfer Matrix Method . . . . .	58
4.1.3	Anisotropic Media . . . . .	65
4.1.4	Focal Plane Fields . . . . .	70
4.2	Tip-Sample Interaction in Apertureless SNOM Spectroscopy . . . . .	77
4.2.1	Tip dipole and Green's function . . . . .	79
4.2.2	A nanorod-antenna: a nanostructure modelled as chains of dipoles . . . . .	84
4.2.3	Tip above a planar, isotropic dielectric material . . . . .	87
4.2.4	SNOM tip above an anisotropic dielectric material . . . . .	93
4.2.4.1	Tip-sample interaction in a self-consistent solution . . . . .	96
4.2.4.2	The measured intensity signal . . . . .	99
<b>5</b>	<b>In-line interferometer</b>	<b>101</b>

5.1	Introduction: Spatial near-fields of a single bowtie antenna . . . . .	102
5.2	Approach curve measurements . . . . .	104
5.3	Near-field and Background Analysis . . . . .	108
5.4	Near-Field Contributions in the Measurements . . . . .	116
5.5	Summary . . . . .	119
<b>6</b>	<b>Local Spectroscopy</b>	<b>121</b>
6.1	Simple expansion of quasi-monochromatic model to broad-bandwidth measurements . . . . .	123
6.2	Tip-sample interaction . . . . .	127
6.2.1	Tip polarizability and effective polarizability . . . . .	128
6.2.2	Illumination of tip and sample: electric field distribution in the laser focus	130
6.2.3	Extraction of distance-dependent near field spectra from measurements	136
6.2.4	Near-field spectra on flat films . . . . .	140
6.3	Local spectra on Squaraine dye molecules . . . . .	144
6.3.1	Introduction to squaraine dyes . . . . .	145
6.3.2	The Dielectric function of squaraine dyes . . . . .	145
6.3.3	Nanoscale spectroscopy . . . . .	154
6.4	Spectroscopic imaging of nanorod antenna modes . . . . .	162
<b>7</b>	<b>Summary &amp; Outlook</b>	<b>173</b>
<b>A</b>	<b>Matlab/Python Programming of SNOM controls</b>	<b>177</b>
A.1	Program Interface . . . . .	177
<b>B</b>	<b>Refractive index and Snell's law for anisotropic materials</b>	<b>181</b>
B.1	Derivation 1: The refractive index . . . . .	181
B.2	Derivation 2: The angle in the medium . . . . .	183
<b>C</b>	<b>Outlook: Local orientations of polymers by polarization resolved SNOM</b>	<b>185</b>
<b>D</b>	<b>Paper attachment: In-line interferometer for broadband near-field scanning optical spectroscopy</b>	<b>191</b>
	<b>Bibliography</b>	<b>215</b>

# Kurzfassung

---

In dieser Arbeit wird ein optisches Rasternahfeldmikroskop vorgestellt, welches durch eine schnelle Zeilenkamera und einen Monochromator erweitert wurde, um lokale Spektroskopie auf der Nanoskala mit Hilfe üblicher Demodulationstechniken zu ermöglichen.

Insbesondere für monochromatische SNOM Messungen werden bereits seit vielen Jahren Modulations- und Demodulationstechniken eingesetzt, um das schwache optische Nahfeldsignal von einem unerwünscht starken optischen Untergrundsignal zu trennen. Mit der hier präsentierten Methode können solche Modulationstechniken erstmals auch auf lokale SNOM Spektroskopie angewandt werden, um so Nahfeldspektren in einem direkten Ansatz zu extrahieren. Um die Trennung bzw. Abschwächung des optischen Untergrunds effizienter und über einen spektral breiten Bereich zu ermöglichen, stelle ich in dieser Arbeit ein intrinsisch stabiles in-line Interferometer vor, welches als Glas-Gold-Glas Mehrfachschicht kostengünstig hergestellt werden kann und übliche Glas Substrate ersetzen kann.

Da die Nahfeldspektren an sich jedoch nicht nur die Probeninformation, sondern auch Information über die gesamte Spitze-Probe Wechselwirkung enthalten, wurde in dieser Arbeit zusätzlich zu den experimentellen Ergebnissen eine theoretische Beschreibung erarbeitet, welche im Folgenden dazu genutzt wird, die Wechselwirkung und damit die lokalen Spektren verschiedener Proben zu simulieren und die Messergebnisse genauer zu verstehen.

Der Einfluss der Spitze auf die spektralen Eigenschaften wird hierbei in einem ersten Schritt an spektral flachen Proben mit bekannter dielektrischer Funktion untersucht, u.a. auf einem 30 nm dicken Goldfilm.

Die neue Spektroskopiemethode wird schließlich auf zwei Proben von wissenschaftlichem Interesse angewendet. Die erste ist ein neuartiger, anisotroper organischer Farbstoff, welcher für organische Photodioden oder organische Solarzellen eingesetzt werden könnte. Es wird gezeigt, dass lokale Absorption auf der Nanoskala gemessen werden kann und die Nahfeldspektren mit strukturellen Eigenschaften der Probe in Zusammenhang gebracht werden können, welche wir mit Hilfe eines quantenmechanischen Modells vorausgesagt haben.

Als zweite Probe untersuchen wir eine plasmonische Nanostruktur, die aus zwei gekoppelten Nanoantennen besteht. Hier nutzen wir die spektrale Auflösung, um die elektrischen Feldkom-

ponenten um die Nanostruktur in der Ebene und aus der Ebene heraus unterscheiden zu können.

**Schlagwörter:** SNOM, Spektroskopie, Squaraine Farbstoff, Nanostrukturen, lokale Absorption, lokale Spektroskopie

# Abstract

---

In this thesis I present a scanning near-field optical microscope (SNOM) that was extended by a fast line camera and a monochromator to enable local spectroscopy on the nanoscale using common demodulation techniques. Particularly for monochromatic SNOM measurements, modulation and demodulation techniques were used for many years to separate the desired weak near-field signal from an undesired large optical background signal. With the SNOM setup presented in this work the same techniques can for the first time be applied to local SNOM spectroscopy and allow to extract near-field spectra in a direct approach.

In order to separate or suppress the optical background more efficiently and over a spectrally broad range, in this thesis I present an intrinsically stable in-line interferometer, which consists of a glass-gold-glass multilayer that is cheap to produce and is used as a replacement for typical glass substrates.

As the measured near-field spectra however not only contain information about the sample, but are influenced by the complete tip-sample interaction, a theoretical description was worked out in addition to the experimental results. It is used throughout this work to simulate the tip-sample interaction and hence the local spectra for multiple samples and understand the measured spectra in more detail.

The influence of the tip on the spectral properties is hereby firstly investigated for spectrally flat samples with a known dielectric function, such as for a 30 nm gold-coated glass substrate.

Finally, this newly introduced spectroscopy method is applied to two samples of interest. The first is a promising new organic squaraine dye, that may find application in organic photodiodes or solar cells. It is shown that we are able to measure local absorption of the dye on a nanometer scale and connect the findings with the structural properties of the sample, which was postulated with a quantum mechanical model. For the second sample, a plasmonic nanoantenna dimer, we demonstrate that we can use spectral discrimination for vectorial field mapping of the near field around a plasmonic nanoantenna.

**Keywords:** SNOM, spectroscopy, squaraine dye, polymer, nanostructures, local absorption, local spectroscopy



# Introduction

# 1

Nanotechnology is of rapidly increasing technological relevance nowadays because plasmonic nano elements as well as processes on the nanoscale show a great potential to drive innovation in research and development of future technologies. Like Richard Feynman already said in 1957, "there is plenty of room at the bottom"[1, 2], and today nano structures are found in the various fields of science, like medicine[3, 4], surface science, organic chemistry, energy storage[5] and many more.

In particular the interaction of light and matter on the nanoscale is of high scientific importance as it is the key to study new physical phenomena arising from structures on the size of small molecules. The computer industry is one example that demonstrates our day to day use of nanotechnology. Tremendous progress has been made over the last years in increasing the processor speed of modern computers, which was mainly achieved by placing more transistors on the small size of a CPU chip. However, at some point this comes to a limit. One cannot make the transistors smaller or pack them more compact, because quantum effects like the tunneling effect come into play and make the control of the current flow in the thin channels challenging. Already today, Intels 10 nm technology shows a minimum metal pitch between the transistors of 36 nm and a transistor density of 100.8 mega transistors per mm<sup>2</sup> [6, 7]

Hence, with electronic transistors a very high increase in CPU speed cannot be expected anymore. However, electrons are much slower than photons, which means replacing electronic transistors by photonic transistors could increase the speed dramatically. This would also be a big step towards new super-computers. The development of such optical transistors, capable of ultrafast, sub-picosecond switching by using plasmonic nanostructures is already started [8].

Research on printed transistors by using organic polymer thin films is another field of research that relies on the principles of nanoscale light matter interaction and could be on a new leap towards foldable electronic devices, e.g. foldable smartphones [9].

More examples that demonstrate the importance of understanding nanoscale light matter interactions are amongst others the light-to-current conversions in artificial photovoltaic devices or the conversion of light into chemical energy in biological light harvesting systems.

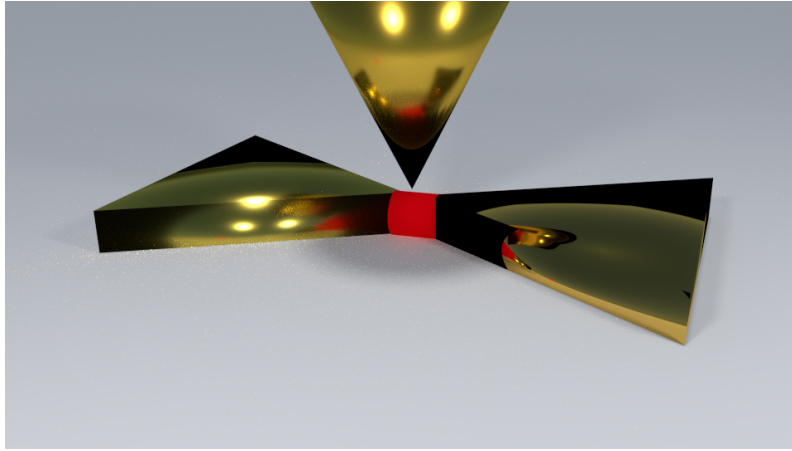


**Figure 1.1:** Visualizaion of a SNOM tip probing the fields of a bowtie nanoantenna

However, probing the optical properties of such nano systems is a challenging task. One way to investigate nanostructures is the use of microscopy and spectroscopy techniques.

On the one hand, tools like scanning electron microscopy (SEM) can resolve structures with a spatial resolution of less than 1 nm, but lack optical or chemical informations and often need a special sample preparation. On the other hand, standard optical far field microscopy is limited by the diffraction limit of light to a spatial resolution of a few hundreds of nanometers. Hence, the study of e.g. biological or chemical systems, such as the functions of proteins or new organic polymer solar cells, can become a difficult task. In most cases one cannot just extract the interesting nano-meter sized parts and investigate them in a macroscopic environment. Especially proteins often only function in their native environment, for example membrane proteins, involved in the energy transfer between light-harvesting complexes in photosynthetic membranes, depend on the presence of other neighboring proteins [10].

As we can see from these examples the challenge is to have a tool to probe topography and optical signals of the light-matter interaction within a spatial resolution in the sub-10 nm regime without altering the sample itself. Scanning near-field optical microscopy (SNOM) has proven to be such a tool. In SNOM the diffraction limit of light is bypassed by making advantage of evanescent fields of a nanometer sized probe which is brought in close proximity to the sample. Especially apertureless designs using a sharp metallic tip have shown big advantages in terms of optical resolution over aperture based designs using etched fiber tips as a probe. In a backscattering type apertureless SNOM used throughout this work an etched gold tip is used as a scatterer that transforms the evanescent near-fields between tip and sample into propagating far-fields, which can be measured by standard far field detection, e.g. a photodiode.

Although scanning near-field microscopy with monochromatic laser light can be already a very powerful tool in revealing the physics behind such nano systems, probing chemical informations

or resonance conditions of plasmonic structures often requires measurements at many different wavelengths, or in other words optical spectroscopy. In addition, when using a broad-band and short pulsed laser beam with pulse durations in the low fs-regime, investigation of time dynamics by the use of pump probe setups becomes possible. This technique already revealed the importance of coherent vibronic coupling between electronic and nuclear motion after electronic excitation for charge separation and transfer in a model organic photovoltaic material [11], but has not been used on a local nanometer spot size.

Thus, combining optical spectroscopy with the high spatial optical resolution of SNOM has a high potential of revealing new insights in nano materials such as organic substrates (dyes, proteins, polymers) or plasmonic structures (nano antennas, nano lenses, plasmonic devices, etc) and could even shed some light on the dynamics of primary light-induced processes such as light harvesting reactions, specific plasmonic structures or other organic materials.

In order to combine SNOM with broad band spectroscopy some experimental hurdles have to be overcome. The main conflict that arises is the way optical signals are recorded by the SNOM. Optical near-fields that are scattered by the SNOM tip into the far field are typically of very low intensities compared to the intensity of the input beam and background signals arising from scattering and reflection at the tip shaft and other optical elements. Hence, the signal to background ratio is very low which makes the direct interpretation of SNOM images nearly impossible. To increase this ratio, a common way is to modulate the tip with a high frequency of some tens of kilohertz and demodulate the optical signals. Since the near-fields arising at the tip show high non-linear components, the scattered near-field signal typically contains modulated signals at a higher orders of the modulation frequency. The background signal has a linear dependence to the input power and vanishes at the higher orders of the tip modulation frequency. Thus, demodulation at a frequency multiple times of the modulation frequency can help to suppress the background contribution.

Such higher order demodulation can easily be applied for one wavelength with existing devices, but becomes challenging when measuring spectra. In the past, various attempts have been made to mix spectral information with SNOM images, e.g. by tuning the wavelength of the laser and measuring an area of the sample for each wavelength again, or indirectly measuring spectra by Fourier Transform Interferometry for each point on the sample [12–14]. Disadvantages like mechanical drift of the sample during the repeated scans or a long recording time for each spectrum in FT interferometry however demand for a new method.

In this PhD thesis a self-built SNOM is presented that can overcome these downsides. I present a way to increase the near-field to background ratio for any given sample by homodyne detection with an inherently stable in-line interferometer using a modified sample substrate. This technique can easily be applied to broad-band nanoscale spectroscopy as well. Further, I will introduce a new direct way of recording SNOM spectra by using a very fast line camera attached

to a monochromator. In this way one is able to record spectra with a very high line rate and is capable of measuring spectra demodulated up to the 4th order of the modulation frequency. Such high spectra recording speeds only became possible during the last years with the increasing readout speed of modern computers. To my knowledge this is the first approach so far which demonstrates a direct measurement of local spectra with commonly known back-scattering-type SNOM setups that involve modulation techniques. Also, it could easily be added to a lot of existing SNOM setups and it is much faster than previous methods. Furthermore, I provide a theoretical description to model such signals and investigate the influence of the tip on the spectra in the visible spectral range. Finally, SNOM nanoscale spectroscopy is used to understand the connection between function and structure of promising new organic solar cell materials and to map the near-field around a plasmonic nanoantenna.

The thesis is divided in 7 chapters:

**Chapter 2** gives an overview of SNOM microscopy and spectroscopy in general and sets the work of this thesis into perspective to previous studies.

**Chapter 3** presents the SNOM setup that is used throughout this thesis in order to measure near-field signals both monochromatically as well as spectrally resolved. For this purpose, also the demodulation process for both cases is explained in detail and a first investigation of background signals in SNOM measurements is presented.

**Chapter 4** introduces a theoretical description of SNOM signals, which is divided in two sections: **Chapter 4.1** introduces models to describe the medium. In particular a quantum mechanical model is established that is later used to describe the dielectric function of a dye based on its optical transmission properties. Furthermore, a transfer matrix model is described that is used at various steps throughout this thesis to calculate the transmission of light through a system of multiple layers with various refractive indices. Finally, the chapter presents a description for anisotropic samples such as the dye investigated in chapter 6. Anisotropic samples have a different dielectric function for different directions within the sample. A way to calculate the transmission spectra of such a medium with a modified transfer matrix method is given.

**Chapter 4.2** takes a closer look at the simulation of the tip-sample interaction. At first, the well-established image dipole coupling model previously introduced by Keilmann & Knoll [15] is presented. A more detailed description of our SNOM signals is then given by a more complete characterization in a Green's function approach that additionally considers the focus fields and can easily be expanded to more specific setups, e.g. with a tilted tip. I will show that under certain circumstances and approximations both models will converge to the same result.

**Chapter 5** presents a way to extract a low near-field signal out of a large background signal

by using an inherently stable in-line interferometer for homodyne mixing of the near field and a reference field. Approach curve measurements and a detailed near-field and background analysis will show the benefit of this newly introduced in-line interferometer for SNOM measurements in general, but also especially as an important step towards SNOM spectroscopy.

**Chapter 6** finally presents our efforts in measuring and modeling local SNOM spectra. Here, I first show spectra measured with the SNOM on a flat gold film evaluated by a simple interference model in **chapter 6.1**.

In the next step, **chapter 6.2** discusses various measurements on flat films by taking into account the complete vectorial tip-sample coupling. The influence of the focus fields and the reference field is discussed here as well. Also, this section exemplarily shows a typical evaluation of the measured, demodulated optical signals and introduces a way to recreate spectrally resolved approach data from the recorded raw data.

**Chapter 6.3** then applies this method to local spectra measured on a more complex sample: an anisotropic squaraine dye spincoated on top of a substrate. To understand this relatively new dye, firstly transmission spectra are presented from which we obtain the dielectric function of the dye by modeling it as a 2-level system in a quantum mechanical model. Secondly, the local SNOM spectra recorded on that sample are analyzed and compared to simulations that take into account the previously found dielectric function. We could demonstrate chemically specific SNOM maps by recording local spectra around a gold nanoparticle placed on top of the dye layer.

**Chapter 6.4** concludes this chapter by discussing SNOM spectra measured around a nanorod antenna. In contrast to the squaraine dye, we are able to show not only coupling to one of the tip's polarization tensor component, but a coupling to both the in-plane and out-of-plane components can be observed spectrally separated in the same measurement and hence allows for a disentangling of in-plane and out-of-plane electric field vector components.

**Chapter 7** summarizes the main results of this thesis.

All in all the thesis provides an analysis of measuring and modeling SNOM signals and demonstrates a way to measure local SNOM spectra with modern techniques that may in the future find application in other setups as well and will help in understanding new physical phenomena.



# Optical Near-field Microscopy and Spectroscopy

---

# 2

Apertureless scanning near-field microscopy has proven to be a very useful tool used in many research areas that can reveal chemical as well as structural contrast in different wavelength regions ranging from optical frequencies up to mid-infrared or even microwave frequencies [16] with a spatial resolution of up to a few nanometers. However, from early on, one of the main challenges in SNOM is the suppression or separation of a background field scattered from the tip shaft. The background field does not contain any relevant information and originates from a rather large area compared to the tip apex radius. The existence of this background field makes qualitative statements of the sample properties difficult as it is interfering with the desired spatially localized near-field. Hence, a proper extraction of the near-field is of high importance to avoid SNOM artifacts and misinterpreted measurements.

To fulfill this task different light detection and analyzing procedures have been developed over the last decade.

This chapter gives an overview over existing microscopy and spectroscopy methods that are available and in particular focuses on the advantages and also difficulties using a scanning near-field microscope. In the second part different detection schemes are presented that point out ways to deal with background suppression in SNOM.

## 2.1 Introduction - The Status Quo

Optically investigating materials with a high spatial resolution has been of high interest for centuries to study biological, chemical and physical samples. However, due to diffraction effects the spatial resolution in classical microscopy is limited roughly to  $0.61/(\lambda \cdot NA)$  (Abbé criterion [17]) which depends on the wavelength  $\lambda$  and the numerical aperture  $NA$ . For conventional wide-field microscopy the limit for small wavelengths is around 250 nm. This wavelength dependency in the Abbé criterion also shows the practical importance of electron microscopy, like transmission electron microscopy (TEM) or scanning electron microscopy (SEM). Hereby, the wavelength of the electron is given by the de Broglie relation  $\lambda = h/p$  with the Planck's constant  $h$  and  $p$  the momentum of the electron. Depending on the acceleration voltage this wavelength can become very small and resolutions of 1 Å can be achieved. However, for electron microscopy the samples often need special preparation, are placed in a vacuum and have to be conductive. This makes imaging e.g. of living cells impossible. Furthermore, the high energies needed in TEM can destroy the sample and in all cases a lack of optical information corresponds to a lack of chemical contrast, i.e. different chemical materials on the sample cannot be identified.

For optical frequencies the spatial resolution of conventional confocal microscopy setups could be reduced to around 180 nm [18–20] by using oil immersion [21] to increase the refractive index and thus the NA.

Still, many samples like cell membranes, dye substrates, computer transistors or fabricated nanostructures show features much smaller. To study such small systems different optical techniques have been developed.

For biological samples the versatile use of fluorescent probes, that could be attached for example to proteins, sped up the development of new microscopy devices that could improve the optical resolution by taking advantage of fluorescence properties [22–25]. Recently, E. Betzig, S. Hell and W. Moerner were rewarded with the Nobel Prize in Chemistry for surpassing the limitations of light microscopy by the invention of stimulated emission depletion (STED) microscopy and single-molecule microscopy [26]. Both techniques rely on the fact that fluorescence of single molecules can be turned on and off. In STED one laser beam stimulates fluorescent molecules, whereas a second beam with a donut-shaped laser profile is forcing a relaxation of the excited electron by stimulated emission leading to a red-shift of the emitted photon that can be filtered out. This process is called stimulated emission depletion and is happening over the whole beam except for a small volume in the middle. The resolution is defined by the small volume that can be as small as 6 nm, which was demonstrated by probing a diamond center vacancy [27]. Even nanoscale dynamics in a living cell could be demonstrated [28]. Other fluorescent techniques have arisen in favor of the flexibility of labeling different parts of a cell with fluophores, like Stochastic Optical Reconstruction Microscopy (STORM) [29] or Photo-Activated Localization

Microscopy (PALM) [30]. All in all, these techniques are mainly used for biological samples as for example specific parts of a protein can easily be linked with a fluorescent dye. Nevertheless, the high power used for example in STED that can lead to the destruction of the fluorescent molecules by photochemical effects and the limited photostability due to bleaching and blinking effects often demand the use of other techniques.

Scanning near-field optical microscopy (SNOM) is a class of instruments that is not limited by fluorescence effects, is not destroying the sample and does not require a special sample preparation, but still allows to measure optical signals at the surface with a spatial resolution much below the diffraction limit. In SNOM a nanometer-sized probe is brought very close to the surface and the evanescent near-fields between probe and sample are utilized to obtain high-resolution optical images by raster scanning the probe over the sample. Over the years many different methods have been developed to make use of the near-field interaction. These can be separated in aperture based SNOM (a-SNOM), using for example an etched fiber with a small aperture as light source, or scattering-type SNOM (s-SNOM) for which the scattered near-fields from a sharp metallic tip are detected in the far-field [10, 31, 32].

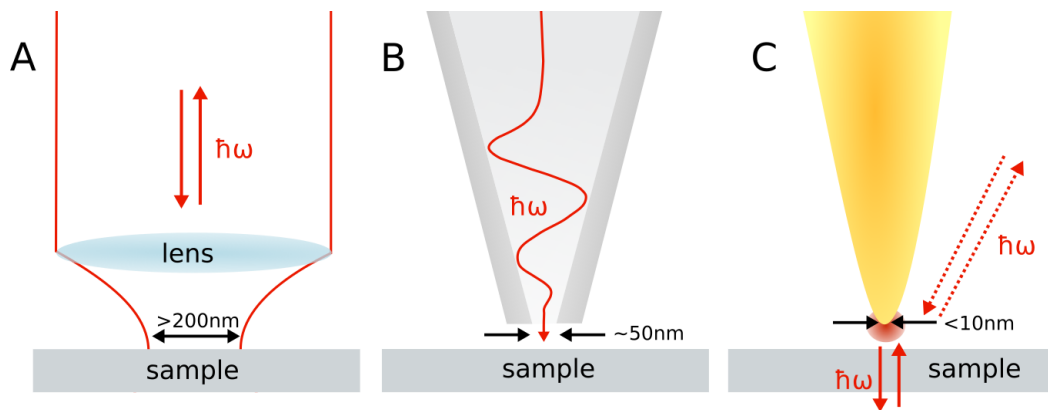


**Figure 2.1:** Different optical measurement methods and their resolution. (A) Confocal microscopy, (B) aperture-SNOM, (C) apertureless scattering-type SNOM.

Historically, a-SNOM was invented first and the idea of using a tiny aperture as a local probe can be dated back to the first concepts of E.H. Syngé in 1928 [33]. He suggested that irradiating a perfectly reflecting screen with a tiny aperture of size  $d$  would lead to spatially confined fields of the size of the aperture. A scatterer will only interact with this confined field if it is within a distance  $d$ . Due to the lack of nanofabrication his idea was forgotten at that time, but it was reinvented several times in later years. The first experimental demonstration for optical frequencies was given by Pohl et al. at the IBM research institute in Switzerland [34] and by Lewis et al. at Cornell university [35]. In most a-SNOM devices an aluminum coated fiber tip with a small, uncoated aperture at its end is used to either guide the light to locally

illuminate the sample (compare figure 2.1B) or collect near-fields from an already irradiated sample. The resolution for this type of SNOM is mainly given by the size of the aperture, but there is a trade-off between light throughput and lateral resolution [36–38]. Practically, this trade-off is limiting the resolution to about 50 nm-100 nm and an improvement is most likely not achievable with the current a-SNOM techniques [10, 39].

In apertureless s-SNOM a solid metal or dielectric probe is brought close to the sample and is scattering the local fields into the far field. The resolution is mainly given by the size of the probe that can be smaller than 10 nm [40, 41]. By making use of nonlinear effects with high field strengths or light localization by means of gap plasmons the resolution can be even smaller [42–45]. SNOM with pointed probes can be seen from two perspectives. In the first case, a sharp metallic tip is scattering the near-fields induced by irradiating the sample itself, thus the tip is locally perturbing the fields of the sample. In the second case the tip itself can be used as a local light source, making use of enhanced fields at the tip apex. Both these scenarios are in principle dependent on each other as a strong field enhancement is a condition for efficient scattering and the other way around [10]. Depending on the sample and the used tip however, one of these effects can predominate as we will outline in 4.2.

A typical sSNOM setup is shown in figure 2.1C. Here, a diffraction limited laser focus illuminates both sample and probe. The illumination can be either from the side or from the bottom (backscattering-s-SNOM). The probe is mostly a sharp metallic or dielectric tip, preferably metal tips are used as they have a better scattering efficiency [46]. The scattered near-field signal is collected in the far field by a detector. To keep the tip-sample distance constant usually an atomic force microscope in tapping mode is used, i.e., the tip is modulated with a frequency  $\Omega$  at some tens of kilohertz normal to the surface and the amplitude of this oscillation is recorded. Short-ranged forces acting on the tip decrease the amplitude that can thus be used as a measure of tip-sample distance and can be kept constant using an electronic feedback acting on the tip or the positioning stage of the sample.

The conceptual idea of using a light-irradiated particle for achieving subwavelength light localization was already outlined by Synge in a prophetic letter to Einstein in 1928. Considering the particle as a structure that efficiently converts energy from the incident radiation into localized energy, this letter can also be seen as the historical root of concept for optical nanoantennas [47, 48]. His idea, however, was not published because of concerns about the large reflected light from the sample that would overshadow the local interaction between particle and sample. In fact, separating the desired near-fields in today's setups from disturbing background fields is still one of the main challenges in s-SNOM. Figure 2.2 illustrates the situation for a backscattering type s-SNOM setup. Here, not only the near-field  $\vec{E}_{\text{NF}}$  is scattered from the tip apex, but a background field  $\vec{E}_{\text{B}}$  from the taper shaft and a field  $\vec{E}_{\text{R}}$ , directly reflected from the sample, propagate to the detector as well. These three fields are interfering and a high ratio

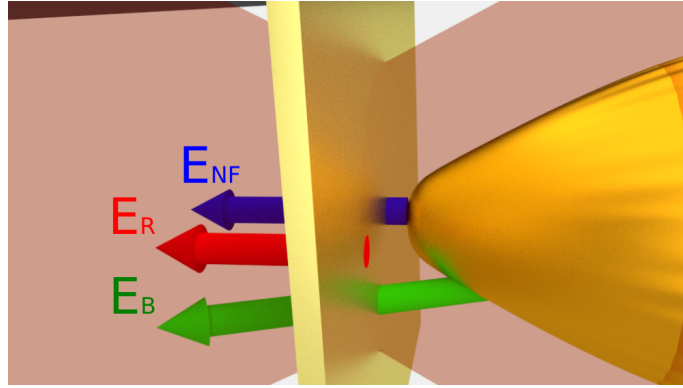


**Figure 2.2:** Visualization of the three fields that interfere on the detector: The near-field  $\vec{E}_{\text{NF}}$ , a background field from the tip shaft  $\vec{E}_{\text{B}}$  and the reflected field from the sample  $\vec{E}_{\text{R}}$

of background-field to near-field often makes a direct extraction of  $\vec{E}_{\text{NF}}$  impossible. Hence, nowadays modulation and demodulation techniques can be found in many SNOM setups with the goal of suppressing the background field. Hereby, the tip, modulated by a tapping mode AFM with a frequency  $\Omega$  in the 10 kHz-range [49], generates a modulated optical signal that is demodulated at the modulation frequency or higher harmonics  $n \cdot \Omega$  with  $n > 1$ . Mostly the scattered near-field signals show a high nonlinear dependence on the tip-sample distance and generate higher harmonics, whereas the background field  $\vec{E}_{\text{B}}$  is largely linear and contributes less to the higher harmonics [50]. This leads to an improved image contrast. Nevertheless, a complete suppression of the background-field is still challenging as the interference of the fields cannot easily be disentangled in the measured intensity signal [51–54]. Hence, over the last decade many interferometric detection techniques have been developed to either enhance the near-field or suppress the background signal. This often involves mixing the weak SNOM signal with a known reference wave in a Michelson interferometer geometry. A detailed discussion of these techniques is given in section 2.2 and 5.3.

Since s-SNOM is not limited to specific wavelengths this further opens up the possibility to apply optical spectroscopy methods to improve the value of information that can be discovered for the sample under investigation. In general optical spectroscopy is a powerful tool as most electronic and vibrational processes have energies in the range of the visible to near-infrared light and therefore can be probed with a broad-band spectrum. In combination with ultrafast pump-probe schemes [55–57], it also allows to probe excited state dynamics or potential coupling mechanisms [58], which for example helped to discover quantum effects in photosynthetic systems [11, 59–61]. Hence, near-field spectroscopy could enable locally confined spectroscopic measurements and thus provide a chemical contrast to many samples or even shed light on the dynamics of primary light-induced processes such as light harvesting and photo-catalytic surface reactions.

Even though combining spectroscopy and SNOM is a challenging task, many research groups have already used the wealth of new local spectroscopic information to expand their knowledge and understanding of materials and nanostructures. Early measurements with aperture-SNOM could for example demonstrate structural phase-selective imaging of organic materials by measuring local absorption spectra with a broad-band laser source coupled into the fiber tip [62, 63]. Furthermore the investigation of chemical contrast in various samples with SNOM in the IR range using a tunable free electron laser [64, 65] became possible and even surface-plasmon resonances in single metallic nanoparticles could be studied [66]. Such a-SNOM measurements were however limited to a resolution around 50 nm-100 nm as outlined before.

Applying broad-band spectroscopy methods to aperture-less s-SNOM setups is more challenging due to the higher order demodulation and advanced detection schemes typically required to suppress the scattered background light. Nevertheless, many approaches have been made. Most of these can be classified into two different groups.

One common approach is to use a tunable laser and repeatedly measure monochromatic SNOM scans at different wavelengths, often around a resonance of the material [7, 12, 40, 67–77]. Amongst others, this method has provided insight into the characterization of individual nanobeads and viruses, secondary structure identification of proteins [14], the phononic enhanced near-field response of SiC samples [76], the local infrared response of semiconductor nanowires [73] or spectroscopic mapping of nano transistors [7]. On the one hand even two measurements, resonant with the sample and off-resonant with the sample, can be used to identify chemical compounds due to a wavelength dependent vibrational contrast [69]. On the other hand, if more than one spectral feature or more resonances occur, then a complete spectral representation is required. With this method however, the overall spectroscopic information is limited by the number of SNOM scans. In addition, systematic errors can occur over the time of the measurement as the sample can drift during repeated scans and the tip can be contaminated or damaged. Consequently, this would result in a different apex radius. Moreover, the optical alignment can vary with each new wavelength setting. In order to interpret the results from the limited amount of spectral information the data points are mostly compared to theoretical models that describe the tip-sample interaction. A requirement to apply these models to the measurement often is the prior knowledge of the sample's dielectric function that has to be obtained either by a separate measurement or a simulation.

The second approach to s-SNOM spectroscopy is to measure full spectra at specific positions or for the full SNOM image by Fourier Transform interferometry (FT-interferometry) [13, 78–82]. Fourier Transform interferometry is a time-domain measurement [83], i.e. two beams from a spectrally broad-band laser are time delayed and interfere e.g. in a Michelson interferometer. The time delay can be varied by a movable delay stage in one of the interferometer arms and for the detection a common photodiode can be used. With the movement of the delay line the time domain is converted into spatial coordinates. By applying Fourier Transformation to the

resulting correlation function the spectrum can be retrieved.

A first combination of FTIR interferometry with SNOM was shown in 2006 [14] using a technique called comb-FTIR [84–87]. Comb-FTIR is based on two Ti:sapphire lasers emitting femtosecond pulse trains with slightly different repetition frequencies. The two beams are each used to generate broad spectra in the mid-infrared by the use of a GaSe source. The interference of both beams on the detector then yields the time-domain interferogram from which the spectrum can be recovered. Thus, comb-FTIR employs time-domain retardation without any mechanically moving stages. Technically, it was therefore more a multiheterodyning technique than a common FTIR interferometer. The spectroscopic information in this case was limited to a set of discrete frequencies and integration times of up to a minute per pixel due to the weak broad-band laser source [14] did not allow for a routine operation of spectroscopic SNOM.

In later years the employment of a single broad-band laser source and a delay stage enabled the measurement of continuous spectra as well [79]. Supported by the development of high-power broad-band laser this technique, also often referred to as nano-FTIR, has provided a new way to measure absorption spectra of molecular fingerprints with 20 nm resolution [13], demonstrated for example on a single tobacco mosaic virus [81]. Unlike conventional FTIR spectrometer, nano-FTIR provides both amplitude and phase information by placing the sample and SNOM tip in one of the interferometer arms and using common SNOM detection schemes. The nano-FTIR measurement itself, however, can still take up to a few seconds per position on the sample, as the delay stage has to be scanned over a range of a few millimeters and needs to be stable over this time. This procedure makes this technique very slow compared to monochromatic SNOM imaging.

As an additional note, phase-stable pulse pairs for optical frequencies may be achieved with a novel interferometry method based on a birefringent delay line. This system is often referred to as Translating-Wedge-Based Identical Pulses eNcoding System (TWINS) [88, 89] and has already been applied for 2D pump probe spectroscopy measurements [90] and may in the future also be used in SNOM for FTIR purposes.

From this scientific horizon it becomes clear that mostly indirect measurement of spectra have been performed so far. Apart from early a-SNOM measurements with limited spatial resolution a direct approach using a spectrometer is rare.

In particular, direct spectra measurements with s-SNOM have only been reported for setups that do not use the common modulation and demodulation techniques. To still achieve background-free measurements different ways have been used e.g. by measuring signals at a different wavelength than the excitation wavelength in local photoluminescence [91] or fluorescence measurements [92]. In the latter case the enhanced near-fields at the apex from a gold tip could be used as a two-photon excitation source for molecular fluorescence, which is related

to a quadratic intensity dependency. Hereby the strong optical background can be decoupled from the desired near-fields by detecting at a different wavelength. Another example of a direct spectra measurement with a resolution of only a few nanometers was recently performed in our own group by the use of an adiabatic nano-focusing SNOM [93, 94]. Hereby, the light scattering from the apex of a gold tip is separated from the excitation by the use of a grating coupler launching surface plasmon polaritons (SPPs) in a large distance from the apex. Due to this separation of excitation and nano-focused light spot nearly no optical background contributes to the measured signal. Thus, no demodulation techniques are required and direct spectra measurement can be carried out. Even though the results are very promising, adiabatic focusing SNOM is a rather new technique that is still under active development. Producing such gold tips with a grating can for example still be a challenging task that requires a focused ion beam milling setup and careful treatment of the tips. In addition, the grating bandwidth is limiting the overall spectral range of the SPP coupling. With the presented adiabatic SNOM setup, employing a gold tip, measurements in the visible to UV region are not possible at all, as the SPPs are limited to phonon energies below the interband absorption of gold and would be absorbed very fast and would not reach the tip apex. In order to retain maximal flexibility regarding wavelength range and also polarization we decided to pursue the development of a sSNOM in back-reflection geometry. The extended homodyne detection with a sSNOM by using an in-line interferometer (cf. chapter 5) as presented in this thesis is restricted in spectral range only by the tip material and allows for broad-band spectroscopic measurements.

Finally, mainly two experimental challenges have to be mastered in order to record local broad-band spectra with common, well-understood s-SNOM setups in a direct spectrometer approach: First, the background signal has to be suppressed efficiently over a broad spectral range. Secondly, spectra have to be recorded with a high sample rate to allow for higher order demodulation of the tip frequency  $n \cdot \Omega$  at multiple wavelengths at once, e.g. using a fast camera or spectrometer. The use of a camera or spectrometer instead of a photodiode also means that lock-in amplifiers cannot be used for the demodulation process anymore, but modulated spectra have to be processed using filtering in the frequency domain by performing a Fourier transform e.g. in a post-processing step with a computer. This sets high demands for processing the 4D data array (2D position plus time and wavelength). With the progress in technology, in particular in modern line cameras, and the high CPU and data transfer speed of modern PCs this task becomes manageable, though. Within this thesis I present to my knowledge the first direct approach using a fast line camera that can record spectra up to the 4th harmonic of the tip frequency, or in other words with a line rate of up to 210 kHz. In order to fulfill also the second requirement, the spectrally broad-band discrimination of the near-field from the background field, I implemented a detection scheme that amplifies the near-field signal by mixing the scattered signal from the tip with a well-controlled reference wave from an

inherently stable in-line interferometer [52]. This concept will be explained in more detail in chapter 5. In the next section the previous development of detection schemes, that were used in SNOM setups to suppress background fields, is presented and their often limited usage for spectroscopic measurements is evaluated.

## 2.2 Detection Schemes in Scanning Near-Field Microscopy

A scanning near-field optical microscope is sensitive to material changes on the nanoscale, since the evanescent near-fields contain informations about the samples properties. However, the near-fields are arising from a very small scattering cross section that is mainly given by the tip apex radius which is much smaller than the focused laser beam exciting the tip dipole. This situation sets particular demands to the detection of these signals, as also a background field is scattered from the tip shaft and a constant reference field is reflected from the substrate. To measure weak near-fields out of a large background it is not sufficient to place a photodiode into the detection path and perform a linear measurement, but due to the interference of these fields more advanced detection techniques have to be applied. The goal of these techniques is to either increase the near-field signal or suppress the background field. Ideally, both is done at the same time.

Apart from the previously mentioned two-photon absorption and fluorescence measurement that depend on the high near-field strength [92] and the recent demonstration of background-free measurement with an adiabatic focusing SNOM [95–98], in general sophisticated detection techniques have to be applied to get rid of the optical background. Many of these detection techniques evolved over the last decade and depend on interferometric measurements and higher order demodulation of the tip-sample distance. In total this allows to measure arbitrary samples without being restricted for example to fluorescent effects. The key feature of most of these techniques is the amplification of the near-field with a strong reference field. This principle is also used in the in-line interferometer presented in chapter 5. In this section an overview of the most common techniques that could be applied to a sSNOM in back-reflection geometry is given. Each of these have some requirements e.g. are restricted to monochromatic measurements, lack information about the optical phase or need special measurement conditions or sophisticated analysis tools.

### 2.2.1 Homodyne detection

A rather simple detection method is called homodyne detection. In interferometry this means the sample and reference beam are from the same source, but only the sample beam is modulated at a given frequency. In the demodulation process only the modulation frequency is involved. Transferred to SNOM this means the tip-sample distance is modulated at a given frequency

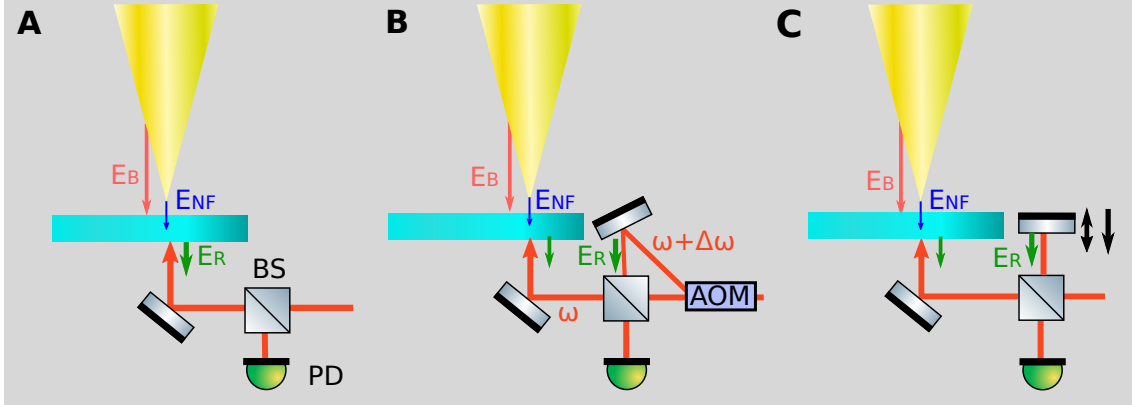


**Figure 2.3:** Visualization of different detection schemes for a sSNOM in back-reflection geometry. (A) Homodyne detection, (B) Heterodyne detection, (C) Pseudo-heterodyne/synthetic optical holographic detection

and the scattered, modulated optical signal is converted to a modulated current signal by a photodiode, which is fed into a lock-in amplifier. The signal used to excite the tip motion can be used as the reference signal and amplitude and phase of the optical signal can be extracted. Homodyne detection has the advantage that it is easy to set up and does not require any additional tools. However, for SNOM the situation is more complex. As visualized in figure 2.3A we do not only have the modulated optical near-field  $\vec{E}_{NF}$  from the tip mixing with a stable reference signal  $\vec{E}_R$  reflected from the substrate, but an additional, modulated background field  $\vec{E}_B$  scattered from the tip shaft is mixing with both fields as well. We can write the interference of the three fields as

$$\begin{aligned}
 I &\propto |\vec{E}_R + \vec{E}_{NF} + \vec{E}_B|^2 \\
 &\propto |\vec{E}_R|^2 + |\vec{E}_{NF}|^2 + |\vec{E}_B|^2 + 2|\vec{E}_R||\vec{E}_B|\cos(\phi_B - \phi_R) + 2|\vec{E}_{NF}||\vec{E}_B|\cos(\phi_B - \phi_{NF}) \\
 &\quad + 2|\vec{E}_R||\vec{E}_{NF}|\cos(\phi_{NF} - \phi_R)
 \end{aligned} \tag{2.1}$$

with  $\phi_B$ ,  $\phi_{NF}$  and  $\phi_R$  denoting the phases of the three involved fields. Both  $\vec{E}_B$  and  $\vec{E}_{NF}$  are modulated by the tip-distance modulation frequency and thus only the term  $|\vec{E}_R|^2$  is suppressed after demodulation. Furthermore, the optical background field  $\vec{E}_B$  in the measurement is in general much larger than the desired near-field  $\vec{E}_{NF}$ . This makes extracting the near-field amplitude and phase difficult. A common trick to suppress the large background is to apply higher order demodulation as the near-field is an evanescent field with exponentially decreasing amplitude for larger tip-sample distances, but the background field scales over distances larger than the wavelength of light. Thus, modulation of the tip with a modulation amplitude on the length scale of the exponential decay leads to a rapid change of the near-field interaction which generates scattered fields at higher harmonics. In contrast, the amplitude of the background

field is decreasing much faster for higher harmonic demodulation.

However, even at higher order demodulation an interference term of the near-field with the lowest order background term remains. That means interference between near-field and background is distorting the measurement even at higher order demodulation. Hence, as a more detailed evaluation in section 5.3 will unveil, the ratio between  $E_R$  and  $E_B$  has to be high to be able to extract almost background free near-field contrast. In most cases, these circumstances make an increased reference field indispensable. This could for example be realized by placing a mirror in the unused path of the beam splitter in figure 2.3A. In that way the reference field would be defined by the reflection from the external mirror rather than by the reflection from the substrate. Such an interferometer on the other hand needs to be stable over the period of the measurement time. This needs precise alignment and very good measurement conditions which are not easy to achieve. A way around this is by using a modified sample substrate and using the substrate as a second mirror of an inherently stable inline interferometer[52]. This method was developed during this thesis and is demonstrated in chapter 5. It further provides the basis for local spectroscopy with a spectrally broad-band laser input.

### 2.2.2 Heterodyne detection

Another way of reducing the signal to background ratio and to extract amplitude and phase information of the optical near-field is by using heterodyne detection visualized in figure 2.3B. In general, heterodyne detections means that two signals are mixed, but the reference signal has a different frequency than the sample signal. Typically one or two crossed acousto optical modulators (AOMs) are used at the very beginning of the setup to produce two beams of the used laser with laser frequencies  $\omega_1$  and  $\omega_2 = \omega_1 + \Delta\omega$  with  $\Delta\omega$  typically in the kilo Hertz regime [54, 99]. Again, after measuring the intensities with a photodiode a lock-in amplifier is used to extract amplitude and phase. In this case however, the signal is demodulated at  $n \cdot \Omega + \Delta\omega$ , with  $n \cdot \Omega$  a multiple of the tip modulation frequency and  $\Delta\omega$  the difference frequency between  $\omega_1$  and  $\omega_2$ .

In detail we have one signal beam with frequency  $\omega_1$  interacting with the tip and one reference beam with frequency  $\omega_2 = \omega_1 + \Delta\omega$  not interacting with the tip. After interaction a near-field and background field from the tip is scattered into the far-field and all three fields interfere [99]:

$$\begin{aligned}
 I &= \left( |\vec{E}_{\text{NF}}| e^{i(\omega_1 t + \phi_{\text{NF}})} + |\vec{E}_{\text{B}}| e^{i(\omega_1 t + \phi_{\text{B}})} + |\vec{E}_{\text{R}}| e^{i((\omega_1 + \Delta\omega)t + \phi_{\text{R}})} \right)^2 \\
 &= |\vec{E}_{\text{NF}}|^2 + |\vec{E}_{\text{B}}|^2 + |\vec{E}_{\text{R}}|^2 \\
 &\quad + 2|\vec{E}_{\text{R}}||\vec{E}_{\text{NF}}| \cos(\Delta\omega + \phi_{\text{R}} - \phi_{\text{NF}}) \\
 &\quad + 2|\vec{E}_{\text{R}}||\vec{E}_{\text{B}}| \cos(\Delta\omega + \phi_{\text{R}} - \phi_{\text{B}}) \\
 &\quad + 2|\vec{E}_{\text{B}}||\vec{E}_{\text{NF}}| \cos(\phi_{\text{B}} - \phi_{\text{NF}})
 \end{aligned} \tag{2.2}$$

After demodulation at  $n \cdot \Omega + \Delta\omega$  only the interference of the near-field with the reference field and the background-field with the reference field remain. The former is the desired signal, from which the amplitude and phase of  $\vec{E}_{\text{NF}}$  can be determined, assuming a spatially independent and constant reference field  $\vec{E}_{\text{R}}$ . Using the same argument as for the homodyne detection, the background field can be suppressed by higher order demodulation of the tip frequency  $n \cdot \Omega$  with  $n > 2$  since the amplitude of the background field is decaying much faster at higher harmonics of the tip frequency [50, 54].

The downside of this method is that the acousto optical modulator not only generates a second laser beam with a different frequency but also with a different output direction than the input laser beam. Therefore both beams have to be carefully aligned. Also AOMs are typically designed for a specific laser frequency which makes this method unusable for broad-band spectroscopic measurements.

### 2.2.3 Pseudoheterodyne detection and phase-shifting interferometry

To overcome the disadvantages of using an acousto optical modulator the so called "pseudoheterodyne detection" is replacing the frequency shift of the heterodyne detection with a sinusoidal phase modulation of a reference beam [100]. As visualized in figure 2.3C this is accomplished by mounting a piezo-electric mirror in the reference arm of the Michelson interferometer, which is modulated with a frequency around some hundred Hertz up to a few kilo-Hertz limited by the resonance frequency of the mirror.

In contrast to homodyne detection, the reference beam is not constant anymore, but is now modulated and can thus be written as

$$\vec{E}_{\text{R}} = |\vec{E}_{\text{R}}| e^{i\gamma \sin(\nu t) + i\Psi_{\text{R}}}, \quad (2.3)$$

with the phase modulation frequency  $\nu$ , the phase modulation depth  $\gamma$  and the phase offset  $\Psi_{\text{R}}$  that accounts for the optical path difference between the tip scattered signal and the reference signal. The phase modulation  $\gamma = \Delta l 4\pi / \lambda$  is further related to the vibration amplitude of the mirror  $\Delta l$  and the wavelength  $\lambda$ .

In general the modulation frequency  $\nu$  is much lower than the tip modulation frequency which means the interference of both signals is similar to an AM modulated signal, resulting in sidebands with frequencies  $f_{n,m} = n\Omega + m\nu$  in the spectral representation as shown in figure 2.4.

At the frequencies with  $m = 0$  the signal again contains a mixture of background field and near-field, but at the sidebands with  $m > 0$  this mixed term is not contained. Similar to heterodyne and homodyne detection we can again demodulate at higher harmonics of the tip frequency to suppress the additional interference of the reference with the background field. As shown by Ocelic et al. [100] a complete recovery of amplitude and phase of the optical

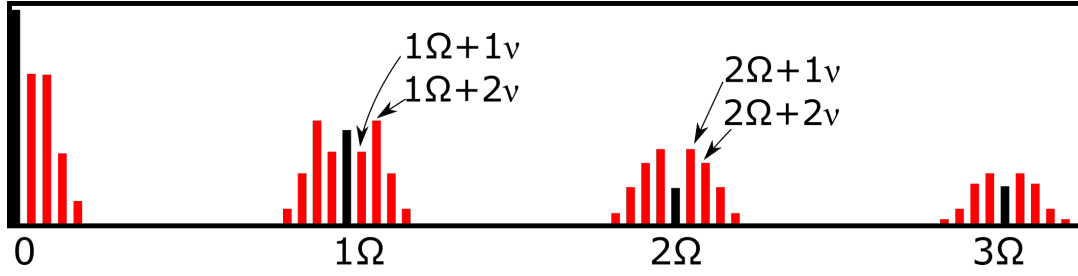


**Figure 2.4:** Spectral components in a pseudoheterodyne sSNOM setup with tip modulation frequency  $\Omega$  and reference mirror modulation frequency  $\omega$ , adapted from [100]

near-field signal is possible by demodulating at two neighboring sidebands, for example with  $n = 2, m = 1$  and  $m = 2$ :

$$E_{\text{NF}} = k \cdot [S_{n,2}/J_2(\gamma) + iS_{n,1}/J_1(\gamma)] \quad (2.4)$$

Here  $S_{n,j}$  denotes the demodulated detector signal at the  $n$ th harmonic of the tip frequency and the  $j$ th sideband. Further,  $J_m$  is the Bessel function of first kind and  $m$ th order and  $k$  is a complex constant that depends on the phase  $\Psi_R$  between near-field and reference field. As we can see from this equation the amplitude of the oscillating mirror is of importance as it is the argument of the Bessel functions. For a modulation of depth  $\gamma = 2.63$  the two Bessel function cross each other and equation (2.4) can be further simplified to

$$E_{\text{NF}} = 2.16k \cdot [S_{n,2} + iS_{n,1}], \quad (2.5)$$

making the retrieval of phase and amplitude very easy.

Overall, using pseudo-heterodyne detection simplifies the extraction of near-field phase and amplitude very much. However, this also requires a long-time stable interferometer, which is not always easy to achieve and to add to existing sSNOM setups and may even requires active stabilization[101]. Furthermore, the simplification of equation (2.4) to equation (2.5) cannot be done for multicolor measurements as the modulation depth  $\gamma = \Delta l 4\pi/\lambda$  depends on the vibration amplitude  $\Delta l$  of the mirror and the wavelength  $\lambda$ . Furthermore, also the parameter  $k$  is depending on the phase  $\Psi_R$  between near-field and reference field that can change with  $\lambda$ . For relative contrast measurements with monochromatic light the parameter  $k$  might be neglected, but analyzing measurements with a spectrally broad input spectrum would require a more detailed evaluation.

Two similar methods which also fit into this category are two-step homodyning [40] and phase-shifting interferometry[102, 103]. In both cases the reference mirror is moved to specific

positions for each pixel on the scan image and the near-field amplitude and phase is recovered after post-processing the different measurements.

In the case of two-step homodyning interferometry, the higher order demodulated signal from the sSNOM is recorded for two positions of the reference mirror at every pixel of the scan image. In particular the first position of the mirror is set to a maximum demodulated detector signal which corresponds to a signal proportional to  $S_n \cos(\phi_n)$ . Then the mirror is moved by  $\lambda/8$  or a phase shift of  $90^\circ$  corresponding to  $S_n \sin(\phi_n)$  and the pixel or the scan line is recorded again[40]. From both the two homodyned interferometric measurements the amplitude and phase can be recovered. Following the same considerations as before this gives access to the amplitude and phase of the near-field using higher order demodulation.

Again, the necessity of having a phase-stable interferometer is a crucial precondition. If the phase of the interferometer fluctuates or the step size of the mirror cannot be controlled precisely, then the condition of having two measurements with  $90^\circ$  phase shift to each other is not fulfilled anymore. Hence, this method introduces an uncertainty related to the stability of the interferometer. Furthermore the need to quickly move the mirror between two positions, for example with a square wave generator, makes this method slow compared to other methods.

Detection with phase-shifting interferometry tries to improve the flaws of previous methods by moving the reference mirror through at least three phase steps and applying a more advanced algorithm to solve for near-field amplitude and phase[102]. Phase shifting interferometry can therefore be seen as a specific data collection and analysis method with different options depending on how the data is recorded and what type of algorithm is chosen for the evaluation. This can range from "Three-Steps Algorithms" to "Least-Square Algorithms" , "Carre Algorithm", "N-bin Algorithm" or others to just name a few [104]. In comparison to pseudo-heterodyne detection as an analysis in the frequency domain, phase-shifting interferometry is analyzing the data in the time-domain.

Phase shifting interferometry used as a detection scheme with a sSNOM setup has been demonstrated by B.Deutsch et al. [102] using a sinusoidal signal to drive the reference mirror in a way that it is moving through a  $2\pi$  phase shift for each pixel and a number of  $N$  equally distributed phase steps is recorded for each pixel, with  $N = 200$  in the mentioned work.

Consequently, each mirror position corresponds to a specific difference phase between the signal field from the tip and the reference field, which can be written in a simplified way as

$$I_i = A + B \cos(\phi + \delta_n), \quad \delta_n = \frac{2\pi n}{N}. \quad (2.6)$$

Here  $\phi$  is the phase change on scattering and  $\delta_n$  is the phase introduced by the reference mirror. To solve for the unknown  $A, B$  and  $\phi$  and thus to retrieve amplitude and phase of the near-field an N-Bin algorithm was used to evaluate the optical measurements.

In comparison to pseudo-heterodyne detection it can easily be seen that this method has the same setup requirements, in both methods a reference mirror is oscillating at a specific frequency. The difference is that the frequency of the mirror movement in the phase-shifting detection is only some tens of Hertz and therefore much slower as in the pseudo-heterodyne detection. In the frequency domain this also generates sidebands around the different harmonics of the tip frequency (compare figure 2.4). However, since the difference frequency is only a few tens of Hertz, the spacing between the sidebands is very small and typically all sidebands fall into the bandwidth of the lock-in demodulation around the harmonics of the tip resonance frequency [103]. This means pseudo-heterodyne interferometry makes the minimum number of measurements to determine amplitude and phase, while in the case of phase-shifting interferometry many redundant measurements are analyzed.

Overall this detection method is more robust against errors like misaligned piezo movement by making use of the flexibility of the phase-recovery algorithms.

By using a spectrally broad-band input this method would be similar to a Fourier Transform interferometry method, superimposing the phase shifts of many wavelengths [105].

#### 2.2.4 Synthetic optical holography

Recently, a new method was introduced in connection with sSNOM near-field detection, which is called synthetic optical holography [106–108]. Hereby, the mirror of the reference arm in figure 2.3C is not modulated for each pixel but rather moved constantly while one line is scanned. That means the phase is varied over a complete scan line in contrast to each pixel in the previous methods.

Probing the sample at position  $\vec{r}$  and moving the mirror with a constant speed  $v_R$  the phase

$$\phi_R(\vec{r}) = \frac{2\pi 2d(\vec{r})}{\lambda} \quad (2.7)$$

that depends on the position  $d$  of the mirror can also be written in a time dependent manner with

$$\phi_R(t) = \omega_{RH}t + \phi_0 \quad (2.8)$$

with  $\omega_{RH} = 2\pi 2v_R/\lambda$  and initial phase  $\phi_0$ . It can be shown that this creates a synthetically reference wave analogous to a plane reference wave in off-axis wide field holography [106]:

$$U_R = A_R e^{i\phi_R} = A_R e^{i\vec{k}_{\parallel}\vec{r}} \quad (2.9)$$

with  $\vec{k}_{\parallel} = (k_x, k_y) = (\omega_{RH}/v_x, \omega_{RH}/v_y)$  and  $v_x$  and  $v_y$  are the scan velocities in x and y direction.

Now, by mixing this field with the scattered field  $E_{s,n}$  coming from the tip (including both background and near-field), demodulating at the  $n$ th order and subsequent Fourier transforming 3 distinct terms are obtained [106]:

$$\tilde{I}_n(\vec{q}) = C_n(\vec{q}) + A_R \tilde{E}_{s,n}^*(\vec{k}_{\parallel} - \vec{q}) + \tilde{A}_R^* E_{s,n}(\vec{k}_{\parallel} + \vec{q}). \quad (2.10)$$

Here all variables  $\tilde{x}$  denote the Fourier transform of  $x$ . Furthermore  $C_n$  is the  $n$ th order demodulated autocorrelation that contains all the mixed terms of the interference of  $E_B$  and  $E_{NF}$ . Moreover, it is clear that multiplication of the signal field with a reference field with k-vector  $\vec{k}_{\parallel}$  corresponds to a shift of  $\pm \vec{k}_{\parallel}$  in the k-space. Now one can perform the same trick as in spectral interferometry: filtering out the part with the desired information and perform an inverse Fourier transform yielding a filtered signal. In this case  $\tilde{A}_R^* E_{s,n}(\vec{k}_{\parallel} + \vec{q})$  contains the signal from the tip enhanced by the reference wave. Again, with demodulation at higher order of the tip frequency ( $n > 2$ ) any additional background field interference with the reference field can be suppressed.

Hence, even though the phase is quasi constant for each point of the scan, the interference of near-field and background field can still be eliminated by applying a holographic method and cutting out only the near-field relevant term in the frequency domain, separated from the other terms. From the filtered signal the near-field amplitude and phase can easily be retrieved. This makes this method much faster than any of the other interferometric methods discussed before, because the mirror movement is running in parallel and is not directly affecting the scan speed. Compared to pseudo-heterodyne detection Schnell et al. could demonstrate an increase in scan speed by a factor of around 30, maintaining the same resolution as in the pseudo-heterodyne measurement [106].

For this method to work properly a stable external interferometer and long travel range, closed-loop piezo devices must be used. Further, the mirror position has to be reset occasionally which can lead to positioning or timing errors. There are works accounting for this by using a sinusoidally varying phase instead of a linearly changed phase and using an advanced inversion algorithm [107]. Another aspect to keep in mind is that a separation of the three terms in (2.10) has to be achieved in order to filter out the the desired part. Consequently, synthetic optical holography might not work for imaging objects with low resolution spanning a few pixels in the scan image. In that case the increased bandwidth can lead to an overlap of the terms.

Combining this method with broad-band spectroscopy techniques still remains a challenging task, requiring a lot of post-processing work, but might be used in future sSNOM setups.

# Experimental Setup

---

# 3

The following chapter gives an overview over the experimental setup and the way signals are recorded, and I evaluate the possibility of discriminating between signal and background.

Hereby, section 3.1 describes the mechanical and optical parts of the SNOM setup, which is used throughout this thesis to record SNOM signals either in a monochromatic or a spectrally resolved configuration. For the latter case, a fast line camera in combination with a monochromator is used to record spectra with a rate that is fast enough to apply higher-order demodulation in a post-processing step. This allows us to analyze spectrally resolved near-field spectra.

The section concludes with two exemplary SNOM scans, one of a bull's eye structure and one of a gold nanoparticle. The first demonstrates a reduction of optical background with higher demodulation order, the latter can be interpreted as a visualization of the local density of states (LDOS) and demonstrates an upper limit for the lateral optical resolution of about 20 nm.

As demodulation plays an important role for the setup and the discussion of SNOM signals, the following section 3.2 explains the lock-in principle and the demodulation of noisy signals in more detail. Here, especially the method to obtain demodulated spectra from the consecutively recorded spectra in a post processing step is documented.

The section 3.3 further analyzes the optical background in SNOM measurements and demonstrates the influence of the tip shape on the optical signals. Hereby, the SNOM tip is retracted from a gold surface and as a consequence no near-field is apparent and thus the separation of background field and reference field can be analyzed. Backed up by simulations the influence of scatterers on the tip shaft on the spectrally resolved background field is demonstrated.

The last section 3.4 then presents a way to separate reference and background field more efficiently and as a consequence to directly gather information about the two fields and as well as about the tip shape. For this, a side-illumination setup with an additional Michelson

interferometer that provides a tunable reference signal is presented. This setup was built by my coworkers at the end of my PhD time and is shown here as an outlook.

### 3.1 AFM and optical setup

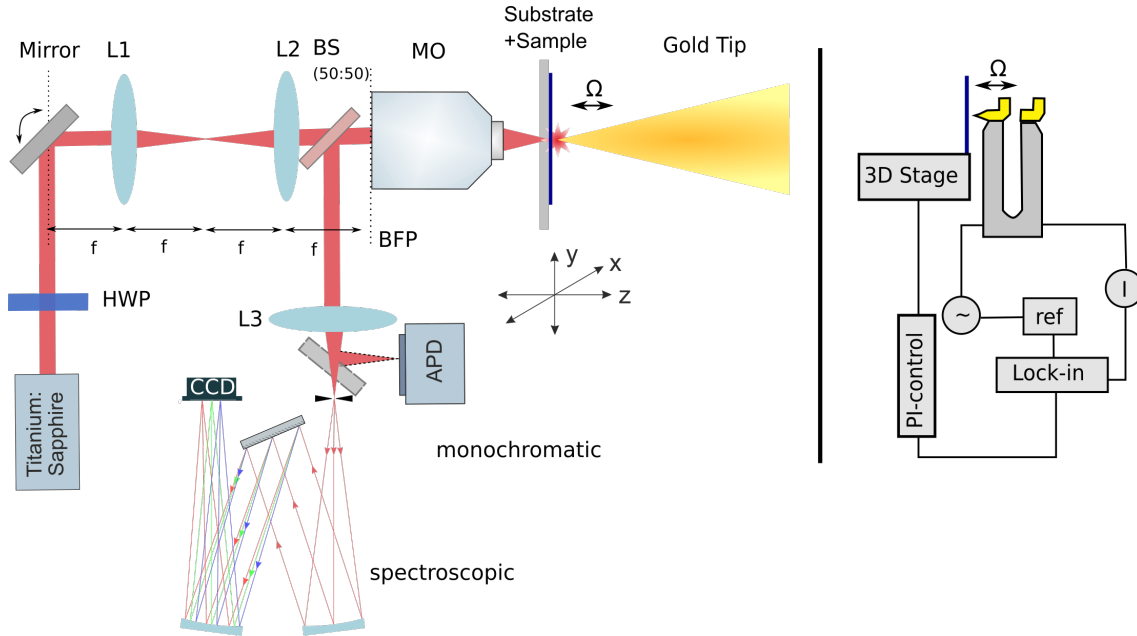


**Figure 3.1:** Back-scattering type SNOM setup. The optical setup on the left shows the beam path: A laser source is focused through the sample onto the tip apex by a high NA objective. The back-scattered light is collected by the microscope objective and a part is reflected by a 50:50 beam splitter and detected on either a photodiode (APD) or a fast line camera mounted at the exit slit of a monochromator. To optimize the focus position onto the tip, a controllable steering mirror in a  $4f$  geometry is implemented. The right image shows the electronic setup: The tip is glued on a quartz tuning fork that is modulated with a frequency  $\Omega$ . The measured current of the tuning fork is amplified and converted to a voltage and is used as an error signal. When the measured current drops, a PI controller is retracting or approaching the sample mounted on a 3D piezo stage to maintain a set tip-sample distance.

Design and realization of the s-SNOM setup was an integral part of this thesis. It is based on a sharply etched gold tip that acts as a near-field scatterer in an optical focus on a sample and that is held in close distance to a surface by a tapping-mode atomic force microscope (AFM). Figure 3.1 shows on the left side the optical setup and on the right side a schematic of the near-field probe on its tuning fork with the electronic distance control feedback loop. The near-field microscope is operating at ambient conditions inside a foam-covered box for vibration isolation. The setup basically enables SNOM measurements in two different configurations, one for monochromatic measurements and one for spectrally resolved near-field measurements. Both are explained in the following.

For quasi monochromatic measurements light from a Titanium:sapphire laser (Spectra Physics, Tsumani) supplying pulses with a relatively narrow spectral bandwidth of around 20 nm centered at a wavelength of 780 nm is used to illuminate tip and sample. For broad-band, spectrally resolved measurements we change the light source to a different Titanium:Sapphire laser

(Femtolasers Rainbow) that provides a broad spectrum with a spectral bandwidth exceeding 100 nm as is exemplary shown in figure 3.2. The maximum output of the broad-band laser is around 300 mW, but only around 10 mW is guided to the SNOM setup. The light of the laser is linearly polarized and the angle of the electric field vector can be changed by a  $\lambda/2$  plate in a rotation holder. The light passes a 50:50 beam splitter and is focused onto the gold tip by a microscope objective with an NA of 0.95 and a working distance of around 300  $\mu\text{m}$ . After passing beam-splitter, lenses and the microscope objective, the power at the tip apex is around 700-1000  $\mu\text{W}$ . In our setup, the tip is fixed and the position of the laser focus as well as of the sample are adjusted with respect to the tip apex. Firstly, to match the focal plane with the tip apex, the microscope objective is mounted on a 1D-piezo translation stage (Piezosystem MIPOS 100 PL) that moves in z-direction (along the tip axis). Secondly, to precisely align the focus position in the focus plane a piezo steering mirror is used in a 4f imaging geometry. The two lenses, with each  $f = 50$  mm focal length, image the plane of the steering mirror onto the back-focal plane of the microscope objective. This 4f geometry ensures that the tilt of the beam induced by the steering mirror results in a displacement of the focus in the focal plane of the microscope objective without distorting the focus. The voltage to drive the steering mirror is delivered by a DA/AD card (Data Translation DT9836) connected to a computer. Typically, before a measurement, a 2D scan of the focus is performed, and the signal that is to be measured later is recorded. The focus position, where the wanted signal is maximum, is determined from this scan and is adjusted for the measurement.

The single-crystalline gold nanotips are produced from polycrystalline, 99.99%-gold wire with a diameter of 125  $\mu\text{m}$ . The gold wire is annealed and electrochemically etched as described in [98]. The process typically results in mono-crystalline tapers with a very smooth surface, with an opening angle of around 30°, and with a sharp apex with a radius of curvature of about 10 nm. Figure 3.3 shows typical SEM images of such a gold nanotip.

In our setup the gold tip is glued on top of one prong of a quartz tuning fork (Auris TC26, UV curing glue Cyberbond U3200) oscillating in resonance at around 26 kHz. To maintain a high Q-factor we glue a piece of the gold wire with similar weight on the other prong of the tuning fork (cmp. right side of figure 3.1). The tuning fork is connected to a home-built transimpedance amplifier with a gain of 1.5E8 V/A, and the AC voltage excitation signal is delivered by a function generator included in a lock-in amplifier (Zürich Instruments

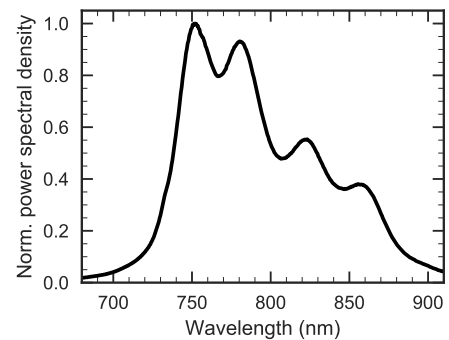


**Figure 3.2:** Laser input spectrum for broad-bandwidth SNOM measurements.

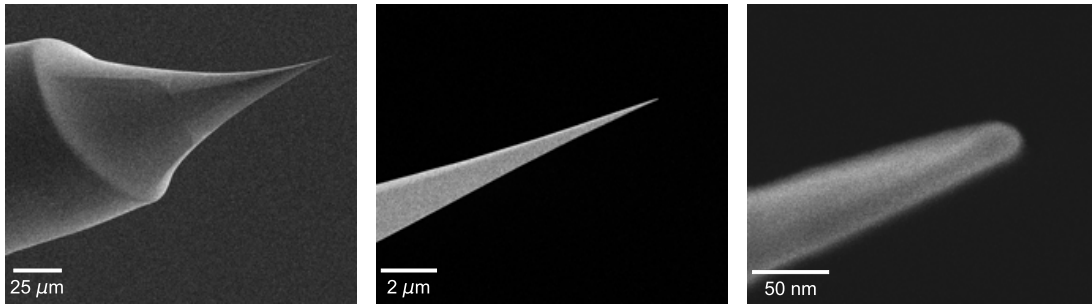


**Figure 3.3:** Typical SEM images of a gold tip with tip diameter  $<20$  nm shown on different scales.

HF2LI). The amplitude of the AC excitation voltage is set to a value around 1 V such that the tip is oscillating with a peak-to-peak amplitude of 30 nm. The current flow at constant voltage is measured, amplified, and converted to a voltage by the pre-amplifier. This voltage can then directly be used as an error signal to control the distance of a sample to the tip. This is in contrast to cantilever-based systems that require an additional laser detection to determine changes in the oscillation amplitude or phase. Hence, connected to a lock-in amplifier (FEMTO LIA-MVD-200H) the amplitude of the tuning forks oscillation can be continuously read out. A resonance curve recorded by this method is shown in figure 3.4.

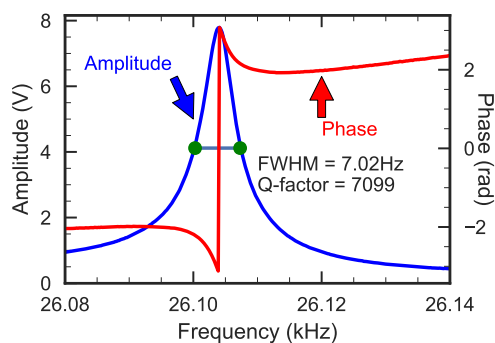


**Figure 3.4:** Typical resonance curve of the tuning fork with attached gold tip as recorded by the Lock-in amplifier. In this example, the resonance is centered around 26.10 kHz with a width of  $\Delta f \approx 7$  Hz, resulting in a Q-factor  $f_{max}/\Delta f \approx 7100$ .

For precise positioning of the sample relative to the tip, the sample is mounted on a combination of two translation stages: a motorized translation stage for coarse alignment, and on top of that a piezo-stage for fine adjustment. The stage for coarse alignment is a long-travel-range 5-axis stage (Newfocus 9081 Five-Axis Aligner). It is used to tilt the sample, such that the surface normal is parallel to the tip axis, to coarsely select the area on the sample that shall be investigated, and to approach the sample to within 5-10  $\mu\text{m}$  distance to the tip. Side-illumination with a white-light LED and observation with a microscope objective (10X EO M Plan Apo, NA=0.28, working distance=33.5 mm) providing a magnified image of the tip and its mirror image facilitates this process. Fine positioning of the sample is achieved by a 3-axis piezo stage (PI P-733-3dd with E-7XX Controller card, 15x15x10  $\mu\text{m}$  travel range). With this stage, the sample is approached towards the tip (traveling in z-direction) with the before described PID

control activated. The approach is stopped and the distance held constant, when the current flow through the tuning fork is decreased to typically 92-95% of the undamped value. This corresponds to a tip-sample distance of a few nanometers. The distance control with this PID is similar to the tapping-mode AFM used in the first demonstration of a super-resolution aperture microscope by Ash and Nicholls [49]. The other two axes of the piezo stage (x and y direction) are used to raster-scan the sample when recording 2D SNOM images, while the tip-sample distance is held constant. By recording the sample's z-position during a scan, a topographical image is created simultaneously with the optical images.

The scanning mode and with this also the speed, with which 2D images can be acquired, differ for monochromatic and spectrally resolved measurements: in the former case, each line is scanned continuously using the internal wave function generator of the piezo stage. As the stage moves, it generates trigger pulses at defined positions, which are used to correlate the position with the optical signals measured with an APD and the lock-in detector. The time required for scanning two lines in a back-and-forth movement and for recording optical SNOM signals at 256 positions per line is about 8 s. For a typical SNOM image with 128 lines this results in an acquisition time of up to 17 minutes. Scan areas were typically around  $2 \times 2 \mu\text{m}$  or  $3 \times 3 \mu\text{m}$ . For rough samples either the PID settings or the scan area was adapted to prevent damaging the tip. When recording complete spectra with the fast line camera, however, the spectra cannot be recorded while continuously scanning a line. Instead, the image is raster-scanned pixel-wise. This means the piezo stage approaches and stops at each position, such that a number of consecutive spectra (typically 60.000) can be recorded for each pixel. The measurement time is then around 276 ms per position and hence often smaller scan areas were evaluated in order to achieve reasonable measurement times before significant sample drift sets in.

The whole scan and data acquisition procedure was programmed by myself using object-oriented programming with Matlab and Python. More detailed information on the program can be found in the appendix A.1.

We detect the light that is backscattered from the tip-sample interaction volume. This light passes through the sample again and is finally reflected off the beam splitter and captured by the detector. For monochromatic measurements we use a fast APD (Hamamatsu C10508-01) as the detector. The signal from the APD is processed by a lock-in amplifier (Zürich Instruments HF2LI) using the tip modulation frequency as the reference signal. For this work we typically demodulate the signal at the fundamental tip modulation frequency ( $1f = 26 \text{ kHz}$ ) as well as at its second ( $2f$ ), third ( $3f$ ) and fourth ( $4f$ ) harmonic, resulting in the signals  $S_{1f}$ ,  $S_{2f}$ ,  $S_{3f}$  and  $S_{4f}$ . Higher than fourth order harmonic signals are usually obscured by noise. For spectrally resolved measurements, where the APD and lock-in detector are replaced by the monochromator and fast line camera, demodulated spectra  $S_{1f}$  to typically also the fourth order

$S_{4ff}$ , are obtained from the consecutively recorded spectra in post processing. This is explained in more detail in the next section 3.2.

In both cases, the signal strengths of  $S_{1f}$  to  $S_{4f}$  crucially depend on the alignment of the laser focus on the nanotip. Therefore, in order to achieve a high signal strength, a 2D scan of the laser focus was performed when the tip was approached to the sample. For this I used the steering mirror in the 4f setup, as explained above, and the 1f to 4f signals were recorded. Figure 3.5 exemplary shows the demodulated signals  $S_{1f}$ ,  $S_{3f}$  and  $S_{4f}$  for two different beam scans. The two beam scans selected for this figure have different general shapes: The three upper images belong to a beam scan where the focus displays one single maximum, while the lower three images show two distinct maxima of roughly equal maximum intensity. This highlights the fact that the nanotip can be excited by either fields parallel or perpendicular to the tip axis. The upper three images correspond to the spatial distribution of  $|E_x|^2$ , i.e., field components perpendicular to the tip axis, and the lower three images to the spatial distribution of  $|E_z|^2$ , i.e., field components along the tip axis. The precise focus fields formed at the tip-facing side of a multilayered sample are calculated later, in Ch. 4.1.4 and are shown in Fig. 4.10. Which of the fields excite the tip predominantly depends on the shape of the particular tip used in the experiment.

Despite these obvious differences, however, both measurements show that the near-field contrast increases with increasing demodulation order: For lower demodulation orders (Fig. 3.5A and D) a background contribution is always apparent. This is particularly visible in Fig. 3.5A, where a substructure surrounds one main maximum. For fourth order demodulation the background contribution has been strongly suppressed and the beam can be precisely adjusted to yield the highest scattering signal from the tip.

In order to demonstrate the improvement of the signal-to-noise ratio with increasing demodulation order, I show two more exemplary SNOM scans, namely of a bull's-eye structure in Fig. 3.6, and of a gold nanoparticle in Fig. 3.7. Figure 3.6 shows an exemplary SNOM scan of a bull's-eye structure. This structure consists of a sub-wavelength central aperture surrounded by several concentric grooves [109–111]. The grooves act as an antenna, coupling incident light into surface plasmons and supporting a strongly enhanced localized plasmonic field at the center. The structure shown here (Fig. 3.6A), however, is resonant for a wavelength outside the spectrum of the incident laser light, such that the enhanced field at the central aperture should not be visible. Instead, I would like to draw the reader's attention to hotspots, localized surface plasmons with highly enhanced field strengths. These hotspots can already be slightly observed in the optical signal demodulated at the first harmonic of the tip modulation frequency (Fig. 3.6B), but are shadowed by a very large optical background. On the image demodulated at the third harmonic (Fig. 3.6C) the hotspots can be observed clearly with a strongly suppressed background. Thus, the measurement nicely demonstrates the predicted improved signal to background contrast for demodulation at higher orders of the tip modulation frequency. When

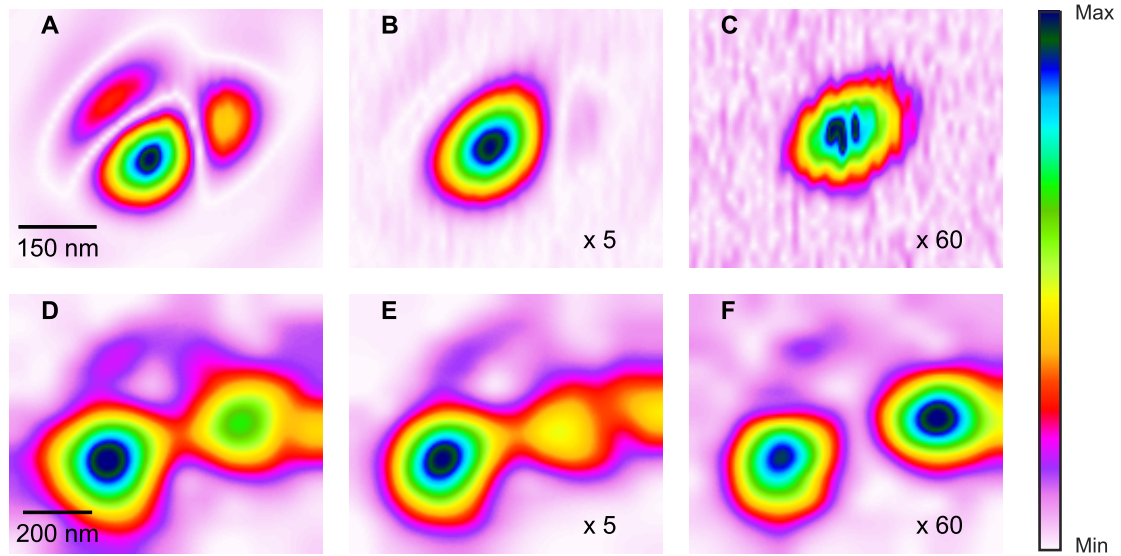


**Figure 3.5:** Beam scans for different order demodulation measured on two different samples. A-C: Typical Beam Scan for first, third and fourth order demodulation respectively measured on a J-aggregate film on top of a glass-gold-glass multilayer structure, D-F: the same measurement for a different tip on a gold-coated quartz substrate. The beam scan is in good approximation a measurement of the focal plane fields. Depending on the tip field enhancement and the sample's properties either the in-plane component or the z-component of the focus fields is dominant and shows a similar pattern as previously shown by the focus calculations.

comparing Fig. 3.6C to 3.6B, the hotspots appear much smaller in diameter. In our case, this is a result of suppressing the background signal. However, a recent numerical study of the spatial distribution of electromagnetic fields between tip and sample in tip-modulated SNOM revealed that in addition to raising the signal-to-background ratio, also the lateral confinement of the fields is enhanced. Thus, the spatial resolution increases with increasing demodulation order [112].

To show the spatial resolution typically achieved with our SNOM, a second example of a SNOM scan, this time of a gold nano-particle on top of a glass substrate is presented in figure 3.7. The optical signal demodulated at the third order of the modulation frequency has a maximum at the edges and in the middle of the long particle. This image should be interpreted as a visualization of the local density of states (LDOS), i.e., the square of the resonant surface plasmon wavefunction [113]. In this case, the imaged SNOM map is reminiscent of a wavefunction with two nodes along the long axis of the nanoparticle, similar to the images shown in [114], but it also seems to be sheared and enhanced at the left side. This may be a superposition of several fundamental resonances, but the asymmetry may also be caused by the specific shape of the nanoparticle, causing the projected LDOS to change when scanning the tip over its surface. Here we use a cross section through the optical signal, indicated by the red line in figure 3.7B to give an

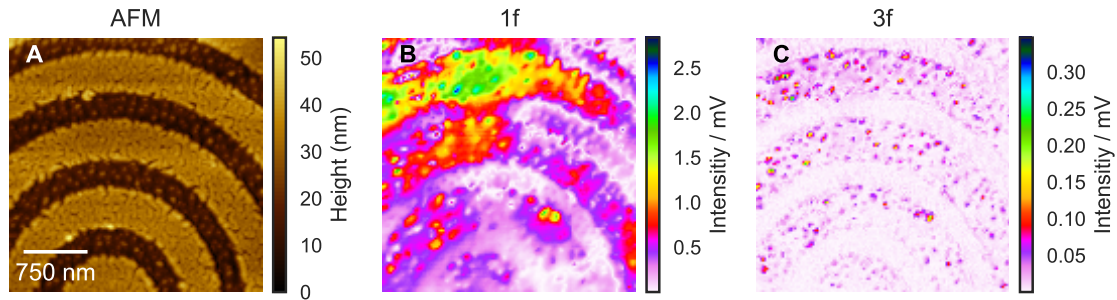


**Figure 3.6:** Exemplary SNOM scan of a bull's eye nanoresonator produced by focused ion-beam milling of a gold film. The AFM image shows irregularities, like holes and small particles on the gold as well as on the glass, which is exposed in the grooves, where the gold has been milled away. Localized fields around the holes of the gold structures are observed in the optical image as well as an improved signal to background contrast for higher order demodulation.

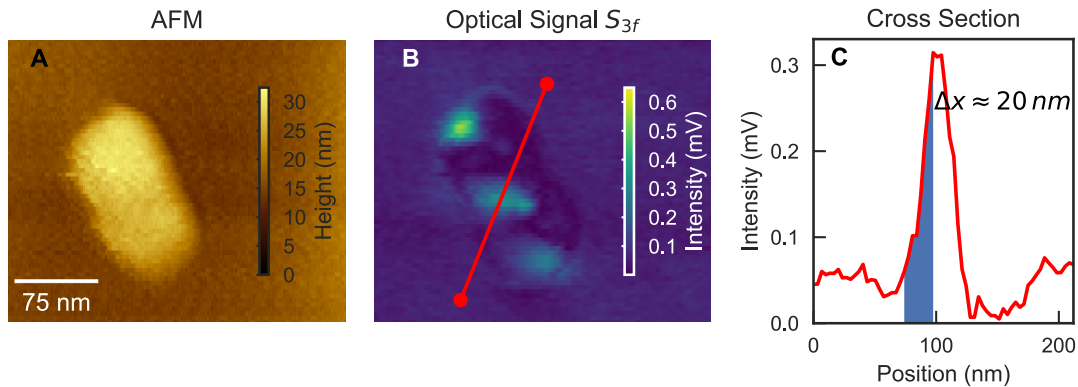


**Figure 3.7:** Exemplary SNOM scan of a gold nanoparticle. (A) shows the AFM image. In (B) the corresponding optical signal demodulated at the third order of the modulation frequency is plotted and in (C) a cross section along the red line in (B) is presented. The spatial optical resolution  $\Delta x$  is defined by the position difference at the intensity maximum from 10% to 90% of the maximum value, indicated by the blue area.

upper limit for the spatial optical resolution. The position difference from 10% to 90% of the maximum intensity value is around 20 nm. This value is given by the convolution of the edge of the projected LDOS and the lateral resolution of our SNOM and is therefore an upper limit for the lateral resolution. In our experiments, the spatial resolution depends mainly on the tip radius that is achieved after the etching process and can be even smaller than 10 nm.

### 3.2 Demodulated near-field signals and spectra

As previously shown, higher order demodulation plays a crucial role in detecting the scattered near-field signals. To understand how the measured signals are evaluated for both the monochromatic and the broad-band spectra measurements, a closer look at the respective evaluation is

given in this section.

For monochromatic measurements it is common to use a lock-in amplifier to extract small periodic signals within a large noisy background. Hereby the optical signal  $I(t)$  impinging on a photodiode is generating an analogous voltage signal  $U_{\text{in}}(t)$  that is connected to the input channel of the lock-in device. To fulfill the task of extracting the desired amplitude and phase information from the noisy signal a second, reference, input signal is needed. The reference signal is a periodic function, typically sinusoidal, with the same frequency  $f_{\text{ref}} = f_{\text{mod}}$  as the signal to be detected and can either be generated by an internal function generator inside the lock-in amplifier itself or fed in via an external connection. The lock-in amplifier then performs a multiplication of the input signal with the reference signal and applies a low-pass filter afterwards. This can be written as:

$$U_{\text{out}}(t) = \frac{1}{T} \int_{t-T}^t \sin [\Omega \cdot t' + \varphi] U_{\text{in}}(t') dt', \quad (3.1)$$

with  $\Omega = 2\pi f_{\text{mod}}$ . This process is already the demodulation at the fundamental frequency  $f_{\text{mod}}$ . To obtain signals demodulated at higher demodulation order  $n$ , multiplication is performed with a multiple of the modulation frequency  $f_{\text{mod}}$ , i. e.,

$$U_{\text{out},nf}(t) = S_{nf} = \frac{1}{T} \int_{t-T}^t \sin [n \cdot \Omega \cdot t' + \varphi] U_{\text{in}}(t') dt'. \quad (3.2)$$

When recording spectra with the high speed camera, we record a dataset that contains both wavelength and time information, i. e.,  $I(\lambda, t)$ . A typical visualization can be seen in figure 3.8. The time signal is modulated by the tip modulation frequency  $f_{\text{mod}}$ . The modulation however is on a very small scale so it cannot be seen directly in figure 3.8A. However, we can analyze the time series of each camera pixel individually. We label such a time series by  $I_\lambda(t)$ , where the index  $\lambda$  denotes the pixel number, corresponding to a wavelength value. We now can perform a Fourier transform along the time axis for each pixel. A typical result is shown in figure 3.8B. In this case the image shows the absolute value of the complex frequency spectrum of the time signal summed over all pixels ( $\sum_\lambda \mathcal{F}(I(\lambda, t))$ ) for a better signal-to-noise ratio and a more obvious result. Clearly, distinct peaks at the modulation frequency of the tip and higher harmonics of this frequency can be observed. The maximum frequency we can resolve from the time signal depends on the line readout frequency of the camera. In our case we use 214 kHz, the maximum readout rate available. This corresponds to a time interval  $\delta t = 4.67 \mu\text{s}$ . The maximum frequency in the Fourier spectrum is given as  $f_{\text{max}} = \frac{1}{2\delta t} = 107 \text{ kHz}$ . Higher order harmonic frequencies than  $f_{\text{max}}$  are detected at lower frequencies,  $2f_{\text{max}} - n \cdot f_{\text{mod}}$  because of the Nyquist theorem and can in principle be detected just as well as orders with  $nf < 107 \text{ kHz}$ .

However, with increasing demodulation order the signal amplitude decreases. This means that while the background suppression improves with increasing demodulation order, the signal-to-noise ratio disimproves. In essence, for orders higher than some maximum  $n_{max}$ , the signal is obscured by noise. In the example shown in Fig. 3.8B, the fifth order demodulated signal is still distinguishable, and sometimes also the 6th order signal is found. Typically, however, in the measurements presented throughout this thesis, we found the fourth order demodulated signal to offer the best balance between signal-to-noise ratio and background suppression.

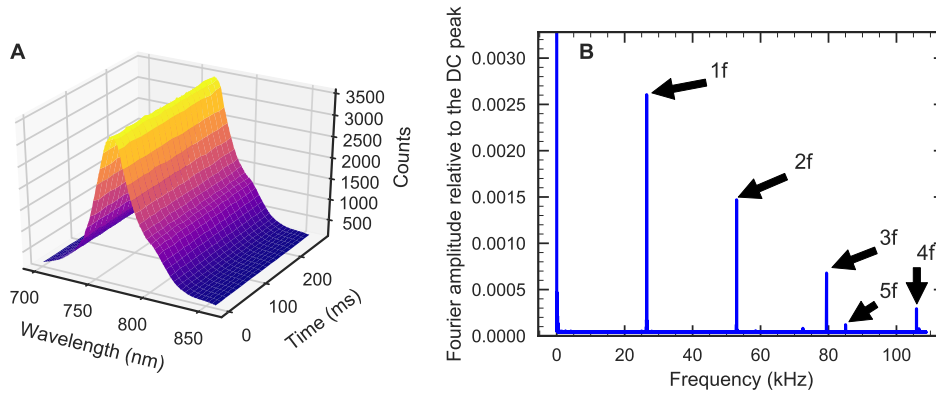


**Figure 3.8:** (A) 3D visualization of a typical SNOM dataset (B) Fourier spectrum summed over all pixel values

Each time series  $I_\lambda(t)$ , recorded for each pixel, constitutes a time series equivalent to the lock-in input voltage  $U_{in}$  in Eqs. (3.1) and (3.2), and hence an output signal  $S_{\lambda,nf}$  can be calculated in an equivalent way, as well. The camera has 512 pixels, and we record typically 60.000 spectra per measurement, making  $I_{\lambda,t}$  a data cube of  $512 \times 60.000$  values. For an easier notation, in the following we use complex Fourier components to describe the higher harmonic demodulated signals. Then, the time series  $I_\lambda(t)$  for each pixel can be approximated by a Fourier series:[115]

$$I_\lambda(t) \approx I_\lambda^F(t) = \sum_{n=-\infty}^{\infty} c_{n,\lambda} \cdot e^{in\Omega t} \quad (3.3)$$

with the complex Fourier coefficients

$$c_{n,\lambda} = \frac{1}{T_0} \int_{-\frac{T_0}{2}}^{\frac{T_0}{2}} I_\lambda(t) \cdot e^{-in\Omega t} dt \quad (3.4)$$

In practice, we can extract five complex valued signals  $c_{n,\lambda}$  with  $n = 0, 1, 2, 3, 4$  for each pixel, and  $c_{-n} = c_n^*$ .

The phase of the complex Fourier components contains information about the starting time of the measurement: If we imagine an ideal measurement, it would start at a time  $t = 0$ , where the tip is closest to the sample. Here we describe the tip-sample distance by

$$d(t) = d_0 + A \cdot \cos(\Omega t + \pi) \quad (3.5)$$

with the modulation amplitude  $A = 30$  nm and  $d_0 \approx 33$  nm, enabling a minimum tip-sample distance of 3 nm. To account for the measurement to start at a different phase in the cycle, it is practical to define an offset time  $t_x$ :

$$d'(t) = d(t + t_x) = d_0 + A \cdot \cos(\Omega(t + t_x) + \pi) \quad (3.6)$$

We would then get different complex Fourier components:

$$c'_{n,\lambda} = \frac{1}{T_0} \int_{-\frac{T_0}{2}}^{\frac{T_0}{2}} I'_\lambda \cdot e^{-in\Omega(t)} dt = \frac{1}{T_0} \int_{-\frac{T_0}{2}}^{\frac{T_0}{2}} I_\lambda(t + t_x) \cdot e^{-in\Omega(t)} dt \quad (3.7)$$

These coefficients can be written as the original Fourier components, multiplied with a phase:

$$c'_{n,\lambda} = \frac{1}{T_0} \int_{-\frac{T_0}{2}}^{\frac{T_0}{2}} I_\lambda(t + t_x) \cdot e^{-in\Omega(t)} dt = \frac{1}{T_0} \int_{-\frac{T_0}{2}}^{\frac{T_0}{2}} I_\lambda(t) \cdot e^{-in\Omega(t-t_x)} dt = c_{n,\lambda} \cdot e^{in\Omega t_x} \quad (3.8)$$

So,  $c_1$  should be rotated in the complex plane by the angle  $\varphi_1 = \Omega \cdot t_x$ ,  $c_2$  by twice that amount,  $\varphi_2 = 2 \cdot \varphi_1$ , etc. Once the phase is known, it can easily be corrected by multiplying with  $e^{-i\varphi_n}$ . In effect, this means setting the starting time of the measurement to  $t = 0$ . After correcting the phase, the resulting real-valued Fourier coefficients constitute what we understand to be the higher-order demodulated near-field SNOM spectra:

$$S_{\lambda,nf} = c'_{n,\lambda} + c.c. = 2\text{Re}(c'_{n,\lambda}) \quad (3.9)$$

The extraction of the Fourier coefficients as described above is an easy and fast procedure to execute in post-processing, when the complete 60.000 spectra per measurement position have been stored and when the tip modulation frequency  $f_{mod}$  is known precisely. During a measurement session and in order to save the time required for storing and reading large amounts of data, it can be of advantage to perform a pixel-wise fast Fourier transform (FFT) and to save only a small number of spectra around the multiples of the modulation frequency. The resolution in the Fourier spectrum is given by  $\Delta f = f_s/N$  with the sampling frequency  $f_s$  and the number of points  $N$ . With a typical recording of 60.000 spectra this corresponds to  $\Delta f = 3.5$  Hz. From the measured resonance curve of the tuning fork the width of the resonance is known to be  $<5$  Hz, and, correspondingly, only one or two frequency positions of the FFT

show a nonzero value. To be on the safe side we then save 11 frequency positions of the FFT around the maximum peak position for each harmonic.

### 3.3 Background signal in SNOM measurements

In the previous sections it was shown, how meaningful data can be obtained by demodulation of the distance-modulated intensity signals that are recorded by the SNOM setup. The near-field, background field and reference field were introduced in Ch. 2, and Sec. 2.2 described the situation in our experiment, where the near field and an unwanted background signal are mixed with a strong reference field to form a homodyne detection scheme. Then the intensity measured at the detector is composed of three fields,  $I \propto |E_R + E_{NF} + E_B|^2$ , (comp. Eq. (2.1)). In this section and the next I want to investigate the influence of the background signal in low demodulation orders. For this, I performed measurements with the tip retracted from the surface, i.e., deliberately setting  $E_{NF} = 0$ . Eq.(2.1) then simplifies to

$$I \propto |E_R + E_B|^2 = E_R^2 + E_B^2 + 2E_R E_B \cos(\varphi). \quad (3.10)$$

For this section 3.3 I first selected one example where the background field is particularly strong and also complex, in order to show how such a complex background signal can make a measurement unfit for evaluation, even if we understand the origin of the measured signals. In the next section I will then show a measurement that is typical for sharp and smooth nanotips as near-field probes, and where the unwanted background signal can easily be removed.

In particular, we evaluate the time series of spectra recorded on a 30 nm thick gold-coated glass substrate with the SNOM tip not in contact with the sample. As the measurement and following analysis will show, the particular nanotip used for this measurement was not as clean and smooth as the ones we usually select for SNOM. Most likely, small gold precipitates of few 100 nm diameter were formed during the etching process and remained in the laser-illuminated area near the taper apex, where they act as efficient scatterers for the incident light [116]. My measurements will reveal the interferences between a reference field and a background field scattered from these unintentionally left scatterers and will yield information on their number and distance from the apex.

In the following a measurement spanning 276 ms and comprising 60.000 single spectra recorded with a rate of 210 kHz was evaluated. The measurement took place with the tip not in contact with the sample, i.e. the tip-sample distance was around hundred of nanometers and was realized by moving the sample away from the tip. The laser focus was still positioned on the tip apex. By moving the sample out of the focus plane, the intensity reflected back from the sample was reduced, and as a consequence, the maximum signal on the camera dropped from 3484 counts to 1799. The spectra recorded during the first 450  $\mu$ s are plotted in Fig. 3.9A, where the

color code gives the counts per pixel on the camera.

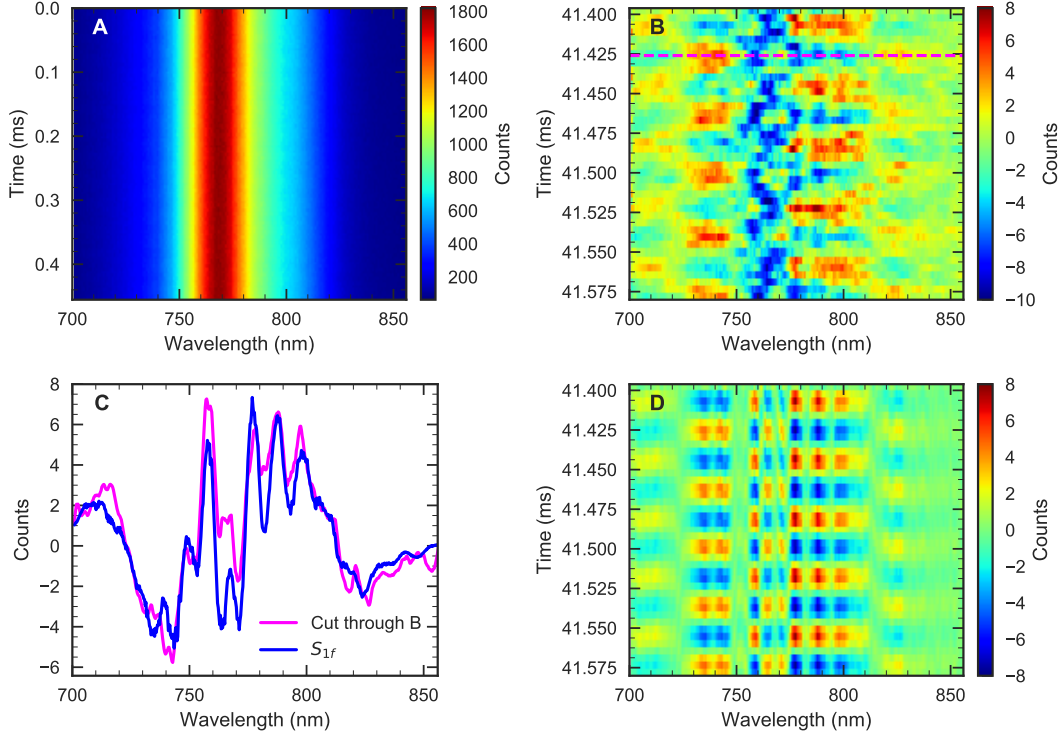


**Figure 3.9:** (A) The recorded dataset  $I_{\lambda,t}$  of the out-of-contact spectra for the first 450  $\mu\text{s}$ . (B) The spectra from (A) in a shorter time interval with the average spectrum subtracted. One can see a distinct modulation in time. (C) The calculated  $S_{1f}$  spectrum (blue) together with a cut through the (B) (magenta), which is shown (B) as the magenta broken line. (D) The same as (B) after fitting a sinusoidal function to each of the recordings  $I_{\lambda}(t)$ .

In a next step, we want to analyze this out-of-contact data in more detail and give an estimation for how many scatterers are on the tip and at which distance from the tip apex they are located. Even though no direct modulation is visible in the raw data, we expect the background field reflected from the tip to still carry a phase shift of the modulation of the tip, and hence by interference with the reference field a temporal intensity modulation should be superimposed on the spectra. In order to verify this, Fig. 3.9B shows the same spectra, where the temporal average spectrum has been subtracted. One can see that after subtraction there are fluctuations of about  $\pm 8$  counts left. From the modulation depth of  $\pm 8$  counts, compared to the maximum of 1799 counts and the fact that the reflected field strength  $E_{R,out}$  has reduced to around 75% of its value from the tip-in-contact measurement, we can determine the reference-to-background ratio,  $E_R : E_B \approx 300 : 1$ .

Furthermore, there is a clear temporal periodicity visible. For clarity, here only a short time span of 180  $\mu\text{s}$  comprising 41 consecutive spectra is shown. This time span contains five oscillation

periods of the tip, clearly visible as alternating red and blue areas.

In order to further investigate these oscillations, I first extract the Fourier coefficients (Eq. (3.4)) from the measured spectra, as described in Sec. 3.2. Specifically, as we are interested in the cross term of reference and background spectrum, the first order demodulated spectrum  $S_{1f} = c'_{\lambda,1f} + c.c.$  is of the highest relevance in this case. The 1f-spectrum,  $S_{1f}$  is shown as a function of wavelength as the blue curve in Fig. 3.9C. The phase of the complex coefficient has already been corrected, such that  $\text{Im}(c_{1f}) = 0$  and  $S_{1f} = 2\text{Re}(c_{1f})$ . A cut through the measured modulation (magenta broken line in Fig. 3.9B) is plotted as the magenta curve together with  $S_{1f}$  in Fig. 3.9C, showing that the two curves overlap well, taking into account that each single measured spectrum is obviously carrying noise.

As an additional demonstration of the strict temporal periodicity, I have fitted sine curves to each time series  $I_{\lambda}(t)$ , recorded by each pixel. The fit parameters for these sine curves are their frequency, offset phase and amplitude. The fitted sine curves are plotted as columns over the wavelength assigned to each pixel, resulting in the plot in Fig. 3.9D. Here the color code is the amplitude of the sine curves as a function of time and wavelength. This plot also closely recreates the measured spectro-temporal modulation.

Next, let us turn to the spectral modulation, i.e., the spectral shape of  $S_{1f}$ . This spectral modulation contains information on the properties of the tip. In this case, where there was no near-field contribution to the signal, the information only concerns the scattering of background field. For a smooth and clean tip, we expect the modulation  $E_R E_B \cos(2kd)$  to show exactly one spatial frequency, corresponding to one scatterer located at distance  $d$  from the position where the reference field  $E_R$  is reflected. However, looking at the spectral shape of  $S_{1f}$  indicates that there is more than one frequency required to create such a complex pattern. In order to identify the spatial modulation frequencies, I transfer the spectrum  $S_{1f}(\lambda)$  to the  $k$ -vector axis  $S_{1f}(k)$  and perform a Fourier transform. The result is shown in Fig. 3.10A, as the normalized Fourier amplitude as a function of optical path difference between reference field and background field. Seven peaks can be identified in Fig. 3.10A and are labeled by their optical path difference between reference and background field. Looking closer at the numbers, they can be fitted to multiple scattering events between three scatterers and the gold film, as sketched in Fig. 3.10B: the smallest optical path difference must correspond to the light traveling from the gold film to the closest scatterer and back to the gold film, where it overlaps again with the reference field. The second peak is at nearly twice this optical path difference and could hence correspond to the background light performing one additional reflection off the gold film and the first scatterer. The third peak labeled in Fig. 3.10A, however, does not correspond to another multiple of this distance and thus indicates a second scatterer, located at a distance of  $\sim 8 \mu\text{m}$  from the first

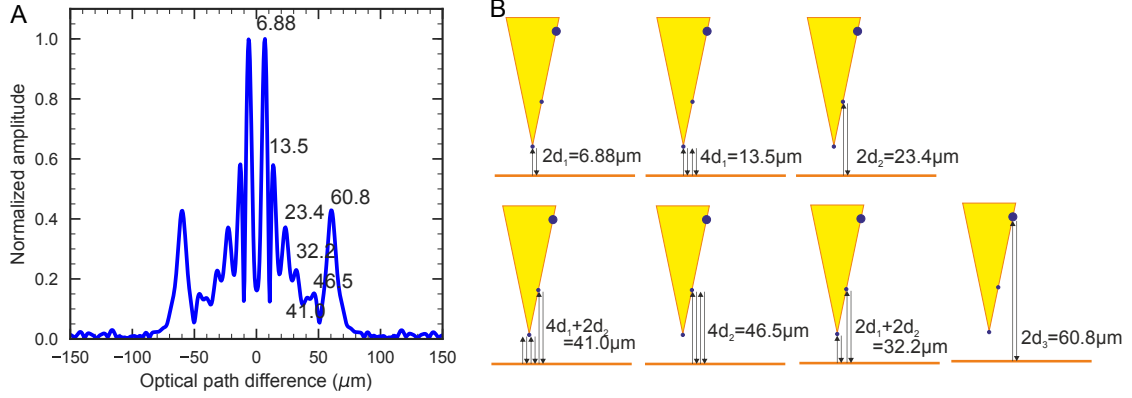


**Figure 3.10:** (A) Fourier transform of  $\text{Re}(S_{1f}(k))$ , with the peak positions labeled. (B) Visualization of the different scattering events.

scatterer. This assumption is supported by the fourth peak, which corresponds to a reflection off the first scatterer and gold film, followed by scattering from the second. Likewise, the fifth and sixth peak can also be understood as multiple scattering events between these two scatterers. Finally, we find one very large peak at a large optical path length difference. This may indicate a single, but very efficient scattering of a very large scatterer like a grain of dust or a grain boundary.

To test our interpretation of the  $S_{1f}$  spectrum as the interference of the reference field and the background field stemming from multiple scattering events, I manually implement the resulting spectral interference pattern. For this, I assume the incident field  $E_{inc}$ , to be the square root of the laser spectrum, and the reference field  $E_R(\lambda) = r_0 E_{inc}(\lambda)$ , with the reflection coefficient of the gold surface. Here I assume  $r_0$  to be spectrally flat, and correspondingly the transmission coefficient  $t$  to be spectrally flat, as well.

The field that is transmitted through the gold film and is scattered by the gold tip (apex or shaft) creates the background field. In the simplest case, i.e., one scatterer  $p$  at distance  $d_p$  from the gold film, this field could be written as

$$E_B(\lambda) = tr_p t E_{inc}(\lambda) e^{2ikd_p + \phi_p} \quad (3.11)$$

Here,  $t$  is the transmission coefficient through the gold film, and  $r_p$  is the reflection coefficient for the scatterer  $p$ . The exponent describes a phase shift between reference and background field due to the displacement, which results in a wavelength-dependent phase  $\phi = 2kd$ , with  $k = 2\pi/\lambda$ , plus a wavelength-independent phase  $\phi_p$ . In order to recreate the complete modulation, I assume three scatterers, and denominate them  $p = 1, 2, 3$ . Taking into account up to three

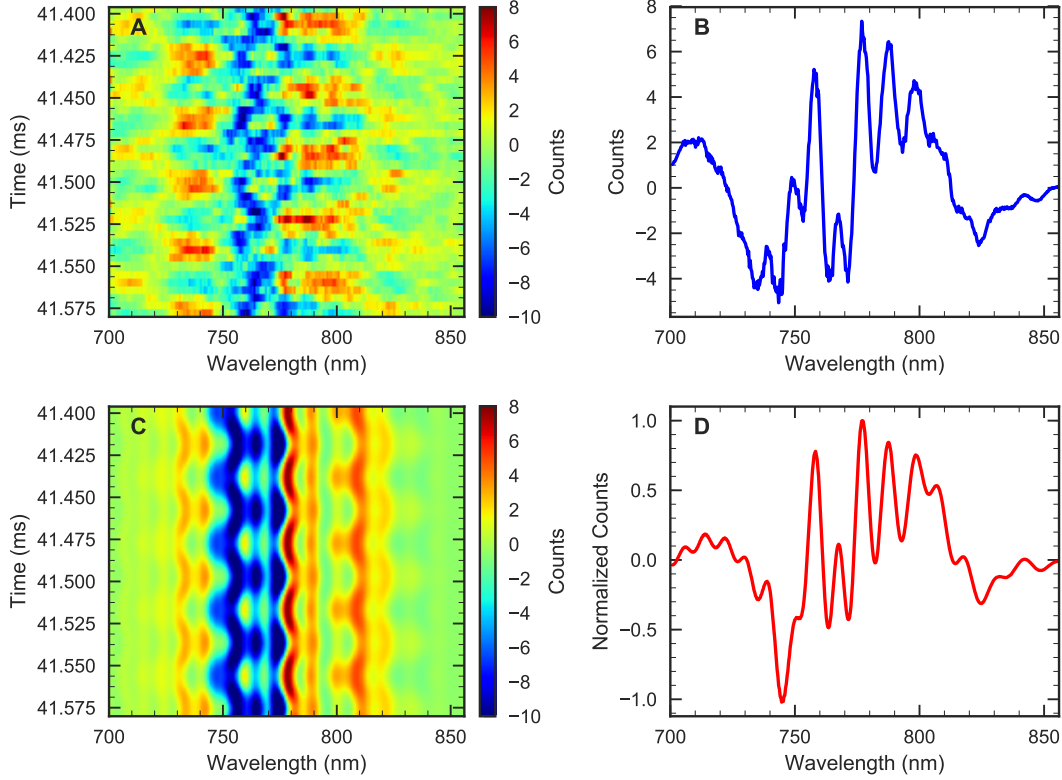


**Figure 3.11:** (A) Modulation of the out-of-contact spectra after subtracting the average laser field. (B) Extracted  $S_{1f}$  from the measurement data. (C) Calculated field  $2\text{Re}(E_R E_B)$  where  $E_B(\lambda)$  was calculated by taking into account various scatterer on the tip shaft. (D) A cut through (C) showing a very good agreement with the  $S_{1f}$  spectrum in (B).

scattering events, the background field can be written in this way:

$$E_B(\lambda) = \sum_p tr_p t E_{inc}(\lambda) e^{i2kd_p + \phi_p} + \sum_{p,p'} tr_p r_0 r_{p'} t E_{inc}(\lambda) e^{i2k(d_p + d_{p'}) + \phi_{p,p'}} + \sum_{p,p',p''} tr_p r_0 r_{p'} r_0 r_{p''} t E_{inc}(\lambda) e^{i2k(d_p + d_{p'} + d_{p''}) + \phi_{p,p',p''}} \quad (3.12)$$

We furthermore need to take into account the tip modulation. This creates an additional, temporally varying phase difference between reference and background field, which is described by multiplying the background field with  $e^{i2kA \cos(\Omega t)}$ . Finally, in order to compare this simple model to the measurement, the reference field is added to the background field and the absolute square is calculated. The result is shown in Fig. 3.11. As a reminder, Fig. 3.11A again shows the measured modulation and 3.11B the  $S_{1f}$  spectrum extracted from the measurement. Fig. 3.11C shows the calculated equivalent, namely the modulation  $2\text{Re}(E_R E_B)$ , which is modulated as a function of wavelength and of time. The simulated modulation recreates most features of the measurement remarkably well. This is even more evident from Fig. 3.11D, which shows the

modulation for a fixed time, i.e., a cut through 3.11C, and which reproduces the  $S_{1f}$  spectrum very well.

In conclusion, I have shown in this section that extracting the Fourier coefficients gives us valuable insight and understanding of the measured SNOM spectra. In this particular case, I could identify three distinct scatterers on the tip and have recreated the complex measured intensity modulation, which is a result of this. Of course, such a tip producing such a strong and complex background field would complicate near-field measurements considerably. Thus we usually take great care to select clean and smooth tips as near-field probes, in order to minimize background contribution. On the other hand, however, a strong scattered field from one, well-defined scatterer, can also be used to create a reference field for spectral interferometry. This has recently been demonstrated within a different project of our group [116].

### 3.4 Improved separation of background and reference fields in a side-illumination setup

In the previous section it was shown that different scatterers on the tip could be reconstructed from the out-of-contact spectra on a gold film. For a very smooth tip, we would expect the background field to be scattered from only one location, very close to the apex. In the previous example, this would correspond to the modulation with the smallest optical path length difference, which was around  $7\ \mu\text{m}$ . When the tip was in contact with the sample, this distance would be even smaller and would result in a modulation period comparable to the spectral bandwidth of our experiment. This was in fact the case for most measurements performed throughout this thesis. Typically the effect can be seen in the lower order demodulated signals but is of little significance in  $S_{3f}$  or  $S_{4f}$  spectra (see, e.g., Ch.5). However, it poses a problem for a reliable evaluation of measurements with low near-field signal strength.

During the last few months of my PhD project, the SNOM setup was modified to further improve discrimination between background and near field signal. This involved illuminating the tip from the side and installing a Michelson interferometer with one arm providing the reference signal. In comparison to the first, back-illumination setup, the new setup offers the advantage that the path length difference between reference field and background and near-field could be adjusted independently. Its disadvantage is that the reference arm of the Michelson interferometer is not intrinsically stable any more.

In the following I will show that the same process as before, using a Fourier transform on the spectra, can be used to extract the background spectrum information from an out-of-contact measurement.

The side-illumination setup has been described in [117], and a simple sketch of the setup is shown in Fig. 3.12. The light from the Titanium:Sapphire laser is incident on a beam splitter

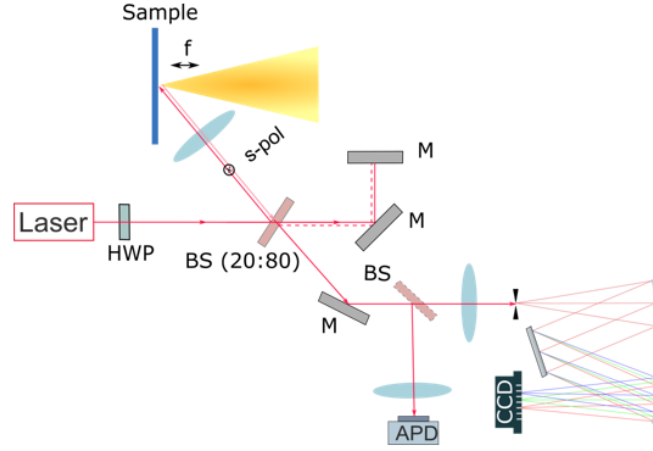


**Figure 3.12:** SNOM side illumination setup with a Michelson interferometer with one arm providing the reference signal. With this setup the path length difference between reference field, background and near-field can be adjusted independently.

(BS), where 20% is reflected and is focused onto the tip from the side, using a reflective MO (Beck Optronics Solutions, model 5003-000) with NA 0.4. 80% of the incident light passes the BS and serves as the reference field  $E_R$ . The reference arm length is adjusted to be shorter than the sample arm by  $\sim 100 \mu\text{m}$  in order to enable spectral interference with a convenient fringe spacing. The reference beam and the light that is scattered from the near-field region and that is collected by the MO in backwards direction are overlapped and can be recorded by either a photodiode (APD) or by the the fast line camera after passing a monochromator.

Here I show spectra recorded with the fast camera with the tip above a flat  $\text{Sb}_2\text{S}_3$  film. The measurements were performed by my colleague Jinxin Zhan for her PhD thesis and are used here to demonstrate the wide applicability of my evaluation using Fourier coefficients. Again, the tip was removed from the sample, setting  $E_{NF} = 0$  and allowing us to record the interference of reference and background field. Similarly to the gold film,  $\text{Sb}_2\text{S}_3$  also shows a very flat spectral response over the spectral range covered in our experiment and is shown in Fig. 3.13.

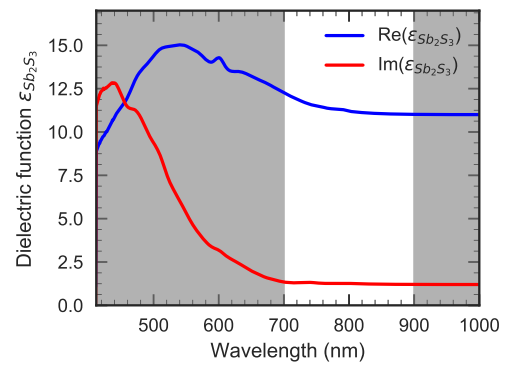


**Figure 3.13:** The dielectric function of  $\text{Sb}_2\text{S}_3$ .

A typical spectral measurement with the fast line camera is shown in Figure 3.14. Like in the previous section, 60.000 spectra were recorded over a time period of around 270 ms. We can observe interference fringes from the interference of the

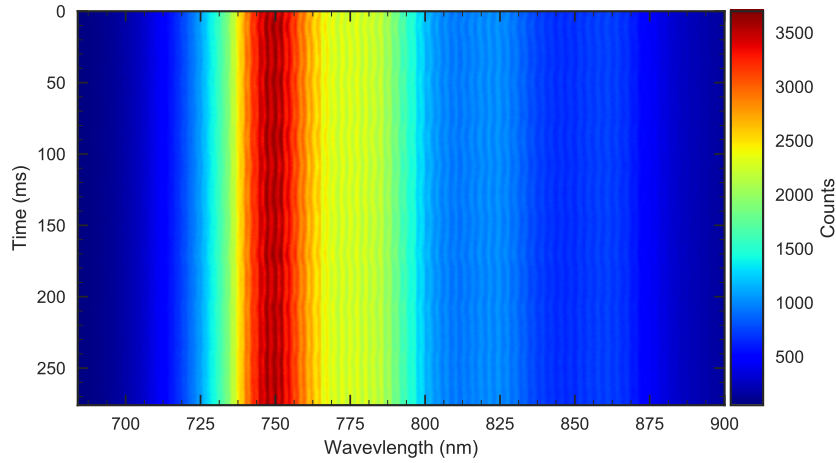


**Figure 3.14:** Spectra as a function of time recorded with a fast line camera and the SNOM tip far away from the sample.

reference beam with the backscattered light from the sample and the tip. A closer look reveals that the interference lines are not straight, but that they shift over the wavelength axis with time. The reason for this shift of the interference pattern is a mechanical drift of the reference mirror.

Figure 3.15A shows the shift of the interference pattern more clearly in a smaller region of Fig. 3.14. Since we measure a spectral interference pattern, however, this drift of the reference mirror can be corrected in post-processing. For this, we apply a Fourier Transformation on each of the 60000 spectra, after they have been converted from the wavelength to the corresponding k-vector axis. The Fourier transform shows a peak corresponding to the fringe spacing of the observed interference pattern, and the phase of the Fourier amplitude at this peak value,  $\phi_R$ , corresponds to the phase of the interference pattern. After low-pass filtering, to remove a fast oscillation of small amplitude, which is due to the modulation of the tip, this phase shows the relative change of the reference arm length with respect to laser wavelength. The so retrieved phase as a function of time is shown in figure 3.15B. This low-pass filtered phase information is used to correct each spectrum by multiplying its Fourier transform of each spectrum with a factor  $\exp(i\phi_{R,low-pass})$ . Afterwards, the inverse Fourier transform is applied to retrieve the filtered spectra. The result is shown in figure 3.15C which clearly demonstrates the phase correction.

The temporal average spectrum is now shown in Fig. 3.16A. It clearly shows a spectral interference pattern. Since the tip was removed from the surface and  $E_{NF} = 0$ , the spectrum can be

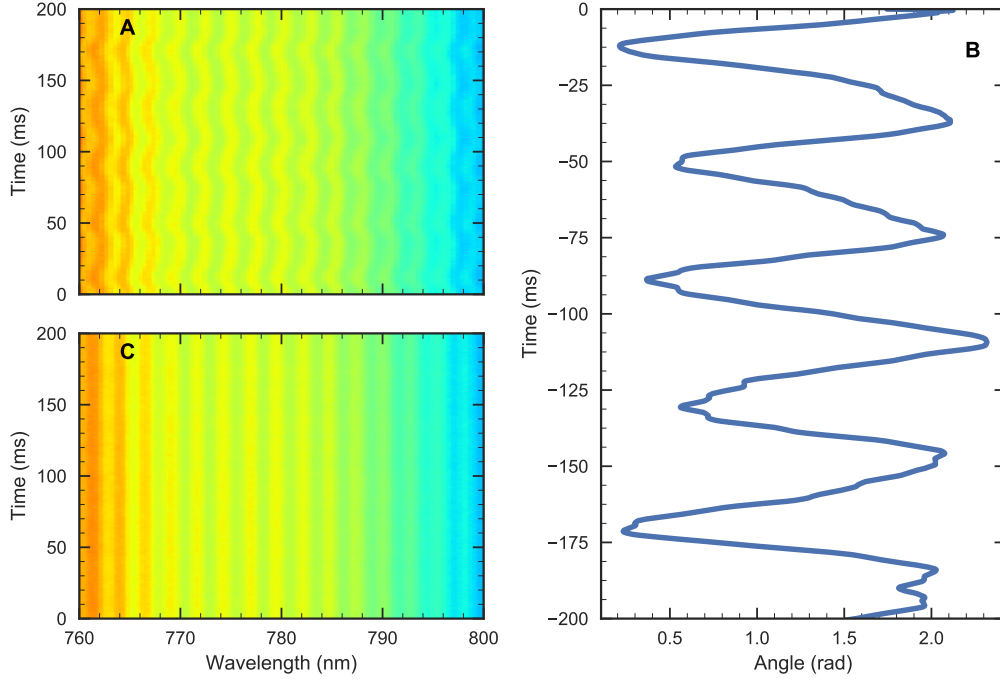


**Figure 3.15:** A: Spectra as a function of time for a zoomed in wavelength range. B: The extracted phase as a function of time. C: The corrected spectra.

described by the interference of reference and background field:

$$I \propto |E_R + E_B|^2 = |E_R|^2 + |E_B|^2 + 2\text{Re}(E_R E_B) \cos(k\Delta L). \quad (3.13)$$

Here,  $\Delta L$  is the constant path length difference between sample and reference arm. Performing a Fourier transform of the spectrum shown in Fig. 3.16A along the  $k$ -axis allows disentangling the constant part,  $E_R^2 + E_B^2$ , and the modulated part,  $E_R \cdot E_B$ . The Fourier transform is shown in Fig. 3.16B. Extracting and performing the inverse Fourier transform of the center peak and one of the side peaks (green line in Fig. 3.16B), the constant part and the modulation are retrieved, respectively. We now have two spectra for the two unknowns,  $E_R$  and  $E_B$ , and can thus completely disentangle the two fields. The result is shown in Fig. 3.16C and D. As expected, the reference spectrum closely resembles the laser spectrum. The background spectrum, however, differs, especially in the short-wavelength range, where the spectrum seems suppressed. This is most probably due to a different coupling of light from the two interferometer arms to the monochromator.

In total, these results clearly demonstrate that reference and background spectra are always mixed together, but can indeed be separated. We have now determined the reference and background spectra using the temporally averaged spectrum, i.e., the  $S_{0f}$  spectrum. In a SNOM measurement with the tip in contact, the higher-order spectra will be dominated by the cross

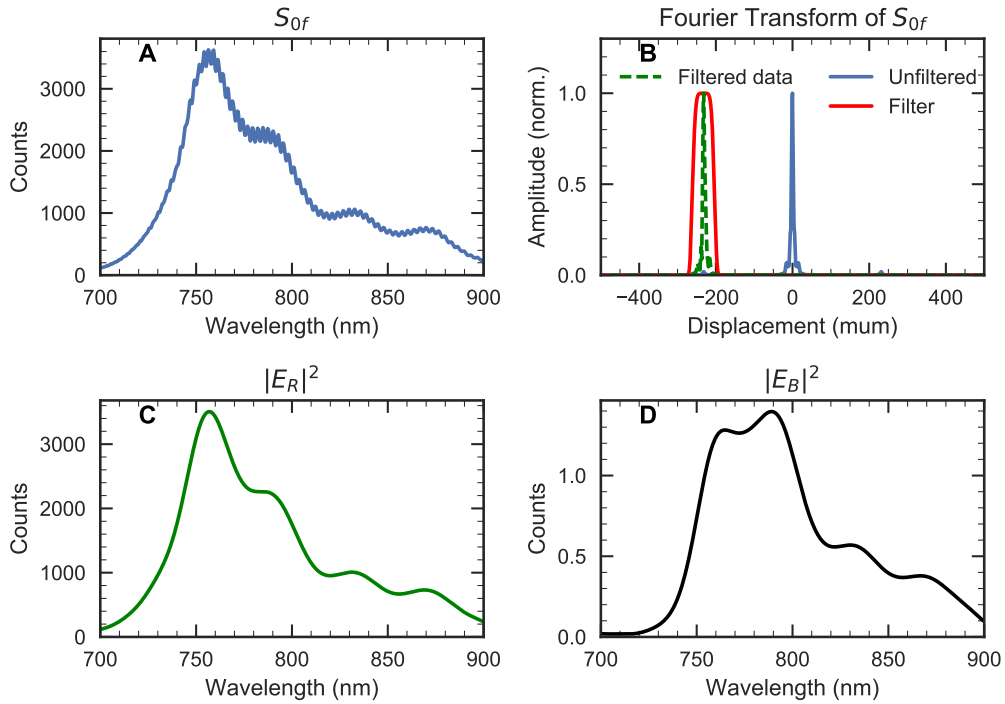


**Figure 3.16:** A: The  $S_{0f}$  spectrum. B: Fourier transform of the  $S_{0f}$  spectrum. From filtering once the DC peak and once the side peak and applying an inverse Fourier transform both the reference spectrum (C) and the background spectrum (D) can be extracted.

term  $E_R \cdot E_{NF}$ , giving access to the near field in an analogous way via the  $S_{nf}$  spectra. In the next chapters I will outline that the separation of near-field and background can also be achieved with less effort, using an in-line interferometer and directly demodulating the recorded spectra at a higher order harmonics of the tip modulation frequency.

# Theoretical Background

# 4

---

The retrieval or verification of material properties is the most challenging goal in analyzing sSNOM measurements, since the optical near-fields are measured only indirectly through the interaction of a probe and sample. Hence, applying a model to explain or predict the near-field scattered by the tip is of high importance. The model is the key to relate monochromatic as well as spectroscopic sSNOM measurements to material properties. Furthermore, explicit knowledge of the complex dielectric function, describing the response of the material to light interaction, prior to the sSNOM measurement, can help to identify the specific material in the post-processing step. It may even reveal new insights into the nanoscale material properties such as alignment properties of dye materials.

Thus, this chapter is divided in two parts. The first part deals with focusing light through layered systems including isotropic and anisotropic thin films. A quantum mechanical model is presented to relate far-field absorption spectra to the characteristically microscopic material properties, such as the refractive index. Together with a transfer matrix method, describing the transmission and reflection of light through a multilayer system, the electric fields after being focused through such systems are derived.

In a second part, these focus fields interact with the tip. Two different models are presented to simulate the near-field through the interaction of sample and tip that can be used to describe and simulate local sSNOM spectra.

## 4.1 Focusing through layered systems with anisotropic thin films

### 4.1.1 Microscopic model of the refractive index

The goal for this section is to introduce quantum mechanical tools to accurately describe and understand the optical properties of atoms and molecules and to achieve a general understanding of the light-matter interaction. In particular a deeper understanding of the origin of absorption spectra is determined.

#### 4.1.1.1 Electronic states

We start with the most simple case of an atom which is considered to be a two niveau system of a ground state  $|1\rangle$  and an excited state  $|2\rangle$ . In this case the Hamiltonian has only two eigenvalues  $E_1$  and  $E_2$  and the equations describing our system reads

$$\hat{H}_0 |n\rangle = E_n |n\rangle, \quad n \in \{1, 2\} \quad (4.1)$$

and we can also write  $\hat{H}$  in matrix notation

$$\hat{H}_0 = \begin{pmatrix} E_0 & 0 \\ 0 & E_1 \end{pmatrix} \quad (4.2)$$

If we prepare the system to be in state  $|n\rangle$  it will remain in this state forever. This is different for the case of a perturbed system. For that case we can write

$$\hat{H} = \hat{H}_0 + \hat{W} = \begin{pmatrix} E_1 + W_{11} & W_{12} \\ W_{12}^* & E_2 + W_{22} \end{pmatrix} = \begin{pmatrix} \tilde{E}_1 & W_{12} \\ W_{12}^* & \tilde{E}_2 \end{pmatrix} \quad (4.3)$$

and  $|1\rangle, |2\rangle$  are no eigenstates anymore. The energies  $E_{+,-}$  of the new states can be calculated by zeroing the determinant  $\det(\hat{H} - E_{+,-} \cdot I) = 0$  which leads to

$$E_{+,-} = \frac{\tilde{E}_1 + \tilde{E}_2}{2} \pm \sqrt{\left(\frac{\tilde{E}_1 - \tilde{E}_2}{2}\right)^2 + W_{12}^2} \quad (4.4)$$

Up to now light-matter interaction was not considered. With an additional optical field we introduce a coupling to the dipole moment of the atom and thus have a time-dependent change of the wave function. The dynamics of such a closed quantum system is governed by the

time-dependent Schrödinger equation acting on the wavefunction  $\Psi$

$$i\hbar \frac{\partial}{\partial t} \Psi = [\hat{H}_0 + \hat{H}_I(t)]\Psi \quad (4.5)$$

with the Hamiltonian

$$\hat{H}_I(t) = -ex\mathcal{E}(t) = -\mu\mathcal{E}(t) \quad (4.6)$$

describing the light interaction. Here we assume a homogeneous electromagnetic field  $\mathcal{E}(t)$  polarized in x-direction.  $\mu$  is the operator for the electric dipole moment [118].

The solution of equation (4.5) can be written as

$$\psi(r, t) = \sum_m a_m(t) e^{-i\epsilon_m t} \psi_m(r). \quad (4.7)$$

This gives us a differential equation for the coefficients  $a_n$  as well:

$$i\hbar \frac{\partial}{\partial t} a_n = -\mathcal{E}(t) \sum_m e^{-i(\epsilon_m - \epsilon_n)t} \langle n | \mu | m \rangle a_m \quad (4.8)$$

We can now consider the field as a perturbation and write

$$a_n = a_n^{(0)} + \Delta a_n^{(1)} + \dots \quad (4.9)$$

and

$$\mathcal{E}(t) \rightarrow \Delta\mathcal{E}(t). \quad (4.10)$$

For first order perturbation one can easily show [118] that  $a_n^{(1)}$  yields

$$a_n^{(1)}(t) = -\frac{1}{i\hbar} \int_{-\infty}^t dt' \mathcal{E}(t') \langle n | \mu | l \rangle e^{-i(\epsilon_l - \epsilon_n)t'} \quad (4.11)$$

assuming the electron was initially (time  $t \rightarrow -\infty$ ) in the state  $|l\rangle$ . The integral can be solved by expressing the field  $\mathcal{E}(t)$  through its Fourier Transform

$$\mathcal{E}(t) = \lim_{\gamma \rightarrow 0} \int \frac{d\omega}{2\pi} e^{-i\omega t} e^{\gamma t}. \quad (4.12)$$

Here the damping factor  $\gamma$  ensures that the electric field is 0 at times  $t \rightarrow -\infty$  and is physically related to a dephasing time  $\tau = 1/\gamma$ .

With equation (4.12) we find

$$a_n^{(1)}(t) = -\frac{\langle n|\mu|l\rangle}{2\pi\hbar} \int d\omega \mathcal{E}(\omega) \frac{e^{-i(\omega+\epsilon_l-\epsilon_n)t}}{\omega + \epsilon_l - \epsilon_n + i\gamma}, \quad (4.13)$$

which describes the first linear term for the amplitude of the wavefunction from equation (4.7). In case of weak electromagnetic fields we can limit ourselves to the linear response. It should be noted however that for strong fields one can use the result from equation (4.13) and solve the time depending Schrödinger equation for higher order perturbation as well. Solutions for higher order perturbation theory will not be covered here, but can be found in many textbooks[119]. Since we now have derived a solution for the wavefunction  $\Psi(r, t)$  with

$$\Psi(r, t) = e^{-i\epsilon_l t} \left[ \Psi_l(r) - \sum_{m \neq l} \frac{\mu_{lm}}{2\pi\hbar} \Psi_m(r) \int d\omega \mathcal{E}(\omega) \frac{e^{-i\omega t}}{\omega + \epsilon_l - \epsilon_m + i\gamma} \right] \quad (4.14)$$

we can relate our results to linear optical properties of a material system, in particular we can calculate the polarization induced by the external field, which is given by the expectation value of the electric dipole moment

$$P(t) = \langle \Psi | \mu | \Psi \rangle = n_0 \int d^3r \Psi^*(r, t) \mu \Psi(r, t). \quad (4.15)$$

Hereby,  $n_0$  denotes the density of atoms .

After inserting the wavefunction we can finally write the result by introducing the linear susceptibility  $\chi(\omega)$  through the relation  $P(\omega) = \epsilon_0 \chi(\omega) \cdot \mathcal{E}(\omega)$  and find [119]

$$\chi(\omega) = \frac{n_0}{\hbar\epsilon_0} \sum_n |\mu_{ln}|^2 \cdot \left[ \frac{1}{\omega - \omega_{ln} - i\gamma} + \frac{1}{\omega + \omega_{ln} + i\gamma} \right], \quad (4.16)$$

with  $\mu_{ln} := \langle l | \mu | n \rangle$  and  $\omega_{ln} := \epsilon_l - \epsilon_n$ .

From this equation it follows that the dielectric susceptibility and thus the absorption spectrum is related to the input Hamiltonian only by the discrete energy levels  $\omega_{ln}$  and the dipole moment  $\mu_{ln}$ .

Furthermore,  $\chi(\omega)$  is directly related to material properties like absorption that can be obtained from optical measurements. Let's assume we have a medium of thickness  $d$  with refractive index  $n$ . The refractive index is linked to the dielectric susceptibility by  $n = \sqrt{\epsilon(\omega)} = \sqrt{1 + \chi(\omega)}$ . For sufficiently dilute media this can also be approximated as  $n \simeq 1 + 0.5\chi(\omega)$  [119]. With a propagating plane wave through the medium described by

$$E(z, t) = E_0 e^{i(kz - \omega t)} + cc. = E_0 e^{i(n(\omega)\omega z/c - \omega t)} + cc. \quad (4.17)$$

the intensity along the medium is given by Beers Law

$$I(z) = I_0 e^{-\alpha z}. \quad (4.18)$$

The absorption coefficient  $\alpha$  is then finally given by

$$\alpha = 2 \cdot \text{Im}(n)\omega/c = \text{Im}(\chi(\omega))\omega/c. \quad (4.19)$$

Consequently, we find that by defining the Hamiltonian for a given system and including light-matter interaction, we can explain absorption spectra measured by propagation of optical plane waves through a medium within a quantum mechanical description.

At this point it should be noted that even though the dielectric susceptibility already describes the relation between the Hamiltonian and the real physical properties, a more complete description of a system including an environment and therefore also relaxation and dephasing processes can be derived by using the density matrix formalism. In that case the time evolution of the quantum system is governed by the Liouville von Neumann equation

$$\dot{\rho}(t) = -\frac{i}{\hbar}[H, \rho(t)], \quad (4.20)$$

which is the equivalent of the time depending Schrödinger equation for the density matrix formalism. The Hamiltonian now includes additional terms for the environment and the interaction between system and environment. To get insight in the dynamics of the system one can now perform a partial trace over the environmental degrees of freedom and thus obtain a master equation for the motion of the original system density matrix. The Lindblad master equation for the reduced density matrix  $\rho = \text{Tr}_{\text{env}}[\rho]$  is the most general type of master equation that preserves the laws of quantum mechanics and is given by

$$\dot{\rho}(t) = -\frac{i}{\hbar}[H(t), \rho(t)] + \sum_n \frac{1}{2} \left[ 2C_n \rho(t) C_n^\dagger - \rho(t) C_n^\dagger C_n - C_n^\dagger C_n \rho(t) \right] \quad (4.21)$$

with  $C_n = \sqrt{\gamma_n} A_n$  and  $A_n$  the operators with which the environment couples to the system and  $\gamma_n$  are the corresponding rates, i.e. relaxation and dephasing rates.

Numerically the Lindblad equation can be solved by a Runge-Kutta algorithm and finally the absorption spectrum can be obtained by Fourier transformation of  $\text{Tr}(H_i \rho(t))$  where  $H_i$  is the light interaction Hamiltonian. For the description of our transmission spectra however, a coupling to an environment is not needed and we can restrict ourselves to the simple relation between the dielectric susceptibility and the Hamiltonian given by equation (4.16).

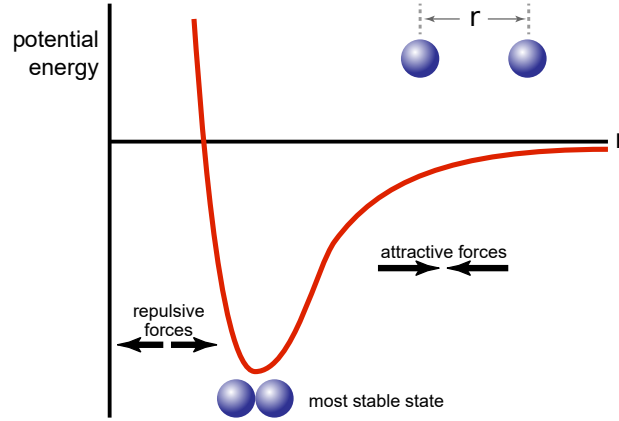


Figure 4.1: Typical anharmonic potential

#### 4.1.1.2 Vibrational modes in a two level system

Up to now only electronic states have been considered. For describing systems like molecules also oscillation modes of the nuclei motion (phonon coupling) have to be taken into account.

An image of a typical anharmonic potential curve for a molecule is shown in figure 4.1.

For low energies the molecule is positioned at the minimum of this curve and therefore in first approximation the nuclei will see a nearly harmonic potential.

The Hamiltonian for an harmonic oscillator is governed by

$$\hat{H} = \frac{\hat{P}^2}{2m} + \frac{1}{2}m\omega^2\hat{X}^2. \quad (4.22)$$

With  $\hat{P}' := \frac{1}{\sqrt{m\hbar\omega}}\hat{P}$  and  $\hat{X}' := \sqrt{\frac{m\omega}{\hbar}}\hat{X}$  this can also be written as [120]

$$\hat{H} = \frac{\hbar\omega}{2} (\hat{X}'^2 + \hat{P}'^2) = \hbar\omega \cdot \left( \hat{a}^\dagger \hat{a} + \frac{1}{2} \right) = \hbar\omega \left( \hat{n} + \frac{1}{2} \right) \quad (4.23)$$

Here  $\hat{a}^\dagger$  and  $\hat{a}$  are the creation and annihilation operators and  $\hat{n} = \hat{a}^\dagger \hat{a}$  is the number operator that counts the number of states. The solutions  $\Psi_n$  of the wavefunctions following the Schrödinger equation  $\hat{H}\Psi = E\Psi$  can be found analytically and are expressed in terms of Hermite polynomials  $H_n$  as

$$\Psi_n(x) = \langle x|n\rangle = \left( \frac{m\omega}{\pi\hbar} \right)^{\frac{1}{4}} \frac{1}{\sqrt{2^n n!}} \cdot H_n \left( \frac{m\omega}{\hbar} \cdot x \right) \cdot e^{-\frac{1}{2} \frac{m\omega}{\hbar} x^2} \quad (4.24)$$

with energy eigenvalues

$$E_n = \hbar\omega \left( n + \frac{1}{2} \right). \quad (4.25)$$

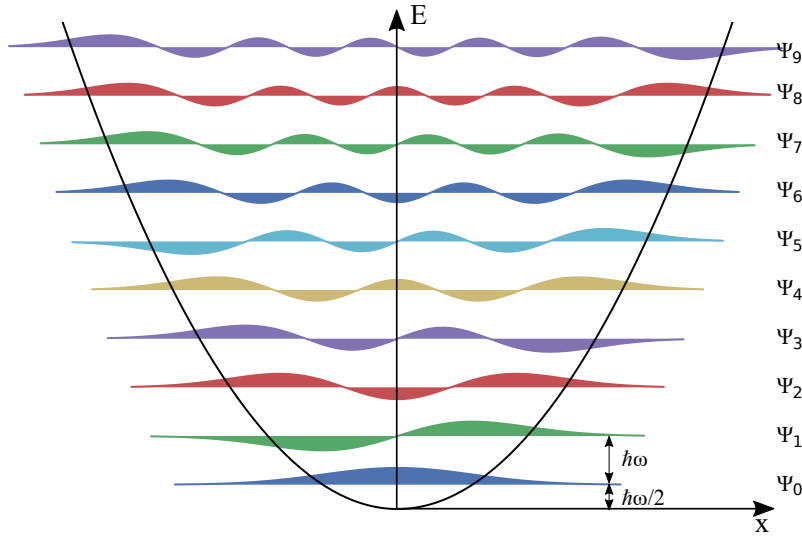


Figure 4.2: Wavefunctions for the harmonic oscillator

The solutions for the wavefunctions of an harmonic oscillator are plotted in figure 4.2. For the vibrational modes we define the energy as  $E_n = \hbar\omega_{vib}(n + \frac{1}{2})$ .

Now, to describe a two level system including vibrational modes we can express our two electronic states as two displaced harmonic oscillators whose 0-0 energy splitting is given as  $E_1 - E_0$  with  $E_0$  the energy of the ground state and  $E_1$  the energy of the 0th order vibrational mode of the excited state.

The existence of a displacement for the potential energy surface (PES) between ground and excited states corresponds to different equilibrium states of the molecule, which is a result of a change in electronic configuration and therefore results in a change of bonding between ions or atoms [121].

Consequently, the total Hamiltonian includes both electronic as well as vibrational terms:

$$\hat{H}_0 = \hbar\omega_0 |0\rangle\langle 0| + \hbar\omega_1 |1\rangle\langle 1| + \sum_n \hbar\omega_{vib}(\hat{n}_n + \frac{1}{2}) + \hbar\omega_{vib} \cdot \left( \lambda \cdot (\hat{a}^\dagger + \hat{a}) + \lambda^2 \right) |1\rangle\langle 1|. \quad (4.26)$$

The first two terms in this equation describe the electronic states, the third term is the Hamiltonian of the non-shifted harmonic oscillator describing the vibrational modes and the last term describes an additional shift of the oscillator along the x-direction. For the last term the relation

$$\hat{X} = \frac{1}{\sqrt{2}}(\hat{a}^\dagger + \hat{a}) \quad (4.27)$$

between the coordinate operator  $\hat{X}$  and the creation and annihilation operators was used.

Additionally,

$$\lambda = -\sqrt{\frac{\omega_{vib}}{2\hbar}} \quad (4.28)$$

was introduced and represents a dimensionless shift of the potential energy surface of the electronic state  $|e\rangle$ .  $\lambda$  is also known as Huang Rhys factor [121, 122].

With equation (4.26) the Hamiltonian of our system is fully described. However, as before, light matter interaction is not yet included and we cannot just use the result for the dielectric susceptibility from equation (4.16), because now also transitions from different vibrational modes have to be considered.

As we have already seen, the intensity for optical transition in the electronic system from one state into another is related directly to the absolute squared value of the transition dipole moment

$$M_{lm} = \langle m|\mu|l\rangle = \int \Psi_m^* \mu \Psi_l d\tau. \quad (4.29)$$

In the present case the wavefunction includes both a nuclear and an electronic part. However, using the Born-Oppenheimer approximation [123] the wavefunctions can be separated into two parts

$$\Psi(R, r) = \xi(R) \cdot \Phi(r), \quad (4.30)$$

with nuclear coordinates  $R$  and electronic coordinates  $r$ . Hence, also the transition dipole moment can be separated in  $M_{rR} = M_r + M_R$  which can be written in Dirac form as [124]

$$M = \langle \xi''(R) | \xi'(R) \rangle \langle \Phi''(r, R) | \mu | \Phi'(r, R) \rangle + \langle \Phi''(r, R) | \Phi'(r, R) \rangle \langle \xi''(r, R) | \mu | \xi'(R) \rangle \quad (4.31)$$

where ' denotes the initial state and '' the end state. The electronic wavefunctions have to be orthogonal such that the second term is zero and the equations simplifies to

$$M = \langle \xi''(R) | \xi'(R) \rangle \langle \Phi''(r, R) | \mu | \Phi'(r, R) \rangle. \quad (4.32)$$

The second factor of this equation is the electronic dipole moment. Since the nuclei are much heavier than the electrons, they are staying at a nearly fixed position  $R_0$  during the electronic transition. This is called the Franck Condon approximation and as a result the electronic dipole

moment can be written as

$$M_{el} = \langle \Phi''(r, R_0) | \mu | \Phi'(r, R) \rangle \quad (4.33)$$

and is now independent of the nuclear coordinates.

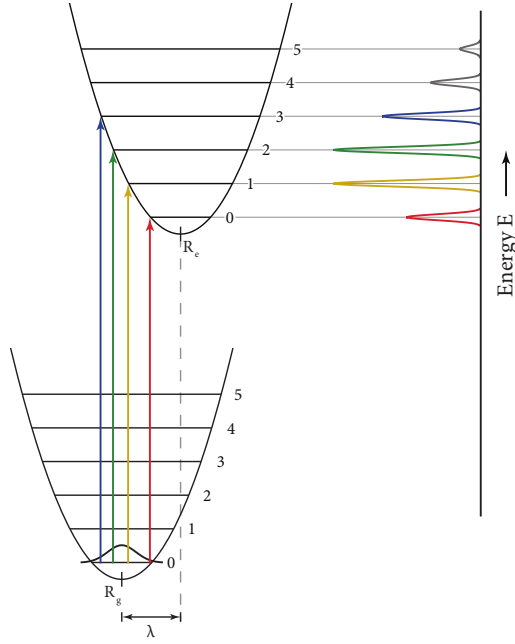


**Figure 4.3:** Franck Condon factors (changed from [121])

In the case of no displacement the integral for the 0-0 transition is 1 and it is 0 for all other 0-n transitions, because the wavefunctions for higher orders are asymmetric. For a larger displacement the overlap with the higher order wavefunctions is nonzero and the intensity of this transitions gets higher.

More precisely, the integral from equation (4.34) can be solved analytically since we have already derived the wavefunctions of an harmonic oscillator in equation (4.24). After performing some mathematical operations[125] we can find the Franck Condon integral for the transition from the vibrational state M of the ground state  $|g\rangle$  into vibrational state N of the excited state  $|e\rangle$  as

$$\langle \xi_{g,M} | \xi_{e,N} \rangle = e^{-\lambda^2/2} \sum_{m=0}^M \sum_{n=0}^N \frac{(-1)^n \lambda^{n+m}}{m!n!} \times \sqrt{\frac{M!N!}{(M-m)!(N-n)!}} \delta_{M-m, N-n} \quad (4.36)$$

The factor  $\lambda$  is again the dimensionless Huang Rhys factor [121, 122] and describes the displacement of the harmonic oscillator potentials of ground state and excited state and hence

The term

$$\langle \xi''(R) | \xi'(R) \rangle \quad (4.34)$$

is the so called Franck Condon integral. The absolute squared value of this integral are the Franck-Condon factors. They define the intensity of a transition from a vibrational state of the electronic ground state into a vibrational state of the electronic excited state. That means the intensity of the transition from one state into another is described by the overlap integral of the nuclear wavefunctions

$$I_{\nu', \nu''} \propto \langle \xi''(R) | \xi'(R) \rangle^2. \quad (4.35)$$

From figure 4.2 we can already conclude that the intensity of the transition is defined by the displacement of the potential surface of the ground state and the excited state.

also represents the strength of coupling to the nuclear degree of freedoms. In this way the Huang Rhys factor is also related to the Stokes Shift that can be observed in fluorescence measurements [121]. For a Huang Rhys factor  $\lambda < 1$  the dependency on the vibrational energy  $\omega_{vib}$  is weak and the main peak in the absorption spectra is centered at the 0-0 transition with the amplitude for the vibronic progression decaying exponentially. For  $\lambda \gg 1$  the strong coupling regime is reached and the maximum intensity is found for a transition to the vibrational level  $\nu \propto \lambda$  [122].

Figure 4.3 shows a visual representation of the Franck Condon principle with the intensities for different transitions of a displaced PES given by the Franck Condon factors.

#### 4.1.2 Transfer Matrix Method

The transfer matrix model is used to simulate transmission and reflection through a multi-layer system consisting of multiple materials with different optical refractive indices.

The advantage of using a transfer matrix model is that one can treat all multiple reflections occurring in such a multilayer system which can change the outcome e.g. for a simple transmission spectrum.

A typical situation of multiple reflections in just a single medium is illustrated in figure 4.4. We are considering one incoming monochromatic laser beam with wavelength  $\lambda$  propagating towards a medium under an angle.

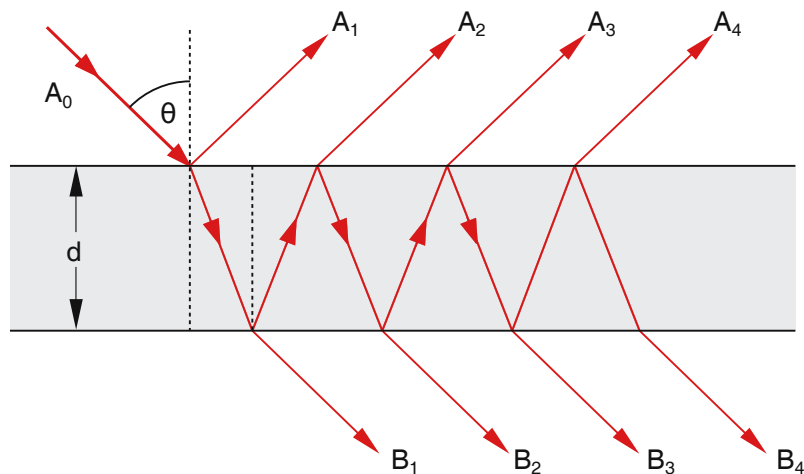
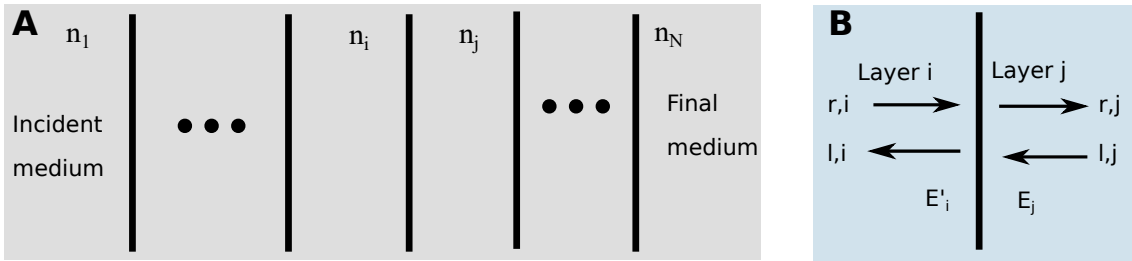


Figure 4.4: Multiple reflections in a single medium (adapted from [126])

Each ray is phase-shifted from the others by multiples of the same factor. The intensity of each ray can be deduced as long as the transmission and reflection coefficients for the interfaces are

known. Taking all reflections into account one can calculate the overall transmitted or reflected light. In general, following the beam like this can be done for a sample consisting of several layers with different refractive indices as well. However, with increasing number of layers this process will get cumbersome.

An easier way is to use a more general approach. Here, I follow the notation of M. Klein and T. Furtak [127] and write the electric field in each layer as a sum of two components  $E_{r,i}$  and  $E_{l,i}$ , one propagating to the right and one propagating to the left in the medium  $i$  with refractive index  $n_i$ , as illustrated in figure 4.5.



**Figure 4.5:** Visualization of the transfer matrix method. A: the multilayer structure, B: Incoming and outgoing fields at interface the between layer  $i$  and  $j$ .

When propagating along an interface from medium  $i$  to medium  $j$  the transmission coefficient  $t_{ij}$  and reflection coefficient  $r_{ij}$  have to be applied. These can be obtained from the Fresnel equations as

$$t_{ij} = \frac{2 \cdot n_i \cdot \cos(\theta_i)}{n_i \cos(\theta_i) + n_j \cos(\theta_j)} = \frac{2 \sin(\theta_j) \cos(\theta_i)}{\sin(\theta_i + \theta_j)} \tag{4.37}$$

$$r_{ij} = \frac{n_i \cos(\theta_i) - n_j \cos(\theta_j)}{n_i \cos(\theta_i) + n_j \cos(\theta_j)} \tag{4.38}$$

for s-polarized light (E perpendicular to the plane of incidence) and

$$t_{ij} = \frac{2 \cdot n_i \cdot \cos(\theta_i)}{n_j \cos(\theta_i) + n_i \cos(\theta_j)} = \frac{2 \sin(\theta_j) \cos(\theta_i)}{\sin(\theta_i + \theta_j) \cos(\theta_i - \theta_j)} \tag{4.39}$$

$$r_{ij} = \frac{n_j \cos(\theta_i) - n_i \cos(\theta_j)}{n_j \cos(\theta_i) + n_i \cos(\theta_j)} = \frac{\tan(\theta_i - \theta_j)}{\tan(\theta_i + \theta_j)} \tag{4.40}$$

for p-polarized light (E in the plane of incidence).

The angles  $\theta_i$  can be obtained from snells law,  $n_i \sin(\theta_i) = n_j \sin(\theta_j)$ . As long as the incident angle to the first layer is given, the angles for all other layers can be calculated. Also,  $n_i$  and  $n_j$  can be imaginary, which leads to imaginary angles.

The electric fields at the right side of the interface of layer i to layer j can be written as a sum of transmitted and reflected fields

$$E_{r,j} = E'_{r,i} t_{ij} + E_{l,j} r_{ji} \quad (4.41)$$

$$E'_{l,i} = E_{l,j} t_{ji} + E'_{r,i} r_{ij} \quad (4.42)$$

The unprimed fields are fields from the left side of one layer and the primed fields are from the right side of one layer, e.g.  $E_{r,j}$  is the field from the left side of the layer j propagating to the right side of layer j.

By using the symmetry relationship of the Fresnel equations  $t_{ij} t_{ji} + (r_{ij})^2 = 1$  and  $r_{ij} = -r_{ji}$  as derived in [127], equations (4.41) and (4.42) can be written as

$$E'_{r,i} = \left( \frac{r_{ij}}{t_{ij}} \right) E_{l,j} + \left( \frac{1}{t_{ij}} \right) E_{r,j} \quad (4.43)$$

$$E'_{l,i} = \left( \frac{1}{t_{ij}} \right) E_{l,j} + \left( \frac{r_{ij}}{t_{ij}} \right) E_{r,j} \quad (4.44)$$

or in matrix form:

$$\begin{pmatrix} E'_{l,i} \\ E'_{r,i} \end{pmatrix} = \frac{1}{t_{i,j}} \begin{pmatrix} 1 & r_{i,j} \\ r_{i,j} & 1 \end{pmatrix} \begin{pmatrix} E_{l,j} \\ E_{r,j} \end{pmatrix} \quad (4.45)$$

Thus, we have two coupled equations connecting the fields on the left side of the interface with the fields on the right side.

Additionally, when passing through a layer we accumulate a phase which is dependent on the thickness of the layer, the angle of incidence and the wavelength:

$$\delta_j \equiv k_z d_j = \frac{2\pi}{\lambda_0} n_j d_j \cos(\theta_j) \quad (4.46)$$

Here  $\theta_j$  is the incident angle in layer  $j$ . Again, the refractive index can be complex, with  $\text{Im}(n) > 0$  describing absorption, with  $\text{Im}(n) < 0$  describing stimulated emission. Since we are only considering monochromatic waves, the refractive index and the angle are just (complex) numbers. To simulate spectra at a later point we just have to reevaluate all equations for different wavelengths.

The phase is changing the electric field on the right side (when propagating from left to right) or the left side (propagating from right to left) respectively:

$$E'_{r,i} = E_{r,j} e^{i\delta_j}, \quad E_{l,j} = E'_{l,j} e^{i\delta_j} \quad (4.47)$$

This effect can also be written in matrix notation and we can define a matrix describing the propagation in layer  $j$ <sup>1</sup>

$$M_j \equiv \begin{pmatrix} e^{i\delta_j} & 0 \\ 0 & e^{-i\delta_j} \end{pmatrix} \begin{pmatrix} 1 & r_{j,j+1} \\ r_{j,j+1} & 1 \end{pmatrix} \frac{1}{t_{j,j+1}} \quad (4.48)$$

In total the complete multilayer can be expressed by multiplying the matrices for each layer interface:

$$M = \frac{1}{t_{1,2}} \begin{pmatrix} 1 & r_{1,2} \\ r_{1,2} & 1 \end{pmatrix} M_2 M_3 \dots M_{N-1} \quad (4.49)$$

The matrix  $M$  contains the information about the whole layer system including multiple reflections.

Finally, we get

$$\begin{pmatrix} E'_{l,1} \\ E'_{r,1} \end{pmatrix} = \begin{pmatrix} M_{11} & M_{12} \\ M_{21} & M_{22} \end{pmatrix} \begin{pmatrix} E_{l,N} \\ E_{r,N} \end{pmatrix}. \quad (4.50)$$

Now, for simplicity, we start with a field amplitude of  $E'_{r,1} = 1$ . The amplitude at the first interface in backward direction is then equal to the reflection coefficient  $r \equiv E'_{l,1}/E'_{r,1}$  and the amplitude at the last interface in forward direction is the overall transmission coefficient through the layers  $t$ . We don't consider any fields propagating in backwards direction after the

<sup>1</sup>We used here a different notation than in [127], the sign in the exponential in equation (4.47) and (4.48) are changed. This way it is consistent with other literature. The reason for a different notation in [127] is a different definition of the propagating wave. We follow the convention of describing a propagating wave by  $\exp(ikz)$ .

last layer, therefore  $E_{l,N} = 0$ . In total we get:

$$\begin{pmatrix} r \\ 1 \end{pmatrix} = M \begin{pmatrix} 0 \\ t \end{pmatrix} = \begin{pmatrix} M_{12} t \\ M_{22} t \end{pmatrix} \quad (4.51)$$

From the two coupled equations the reflection coefficient  $r$  and the transmission coefficient  $t$  can be derived as

$$t = \frac{1}{M_{22}} \quad r = \frac{M_{12}}{M_{22}} \quad (4.52)$$

The transmitted and reflected intensity can now be calculated by:

$$T = |t|^2 \frac{n_N \cos(\theta_N)}{n_1 \cos(\theta_1)} \quad R = |r|^2 \quad (4.53)$$

$n_N$  and  $n_1$  are the refractive indices of the last and first medium and  $\theta_N$  and  $\theta_0$  are the angles of the beam propagating in the last medium and first medium respectively. The origin of the intensity equations stems from calculations of the pointing vector, the net power flowing forward through the structure, and considering energy conservation as shown in [127]. One should note that equation (4.53) is only valid when the refractive indices of the first and last layer are not complex. This is usually the case, since the incident and final media are mostly non-absorbing, e.g. air. For absorbing end layers the angles in equation (4.53) can become complex and we have to use the real part and complex conjugates of the complex angles. A more detailed derivation for these special cases can be found in [128].

Another thing to consider are thick layers, i.e. layers thicker than the wavelength of light. Let us have a look at a typical sample. Figure 4.6A shows a 30 nm gold layer on top of a 180  $\mu\text{m}$  thick glass substrate. To simulate the gold layer we use  $n = \sqrt{\epsilon}$ , whereas  $\epsilon$  is taken from known data measured by Olmon et al. [129]. For the refractive index of glass we use the Sellmeier equation for a BK7 glass substrate.

The result of the simulated transmission spectrum is shown as the green curve in figure 4.6B.

For thick films, layers that are much larger than the wavelength, we will see fringes in the simulated spectrum, because of interference of the waves from the frontside and the backside of that layer. These narrow Fabrit-Perot oscillations are normally not seen in measurements (blue curve in figure 4.6B), because different effects destroy the interference. These effects can be nonparallel surfaces of the thick film, rough surfaces, or the fact that the light propagation through the layer is slightly focused or divergent. In all cases the phases of the multiple reflected

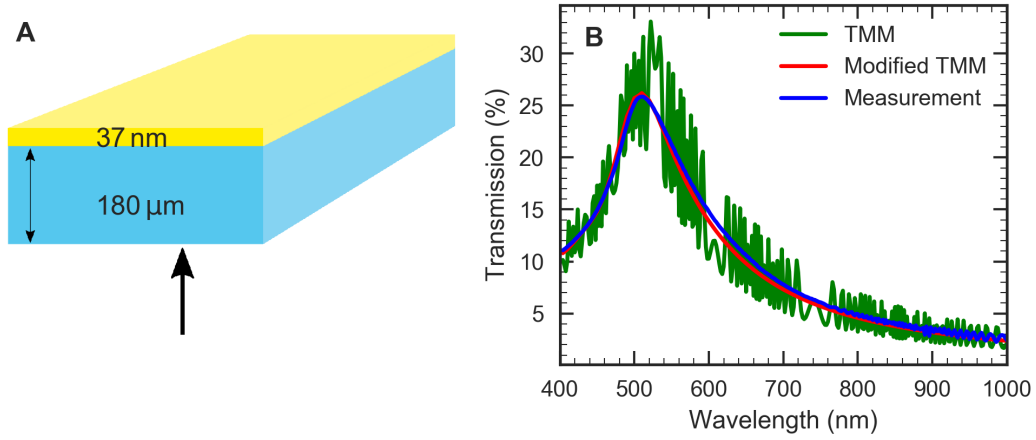


**Figure 4.6:** (A) Visualization of a sample of gold on a glass substrate in air, (B) Transmission through a glass-gold layer. Blue curve: TMM simulation with air-glass-gold-air, red curve: modified TMM as explained below, green: measurement for a 30nm gold film.

light waves in the thick layer are incoherent.

To account for these effects and suppress the fringes Katsidis et al. [130] proposed a modified incoherent transfer matrix method. Hereby, we assume to have a set of  $N$  layers with one of them being a thick “incoherent” layer at layer position  $m$ . All thin layers before and after this incoherent layer are treated the same way using the transfer matrix method as explained above. So we divide the layer system in two “coherent” multilayer connected by the incoherent layer. The final complex transmission coefficients  $t_{0,m}$  and  $t_{m,N+1}$  (and reflection coefficients  $r_{0,m}$  and  $r_{m,N+1}$ ) of each of the two multilayer systems are then given by equation (4.52). Now these coefficients are replaced with their square amplitudes to get intensities instead of amplitudes. Following a similar approach one can formulate modified intensity matrices. These intensity matrices are then multiplied with a propagation matrix ( $P_m$ ) of the incoherent layer to get the overall transmission through all layers:

$$\begin{aligned}
 M^{\text{inc}} = M_{0/m} P_m M_{m/N+1} &= \frac{1}{|t_{0,m}|^2} \begin{bmatrix} (|t_{0,m} t_{m,0}|^2 - |r_{0,m} r_{m,0}|^2) & |r_{0,m}|^2 \\ -|r_{m,0}|^2 & 1 \end{bmatrix} \times \begin{bmatrix} |e^{-i\delta_m}|^2 & 0 \\ 0 & |e^{i\delta_m}|^2 \end{bmatrix} \\
 &\times \frac{1}{|t_{m,N+1}|^2} \begin{bmatrix} (|t_{m,N+1} t_{N+1,m}|^2 - |r_{m,N+1} r_{N+1,m}|^2) & |r_{m,N+1}|^2 \\ -|r_{N+1,m}|^2 & 1 \end{bmatrix}
 \end{aligned} \tag{4.54}$$

Similar to equation 4.52 the transmission and reflection are given by <sup>2</sup>:

$$T = \frac{1}{M_{22}^{\text{inc}}}, \quad R = \frac{M_{12}^{\text{inc}}}{M_{22}^{\text{inc}}}$$

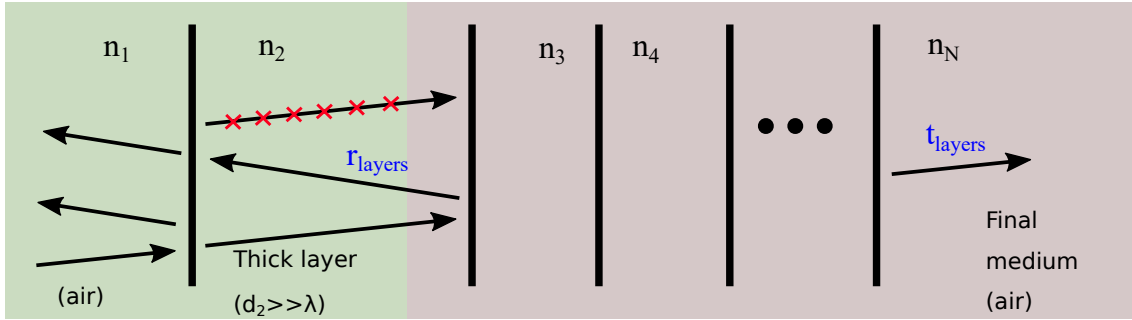


**Figure 4.7:** Visualization of the modified TMM including a thick layer.  $r_{\text{layers}}$  and  $t_{\text{layers}}$  are the reflection and transmission amplitudes for layer 3 to N.

In our case the thick layer, the glass substrate, is always the second layer if the incident medium (air) is labeled as layer one. We now use a similar approach as introduced by Kwatsidis et al. [130], i.e. we split our multilayer system in two parts. The first part consists of the incident medium (air) and the thick glass layer (denoted as the 2<sup>nd</sup> layer). The second part starts from the interface of the glass to layer 3 as illustrated in figure 4.1.2. In order to suppress the narrow oscillations, we only consider the first two reflections at the interfaces of the 2<sup>nd</sup> layer. In detail, we start at the interface air–glass. There, a fraction is transmitted and reflected. The transmission and reflection amplitude  $t_{\text{air,glass}}$  and  $r_{\text{air,glass}}$  for a glass interface is given by the Fresnel equations (eq. (4.37) - (4.40)). To take into account the propagation through glass we add a phase term  $e^{i\delta}$  with  $\delta = \frac{2\pi}{\lambda_0} n_{\text{glass}} d_{\text{glass}}$ . At the interface to layer 3 once more a part of the light is reflected and a part is transmitted. The transmission amplitude  $t_{\text{layers}}$  for the remaining layers 3 to N can be calculated as before by using the transfer matrix method. The reflected part at layer 3 (given by the reflection amplitude  $r_{\text{layers}}$ ) propagates through the glass layer again, which is accounted for by adding another phase term  $e^{-i\delta}$ . Now at the first interface from glass to air only transmission takes place and the reflection is suppressed.

Hence we can write the transmission coefficient for layers 1 to N by:

$$t_{\text{glass+layers}} = t_{\text{layers}} \cdot t_{\text{air,glass}} \cdot e^{i\delta} = t_{\text{layers}} \cdot t_{\text{air,glass}} \cdot e^{i\frac{2\pi}{\lambda_0} n_{\text{glass}} d_{\text{glass}}} \quad (4.55)$$

<sup>2</sup>We changed the indices in the matrix compared to the equation given by Katsidis et al. [130] so the formulation is consistent with our notation of the coherent transfer matrix model.

Analogous we have for the reflection amplitude:

$$r_{glass+layers} = \underbrace{t_{air,glass} e^{i\delta}}_{\text{field amplitude after glass}} \cdot r_{layers} \cdot t_{glass,air} \cdot e^{-i\delta} + r_{air,glass} \quad (4.56)$$

The resulting transmission  $T = |t_{glass+layers}|^2 \frac{n_N \cos(\theta_N)}{n_1 \cos(\theta_1)}$  for the glass-gold layer system is included in figure 4.6 as the red curve. As expected we can clearly see, that the transmission spectrum calculated by this method is like an average over the interference fringes shown in the green curve of figure 4.6. The transfer matrix method can now be used to simulate transmission spectrum though all kinds of isotropic layered media. To also include anisotropic media, the transfer matrix method has to be slightly adapted, as will be outlined in the next section.

### 4.1.3 Anisotropic Media

In isotropic media molecules are oriented along totally random directions or are isotropic themselves, like in gases, liquids or amorphous solids. If the measurable optical properties depend on the direction of the medium, the medium is called to be anisotropic. In this case either the molecules are anisotropic or are not oriented randomly anymore, but follow specific directions, for example of a crystal lattice [131]. Well-known anisotropic materials are calcite crystals or  $\beta$ -Barium Borate (BBO-) crystals. The latter is one of the most versatile nonlinear optical crystals widely used in second or third harmonic generation for high power laser sources. Also squaraine dye molecules used throughout this work show anisotropic behavior. To be able to describe the beam propagation in such media [132] an extended description is necessary. In particular we have to derive new transmission and reflection coefficients at the interface of these media.

To understand the physics behind anisotropic media we start with the Maxwell's equations in the absence of charges and currents:

$$\vec{\nabla} \cdot \vec{D} = 0 \quad (4.57)$$

$$\vec{\nabla} \cdot \vec{B} = 0 \quad (4.58)$$

$$\vec{\nabla} \times \vec{E} = -\frac{\partial \vec{B}}{\partial t} \quad (4.59)$$

$$\vec{\nabla} \times \vec{H} = \frac{\partial \vec{D}}{\partial t} \quad (4.60)$$

From (4.57) it follows with  $\vec{D} = \vec{D}_0 \exp(i(\vec{k}\vec{r} - \omega t))$  that  $\vec{D} \cdot \vec{k} = 0$  and therefore that the k-vector is perpendicular to the displacement vector at all times.

For isotropic media this consequently means that the wave vector is also perpendicular to the electric field  $\vec{E}$  as the displacement vector is parallel to the electric field vector and

$$\vec{D} = \epsilon \vec{E} = \epsilon_0 \vec{E} + \vec{P}, \quad (4.61)$$

with the polarization  $\vec{P} = \epsilon_0(\epsilon - 1)\vec{E}$  and the dielectric constant of the medium  $\epsilon$ . For anisotropic media the relation  $\vec{E} \parallel \vec{k}$  does not hold anymore as the dielectric constant  $\epsilon$  is a tensor that can have different values for different directions. In particular in the principle coordinate system we can write

$$\overleftrightarrow{\epsilon} = \begin{pmatrix} \epsilon_x & 0 & 0 \\ 0 & \epsilon_y & 0 \\ 0 & 0 & \epsilon_z \end{pmatrix}. \quad (4.62)$$

Assuming non-magnetic media with constant magnetic constant  $\mu$  and  $\vec{H} \parallel \vec{B}$  the remaining three Maxwell equations reveal that  $\vec{H} \perp \vec{k}$ ,  $\vec{H} \perp \vec{D}$  and  $\vec{H} \perp \vec{E}$  and thus show that also the pointing vector  $\vec{S} \propto \vec{E} \times \vec{H}$  is in general not pointing in the direction of the k-vector anymore. The results are visually summarized in figure 4.8A.

In order to calculate the transmission or reflection coefficients for an interface between isotropic and anisotropic media we have to formulate the Fresnel equations for anisotropic media. Combining equations (4.59) and (4.60) leads to an expression for  $\vec{D}$  [127]:

$$\vec{D} = \epsilon_0 n^2 [\vec{E} - \hat{s}(\hat{s} \cdot \vec{E})] \quad (4.63)$$

Here,  $\hat{s}$  is the unit vector in the direction of  $\vec{k}$  and  $n$  is the refractive index associated with the direction of  $\hat{s}$ . From these 3 equations for 3 unknown  $E_i$  we can eliminate  $\vec{E}$  assuming that  $\vec{E} \neq \vec{0}$  and we are left with the Fresnel equation

$$\frac{1}{n^2} = \frac{s_x^2}{n^2 - n_x^2} + \frac{s_y^2}{n^2 - n_y^2} + \frac{s_z^2}{n^2 - n_z^2}. \quad (4.64)$$

$n_x, n_y, n_z$  are the refractive indices in the direction of the x,y,z axis respectively and  $n_i = \sqrt{\epsilon_i}$ . In general all three refractive indices can be different  $n_x \neq n_y \neq n_z$ . In this case the the medium is called a biaxial anisotropic medium. Equation (4.64) can now also be written in a slightly different notation (cf. appendix B.1) as

$$s_x^2 n_x^2 (n^2 - n_y^2)(n^2 - n_z^2) + s_y^2 n_y^2 (n^2 - n_x^2)(n^2 - n_z^2) + s_z^2 n_z^2 (n^2 - n_x^2)(n^2 - n_y^2) = 0 \quad (4.65)$$

In this work we are considering only uniaxial media for which two refractive indices are the same:  $n_x = n_y \neq n_z$ . It is common terminology to define a ordinary index of refraction  $n_o$  and an extraordinary index of refraction  $n_e$ . Hence, a ray of light going through a uniaxial material is typically split into two rays. The ordinary ray is passing the medium without any deviation, whereas the extraordinary ray is deviated at the interface to another isotropic medium. Within this description we define the refractive index in the xy plane as the ordinary index  $n_x = n_y = n_o$  and the refractive index in the z-plane as the extraordinary index  $n_z = n_e$ .

Equation (4.65) then simplifies to

$$(n^2 - n_o^2)[n_o^2(s_x^2 + s_y^2)(n^2 - n_e^2) + s_z^2 n_e^2(n^2 - n_o^2)] = 0 \quad (4.66)$$

This equation has two solutions for the two orthogonally polarized waves in the s-plane with  $n = n_o$  and the p-plane with

$$\frac{1}{n^2} = \frac{s_x^2 + s_y^2}{n_e^2} + \frac{s_z^2}{n_o^2}. \quad (4.67)$$

The last equation can also be written in spherical coordinates with  $s_x = \sin(\theta) \cos(\phi)$ ,  $s_y = \sin(\theta) \sin(\phi)$  and  $s_z = \cos(\theta)$ , with  $\theta$  denoting the angle between the wave vector and the optical axis and  $\phi$  is the azimuth angle around the optical axis. In the case of uniaxial media we easily find that the azimuth angle does not even need to be considered:

$$\frac{1}{n^2} = \frac{\cos^2(\theta)}{n_o^2} + \frac{\sin^2(\theta)}{n_e^2} \quad (4.68)$$

This finally leads to

$$n(\theta) = \frac{n_o n_e}{\sqrt{n_o^2 \sin^2(\theta) + n_e^2 \cos^2(\theta)}}. \quad (4.69)$$

As a result we find that the refractive index of a p-polarized wave in a spatially homogeneous uniaxial anisotropic material with its optical axis oriented along the z coordinate strongly depends on the angle  $\theta$  between the wave vector and the optical axis and is a mixture of both refractive indices  $n_o$  and  $n_e$ . For an angle  $\theta = 0$  we get  $n(0) = n_o$ , the electric field is oscillating perpendicular to the z-plane and only experiences the ordinary index of refraction, whereas for an angle  $\theta = 90^\circ$  the field only experiences the extraordinary index of refraction.

Now we want to derive the transmission and reflection coefficients at an interface of an isotropic to an anisotropic medium. The propagation as well as the extraordinary axis is in z-direction. We now treat the situation separately for s- and p-polarization. In the case of s-polarization the electric field is only oscillating in the xy-plane with

$$\vec{E} \propto \begin{pmatrix} \sin(\phi) \\ \cos(\phi) \\ 0 \end{pmatrix} e^{i(\vec{k} \cdot \vec{r} - \omega t)} \quad (4.70)$$

Thus, no z-component has to be considered and the expression for the refractive index simplifies to  $n(\theta) = n_o$ . That means the transmission and reflection for an s-polarized wave can be treated the same way as transmission and reflection at an isotropic medium with refractive index  $n_o$  of

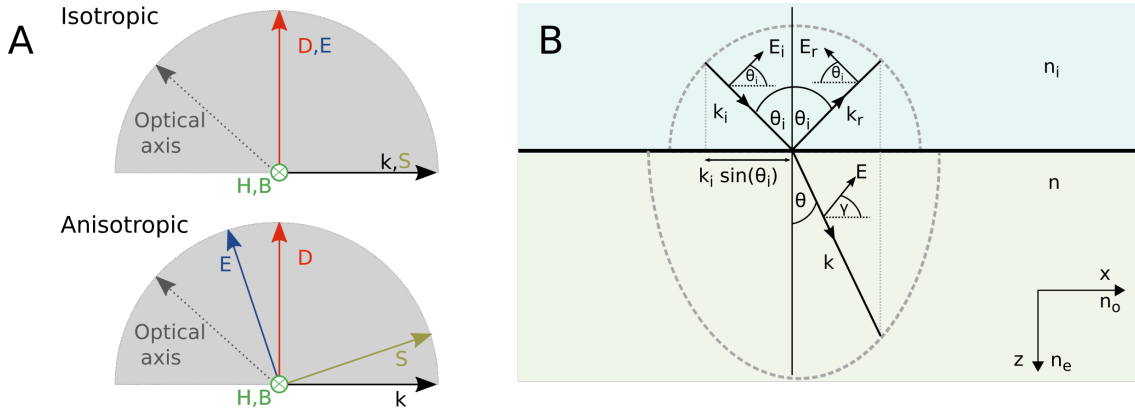


**Figure 4.8:** A: Visualization for different vectors for the case of an isotropic and anisotropic medium. For anisotropic media the wave vector  $\vec{k}$  does not point in the same direction as the Poynting vector  $\vec{S}$ . The same is true for the electric field  $\vec{E}$  and the displacement  $\vec{D}$ .  $\vec{E}$  and  $\vec{S}$  as well as  $\vec{D}$  and  $\vec{k}$  are perpendicular to each other. The magnetic field vector  $\vec{H}$  is perpendicular to all other vectors. B: A wave at the interface of a uniaxial anisotropic medium. The dotted curves indicate the  $k$ -surface of a sphere for an isotropic medium and an ellipse for the anisotropic medium. The optical axis is assumed chosen to be perpendicular to the interface and the refractive index is assumed to be  $n_x = n_y = n_o$ , the ordinary refractive index in the  $xy$  plane and  $n_z = n_e$ , the extraordinary index along the  $z$ -axis as indicated in the lower right.

the uniaxial medium.

For p-polarized waves the situation is more challenging as for the wave vector  $\vec{k} = (k \sin(\theta), 0, k \cos(\theta))$  and the electric field a  $z$ -component has to be considered and the refractive index is now not constant anymore, but is a function of the incident angle as shown before. The situation for p-polarized waves is sketched in figure 4.8B.

From the continuity equation  $E_{\parallel} = \text{const}$  at the interface with  $z = 0$  we then find the condition

$$E_x^i e^{ik_x^i x} = E_x e^{ik_x x}. \quad (4.71)$$

It follows directly that  $k_x^i = k_x$  with the upper index  $i$  denoting the medium of the incident wave. From  $k_x^i = k_x$  we directly get Snell's law

$$n_i \sin(\theta_i) = n(\theta) \sin(\theta) \quad (4.72)$$

Because the refractive index is not constant, the relationship between the incident angle  $\theta_i$  and the angle in the medium is more complicated than for Snell's law of isotropic media. Note that  $n(\theta)$  is only defined for angles  $\theta$  to the optical axis and the relation from equation (4.72) only holds if the optical axis is normal to the interface. For any arbitrary angle of the optical axis the angle of the refracted beam has to be related with the angle to the optical axis first. For the treatment of arbitrary angled biaxial layers the reader is referred to calculations in a 4x4

Transfer matrix method shown for example by Yeh [133, 134], Berreman [135] and others [136–138].

In the case of the optical axis perpendicular to the interface a relation between the incident angle and the angle  $\theta$  can be found by replacing  $n(\theta)$  in equation (4.72) with equation (4.69) (cf. appendix B.2):

$$\theta = \arcsin \left( \frac{a}{\sqrt{1 - a^2(b - 1)}} \right) \quad (4.73)$$

with  $a = n_i/n_o \sin(\theta_i)$  and  $b := n_o^2/n_e^2$ .

By applying the boundary conditions

$$\vec{E}_{\parallel}^i = \vec{E}_{\parallel} \quad (4.74)$$

$$\vec{D}_{\perp}^i = \vec{D}_{\perp} \quad (4.75)$$

we find the equations to relate the electric fields at the interface

$$E_i \cos(\theta_i) - E_r \cos(\theta_i) = E \cos(\gamma) \quad (4.76)$$

$$n_i^2 E_i \sin(\theta_i) + n_i^2 E_r \sin(\theta_i) = n_e^2 E \sin(\gamma) \quad (4.77)$$

For the last equation we used  $D_z = \epsilon_z E_z = n_z^2 E_z$ . Furthermore the angle  $\gamma$  of the electric field with respect to the normal of the  $k$ -vector is different from the angle  $\theta$ , because the electric field in the anisotropic medium is not perpendicular to  $\vec{k}$ . The relation between  $\gamma$  and  $\theta$  can be obtained geometrically from figure 4.8:

$$\tan(\theta) = -\frac{D_z}{D_x} = -\frac{\epsilon_z E_z}{\epsilon_x E_x} = \frac{n_e^2}{n_o^2} \tan(\gamma). \quad (4.78)$$

Finally, equations (4.76) and (4.77) can easily be solved to obtain the transmission and reflection coefficient

$$t_p = \frac{E}{E_i} = \frac{2n_i^2 \cos(\theta_i) \sin(\theta_i)}{n_i^2 \sin(\theta_i) \cos(\gamma) + n_e^2 \sin(\gamma) \cos(\theta_i)} \quad (4.79)$$

$$r_p = \frac{E_r}{E_i} = \frac{n_e^2 \sin(\gamma) \cos(\theta_i) - n_i^2 \sin(\theta_i) \cos(\gamma)}{n_e^2 \sin(\gamma) \cos(\theta_i) + n_i^2 \sin(\theta_i) \cos(\gamma)} \quad (4.80)$$

These last two equations in combination with the definition of the angle  $\theta$  (eq. (4.73)) and  $\gamma$  (eq. (4.78)) are everything we need to calculate the transmission and reflection of an anisotropic layer. The equations can be used in the transfer matrix model as well. For that the calculation of the transmission and reflection coefficient is replaced by the above equations and the angle  $\theta$  in the additional phase term  $\beta = k_z d = k \cos(\theta) d = 2\pi/\lambda n(\theta) \cos(\theta) d$  of the anisotropic layer is replaced by the angle calculated from equation (4.73).

As a last remark, an analogous representation of equations (4.79) and (4.80) combining the previous findings and expressing the transmission and reflection coefficient only with respect to the input angle  $\theta_i$  can be found in [139] and reads

$$t_p = \frac{E}{E_i} = \frac{2n_i \cos(\theta_i) \sqrt{n_i^2 \sin^2(\theta_i) (n_o^2 - n_e^2) + n_e^4}}{n_e (n_o n_e \cos(\theta_i) + n_i \sqrt{n_e^2 - n_i^2 \sin^2(\theta_i)})} \quad (4.81)$$

$$r_p = \frac{E_r}{E_i} = \frac{n_o n_e \cos(\theta_i) - n_i \sqrt{n_e^2 - n_i^2 \sin^2(\theta_i)}}{n_o n_e \cos(\theta_i) + n_i \sqrt{n_e^2 - n_i^2 \sin^2(\theta_i)}} \quad (4.82)$$

Either equations (4.79)-(4.80) or (4.81)-(4.82) can now be used to describe transmission and reflection through anisotropic media, which is extensively used throughout this work to explain SNOM intensity measurements of a squaraine dye layer sample.

#### 4.1.4 Focal Plane Fields

In the previous sections I outlined how the refractive index is determined by the microscopic sample properties and how optical transmission and reflection measurements are directly connected to the refractive index of the material. A transfer matrix then was introduced to calculate the overall transmission and reflection through a stack of layers with different material properties. Lastly, an extension of this formalism to anisotropic media was given. In the last part of this section, the description of the electromagnetic fields after being focused through such multilayer systems is derived. To complete the theoretical description of SNOM measurements, section 4.2 outlines the interaction of these focus fields with the SNOM tip following the notation of Novotny and Hecht (cmp. [140]).

In general, focusing of an incoming laser beam is crucial to SNOM, because the tip has a very small scattering cross section and by focusing we artificially generate also a z-component in the focus, whereas the incoming field is in general polarized along x or y-direction and has no z-component.

To calculate the electric fields in the focus of a lens or microscope objective we consider a situation as illustrated in figure 4.9A.

A plane wave is propagating towards a lens and the direction of the incoming wave vectors is changed after refraction, i.e. the k-spectrum  $\hat{E}(k_x, k_y)$  is no longer constant. In particular the lens generates concentric rings of light rays that propagate in the direction given by the angles  $\theta$  and  $\phi$  as visualized in figure 4.9A. Thus, the refracted field can be composed of a s-polarized component and a p-polarized component. We call this field  $\vec{E}_\infty$  with the subscript indicating that this field is evaluated at a large distance from the focus that is defined for  $x=y=z=0$ . With

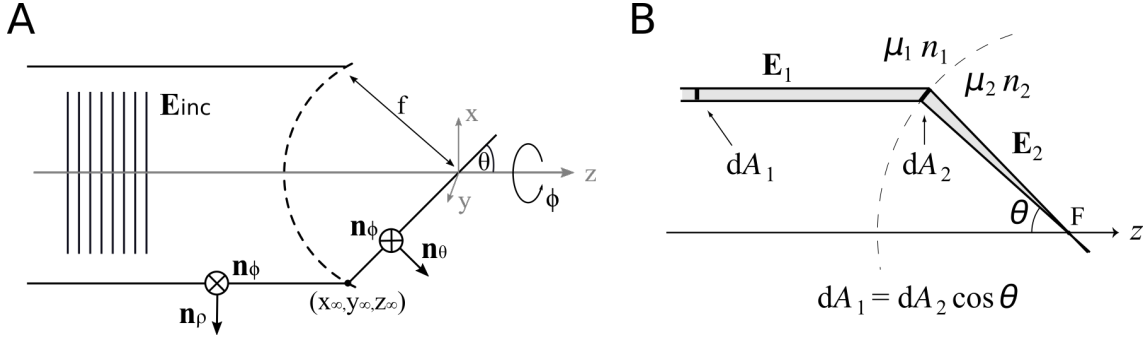


**Figure 4.9:** (A) Sketch of the focusing process. A linear polarized field  $\vec{E}_{inc}$  expressed in polar coordinates by the unity vectors  $\vec{n}_\rho$  and  $\vec{n}_\theta$  is transformed into spherical coordinates. (B) Visualization of the infinitesimal beam element that is transformed at the lens interface. To conserve energy an additional term  $\cos(\theta)$  has to be considered. (Adapted from [140])

the unity vectors

$$\vec{n}_\rho = \cos(\phi)\vec{n}_x + \sin(\phi)\vec{n}_y \quad (4.83)$$

$$\vec{n}_\phi = -\sin(\phi)\vec{n}_x + \cos(\phi)\vec{n}_y \quad (4.84)$$

$$\vec{n}_\theta = \cos(\theta)\cos(\phi)\vec{n}_x + \cos(\theta)\sin(\phi)\vec{n}_y - \sin(\theta)\vec{n}_z \quad (4.85)$$

it follows

$$\vec{E}_\infty = \left[ t^s \left[ \vec{E}_{inc} \cdot \vec{n}_\phi \right] \vec{n}_\phi + t^p \left[ \vec{E}_{inc} \cdot \vec{n}_\rho \right] \vec{n}_\rho \right] \sqrt{\frac{n_1}{n_2}} \cos(\theta)^{\frac{1}{2}} \quad (4.86)$$

The refraction at the lens hereby transforms the cylindrical coordinates  $\vec{n}_\rho, \vec{n}_\phi$  to spherical coordinates  $\vec{n}_\theta, \vec{n}_\phi$ . Furthermore, the term  $\cos(\theta)^{\frac{1}{2}}$  is a consequence of energy conservation and is accounting for the change in cross section area of the incoming and refracted beam as illustrated in figure 4.9B.  $t^s$  and  $t^p$  denote the Fresnel transmission coefficients for the interface of the lens and  $n_1$  and  $n_2$  are the refractive indices of the medium before and after the lens. In our work we do not use oil immersion and only have a microscope objective in air. Thus, we can set  $n_1 = n_2 = 1$  and also the transmission coefficients can be set to 1 for simplicity. Hence, equation (4.86) can be written as

$$\vec{E}_\infty = (\vec{E}_s^\infty + \vec{E}_p^\infty) \cos(\theta)^{\frac{1}{2}} \quad (4.87)$$

When the unity vectors  $\vec{n}_\phi$ ,  $\vec{n}_\rho$  and  $\vec{n}_\theta$  are expressed in terms of Cartesian coordinate unit

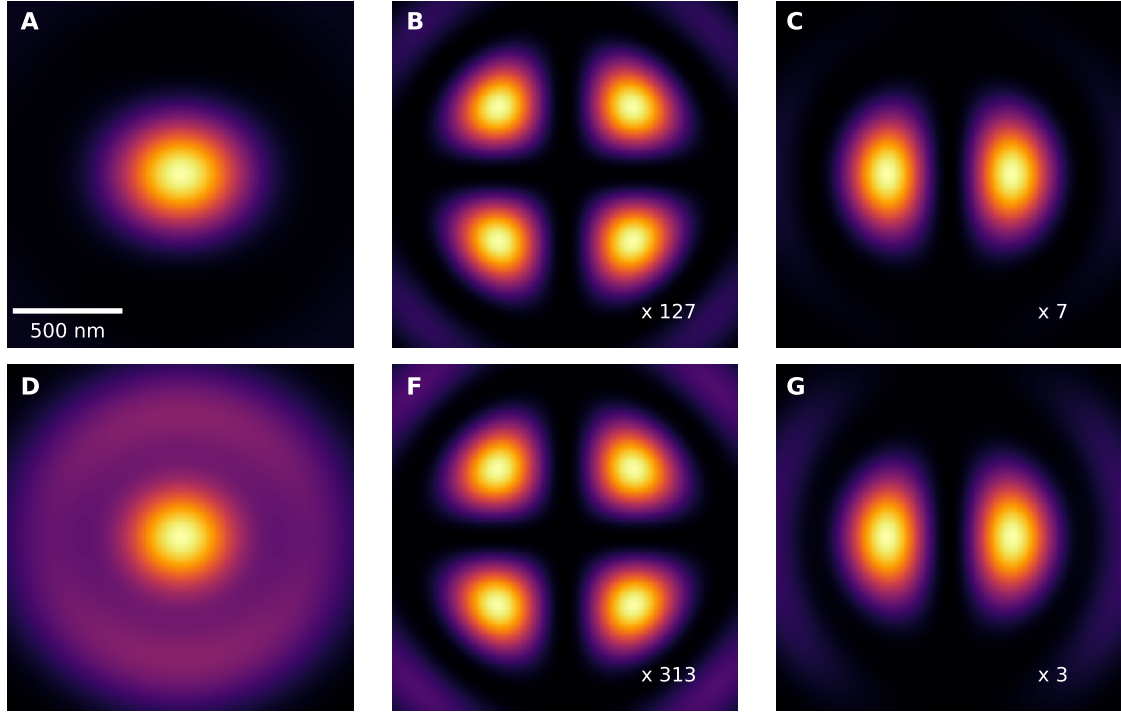


**Figure 4.10:** (A-C) Focal plane fields  $|E_x|^2$ ,  $|E_y|^2$  and  $|E_z|^2$  respectively, calculated for a Gaussian beam, a NA of 0.95 and a wavelength of 800 nm. Images (D-G) outline the same calculation, this time including a substrate and sample modeled by an anisotropic media (cmp text).

vectors the fields  $\vec{E}_s$  and  $\vec{E}_p$  are given by

$$\vec{E}_s^\infty(\theta, \phi) = \left[ \vec{E}_{\text{inc}}(\theta, \phi) \cdot \begin{pmatrix} -\sin(\phi) \\ \cos(\phi) \\ 0 \end{pmatrix} \right] \begin{pmatrix} -\sin(\phi) \\ \cos(\phi) \\ 0 \end{pmatrix} \quad (4.88)$$

$$\vec{E}_p^\infty(\theta, \phi) = \left[ \vec{E}_{\text{inc}}(\theta, \phi) \cdot \begin{pmatrix} \cos(\phi) \\ \sin(\phi) \\ 0 \end{pmatrix} \right] \begin{pmatrix} \cos(\phi) \cos(\theta) \\ \sin(\phi) \cos(\theta) \\ -\sin(\theta) \end{pmatrix} \quad (4.89)$$

This equation clearly shows that only for p-polarized light a z-component is generated that depends on the angle  $\theta$  limited by the angle  $\theta_{max}$  that is defined by the numerical aperture (NA) of the microscope objective.

In the case of an incident wave polarized along the x direction with  $\vec{E}_{\text{inc}} = E_{\text{inc}} \vec{n}_x$  the expression

for  $\vec{E}_s^\infty$  and  $\vec{E}_p^\infty$  simplifies to

$$\vec{E}_s^\infty(\theta, \phi) = E_{\text{inc}}(\theta, \phi) \cdot \begin{pmatrix} \sin(\phi)^2 \\ -\cos(\phi)\sin(\phi) \\ 0 \end{pmatrix} \quad (4.90)$$

$$\vec{E}_p^\infty(\theta, \phi) = E_{\text{inc}}(\theta, \phi) \cdot \begin{pmatrix} \cos(\phi)^2 \cos(\theta) \\ \cos(\phi)\sin(\phi)\cos(\theta) \\ -\cos(\theta)\sin(\theta) \end{pmatrix} \quad (4.91)$$

The fields  $\vec{E}_s^\infty$  and  $\vec{E}_p^\infty$  can either be written as a function of the angles  $\theta$  and  $\phi$ , or as a function of spatial frequencies  $k_x, k_y$ . Using the substitutions  $k_x = k \sin(\theta) \cos(\phi)$ ,  $k_y = k \sin(\theta) \sin(\phi)$ ,  $k_z = k \cos(\theta)$  and  $k = \omega/c = 2\pi n/\lambda$ , we find for the simplified case of a x-polarized incident wave, that the fields can be described by

$$\vec{E}_s^\infty(k_x, k_y) = E_{\text{inc}}(k_x, k_y) \cdot \frac{1}{k_x^2 + k_y^2} \cdot \begin{pmatrix} k_y^2 \\ -k_x k_y \\ 0 \end{pmatrix} \quad (4.92)$$

$$\vec{E}_p^\infty(k_x, k_y) = E_{\text{inc}}(k_x, k_y) \cdot \frac{1}{k_x^2 + k_y^2} \cdot \begin{pmatrix} k_x^2 k_z / k \\ k_x k_y k_z / k \\ -(k_x^2 + k_y^2) k_x / k \end{pmatrix} \quad (4.93)$$

Now we want to find the field at the focus position with  $z=0$ . In general the propagation of an electric field along the z-axis from a plane  $z=0$  to a plane  $z = z_0$  in the k-space notation is given by

$$\hat{\vec{E}}(k_x, k_y, z) = \hat{\vec{E}}(k_x, k_y) \cdot e^{\pm i k_z z}, \quad k_z(k_x, k_y, \omega) = \sqrt{\left(\frac{\omega}{c}\right)^2 - (k_x^2 + k_y^2)}. \quad (4.94)$$

The electric field in real coordinates is then obtained by the angular spectrum representation:

$$\vec{E}(x, y, z) = \iint_{-\infty}^{\infty} \hat{\vec{E}}(k_x, k_y) e^{i[k_x x + k_y y]} e^{\pm i k_z z} \frac{1}{k_z} dk_x dk_y \quad (4.95)$$

In the case that near-fields can be neglected, it can be shown that the Fourier spectrum  $\hat{\vec{E}}$  can be expressed in terms of the far-field  $\vec{E}_\infty$  as [140]

$$\hat{\vec{E}}(k_x, k_y) = \frac{i r e^{-i k r}}{2\pi k_z} \vec{E}_\infty(k_x, k_y) \quad (4.96)$$

with  $r = \sqrt{x^2 + y^2 + z^2}$  the distance from the origin point located in the plane  $z=0$  and thus

equation (4.95) reads

$$\vec{E}(x, y, z) = \frac{ir e^{-ikr}}{2\pi} \iint_{-\infty}^{\infty} \vec{E}_{\infty}(k_x, k_y) e^{i[k_x x + k_y y]} e^{\pm i k_z z} \frac{1}{k_z} dk_x dk_y. \quad (4.97)$$

Hence, the field at any position in space is described by the Fourier transform of its far-field representation.

For our case the field at a large distance from the focus is governed by equation (4.87) with  $r = f$  the focal length of the microscope objective equation. Eq. (4.97) in coordinates of the angles  $(\theta, \phi)$  transforms to

$$\vec{E}(\rho, \varphi, z) = \frac{ikf e^{-ikf}}{2\pi} \int_0^{\theta_{\max}} \int_0^{2\pi} \vec{E}_{\infty}(\theta, \phi) e^{ikz \cos(\theta)} e^{ik\rho \sin(\theta) \cos(\phi - \varphi)} \sin(\theta) d\phi d\theta. \quad (4.98)$$

Here  $\rho$  and  $\varphi$  are related to the x and y coordinate in the plane of  $z = \text{const}$ , or in other words  $x = \rho \cos(\varphi)$  and  $y = \rho \sin(\varphi)$ .

To calculate the field in the focus, equation (4.98) has to be evaluated for  $z = 0$ . In addition, we can account for a Gaussian beam spot and the aperture size of the lens, by expanding the incident electric field  $\vec{E}_{\text{inc}}$ . For an incoming field polarized in x- direction and a beam waist of  $w$  the field may be written for the (0,0) Hermite Gaussian mode as

$$\vec{E}_{\text{inc}} = E_0 e^{-(x^2 + y^2)/w^2} \vec{n}_x, \quad (4.99)$$

which can be expressed in terms of angles  $\theta$  using the substitution  $\sin(\theta) = r/f = (x^2 + y^2)/f$  as

$$\vec{E}_{\text{inc}} = E_0 e^{-f^2 \sin(\theta)^2 / w^2} \vec{n}_x. \quad (4.100)$$

The factor  $f_w(\theta) = \exp\left(-\frac{f^2 \sin(\theta)^2}{w^2}\right)$  is called the apodization function and can be expressed in terms of the filling factor  $f_0 = \frac{w}{f \sin(\theta_{\max})}$ . as

$$f_w(\theta) = e^{-\frac{\sin(\theta)^2}{f_0^2 \sin(\theta_{\max})^2}} \quad (4.101)$$

For an overfilled microscope objective a filling factor  $f_0$  of 2 is reasonable.

A typical simulation result of the focus field components  $|E_x|^2$ ,  $|E_y|^2$  and  $|E_z|^2$  is shown in figure 4.10A-C. In that simulation equation (4.98) was evaluated for a filling factor of 2, a numerical aperture  $\text{NA} = 0.95$  and a wavelength of 800 nm. Hereby, the x-component of the electric field has the highest amplitude and shows a single diffraction limited spot at the center position  $x = y = 0$ . The y-component of the electric field shows a quadrupolar intensity pattern,

but the maximum intensity value is reduced by a factor 127 compared to the x-component and is almost negligible. The z-component of the field shows two spots, but no intensity at the  $x=y=0$  position. The maximum intensity of the two spots is a factor 7 smaller than that of the x-component. Depending on the field enhancement of the SNOM tip and the position of the tip within the focal plane, the z-component of the field can have a strong influence on the tip-sample interaction and therefore the detected SNOM signals. This influence will be discussed in more detail in chapter 6.

Up to now the fields have been calculated only for focusing through air. In SNOM measurements however, the beam is focused through a substrate and sample before the interaction with the tip can occur. Hence, transmission through the layers for each angle  $\theta$  has to be taken into account. Typically, the transmission coefficients  $t_s$  and  $t_p$  for either s- or p-polarization can be calculated for each incident angle  $\theta$  by a transfer matrix model. Consequently, these coefficients replace the transmission coefficients from equation (4.86).

As the transmission coefficients depend on the angle  $\theta$  we have in total:

$$\vec{E}(\rho, \varphi, z) = \frac{ikfe^{-ikf}}{2\pi} \int_0^{\theta_{\max}} \int_0^{2\pi} [(t^s(\theta)\vec{E}_s + t^p(\theta)\vec{E}_p)] \sqrt{\cos(\theta)} e^{ikz \cos(\theta)} \times e^{ik\rho \sin(\theta) \cos(\phi-\varphi)} \sin(\theta) d\phi d\theta \quad (4.102)$$

or

$$\vec{E}(x, y, z) = \frac{ife^{-ikr}}{2\pi} \iint_{-\infty}^{\infty} [t^s(k_x, k_y)\vec{E}_s^\infty(k_x, k_y) + t^p(k_x, k_y)\vec{E}_p^\infty(k_x, k_y)] \times \sqrt{k_z/k} e^{i[k_x x + k_y y]} e^{ik_z z} \frac{1}{k_z} dk_x dk_y \quad (4.103)$$

The resulting fields after being focused through a multilayer system with an anisotropic media are shown in figure 4.10D-G. The x-component of the focus field now shows a reduced maximum intensity value such that diffraction rings around the center spot become visible. Additionally, the ratio of maximum intensity of the x-component to the z-component is reduced, such that now the z-component is only a factor 3 smaller.

To complete the description of focal fields, we can calculate the focal fields e.g. at a glass interface. Let the interface be at a position  $z = z_0$  as indicated in figure 4.11. In this case the total field for distances  $z < z_0$  is given as the sum of the field before the interface  $E_f$  and the field reflected from the interface  $E_r$ . For distances  $z > z_0$  the field is given by the transmitted field  $E_t$ . The reflected field can be easily calculated by a wave propagating in the opposite direction with  $k_{z,r} = -k_z$  and an additional phase factor  $\exp(2ik_z z_0)$  is accumulated. The wave in the medium propagates with the new wavenumber  $k_{z2} = (2\pi/\lambda)n_2 \cos(\theta_2) = k_2 \cos(\theta_2)$ . The  $k_x$  and  $k_y$  components at the interface are constant. Furthermore we have to account for an additional phase  $\exp(i(k_z - k_{z2})z_0)$  for the transmitted wave in the medium and energy

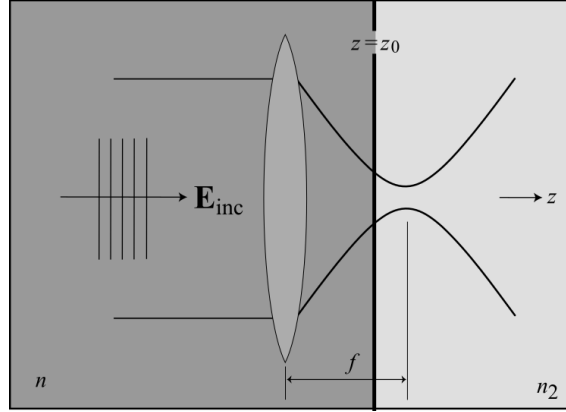


Figure 4.11: Visualization of the focus near an interface (from [140])

conservations demands an extra factor  $\frac{k_{z2}}{k_z} = \frac{n_2 \cos(\theta_2)}{\cos(\theta)}$ . In total this yields:

$$\vec{E}_f = \frac{if e^{-ik_1 f}}{2\pi} \iint \vec{E}_\infty(k_x, k_y, k_{z1}) \frac{1}{k_{z1}} e^{i(k_x x + k_y y + k_{z1} z)} dk_x dk_y \quad (4.104)$$

$$\vec{E}_r = \frac{if e^{-ik_1 f}}{2\pi} \iint \vec{E}_\infty^r(k_x, k_y, -k_{z1}) \frac{1}{k_{z1}} e^{i(k_x x + k_y y - k_{z1} z)} e^{2ik_{z1} z_0} dk_x dk_y \quad (4.105)$$

$$\vec{E}_t = \frac{if e^{-ik_1 f}}{2\pi} \iint \vec{E}_\infty^t(k_x, k_y, k_{z2}) \frac{1}{k_{z2}} e^{i(k_x x + k_y y + k_{z2} z)} e^{i(k_{z1} - k_{z2}) z_0} \frac{k_{z2}}{k_{z1}} dk_x dk_y \quad (4.106)$$

Hereby  $E_\infty^r(k_x, k_y, -k_{z1})$  and  $E_\infty^t(k_x, k_y, k_{z2})$  are used as a short notation for the sum of the p-polarized part and the s-polarized part multiplied by the reflection or transmission coefficient respectively. Figure 4.12 shows a contour plot of constant intensity  $|\vec{E}|^2$  for the interface between air and glass. The interface is located in the focal plane  $z_0 = 0$  of the microscope objective and a numerical aperture of 0.95 and a wavelength of 800 nm was used for the simulation. A standing wave pattern is forming because of the interference of incoming and reflected wave at the air/glass interface. Additionally, figure 4.12 nicely outlines the energy flow of the wave inside and outside the medium. As the refractive index changes this causes a variation in angles of the adjacent contour lines.

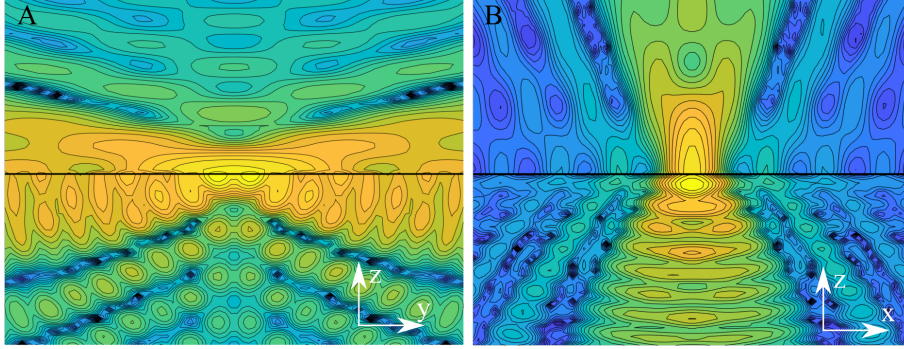


**Figure 4.12:** Contour plot of the intensity  $|\vec{E}|^2 = |E_x^2 + E_y^2 + E_z^2|$  near a glass(top)/air(bottom) interface in a logarithmic scale for the interface with  $z_0 = 0$  in the  $yz$ -plane with  $x = 0$  (A) and the  $xz$ -plane with  $y = 0$  (B)

## 4.2 Tip-Sample Interaction in Apertureless SNOM Spectroscopy

When using sSNOM to measure the optical properties of a sample, typically a nanometer-sized probe, such as for example a sharply etched metal tip, is raster-scanned over the sample surface. Here the tip acts as a scatterer that transforms near fields into far-field radiation that is finally measured by a detector. The near field of a sample varies on much shorter length scales than the far field. Because of that, the near field can on the one hand be used to extract information on the optical sample properties on a nanometer-length scale; on the other hand, however, this also makes the near field more complicated to interpret: it is measured only by the indirect interaction of a probe and the sample, and in addition, it is usually obscured by the slowly-varying far fields.

In order to interpret the measured signal and to relate them to the optical properties of the sample, a number of different models of the probe-sample interaction have been employed in the recent years. Besides varying degrees of numerical effort and whether the models take into account retardation effects, the different approaches can be classified by the number of consecutive scattering processes they consider. Let us write the scattered field as a superposition of fields originating from different scattering events in a simplified form [141, 142]:

$$\vec{E}_{scat} = \sum_{n=1}^{\infty} (T + S)^n \vec{E}_{inc} \quad (4.107)$$

Here,  $T$  and  $S$  represent single scattering events of the tip and the sample, respectively, acting on the incident field  $\vec{E}_{inc}$ , and  $n$  denotes the scattering order (see Fig. 4.13). The exact formulation of the scattering events will be performed in the following subsections, for several specific cases chosen for illustration.

The first-order scattering events,  $T$  and  $S$ , do not contain any tip-sample interaction. They

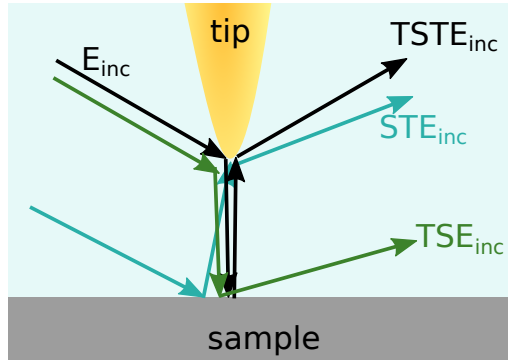


**Figure 4.13:** Scattering events after illuminating the tip. For simplicity side illumination is visualized, the concept is analogous for illumination from the bottom.

represent a slowly varying contribution that is normally regarded as background. The same holds for terms of the kind  $T^n$ ,  $S^n$  that arise when considering scattering orders  $n > 1$ .

The first combination of scattering event giving rise to near-field contributions occurs, when truncating the series in Eq. (4.107) after  $n = 2$ :  $TS$  and  $ST$ . For tip-sample distance much smaller than the distance of either to the detector, these two sequences of scattering events yield the same contribution [142]. This is one limiting case of the classification by the numbering of scattering events, termed the weak tip regime [141, 142] or also the weak coupling regime [143]. In this limit, evaluation of the measured signal is straight-forward, and the tip can simply be used to image the sample near field. A typical example of the weak-tip limit case would be the mapping of the near-field around a plasmonic nanoantenna by a weakly interacting probe, i.e., a nanometer-sized dielectric probe, such as, for example, a single carbon nanotube mounted on an AFM cantilever [143].

In most cases, however, the probe polarizability is of the same order or even larger than that of the sample, and higher order interactions than  $n = 2$  have to be considered. In the limit case of a strong tip, or rather, in the strong interaction regime, the two dipoles interact very effectively. The induced tip dipole then alters the field distribution of the sample, such that direct mapping becomes impossible. The fields must be deduced from the measured signals. To achieve this, often a priori knowledge of probe and sample is employed to reduce the complexity, or sophisticated experimental setups are designed that, for example, limit the polarization directions of incident and scattered light, thereby eliminating several elements of the polarizability tensors [73, 142, 144].

In the cases investigated in this thesis, the probe was a sharply-etched metal taper with a considerable polarizability. The samples ranged from layers of dye molecules, where delocalized electrons in conjugated  $\pi$ -bonds give rise to a finite polarizability, to plasmonic antennae formed by metal nanoparticles. In most of these cases, with the exception of nanostructures with a

strong near field localization, the limit case of a weakly interacting tip is fulfilled, such that interpretation of the measured signals makes a more detailed description of the tip-sample interaction necessary. In the following sections, some relevant models for the tip-sample interaction are presented, in increasing order scattering events. I give some examples, where these models were applied within this thesis. The first of these sections, 4.2.1, investigates the polarizability of the gold nanotips that are used as the near-field probes. This section also introduces the Green's tensor, which allows calculating the field scattered by such a single dipole. Expanding the model to a superposition of the fields originating from several, accordingly chosen dipoles enables the representation of somewhat more complex nanostructures. In section 4.2.2 this is employed to simulate near fields of a plasmonic nanoantenna and to compare them to FEM simulations as well as to SNOM measurements of an antenna structure.

When such a tip is in close proximity to the surface of a planar, isotropic sample, the scattered fields can be described efficiently by considering the excitation of an image dipole in the sample, which is shown in section 4.2.3. In section 4.2.4, this model is expanded to also include anisotropic samples. Finally, to be able to simulate the strong interaction of a metal nanotip with an inhomogeneous and anisotropic sample, in section 4.2.4.1 a self-consistent solution of the scattered field is derived.

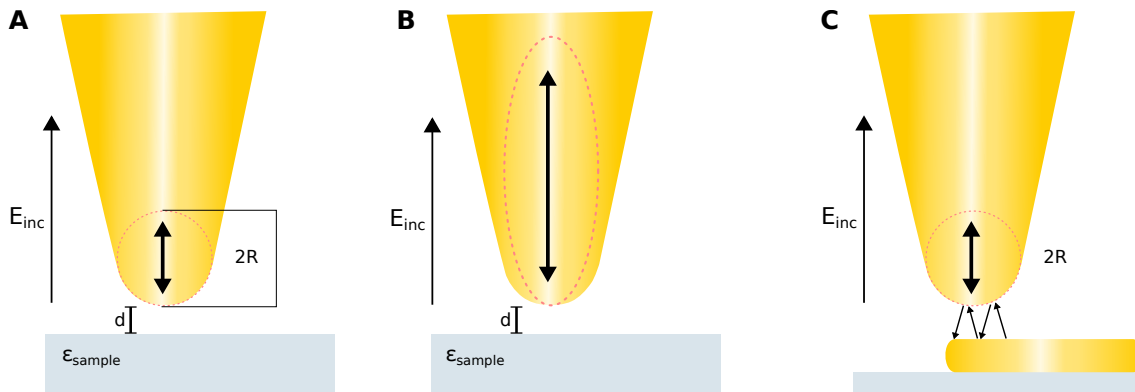


**Figure 4.14:** Visualization of different models to describe the tip. A: The tip dipole is described by a single sphere of radius  $R$ . B: An extension of the sphere model by using an elongated ellipse to describe the tip dipole. C: A scattering model involving nanostructures.

### 4.2.1 Tip dipole and Green's function

In a very simple picture, the sharply etched gold tip is sometimes modelled as a gold sphere with the radius given by the apex radius of curvature of the actual taper (cmp Fig. 4.14).

When an electric field  $\vec{E}_{inc}$  is incident on a small metal sphere, the free electrons of the metal respond to the force exerted by the field. If the size of the sphere is small compared to the

wavelength of the incident light and also compared to the skin depth of the electromagnetic field, the force experienced by the free electrons is homogeneous over the whole sphere. The electrons are collectively displaced from their equilibrium position around the positively charged lattice. This in turn creates a restoring force, which is proportional and in opposite direction to the displacement. Hence the free electrons of the metal sphere perform a collective oscillation termed a localized surface plasmon (LSP) [145–149]. Due to the electron oscillation, the metal sphere attains a dipole moment as response to the incident electric field:

$$\vec{p}_{sphere} = \overset{\leftrightarrow}{\alpha}_{sphere} \vec{E}_{inc} \quad (4.108)$$

The polarizability  $\overset{\leftrightarrow}{\alpha}_{sphere}$  of a homogeneous metal sphere has to be isotropic and can hence be written as a scalar multiplied with the unit dyad  $\overset{\leftrightarrow}{I}$ ,

$$\overset{\leftrightarrow}{\alpha}_{sphere} = \alpha_{sphere} \overset{\leftrightarrow}{I} \quad (4.109)$$

The spectral function of the amplitude of the polarizability is given by the dielectric function of the sphere material, which is the tip material,  $\epsilon_{tip}$ , and that of the surrounding material  $\epsilon_2$ . Furthermore, the polarizability scales with the volume of the sphere, as long as the radius  $R$  is much smaller than the wavelength of the exciting electromagnetic wave and the quasistatic approximation holds:

$$\alpha_{sphere} = 4\pi\epsilon_0\epsilon_2 R^3 \frac{\epsilon_{tip} - \epsilon_2}{\epsilon_{tip} + 2\epsilon_2} \quad (4.110)$$

Fig. 4.15 shows as an example the polarizability of a gold sphere with Radius  $R = 10$  nm, which corresponds to the radius of curvature typically achieved in our etching process, embedded in air for which we set  $\epsilon_2 = 1$ . Such a tip should exhibit an LSP resonance when excited with light with a wavelength around 500 nm. In the near-infrared spectral range around 700 nm-800 nm that is used for nano-spectroscopy within this thesis, the spectral function of the sphere polarizability is rather flat, which makes such a small gold sphere a good near field probe.

The dipole formed by such a sphere was used to describe near-field optical measurements successfully in several cases [151], but it was not able to quantitatively reproduce measurements of coupling-induced frequency shifts of polariton resonances [76, 152], or of LSPs forming in small particles [153]. Moreover, the model is also not applicable when the tip-sample distance is below the tip diameter, as in this region an additional field confinement into gap-plasmons takes place [154].

In fact, the real SNOM tip in the experiments is etched from a gold wire and is elongated along z-direction. Hence, modeling the tip geometry by an ellipse rather than by a sphere is an intuitive next step to address the mismatch in measurement and simulation (cmp. Fig. 4.14B).

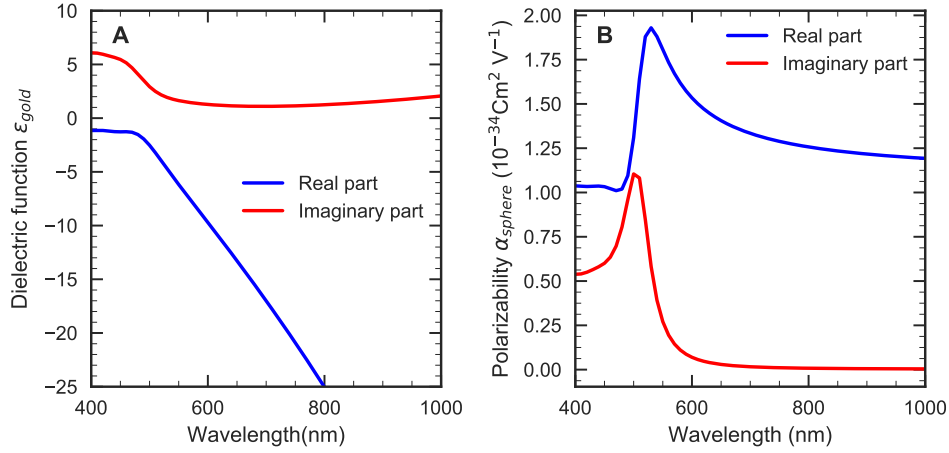


**Figure 4.15:** (A) Dielectric function of gold from measurements by Olmon et al. [150]. (B) Polarizability of a sphere with  $R=10$  nm radius.

Following Mie scattering theory the polarizability of an ellipse is expressed by [155–157]

$$\alpha_{tip,z} = \frac{4}{3} \pi R_x R_y R_z \frac{\epsilon_{tip} - 1}{1 + D_z (\epsilon_{Au} - 1)}. \quad (4.111)$$

Hereby,  $R_x, R_y$  and  $R_z$  describe the lengths of the half axes of the ellipsoid and  $D_j$  is the depolarization factor that is given by

$$D_j = \frac{1}{2} R_x R_y R_z \int_0^\infty \frac{ds}{(s + R_j^2) \sqrt{(s + R_x^2)(s + R_y^2)(s + R_z^2)}} \quad (4.112)$$

and is satisfying the condition  $D_x + D_y + D_z = 1$ .

When the tip is described by an ellipse we can further set  $R_x = R_y < R_z$ . Depending on the ratio of  $R_z/R_x = R_z/R_y$ , the depolarization factor and hence the resonance condition in the denominator of equation (4.111) will change. If  $R_x = R_y = R_z$  it follows  $D_x = D_y = D_z = 1/3$  and the polarizability of a sphere is recovered. For larger ratios the factor  $R_z$  decreases and the plasmon resonance will shift towards longer wavelength as is shown in figure 4.16A and B. Depending on the tip shape the resonance can strongly influence spectral SNOM measurements in the visible frequency range.

At the same time, the decreasing depolarization factor also indicates a considerably longer lifetime of the plasmon, which leads to a narrowing that accompanies the red-shift of the resonance. The longer lifetime of elliptical nanoparticles as compared to spheres is indeed a very strong effect that was demonstrated experimentally in 2002 by Sönnichsen et al. [158]. Using such a modified resonance was a successful approach to calculate approach curves that showed an improved agreement with experimental results [159]. However, an improved

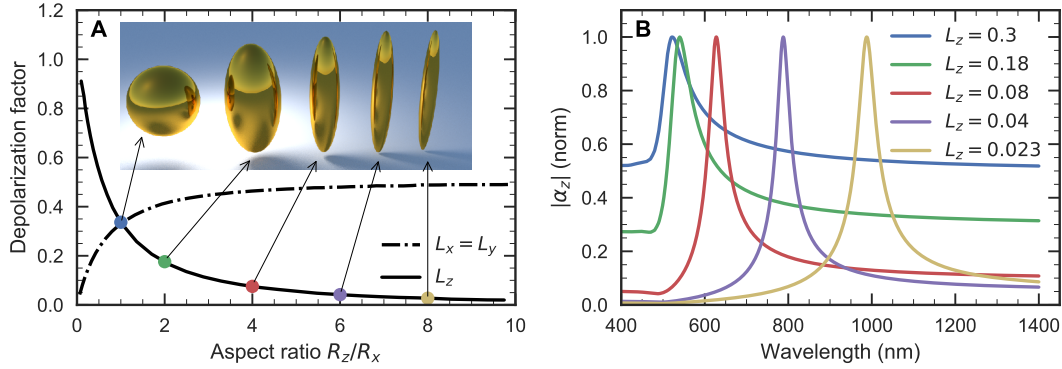


**Figure 4.16:** (A) Depolarization factor for different aspect ratios  $R_z/R_x$  that describe the elongation of a spheroidal particle. (B) Corresponding resonances of the polarizability calculated by Mie theory.

agreement with this model was mostly tested for monochromatic measurements or for spectra measurements in the infrared region. In contrast, our own spectrally resolved measurements in the visible spectral range, which are presented throughout this thesis (e.g. Fig. 6.2), show a much more spectrally flat response of sharply etched gold tapers as near-field probes, even in the near-infrared spectral region. This does not match the narrow resonance expected from an ellipse (Fig. 4.16B).

Furthermore, the broad spectral bandwidth of sharply etched gold tapers like the ones that were used in this work is by now well established by a number of different experiments: In recent years, these gold nanotips have received much attention as broad-bandwidth plasmonic nanoantennae [98, 160, 161], and as emitters of ultra-short bunches of photoelectrons using few-cycle laser pulses [162–165]. In the frame of this high interest in the broad-bandwidth capability of gold nanotapers, their resonances have recently been investigated using electron energy loss spectroscopy (EELS) [166–168]. EELS simulations indicate that the localized plasmon at the taper apex supports a very wide bandwidth, ranging approximately from 620 nm to  $>1500$  nm, and has a very short lifetime of  $\approx 1$  fs [160]. With view on these recent experiments and calculations, it seems much more reasonable to model the tip resonance onto the EELS measurements rather than assuming an isolated ellipse.

The tip polarizability along the x and y direction is then still modelled by the polarizability of a sphere with 10 nm radius:  $\alpha_{tip,xx} = \alpha_{tip,yy} = \alpha_{sphere}$ , but for the polarizability along the taper axis we found that assuming a Lorentz oscillator, centered at about 800 nm and with a wide bandwidth exceeding 200 nm is a good match to experimental observations. This is similar to the ansatz used successfully to explain similar earlier experiments performed in our group [93].

Following the results from Esmann et al.[93], the tip z-polarizability reads:

$$\alpha_{tip,zz} = \alpha_{tip,zz}(\omega, \omega_0, \gamma) = -|\mu_{tip}|^2 \frac{1}{\hbar} \left( \frac{1}{\omega - \omega_0 + i\gamma} - \frac{1}{\omega + \omega_0 + i\gamma} \right) \quad (4.113)$$

with the dipole moment  $\mu_{tip}$ , and the center frequency and damping of the resonance  $\omega_0$ , and  $\gamma$ , respectively. Roughly following the EELS measurements we use  $\hbar\omega_0 = 1.55$  eV for the center frequency and we estimate the damping from the fast decay of the resonance of these tapers: with the decay time  $T_2 = 1$  fs we obtain  $\hbar\gamma = \hbar/2T_2 = 0.33$  eV. The dipole moment is determined by calculating the field at the surface of the taper apex and then setting  $|\mu_{tip}|^2$  to a value such that the field enhancement at the surface reaches a value of  $f = |\vec{E}_{surf, x=y=0}|/|\vec{E}_{inc}| = 7$ .

After we have introduced the polarizability of the sphere, we can now calculate the electric field around a dipole that is excited by an incident field  $\vec{E}_{inc}$ .

In the following we will introduce the Green's function formalism to perform such a calculation. The Green's function formalism will later enable us to explain coupling to structured samples as well. Additionally, in 4.2.4 we will extend the description to anisotropic samples that are part of this thesis.

In general, in electromagnetic theory the Green's function acts as a propagator, i.e. the Green's function describes the field  $\vec{E}$  at a position  $\vec{r}$  due to a point-like dipole excitation with dipole moment  $\vec{p}$  at position  $\vec{r}_0$  [140]:

$$\vec{E}(\vec{r}) = \mu_0 \omega^2 \overset{\leftrightarrow}{G}(\vec{r}, \vec{r}_0, \omega) \vec{p} \quad (4.114)$$

For electric fields the Greens function that solves the Helmholtz equation is already well known. A derivation can be found in many optics textbooks [140] and reads

$$\overset{\leftrightarrow}{G}(\vec{r}, \vec{r}_0) = \left[ \overset{\leftrightarrow}{I} + \frac{1}{k_0^2} \nabla \nabla \right] G_0(\vec{r}, \vec{r}_0) \quad (4.115)$$

with the scalar Greens function

$$G_0(\vec{r}, \vec{r}_0) = \frac{e^{k_0|\vec{r}-\vec{r}_0|}}{4\pi|\vec{r}-\vec{r}_0|}. \quad (4.116)$$

$G_0(\vec{r}, \vec{r}_0)$  represents a spherical wave propagating out of dipole position  $\vec{r}_0$ . In cartesian coordinates Eq. (4.116) can be written as [169, 170]

$$\overset{\leftrightarrow}{G}(\vec{r}, \vec{r}_0)_{ij} = - \left( \overset{\leftrightarrow}{I}_{ij} + \overset{\leftrightarrow}{I}_{ij} \frac{ik_0|\vec{R}|-1}{k_0^2|\vec{R}|^2} + \vec{R}_i \vec{R}_j \frac{3-3ik_0|\vec{R}|-k_0^2|\vec{R}|^2}{k_0^2|\vec{R}|^4} \right) G_0(\vec{r}, \vec{r}_0) \quad (4.117)$$

with  $\vec{R} = \vec{r} - \vec{r}_0$ .

Hence, knowledge of the Green's function allows us to calculate the electric field  $\vec{E}$  of a dipole for every position in space following equation (4.114). As an example figure 4.17 shows the electromagnetic field around the gold tip after applying equation (4.117). Hereby only one dipole is used and is placed at a distance of around 13.3 nm away from apex surface along the z-axis into the tip material. This way the spatial mode distribution is reproduced very well compared to previous FEM simulations of such tip fields [96, 154]. Additionally, we find that for the gold nanotip the amplitude of  $\alpha_{tip,zz}$  is around 10 times the amplitude of  $\alpha_{tip,xx} = \alpha_{tip,yy}$ . Hence, the polarizability of the tip along z-direction is the dominant factor of the tip polarizability tensor. Thus, for isotropic samples the coupling to the xy-component can often be neglected as it is much weaker. However, for samples with a high coupling to the xy-component, like anisotropic dyes, the interaction in all three components has to be considered.

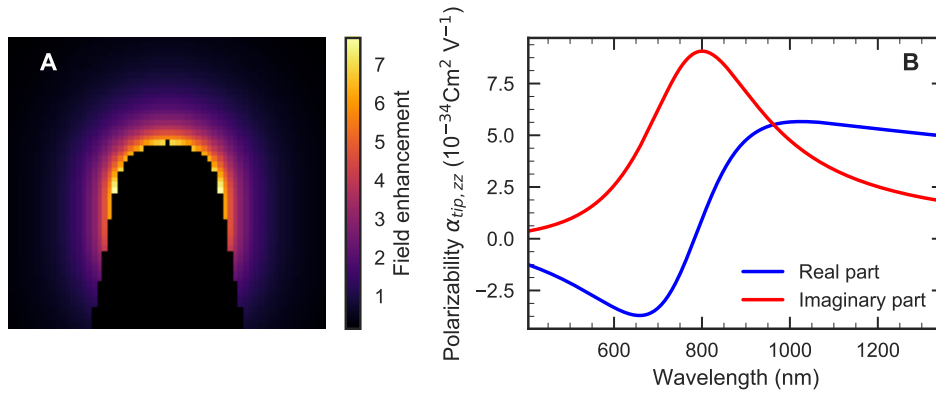


**Figure 4.17:** (A) Absolute of the field  $|E|$  around the tip for a wavelength of 800 nm. (B) The corresponding tip polarizability with a tip resonance centered around 800 nm.

#### 4.2.2 A nanorod-antenna: a nanostructure modelled as chains of dipoles

As the Green's function is a linear operator the calculation for one dipole can easily be extended to also describe the field from more complex structures. Such structures can be modelled by assuming more than one dipole. As an example, in this section I show the reconstruction of fields around a nanorod antenna.

In this way, we describe the nanostructure as a number of individual dipoles  $i = 1, 2, \dots, N$ , for example arranged in a chain. The  $i$ -th dipole at position  $\vec{r}_i$  shall be described by the polarizability tensor  $\overleftrightarrow{\alpha}_i$ . The field that excites the  $i$ -th dipole is a superposition of the incident field at the

dipole position,  $\vec{E}_{inc}(\vec{r}_i)$  and the secondary fields of all the other dipoles:

$$\vec{E}_{exc,i} = \vec{E}_{inc}(\vec{r}_i) + \mu_0\omega_0^2 \sum_{j \neq i} \overleftrightarrow{G}(\vec{r}_i, \vec{r}_j) \overleftrightarrow{\alpha}_j \vec{E}_{inc,j}(\vec{r}_j) \quad (4.118)$$

Here,  $\overleftrightarrow{\alpha}_j$  is the polarizability tensor of dipole  $j$ . Equation (4.118) is an implicit equation, but it is also possible to express the excitation field  $\vec{E}_{exc,i}$  at each dipole in terms of the incident field. In order to do so, we can, in a first step, rewrite equation (4.118) to obtain

$$\vec{E}_{inc}(\vec{r}_i) = \sum_j \overleftrightarrow{Q}_{i,j} \vec{E}_{inc,j}(\vec{r}_j) \quad (4.119)$$

with

$$\overleftrightarrow{Q}_{i,j} = \delta_{i,j} - \mu_0\omega^2(1 - \delta_{i,j}) \overleftrightarrow{G}_{i,j} \overleftrightarrow{\alpha}_j \quad (4.120)$$

$\overleftrightarrow{Q}$  is a block-matrix, where each element  $\overleftrightarrow{Q}_{i,j}$  contains a 3x3 matrix. As long as the matrix  $\overleftrightarrow{Q}$  is known the resulting electromagnetic near- and far- fields can be calculated at any position  $\vec{r}$  in space by inverting this block matrix  $\overleftrightarrow{Q}$ . Consequently, we find the expression of the field at the  $i$ th dipole

$$\vec{E}_{exc,i} = \sum_j (\overleftrightarrow{Q}^{-1})_{i,j} \vec{E}_{inc}(\vec{r}_j) \quad (4.121)$$

This ansatz can be used for any kind of nanostructures. In this thesis however, we are mostly dealing with nanorods and nanorod antennas. Here, the spectral response of the system is dominated by only one fundamental mode along the rod axis. In the case of a rod that is a few tens of nanometer long, already the first higher excited longitudinal mode falls into the UV spectral range. Moreover, an optical mode excited perpendicular to the rod axis, is much weaker than the mode excited along the rod axis. Hence, in the case of the nanorod that is modelled by a line of dipoles pointing along the rod  $x$ -axis, the polarizability tensor  $\overleftrightarrow{\alpha}_i$  can be reduced to only contain one nonzero component  $\alpha_{i,xx}$ .

In addition, for nanorods the above mentioned procedure can be further simplified, because the nanorod can be modelled as a metallic wire of a length  $2L$  capped by two half spheres with radius  $R$ . The current density for the dipolar resonance inside such a metallic wire is known analytically and reads [171]

$$j(x) \propto \cos\left(\frac{\pi x}{2L + 4R}\right) \quad \text{for } |x| \leq L + R, \quad 0 \text{ otherwise.} \quad (4.122)$$

Here,  $x$  is the coordinate along the rod axis, with  $x = 0$  describing the center of the rod (cmp. figure 4.18).

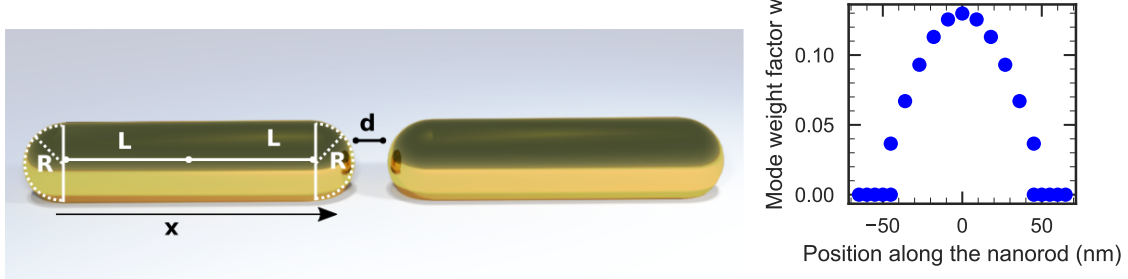


**Figure 4.18:** Left: Visualization of a nanorod antenna and the specific dimension of each rod. Right: The mode profile as expressed by the weight factor for one nanorod for 11 dipoles and  $L = 45$  nm and  $R = 5$  nm.

As the currents are the source of dipolar fields we can relate the current density to a line density of the polarizability  $j(\omega, x) \propto \rho(\omega, x) = \rho_0(\omega) \cos\left(\frac{\pi x}{2L+4R}\right)$ , which in fact relates to a dipole moment  $\vec{p}$  oriented along the rod axis [95].

This gives the spatial distribution of the polarizability. For the spectral function  $\rho_0(\omega)$  we use that of an ellipse. As it was shown in the previous section the polarizability of an ellipse can be obtained from Mie theory and the result was given in equation (4.111).

With a mixture of both approaches the nanorod can be fully described: the first ansatz is used to calculate the fields around the nanorod, whereas the polarizability of an ellipse can be used to define the spectral properties.

Finally, instead of defining the tensor  $\overleftrightarrow{Q}_{i,j}$ , we can directly imprint a phase relation between the dipoles and define a weight factor for each dipole by

$$w_i = \frac{\alpha_{i,xx}(\omega)}{\alpha_{xx,total}(\omega)} = \frac{\cos\left(\frac{\pi x_i}{2L+4R}\right)}{\sum_i \cos\left(\frac{\pi x_i}{2L+4R}\right)} \quad (4.123)$$

with  $\sum w_i = 1$ . Here,  $\alpha_{xx,total}(\omega)$  is the totally integrated polarizability over the complete structure along the rod axis. An example of the weight factor is given in figure 4.18 for a nanorod of half length  $L = 45$  nm and capped by a half sphere with  $R = 5$  nm. The polarization as a response to an electromagnetic field then results in

$$\vec{p}_i(\omega) = \overleftrightarrow{\alpha}(\omega) \sum_j w_j w_j \vec{E}_{inc}(\vec{r}_j) = \overleftrightarrow{\alpha} \vec{E}_{inc}(\vec{r}_i) \quad (4.124)$$

$\overleftrightarrow{\alpha}$  is a non-local polarizability for the given mode of the nanorod structure. Conclusively, the

field around the nanorod can be calculated by

$$\vec{E}(\vec{r}) = \mu_0 \omega_0^2 \sum_i \overleftrightarrow{G}(\vec{r}, \vec{r}_i) \vec{p}_i \quad (4.125)$$

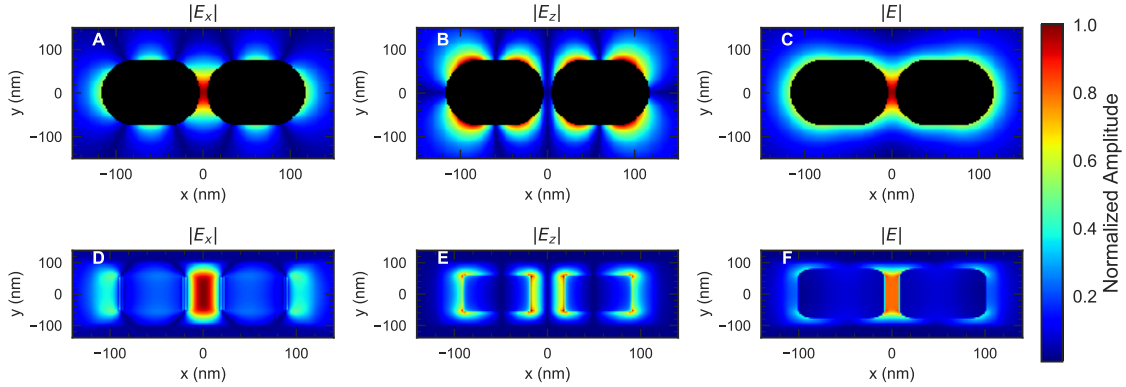


**Figure 4.19:** Electric fields  $|E_x|$ ,  $|E_z|$  and  $|E|$  of a nanorod antenna with nanorod dimensions of  $90 \times 60 \times 30$  nm in the  $xz$  plane with  $y = 0$  calculated once by the Green's function formalism (A-C) and once by FEM calculations using the program Lumerical (D-F). The FEM calculations were performed by V. Smirnov.

As a demonstration a 2D simulation of a nanorod antenna using 11 dipoles for each rod, a Lorentzian resonance for the nanorod with  $\hbar\omega = 1.55$  eV, a linewidth of  $\hbar\gamma = 0.04$  eV and nanorod dimensions of  $L' = 2 \cdot 45$  nm +  $4 \cdot 5$  nm is shown in figure 4.19 together with FEM calculations on the same structure. Hereby we used the same phase relation for each nanorod, i.e. the weight factors  $w_i$  for the two nanorods with each 11 dipoles are the same. The FEM simulations were performed with the program Lumerical using a plane wave polarized along the rod axis as an excitation field. Both calculations yield the same spatial field components around the antenna structure and demonstrate how a relatively simple approach using the Green's function operator yields realistic results of the fields around a nano structure.

### 4.2.3 Tip above a planar, isotropic dielectric material

Up to now the tip polarizability  $\overleftrightarrow{\alpha}_{tip}$  was introduced and the calculation of fields around nanostructures within the Green's formalism was shown. For nanostructures that have a much larger polarizability than the tip, these calculations already resemble the result of a SNOM measurement, because the tip just images the field of the structure. An example of such a measurement can be found in chapter 5.1.

Now we want to analyze the situation where both the tip as well as the sample are polarizable, but this time the tip polarization is comparable to or exceeding that of the sample. This will result in an interaction between tip and sample and the term  $TST$  in equation (4.107) with

$n = 3$  becomes dominant. The description that follows is well known as the image dipole model [15], which was commonly used in the nano-imaging research area over the recent years. In the image dipole model, the tip is assumed as a sphere with isotropic polarizability. It is positioned above a planar, isotropic dielectric material. As both, the tip and sample are isotropic, it is sufficient to take into account one component of the electric field and the corresponding element of the polarizability tensor. In the next section of this chapter, I will present the extension towards anisotropic materials, where the full vectorial fields will be considered.

The idea of the image dipole model is sketched in figure 4.20.

Hereby, only the apex of the tip is considered to play a role in the scattering process. The tip apex is modelled as a polarizable metallic sphere with radius  $R$  in some distance  $d$  to the sample surface. The sample in this model is modelled as a half-space with constant material contrast expressed by the dielectric function  $\epsilon_{\text{sample}}$ .

Let's assume an incident field polarized along the taper axis in the  $z$ -direction:  $\vec{E}_{\text{inc}} = E_{\text{inc}}\hat{z}$ . This incident field now induces a dipole in the tip along the  $z$ -direction:

$$\vec{p}_{\text{tip}} = \alpha_{\text{tip},zz} E_{\text{inc}} \hat{z} = p_{\text{tip}} \hat{z} \quad (4.126)$$

The electric field emitted by the tip dipole is now inducing an image dipole, oriented along

$\hat{z}$ , and located at a distance  $D = d + z_0$  below the interface, or at a distance  $2D$  from the tip dipole. Here,  $d$  is the tip-sample distance,  $z_0$  is the distance between the tip dipole and the tip surface at the apex (see Fig. 4.20). The dipole moment of the image dipole is given by

$$p_{ID} = \beta p_{\text{tip}} = \frac{\epsilon_{\text{sample}} - 1}{\epsilon_{\text{sample}} + 1} p_{\text{tip}}. \quad (4.127)$$

In the case of an electric field polarized along the tip axis and by using the approximation that the phase delay between the two dipoles can be neglected (electrostatic limit) we can write the field of the image dipole at the position of the tip as

$$E_{ID}(\vec{r}_{\text{tip}}) = \frac{p_{ID}}{2\pi\epsilon_0(2D)^3} \quad (4.128)$$

This image dipole is now furthermore enhancing the field at the tip which means the local electric field at the tip dipole is a superposition of the incident field  $E_{\text{inc}}$  and the field from the

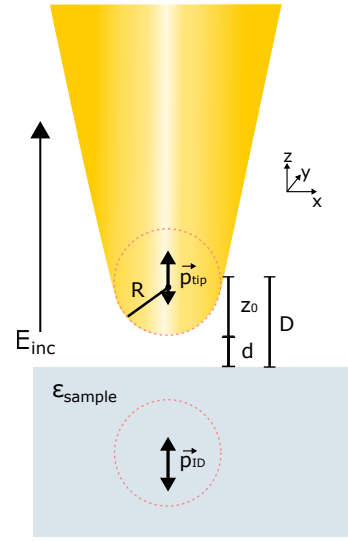
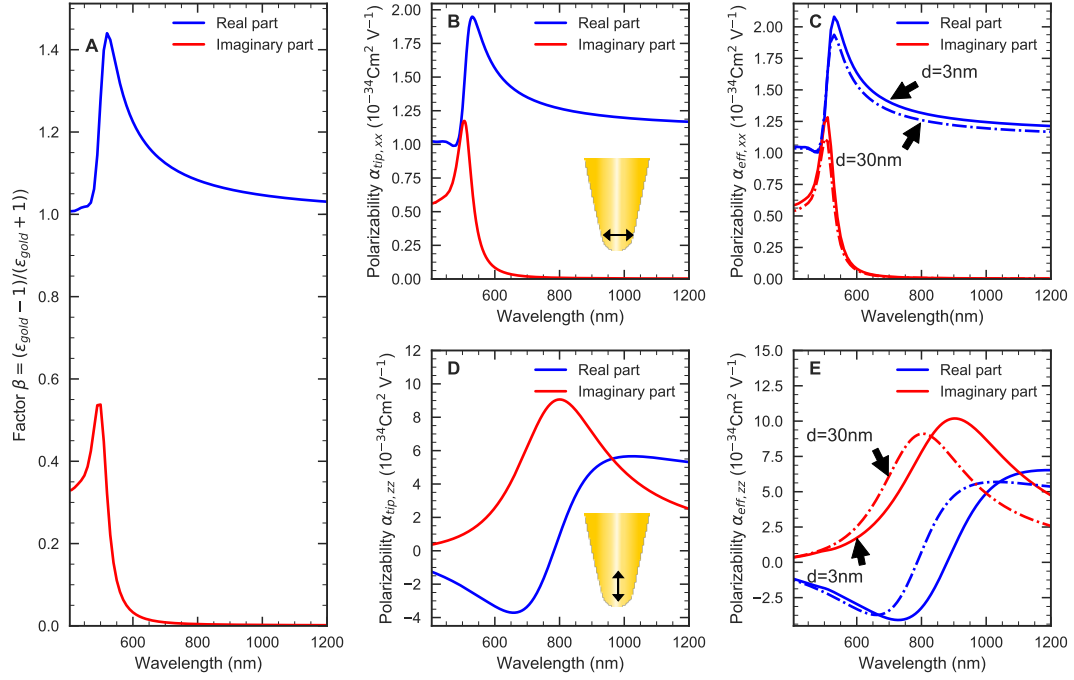


Figure 4.20: Visualization of the image dipole model.



**Figure 4.21:** (A) The factor  $\beta = (\epsilon_{Au} - 1)/(\epsilon_{Au} + 1)$  for a gold surface. (B) The tip polarizability  $\alpha_{tip,xx}$  modeled by a gold sphere with 10 nm diameter. (C) The effective polarizability for polarization parallel to the surface. (D) The tip polarizability  $\alpha_{tip,zz}$  modelled by a spectrally broad Lorentzian centered around 800 nm for a field enhancement at the tip apex of around 7. (E) The effective polarizability  $\alpha_{eff,zz}$  for polarization parallel to the tip axis.

image dipole  $E_{ID}$ . In total we can write the dipole moment of the tip as

$$p = \alpha_{tip} \left( E_{inc} + \frac{p_{ID}}{16\pi\epsilon_0 D^3} \right) = \frac{\alpha_{tip}}{1 - \frac{\alpha_{tip}\beta}{16\pi\epsilon_0 D^3}} E_{inc}. \quad (4.129)$$

The total fields scattered to the detector is a superposition of the tip dipole and the image dipole fields. This allows us to define an effective polarizability of the tip-sample system by [15]

$$\alpha_{eff} = \frac{\alpha_{tip}}{1 - \frac{\alpha_{tip}\beta}{16\pi\epsilon_0 D^3}}. \quad (4.130)$$

Analogous we find for an incident field polarized perpendicular to the taper axis (e.g.  $\vec{E}_{inc} = E_{inc}\hat{x}$ ) the condition

$$\alpha_{eff,xy} = \frac{\alpha_{tip}}{1 - \frac{\alpha_{tip}\beta}{32\pi\epsilon_0 D^3}}. \quad (4.131)$$

Exemplary calculations of  $\beta$ ,  $\alpha_{tip}$  and  $\alpha_{eff}$  for a gold tip over a gold surface are shown in Fig. 4.21 for both polarization parallel and perpendicular to the tip axis. Hereby, the factor  $\beta$  in

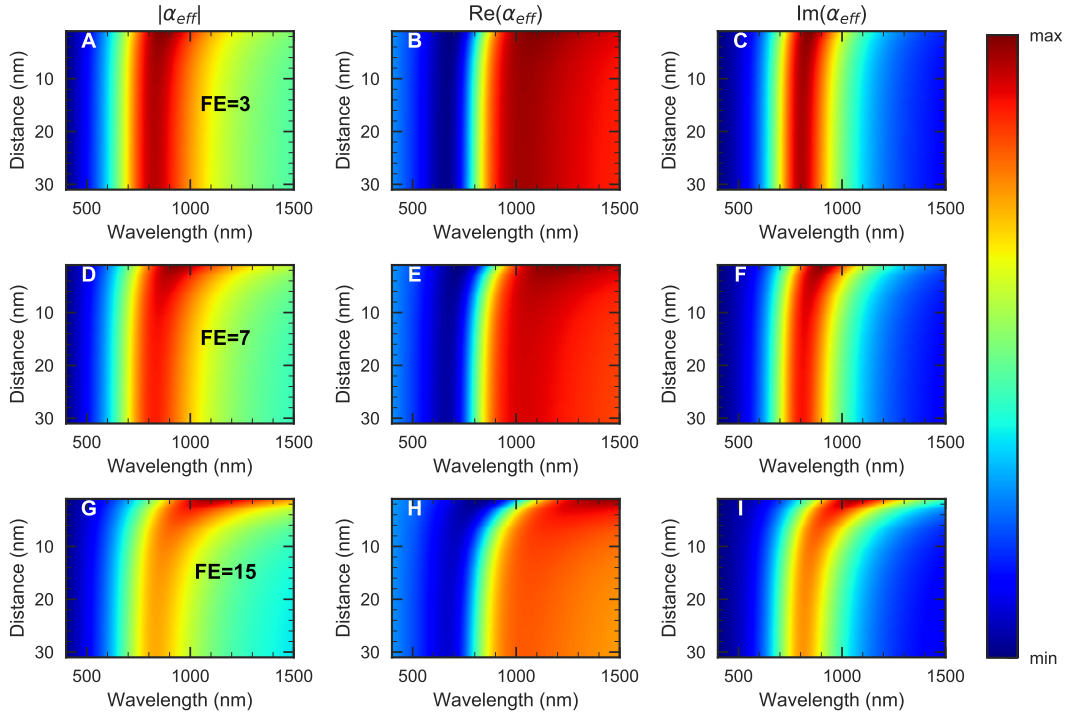


**Figure 4.22:**  $\alpha_{eff,zz}$  for a gold tip approached to a gold surface, whereas the tip polarizability is modelled by a Lorentzian oscillator. Shown are calculations as a function of tip-sample-distance  $d$  and wavelength  $\lambda$  for different field enhancement (FE) factors.

Fig. 4.21A shows a resonance around 500 nm. For longer wavelengths within our measurement range, the real part is slightly monotonous decreasing and the imaginary part is almost 0.  $\beta$  is only dependent on the dielectric function of gold and as the considerations using a Green's formalism in the next section will show,  $\beta$  can be understood as a reflection coefficient for the evanescent waves reflected at the surface.

Following the previous analysis of the tip dipole, the tip polarizability for the in-plane component  $\alpha_{tip,xx}$  is modeled here again by a gold sphere with 10 nm radius shown in Fig. 4.21B. We again observe the typical resonance for a small sphere around 500 nm that was already found in Fig. 4.16. For longer wavelengths the polarizability for the sphere does not show any resonances and for a typical spectral range between 700 nm and 900 nm, that is supported by our laser system, the polarizability can be approximated as a constant with almost negligible imaginary part.

Fig. 4.21C shows the effective polarizability for the tip polarizability  $\alpha_{tip,xx}$  for two tip-sample distances of 3 nm and 30 nm. As was expected in this case the effective polarizability shares the spectral shape of the tip polarizability and is decreasing in amplitude with larger tip-sample distances. Thus, in this case and in our wavelength range, we expect the effective polarizability to carry the spectral information of the sample if we only have a coupling to the x-component

of the tip.

This is different in the case of the polarizability assumed for the the z-component  $\alpha_{tip,zz}$  that is shown in Fig. 4.21D. Here, we introduced a broad Lorentzian-shaped resonance centered around 800 nm. The amplitude of the polarizability was set such that the field amplitude at the tip apex position is enhanced by a factor of around 7. The field at the tip apex was calculated with the Greens function formalism and the tip was modeled by one dipole positioned around  $z_0 = 13.3$  nm away from the apex (cmp. Fig. 4.20), because this matches experimental observations from our own group [172]. The effective polarizability considering only coupling to the z-component of the field and hence a polarizability parallel to the tip axis is shown in Fig. 4.21E for the same two tip-sample distances of 3 nm and 30 nm. Clearly, we can observe a spectral shift towards longer wavelengths as well as an increase in amplitude with decreasing tip-sample distance.

This spectral shift highly depends on the field enhancement at the tip apex, the tip sample distance and the value of  $\beta$ . This is demonstrated in Figure 4.22 by plotting the real, imaginary and absolute value of the same effective polarizability from Fig. 4.21E, but this time for 3 different field enhancement factors FE=3, FE=7 and FE=15 depending on the wavelength as well as on the tip-sample distance.

Depending on the etching process and the geometrical shape of the tip apex, the field enhancement factor can vary in tip production. Clearly, we can observe a strong shift towards longer wavelengths and a broadening of the resonance only for small tip-sample distances, whereas for larger distances the effective polarizability reflects that of the tip polarizability. This effect is increased for higher field enhancement factors. In fact, in these cases the factor  $\frac{\alpha_{tip,zz}\beta}{16\pi\epsilon_0 R^3}$  is close to one and hence the denominator of  $\alpha_{eff}$  is close to 0. For small field enhancement factors or large tip sample distances we can approximate  $\alpha_{eff}$  by a Taylor series around  $\alpha_{tip,zz}$ :

$$\alpha_{eff,zz} \approx \alpha_{tip,zz} + \frac{\alpha_{tip,zz}^2 \beta}{16\pi\epsilon_0 D^3} + \frac{\alpha_{tip,zz}^3 \beta^2}{(16\pi\epsilon_0 D^3)^2} + \dots \quad (4.132)$$

Here, the first term describes the polarizability of the tip alone. The second term describes one reflection, where the field from the tip is reflected at the surface and is acting back on the tip. Higher order terms then account for multiple reflections.

This mirrors the findings of using the Green's function formalism that will be shown in the next section. There, I demonstrate that the effective polarizability can be derived by the Greens function formalism in a self-consistent solutions by taking into account multiple reflections between tip and sample. A similar view on the vectorial near-field coupling was recently shown for a SNOM measurement on a nanorod where the interaction was described by a perturbation series of multiple tip-sample scattering orders[93]. Also note, that in equation (4.132) the tip-sample distance term in the denominator is increasing for multiple reflections. Already for two reflections the distance dependency is proportional to  $1/D^6$ . Hence, for large tip-sample

distances multiple reflections are negligible and don't affect the effective polarizability. Only for small distances multiple reflections can have a noticeable effect. As Fig. 4.22 shows, in this case it highly depends on the field enhancement factor (and on the sample properties entering in  $\beta$ ) if we can observe the spectral shifts of the resonances.

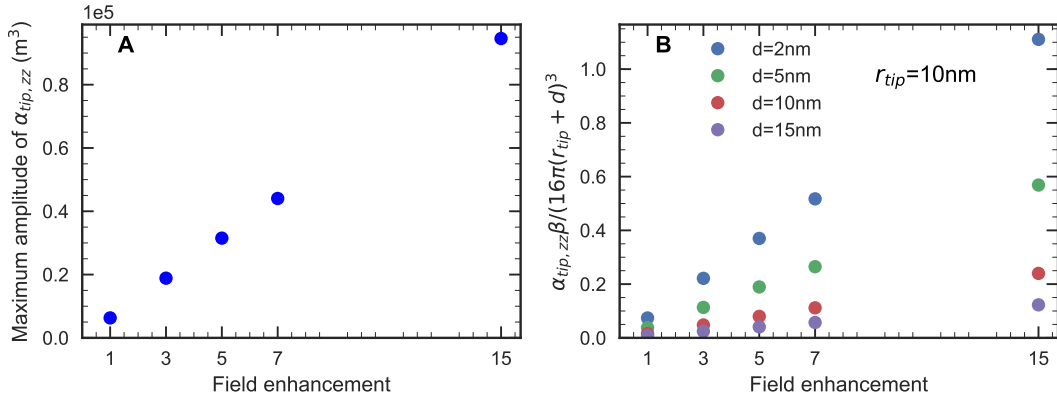


**Figure 4.23:** (A) Amplitude of the Lorentzian tip resonance as a function of field enhancement factor. (B) The factor  $\frac{\alpha_{tip,zz}\beta}{16\pi(r_{tip}+d)^3}$  as a function of field enhancement factor. The tip radius  $r_{tip}$  was assumed to be 10 nm.

An estimation about how critical this spectral response depends on the tip-sample distance and the field enhancement factor is done by plotting the factor  $\frac{\alpha_{tip,zz}\beta}{16\pi z_0^3}$  in figure 4.23. Obviously, only for small field enhancement factors (1-5) and large tip-sample distances (at least  $d > 5$  nm) the factor in the denominator is small and no strong spectral shifts are expected. Otherwise, spectral shifts with decreasing tip-sample distance are expected and must be taken into considerations.

If the factor  $\alpha_{tip}\beta = 16\pi\epsilon_0 D^3$  is close to 1 in the denominator of eq. (4.129), this can also be considered as a localized surface exciton polariton [173] that will be excited. The existence of such surface exciton polaritons has been shown experimentally e.g. by Schneider et al. [174] and Kehr et al. [175] in the mid-infrared region for wavelengths around 10-25  $\mu m$ .

Consequently, the spectral response of the tip-sample system highly depends on the tip polarizability amplitude (defined by the tip shape and the field enhancement), as well as on the sample dielectric function  $\beta$  and the tip-sample distance and has to be considered in the data evaluation. In the case of a gold tip with 10 nm radius a field enhancement factor of up to  $FE=7$  is feasible [15, 151, 157, 176]. In our experiments however, we never observed a shift of a resonance for small distances. Thus, most of the SNOM tips used in this work probably have either a lower field enhancement, or the tip size was bigger than 10 nm, or the tip-sample distance was larger than assumed.

#### 4.2.4 SNOM tip above an anisotropic dielectric material

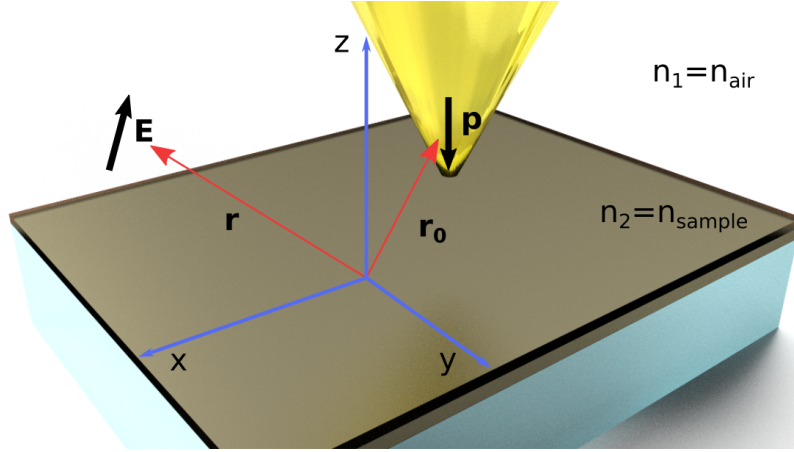


**Figure 4.24:** Visualization of the tip dipole over a sample surface. The dipole of the tip is located at  $\vec{r}_0$ , whereas the field from this dipole can be calculated at every position  $\vec{r}$ .

In a last step, we want to expand the description of the fields from SNOM tip above a isotropic material to also be applicable to anisotropic samples. In this case, the image dipole model does not hold anymore, because the sample's dielectric function cannot be modelled by a single constant  $\beta$ , but rather has a different dielectric constant for each direction  $x, y, z$ . Consequently, we will use the Green's function method to calculate the scattered field of the tip-sample system in all directions and for arbitrary samples with different dielectric functions. As an outcome we will learn, that the previously introduced coupling dipole model for isotropic dielectric materials can be reproduced by the more complete Green's function approach using specific assumptions and simplifications. Moreover, in the end of this section we will provide an analytically derived pendant to the measured intensity signal of the SNOM, such that measured SNOM signals can directly be compared with a simulation.

From now on, the fundamental equation we are going to use for modeling the tip sample interaction is eq. (4.114),  $\vec{E}(\vec{r}) = \mu_0 \omega^2 \overleftrightarrow{G}(\vec{r}, \vec{r}_0, \omega) \vec{p}$ , which connects the Green's function with the dipole moment and hence the electric field. The coordinate system and the geometry we are going to use for the following description is visualized in in figure 4.24. In the simplest case we can now describe our tip as a dipole near a planar interface. For a dipole with dipole moment  $\vec{p}$  at position  $\vec{r}_0 = (x_0, y_0, z_0)$  near a planar interface the solution for the Greens function can be written in terms of an s-polarized and a p-polarized part as [140]

$$\overleftrightarrow{G}_0(\vec{r}, \vec{r}_0) = \frac{i}{8\pi^2} \iint_{-\infty}^{\infty} [\overleftrightarrow{M}^{\leftrightarrow s} + \overleftrightarrow{M}^{\leftrightarrow p}] e^{i[k_x(x-x_0)+k_y(y-y_0)+k_z|z-z_0|]} dk_x dk_y \quad (4.133)$$

with

$$\overset{\leftrightarrow}{M} = \frac{1}{k_z(k_x^2 + k_y^2)} \begin{pmatrix} k_y^2 & -k_x k_y & 0 \\ -k_x k_y & k_x^2 & 0 \\ 0 & 0 & 0 \end{pmatrix} \quad (4.134)$$

and

$$\overset{\leftrightarrow}{M} = \frac{1}{k^2(k_x^2 + k_y^2)} \begin{pmatrix} k_x^2 k_z & k_x k_y k_z & \mp k_x (k_x^2 + k_y^2) \\ k_x k_y k_z & k_y^2 k_z & \mp k_y (k_x^2 + k_y^2) \\ \mp k_x (k_x^2 + k_y^2) & \mp k_y (k_x^2 + k_y^2) & (k_x^2 + k_y^2)^2 / k_z \end{pmatrix}. \quad (4.135)$$

Here, the inhomogeneous Helmholtz equation and the representation of the dipole's vector potential with an integration in k-space were used. The latter is also known as the Weyl decomposition or Weyl identity [140]. These equations define the angular spectrum representation of the Greens function for a dipole located at position  $\vec{r}_0$  in space. The  $\mp$  sign either denotes a solution for  $z > z_0$  (-) or  $z < z_0$  (+) with  $z_0$  the z-distance of the dipole from the surface. In the next step the fields emitted from the tip dipole are reflected at the interface. The effective field at the tip dipole can be described as the superposition of the field at the tip and the field emitted by the tip dipole which is reflected at the surface and propagates back to the tip dipole. This process can also happen multiple times resulting in multiple reflections between tip and sample. In first approximation considering just one reflection, we can write this as

$$\vec{E} = \omega^2 \mu_0 \mu_1 [\overset{\leftrightarrow}{G}_0(\vec{r}, \vec{r}_0) + \overset{\leftrightarrow}{G}_R(\vec{r}, \vec{r}_0)] \vec{p} \quad (4.136)$$

with the Greens function of the reflected field  $\overset{\leftrightarrow}{G}_R(\vec{r}, \vec{r}_0)$ . As we want to evaluate the field at the tip position we do not have any change in x and y direction so that we can set  $\vec{r} = \vec{r}_0$ . The reflected Greens function is then described by [140]:

$$\overset{\leftrightarrow}{G}_R(\vec{r}_0, \vec{r}_0) = \frac{i}{8\pi^2} \iint_{-\infty}^{\infty} [r^s(k_x, k_y) \overset{\leftrightarrow}{M}_r^s - r^p(k_x, k_y) \overset{\leftrightarrow}{M}_r^p] e^{i2k_z z_0} dk_x dk_y \quad (4.137)$$

with  $\overset{\leftrightarrow}{M}_r^s = \overset{\leftrightarrow}{M}^s$  and

$$\overset{\leftrightarrow}{M}_r^p = \frac{1}{k^2(k_x^2 + k_y^2)} \begin{pmatrix} k_x^2 k_z & k_x k_y k_z & k_x (k_x^2 + k_y^2) \\ k_x k_y k_z & k_y^2 k_z & k_y (k_x^2 + k_y^2) \\ -k_x (k_x^2 + k_y^2) & -k_y (k_x^2 + k_y^2) & -(k_x^2 + k_y^2)^2 / k_z \end{pmatrix}. \quad (4.138)$$

It is important to note that we have an integration over all k-vectors. This also includes evanescent waves with  $k_x, k_y > k_{max} = k \cdot NA$ . As a consequence the sample properties enter mainly in

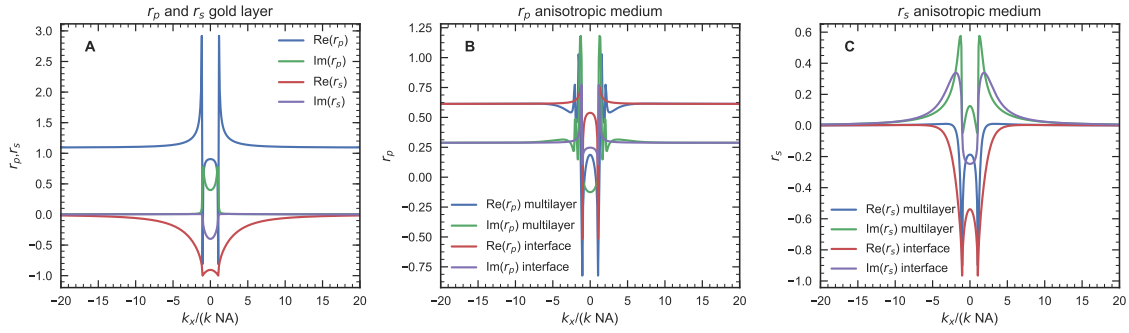


**Figure 4.25:** Simulated reflection coefficients  $r_p$  and  $r_s$  for a gold layer (A) as well as for an anisotropic medium (B) and (C) as a function of  $k_x/(k NA)$ . In (B) and (C) simulations on both a multilayer structure as well as on a single interface are plotted.

the complex reflection coefficients  $r_p$  and  $r_s$ . These are defined by the Fresnel coefficients for anisotropic or isotropic media that are calculated from the dielectric functions of both materials at the air/medium interface. For a multilayer system  $r_p$  and  $r_s$  can be calculated by transfer matrix calculations.

Figure 4.25 shows an exemplary calculation of the reflection coefficients, once for a gold-coated glass substrate and once for an anisotropic thin dye film on top of a multilayer system of 180  $\mu\text{m}$  glass, 20 nm gold and 107 nm glass, used in later chapters (cmp. figure 4.26 for a visualization). The exact dielectric function of the in-plane component  $\epsilon_o$  and the z component  $\epsilon_z = \epsilon_e$  used for this simulation is of no particular interest for the following discussion, but can be found in chapter 6.3 that deals with the local SNOM spectra of an anisotropic squaraine dye material. As the simulation results plotted in figure 4.25 clearly point out, both reflection coefficients  $r_p$  and  $r_s$  are constant for large  $k_x$  values. Comparison of the multilayer structure with a single air/medium interface further shows a difference only in the part around  $k_x = -10k_{max}$  to  $k_x = +10k_{max}$ , which means the multilayer structure contributes mainly to the propagating k-vectors resulting in different phase changes. For high values of  $k_x$  only the last layer plays a role. This is plausible as the amplitude of evanescent waves is decaying exponentially at the interface.

Further, we can infer from figure 4.25 that the s-polarized reflection coefficient is going to zero for large  $k$  values. Moreover, when considering a tip with its axis positioned parallel to the surface normal, we consider mainly a contribution from the dipole in z-direction. As only the p-polarized component contributes to the z-component of the electric field, we can conclude a contribution of the tip-sample interaction signal from the p-polarized reflection coefficient only. The reflection coefficient  $r_p$  can further be expressed as a function of  $k_x$  and  $k_y$  that can be found in many textbooks. For an interface between two isotropic media with refractive index

$n_1$  and  $n_2$  this reads

$$r_p(k_{\parallel}) = \frac{1 - (n_1/n_2)^2 \sqrt{\frac{(n_2 k_0)^2 - k_{\parallel}^2}{(n_1 k_0)^2 - k_{\parallel}^2}}}{1 + (n_1/n_2)^2 \sqrt{\frac{(n_2 k_0)^2 - k_{\parallel}^2}{(n_1 k_0)^2 - k_{\parallel}^2}}} \quad (4.139)$$

with  $k_{\parallel} = \sqrt{k_x^2 + k_y^2}$  the in-plane k-component. Evaluating this for large values  $k_{\parallel} \gg k_{max}$  the  $k_z$  component becomes the imaginary part of the in-plane k component,  $k_z = \sqrt{(n_2 k_0)^2 - k_{\parallel}^2} \approx ik_{\parallel}$ , and the reflection coefficient simplifies to

$$r_p(k_{\parallel} \rightarrow \infty) = \frac{n_2^2 - n_1^2}{n_2^2 + n_1^2} = \frac{\epsilon_2 - \epsilon_1}{\epsilon_2 + \epsilon_1}. \quad (4.140)$$

This is the same sample dependent factor  $\beta$  as defined in equation (4.127) in the image dipole coupling model from Keilmann and Knoll [15] discussed in the previous section. Conclusively, this derivation shows that the factor  $\beta$  in the image dipole model describes the reflection of the evanescent waves at the sample surface. For anisotropic samples the factor  $\beta = r_p(k_{\parallel} \rightarrow \infty)$  will be different, because the refractive indices  $n_1$  and  $n_2$  then also depend on  $k_{\parallel}$ . A solution to this problem will be covered in the following section.

#### 4.2.4.1 Tip-sample interaction in a self-consistent solution

To calculate the electric fields from the tip-sample interaction  $\vec{E} = \omega^2 \mu_0 \mu_1 [\overset{\leftrightarrow}{G}_0(\vec{r}, \vec{r}_0) + \overset{\leftrightarrow}{G}_R(\vec{r}, \vec{r}_0)] \vec{p}$ , the dipole moment  $\vec{p}$  has to be defined as well. We already know the dipole moment vector is proportional to the polarizability tensor  $\overset{\leftrightarrow}{\alpha}$  given as  $\vec{p} = \overset{\leftrightarrow}{\alpha} \vec{E}$ . For the SNOM tip this tensor is characterized by

$$\overset{\leftrightarrow}{\alpha} = \begin{pmatrix} \alpha_{xy} & 0 & 0 \\ 0 & \alpha_{xy} & 0 \\ 0 & 0 & \alpha_z \end{pmatrix} \quad (4.141)$$

whereas  $\alpha_{xy}$  is typically small compared to  $\alpha_z$  for a tip with its axis normal to the sample surface. Further, for a tilted tip with respect to the sample surface, also the off-diagonal elements of the tensor have to be considered. As mentioned before, the electric field at the dipole position is now given by the superposition of the field incident on the dipole  $\vec{E}_{inc}$  and the field generated by the dipole and reflected off the sample,  $\vec{E}_R$ . Hence, in total we have

$$\vec{p} = \overset{\leftrightarrow}{\alpha} \vec{E} \quad (4.142)$$

$$= \overset{\leftrightarrow}{\alpha} (\vec{E}_{inc} + \vec{E}_R) \quad (4.143)$$

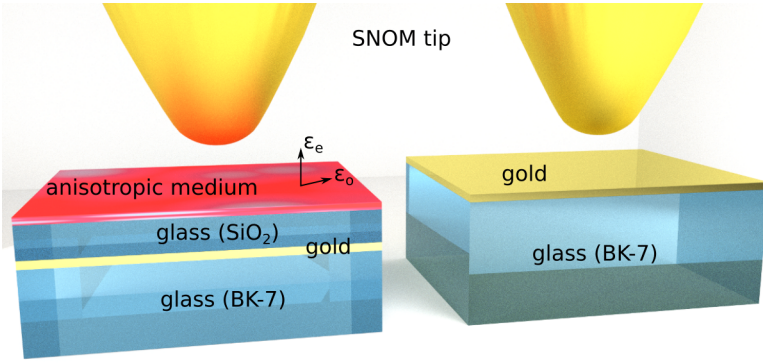


**Figure 4.26:** Visualization of a SNOM tip over the layered system with an anisotropic medium as the last layer and for a gold-coated glass substrate.

$$= \overset{\leftrightarrow}{\alpha} (\vec{E}_{inc} + \omega^2 \mu_0 \mu_1 \overset{\leftrightarrow}{G}_R \vec{p}) \quad (4.144)$$

Solving for  $\vec{p}$  gives us a self-consistent solution for the dipole moment that includes all multiple reflections between tip and sample:

$$\vec{p} = \frac{\overset{\leftrightarrow}{\alpha}}{\overset{\leftrightarrow}{I} - \omega^2 \mu_0 \mu_1 \overset{\leftrightarrow}{\alpha} \overset{\leftrightarrow}{G}_R} \vec{E}_{inc} = \frac{\overset{\leftrightarrow}{\alpha}}{\overset{\leftrightarrow}{I} - (k^2/\epsilon_0) \overset{\leftrightarrow}{\alpha} \overset{\leftrightarrow}{G}_R} \vec{E}_{inc} \quad (4.145)$$

This result looks very familiar to the dipole moment defined in the coupling dipole model in equation (4.129). In fact we can now directly derive the previous model.

Under the assumption that the propagating  $k$ -vectors do not contribute to the overall signal the coefficient  $r_p = \beta$  is independent of  $k_x$  and  $k_y$  and can be taken out of the integral of the Greens function  $\overset{\leftrightarrow}{G}_R$  so that we have

$$\vec{p} = \frac{\overset{\leftrightarrow}{\alpha}}{\overset{\leftrightarrow}{I} - (k^2/\epsilon_0) \beta \overset{\leftrightarrow}{\alpha} \overset{\leftrightarrow}{G}'_R} \vec{E}_{inc} \quad (4.146)$$

The coupling dipole model further assumes a field in  $z$ -direction so that only the  $z$ -component of the dipole moment  $p_z$  is considered. This is equivalent of evaluating  $(\overset{\leftrightarrow}{G}'_R)_{zz}$ :

$$(\overset{\leftrightarrow}{G}'_R)_{zz} = \frac{i}{8\pi^2} \iint_{-\infty}^{\infty} \frac{(k_x^2 + k_y^2)^2}{k^2 k_z (k_x^2 + k_y^2)} e^{i2k_z z_0} dk_x dk_y \quad (4.147)$$

Using the definition for the in-plane component  $k_{||} = \sqrt{k_x^2 + k_y^2}$  the double integration simplifies

to an integration over ring segments with radius  $k_{\parallel}$ :

$$(\overleftrightarrow{G}'_R)_{zz} = \frac{i}{8\pi^2 k^2} \int_0^{\infty} \frac{k_{\parallel}^4}{k_z k_{\parallel}^2} e^{i2k_z z_0} 2\pi k_{\parallel} dk_{\parallel} \quad (4.148)$$

Since we are neglecting the  $k$ -vectors of the propagating waves we can again set  $k_z = ik_{\parallel}$  and we get

$$(\overleftrightarrow{G}'_R)_{zz} = \frac{1}{4\pi k^2} \int_0^{\infty} k_{\parallel}^2 e^{-2k_{\parallel} z_0} dk_{\parallel} = \frac{1}{4\pi k^2} \frac{2!}{(2z_0)^2} = \frac{1}{16\pi z_0^3 k^2} \quad (4.149)$$

The factor  $k^2$  cancels out and we are left with the exact same equation (4.129) previously used in the coupled image dipole model

$$p_z = \frac{\alpha_{tip,zz}}{1 - \frac{\alpha_{tip,zz}\beta}{16\pi\epsilon_0 z_0^3}} E_{inc,z} \quad (4.150)$$

This is an important result and directly shows how powerful the Green's function formalism can be. We can infer that the coupled image dipole model is the simplified result of the complete description, when a few approximations and assumptions are made, such as only considering the field in  $z$  direction (or separately only  $x$  direction) and neglecting the propagating waves. In contrast to the simple model, the Green's function approach can be widely adjusted and can simulate a more complete system. For instance, in the coupled dipole model either a field in  $z$  direction excites the tip dipole oriented along  $z$ -direction or a field polarized in  $x$ -direction excites the dipole in the  $xy$ -plane. For our model the polarizability of the tip dipole is clearly defined by a tensor, such that we can simulate directly the total response to a given input field. Also a tilted tip could easily be accounted for by using a polarizability tensor with nonzero components on the non-diagonal entries.

Additionally, it is now straightforward to include anisotropic materials into our model. As  $\beta$  defines the reflection coefficient  $r_p$  for evanescent waves we can define the incident angle  $\theta_i$  by

$$\theta_i = \arcsin \left( \frac{\sqrt{k_x^2 + k_y^2}}{k_0} \right) \quad (4.151)$$

which will become imaginary for large  $k_x, k_y$  values. The angle could then be used in our previously derived equation for the reflection coefficient for anisotropic media (compare equations (4.79)). Another way is to express the reflection coefficient in terms of  $(k_x, k_y)$  values and solve the electrostatic image method for an anisotropic half space. An extensive derivation for such a model was published by Lindell et al [177] and applied to sSNOM by Schneider et al. [178]. It

could be shown that the factor  $\beta$  can be written as

$$\beta = \frac{\sqrt{\epsilon_e \epsilon_o} - 1}{\sqrt{\epsilon_e \epsilon_o} + 1}. \quad (4.152)$$

Hence, by using anisotropic media, the SNOM tip is probing the geometrical mean of the ordinary and extraordinary refractive index. This is also intuitively clear as for large  $k$ -values the  $z$  component of the  $k$ -vector  $k_z$  is equal to the imaginary part of the in-plane component  $k_{||}$ , thus they have the same amplitude.

#### 4.2.4.2 The measured intensity signal

In the previous section we have derived the vectorial electric fields after being focused through a layered system including anisotropic thin films. These fields then excite the SNOM tip dipole and the interaction between tip and sample was deduced in a complete Greens function approach. To understand or predict measurement results, we are interested in a simulation of the intensity signal that is measured by the sSNOM in back-reflection geometry. This means, in a last step, the fields from the tip-sample interaction propagate through the sample once more and interfere with the field  $\vec{E}_R$ , reflected from the sample side pointing towards the microscope objective. To keep it simple, we further assume higher order demodulation is applied and contributions from a background field are negligible.

The field  $\vec{E}$  directly after going through the sample of thickness  $d$  is then given by

$$\vec{E} = \omega^2 \mu_0 \mu_1 \overleftrightarrow{G}_t(x_0 \hat{n}_x + y_0 \hat{n}_y + d \hat{n}_z, \vec{r}_0) \vec{p} \quad (4.153)$$

with the Greens function for transmission

$$\overleftrightarrow{G}_t(x_0 \hat{n}_x + y_0 \hat{n}_y + d \hat{n}_z, \vec{r}_0) = \frac{i}{8\pi^2} \iint_{k_x^2 + k_y^2 < k^2} [t^s(k_x, k_y) \overleftrightarrow{M}_t^s + t^p(k_x, k_y) \overleftrightarrow{M}_t^p] e^{ik_z z_0} dk_x dk_y \quad (4.154)$$

and  $\overleftrightarrow{M}_t^s = \overleftrightarrow{M}^s$  and  $\overleftrightarrow{M}_t^p = \overleftrightarrow{M}^p$  using + sign for the lower half-space. The integration is in this case limited to only propagating wave vectors that are seen by the microscope objective.  $t_p$  and  $t_s$  are the complex transmission coefficients that are in general calculated by transfer matrix method and were already used to calculate the focus fields.

The field after propagation through the layers for each  $k$ -vector is given by equation (4.153):

$$\vec{E}_t(k_x, k_y) = k^2 \overleftrightarrow{G}_t(\vec{r}, \vec{r}_0) \vec{p} \quad (4.155)$$

Finally, the measured SNOM intensity signal of the near-field can lastly be expressed as the

interference of the scattered and transmitted field  $\vec{E}_t$  and the reflected field from the sample surface  $\vec{E}_R$

$$I \propto \left| \operatorname{Re} \left( \iint_{k_x^2 + k_y^2 \leq k^2} E_R(k_x, k_y)^* E_t(k_x, k_y) dk_x dk_y \right) \right| \quad (4.156)$$

Hereby, we again assume higher order demodulation, in which case terms like  $E_R^2$  or  $E_t^2$  do not contribute to the measurement signal. Equation (4.156) concludes the full simulation of measured SNOM signals. Moreover, all equations derived so far are dependent on the wavelength, such that a spectral representation of the focus field at a given position is straightforward. An extensive discussion of the wavelength dependent focus fields can be found in chapter 6.

# In-line interferometer

# 5

In this section we will introduce a new way of spectrally broad-band enhancing of the near-field signals by the use of an in-line interferometer. The interferometer consists of a glass substrate with a thin layer of gold coated on top and finally another layer of evaporated SiO<sub>2</sub> (cmp. Fig. 5.1). By measuring and evaluating SNOM approach curves for three different substrates, demodulated at multiple harmonics of the tip oscillation frequency, we show that the in-line interferometer indeed is needed as a replacement of a normal glass substrate in order to make meaningful conclusions from SNOM measurements.<sup>1</sup>

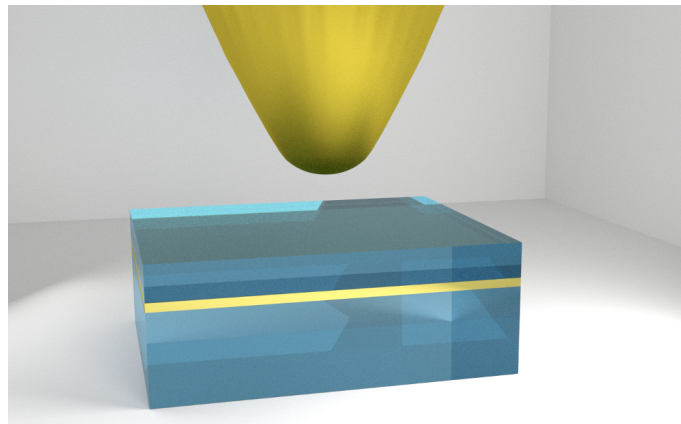


**Figure 5.1:** Visualization of a SNOM tip over the in-line interferometer, consisting of a glass-gold-glass layer system.

<sup>1</sup>Parts of this chapter are taken from the peer-reviewed publication "Brauer, J., Zhan, J., Chimeh, A., Korte, A., Lienau, C., & Gross, P. (2017). In-line interferometer for broadband near-field scanning optical spectroscopy. *Optics Express*, 25(13), 15504". My part was the planning of the experiment, measurement of the data, literature research, setting up the equations as well as simulating and plotting of the results. The paper is attached in appendix D.

## 5.1 Introduction: Spatial near-fields of a single bowtie antenna

The near-field signal that is scattered by the SNOM tip has in general a very small power compared to any background-fields and has to be enhanced by a suitable detection scheme as outlined in chapter 2.2. The amount of the scattered near-field signal and the signal to background ratio however also highly depends on the near-field generated by the sample itself. To demonstrate this, firstly I explore plasmonic structures resonant with the exciting laser wavelength, that themselves already generate a high near-field.

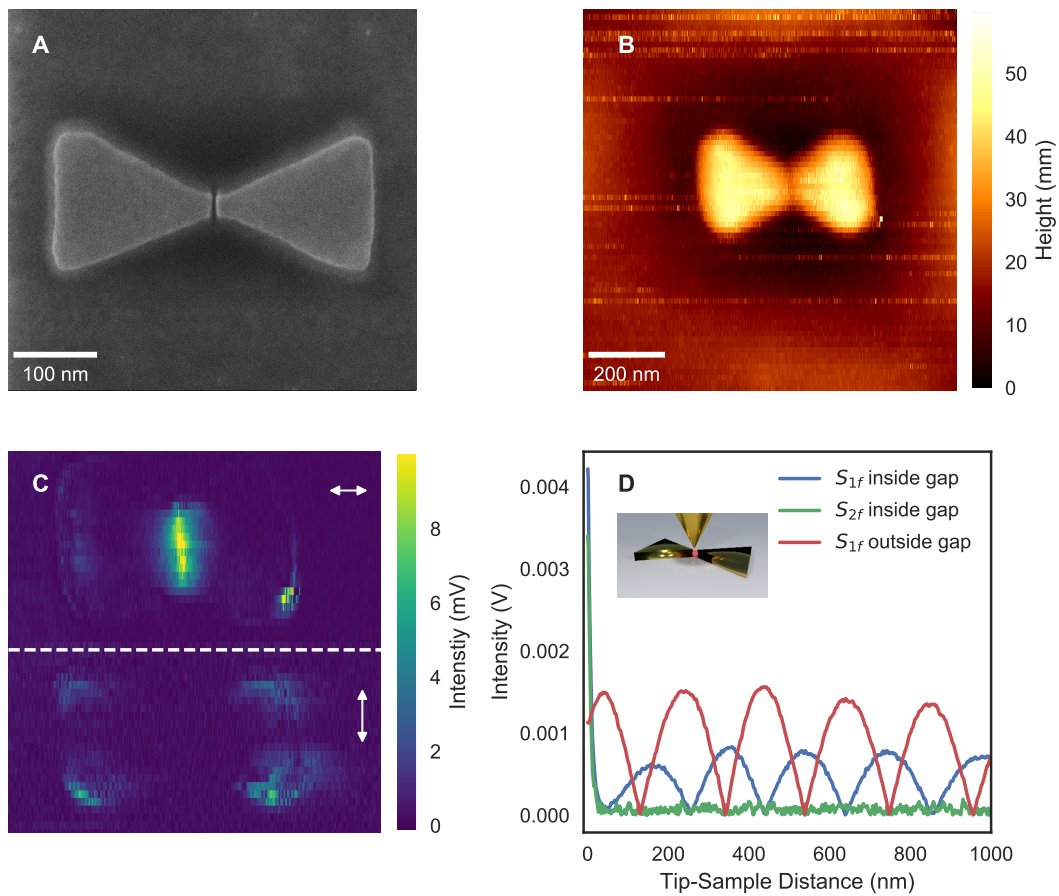


**Figure 5.2:** (A) Bowtie SEM image, (B) Bowtie AFM image (C) bowtie optical image for both parallel (top) and vertical (bottom) polarization, (D) approach curve inside and outside the gap including simulation results

As one example for such a structure I investigate nano antennas that are composed of a metal material like silver or gold placed on top of a glass or dielectric substrate. In the simplest case nano antennas consist of two parts that are brought close together spanning a gap of only a few nanometers. The antenna dimensions and the gap size define the resonance frequency and the near-field enhancement factor. The shape of these two parts can be different: Commonly studied

antennas are rod antennas consisting of two nano wires and bowtie antennas with two triangles facing each other. More complex antennas, like Yagi-Uda nano antennas, can be constructed as well and have been used because of their very good directivity [179], recently demonstrated by measuring the unidirectional emission of a single emitter coupled to a nanofabricated Yagi-Uda antenna [180]. The resulting quantum dot luminescence in that experiment was strongly polarized and highly directed into a narrow forward angular cone which could be tuned by the dimension of the antenna.

The general function of these nano antennas is similar to that of normal FM/AM antennas that we can find in our everyday life. In both cases an incoming wave interacts with the antenna and an outgoing field is emitted by the antenna. In the simplest case this is a Hertz dipole. Depending on the antenna shape this emission can be in a specified direction and an antenna gain can be achieved.

For optical antennas however there is one fundamental difference to wire antennas in the radio frequency (RF) range. In contrast to almost perfectly conducting wires in the RF range for infrared or optical frequencies the dielectric function of metals has a negative real part and a nonzero imaginary part. As a consequence localized plasmons form at the metal-dielectric interface with little penetration into the metal or the embedding dielectric media [181]. Due to the finite electron density this results in a delay between the driving field and the electronic response and consequently the electrons in the metal do not respond to the wavelength  $\lambda$  but to an effectively shorter wavelength  $\lambda_{eff}$  [182].

Finite Difference Time Domain (FDTD) simulations on nano antennas [179] as well as measurements [8] demonstrated very high near-field enhancement factors of up to a few hundreds of the amplitude of the emitted field with respect to the incoming field.

In the following we will have a look at the SNOM approach curve on a gold nano bowtie antenna of around 30 nm height. The antennas were produced by H. Kollmann by cutting the structure out of a gold film with a focused gallium ion beam. Then, a focused helium ion beam was used to produce the few-nanometer gap between the two antenna elements. Helium ions have a much smaller mass than gallium ions and have a smaller interaction volume [183], thus allowing for a considerable reduction of gap size and therefore increased near-field enhancement and polarization contrast [8].

Figure 5.2 shows a scanning electron microscopy (SEM) image and the AFM topography of the used bowtie antenna. A SNOM scan was recorded with p- and s-polarized light, indicated as the electric field direction by the white arrows in figure 5.2C. It can be seen that only with p-polarized light we excite the antenna resonant with a field enhancement inside the gap. With s-polarized light we excite another mode of the antenna, enhancing the intensity at the edges of the antenna. The enhancement of this mode is much weaker than that of the gap mode by using p-polarized light. This was expected as we have a high spatial confinement of the local plasmons in the gap in the sharp tip geometry and an electrodynamic coupling between the

two antenna parts [184].

Finally, figure 5.2D presents the approach curves in the antenna gap. Hereby, the blue curve shows the approach curve of the intensity signal demodulated at the modulation frequency ( $S_{1f}$ ), whereas the green curve shows the same measurement for a demodulation frequency of twice the modulation frequency ( $S_{2f}$ ). The red curve is a measurement of the  $S_{1f}$  signal outside the gap, but still on the antenna.

Clearly, outside the gap the  $S_{1f}$  signal is mainly determined by a distance-dependent sinusoidal interference pattern that can be attributed to the interference of the background field with the reference field. Inside the gap however, we can observe a strongly enhanced near-field for small distances in the  $S_{1f}$  signal, manifesting in a significant exponential increase. The short range exponential increase at small tip-sample distances can be attributed to the evanescent behavior of the near-field. At the same time we can still observe long-ranging background interference pattern. Demodulation at the second harmonic of the tip frequency already shows a nearly background-free approach curve in the gap. Outside the gap such an exponential decay with increasing distance is not clearly distinguishable at all, indicating a much lower near-field signal to background-field ratio.

The results nicely demonstrate the strong near-field enhancement properties of the antenna which make them very interesting for studying strong coupling behavior of coupled systems.

In the scope of this thesis however, the goal is to investigate and understand local spectra on a new dye material and to study these spectra on an area much larger than the gap size of the antenna. Hence, we have a sample on top of a non resonant substrate material. As we can easily conclude already from the measurement outside the antenna gap, for these kind of non resonant materials the near-field to background-field ratio has to be increased in order to extract useful near-field information. This could be done e.g. by higher harmonic demodulation and by enhancing the reflected field of the sample substrate.

As we will show in the following, an in-line interferometer is able to fulfill this task and will allow to measure near-field signals on various samples without being restricted to a high near-field from the sample itself.

## 5.2 Approach curve measurements

In the following we record signals  $S_{0f}$  to  $S_{4f}$  with the setup as described in chapter 3.1 as a function of the distance between tip and sample. To control the tip-sample distance the  $z$ -position of the sample is adjusted by the piezo stage. The approach is stopped when the tuning fork oscillation amplitude is reduced by 5%, which we take as the point of contact or zero distance. We record such approach curves for the three mentioned substrates, namely for a quartz surface covered with a semitransparent (20 nm thick) gold film, for an uncoated quartz

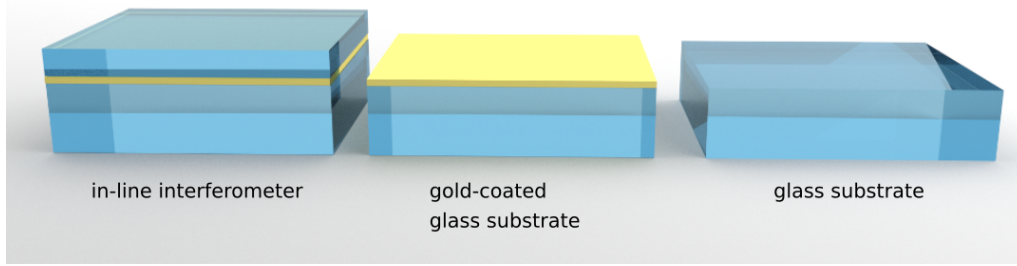


**Figure 5.3:** Visualization of the three substrates that were investigated: A quartz glass substrate, a gold coated quartz substrate and the in-line interferometer consisting of an additional glass layer on top of the gold coated quartz substrate.

surface, and for a quartz surface covered with a 200 nm thick  $\text{SiO}_2$  film on top of the 20 nm thick semitransparent gold film (cmp. figure 5.3).

Figures 5.4A and 5.4B show the optical signals when the sample with the semi-transparent gold film is approached to the tip. Upon approach, the unmodulated signal  $S_{0f}$ , which is measured using a standard silicon photodiode and without lock-in detection, displays a weak modulation with a period of  $\sim 390$  nm, corresponding to half the wavelength of the excitation laser (see the red fit curve of a sinusoidal function on top of a linear function, plotted together with the experimentally measured black curves in Fig. 5.4A). This modulation is a result of the interference of the light reflected from the tip shaft,  $\vec{E}_B$ , and from the gold-coated surface of the substrate facing the tip,  $\vec{E}_R$ . This modulation is weak, because the electric field strength of  $\vec{E}_B$  is only a small fraction of that of  $\vec{E}_R$ . Furthermore,  $\vec{E}_R$  decreases steadily as the reflecting gold surface is moved out of the laser focus, causing the constant slope underneath the modulation. As expected, a near-field contribution cannot be discerned in the DC optical signal.

The experiment is repeated with the APD and lock-in detector, and the demodulated signals  $S_{1f}$  to  $S_{4f}$  are recorded as a function of tip-sample distance. Figure 5.4B shows the amplitude of the lock-in-detector signal during the approach at the respective demodulation frequency, for the gold-coated sample. The optical signal demodulated at the fundamental tip modulation frequency,  $S_{1f}$  (blue curve in Fig. 5.4B), still shows a strong modulation for both samples, now at a period of a quarter wavelength due to plotting the amplitude of the lock-in signal. The optical signal demodulated at the second harmonic,  $S_{2f}$  (not shown in Fig. 5.4 for the sake of clarity), shows a similar behavior and has an amplitude comparable to that of  $S_{1f}$ . When demodulating at the third harmonic, however,  $S_{3f}$  (green curve) still shows some modulation, but the amplitude is reduced by roughly a factor 4. Finally, demodulating at the fourth harmonic (red curve), the amplitude of  $S_{4f}$  is not above noise level.

In close vicinity to the gold surface (compare the steep decrease of the tuning fork amplitude, i. e., the black curve in the inset in Fig. 5.4B), a weak deviation from the sinusoidal curve by less than 15% is discernible on the first-harmonic optical signal  $S_{1f}$ , and there is a clear near-field

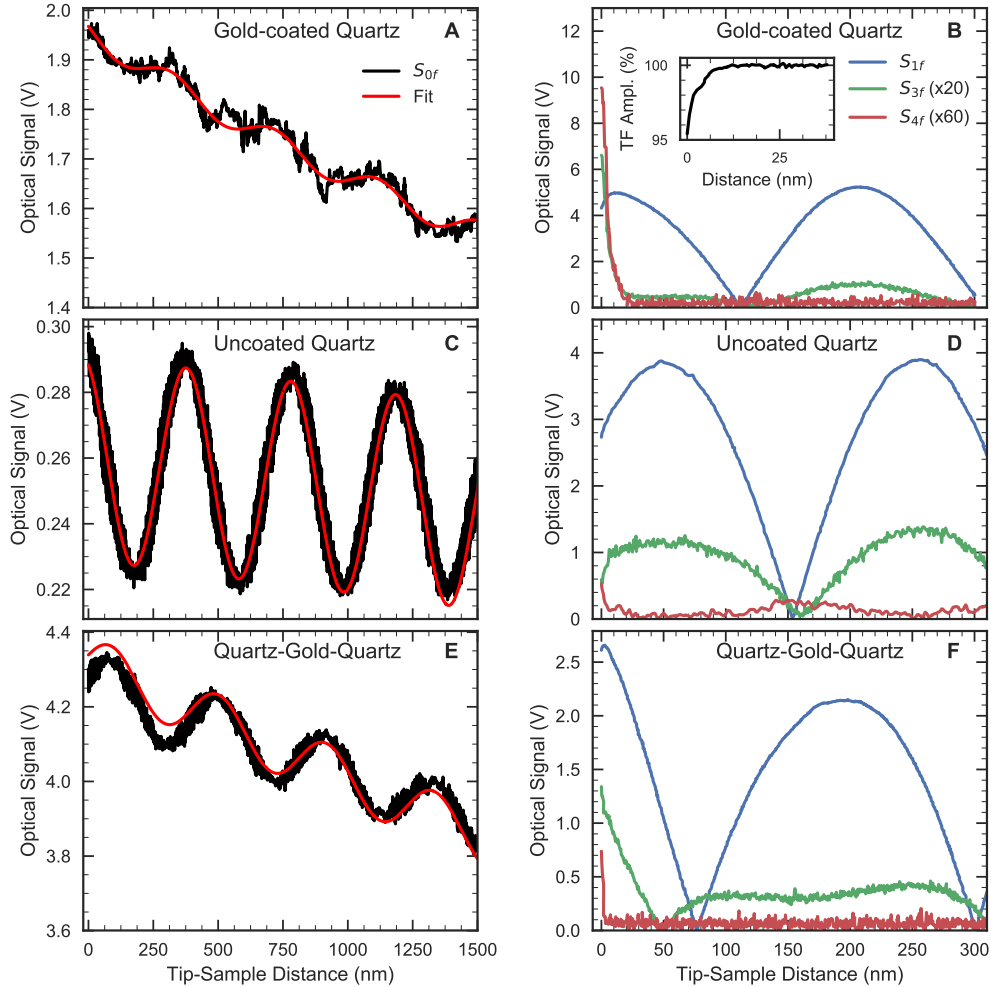


**Figure 5.4:** The measured optical signals  $S_{0f}$  plotted together with a sinusoidal fit (black and curves in the left hand graphs) and  $S_{1f}$ ,  $S_{3f}$ , and  $S_{4f}$  (blue, green and red curves, respectively, in the right hand graphs) recorded during the approach of the three different substrates towards the gold nanotip. **A, B:** Approach of a gold-coated quartz microscope slide to the nanotip. **A**, The DC signal  $S_{0f}$  is weakly modulated and **B**, there is a strong near-field signal when the gold surface is in close proximity to the tip. The inset shows the tuning fork amplitude; the point of contact is defined as the position when the tuning fork amplitude is decreased by 5%. **C, D:** Approach of an uncoated quartz substrate to the nanotip. **C**, The DC signal is strongly modulated, and **D**, the near-field signal is very weak on the glass surface. **E, F:** Approach of the in-line interferometer to the gold tip, i. e., a quartz surface covered with a  $\sim 200$  nm thick  $\text{SiO}_2$  film on top of the  $\sim 20$  nm thick semitransparent gold film. **E**, The DC signal is moderately modulated, and **F**, when bringing the glass surface in close proximity to the tip, a near-field contribution is clearly visible. The in-line interferometer enables homodyne measurement of a weak near-field signal, such as on a glass surface in vicinity to a gold nanotip.

contribution apparent of both  $S_{3f}$  and  $S_{4f}$ . The near-field signal resembles a strong exponential signal increase with a  $1/e$ -decay length of 8 nm. On the fourth-harmonic optical signal,  $S_{4f}$ , this near-field signal strength is more than 20 times above the noise level. Such a near-field enhancement is similar to what has been observed in earlier work and what is expected from the interaction of a gold tip and a gold surface [50, 151]

For comparison, the measurements of the optical signals  $S_{0f}$  and  $S_{1f} - S_{4f}$  are repeated with the uncoated quartz substrate and are shown in Figs. 5.4C and 5.4D, respectively. The DC signal  $S_{0f}$  for the uncoated quartz microscope slide is much stronger modulated than in the case of the gold-coated sample (Fig. 5.4C), showing that the interfering fields reflected from the tip shaft and from the quartz surface are well balanced. There is no near-field contribution to  $S_{0f}$  discernible in Fig. 5.4C. Even when demodulating the photodiode signal, the effect when approaching the uncoated sample to the gold tip is weak:  $S_{1f}$  does not display any deviation from the behavior far from contact (blue curve in Fig. 5.4D). The signal  $S_{3f}$  shows a small roll-off near contact, of less than one third of its maximum amplitude, and  $S_{4f}$  simultaneously displays an increase of slightly less than its signal amplitude out of contact (green and red curves in Fig. 5.4D). Thus, there is evidence of a near-field signal when demodulating at the third or fourth harmonic, but it seems still overrun by background signal ( $S_{3f}$ ) or is on the order of the background signal ( $S_{4f}$ ).

Finally, we turn to the optical signals measured when approaching the in-line interferometer, i. e., a quartz substrate coated with a 20 nm thick gold film and a 200 nm thick  $\text{SiO}_2$  film on top of the gold film, to the gold nanotip. The modulation depth of the DC signal  $S_{0f}$  is in between that of the gold-coated and the uncoated sample (Fig. 5.4E), indicating a lower reflectivity of the in-line interferometer gold film than that of the gold-coated substrate. However, the modulation is clearly sufficiently strong to facilitate using  $\vec{E}_R$  as a reference field in our in-line interferometer homodyne scheme. This can be seen more clearly in the approach curves shown in Fig. 5.4F: There is a near-field contribution discernible in all three signals  $S_{1f}$ ,  $S_{3f}$ , and  $S_{4f}$ . The near-field increase is less pronounced than in the case that the tip is directly in contact with the gold film; the fourth-harmonic signal  $S_{4f}$  shows an increase of 7 times the noise level (compared to 20 times observed for the gold film). Considering that the near field signal that is measured when the gold tip is in contact with a glass surface (Fig. 5.4D) is just on the order of the noise level, we conclude that the enhancement by a factor 7 is due to interference of the near field  $\vec{E}_{\text{NF}}$  and the field reflected from the semi-transparent gold film,  $\vec{E}_R$ .

Thus, on the one hand the multi-layer structure of the in-line interferometer indeed seems to enable the measurement of rather small near-field contributions, which can hardly be detected otherwise. On the other hand, the measured signals are a result of mixing on the field level, and knowledge of the electric field strengths of  $\vec{E}_R$  and  $\vec{E}_B$  is required in order to determine the actual near-field strength.

In the next section we derive expressions that allow disentangling the contributions of the fields

to each of the measured signals  $S_{0f}$  to  $S_{4f}$ .

### 5.3 Near-field and Background Analysis

In the following we want to derive an analytical derivation of the optical signals measured after lock-in demodulation up to the 4th order of the tip frequency for a sSNOM setup using homodyne detection as used in later experiments. The goal is to provide a tool to disentangle the measured signals and allow for a separate analysis of near-field and background field contribution. For that task we consider the interference of three fields that are present in each SNOM measurement. These fields are labeled the near-field  $\vec{E}_{\text{NF}}$ , the background field  $\vec{E}_{\text{B}}$  and the reference field  $\vec{E}_{\text{R}}$ . Figure 5.5 shows a graphical depiction of the sample, the tip and the origin of the three interfering fields. Here, a gold tip is positioned close to the surface of a sample that can consist of multiple layers. The plane wave incident field  $\vec{E}_{\text{in}}$  is focused and propagates in a direction parallel to the tip axis. The reference field  $\vec{E}_{\text{R}}$  is the part of the incident field that is reflected before it reaches the tip. The background field is considered as a field that is reflected at the tip shaft at some distance  $d$  from the apex since the diameter of the focused incident light is much bigger than the tip apex diameter. The near-field originates at the apex of the nanotip at small distances and is in most cases very weak compared to the other fields.

In all our following analysis we can restrict our considerations to temporal variations of the order of the tip modulation period since the integration time for the optical signals is much longer than the inverse of the light carrier frequency and the pulse repetition frequency. Furthermore the detector is placed at a distance of several tens of cm from the light-sample-interaction region. This allows us to restrict the electric fields to quasi-monochromatic and quasi-static plane waves. Lateral variations of the electric field strength are neglected. Also, in this field analysis we focus on monochromatic waves, an extension to simulate a broad-band spectrum is done later, simply by evaluating the equations for each wavelength.

We begin with the expression for the reference field  $\vec{E}_{\text{R}}$ . As this field does not depend on the tip-sample distance  $z$  we can chose the reference phase  $\phi_{\text{R}} = 0$  and  $\vec{E}_{\text{R}}$  becomes a constant:

$$\vec{E}_{\text{R}}(z) = \vec{E}_{\text{R}} = \text{const.} \quad (5.1)$$

In contrast to  $\vec{E}_{\text{R}}$ , the background field  $\vec{E}_{\text{B}}$  is dependent on the tip-sample distance.  $\vec{E}_{\text{B}}$  originates from the large focus diameter in comparison to the few nanometer sized tip apex. The field is scattered from the tip shaft at a distance  $d'$  to the tip apex. Consequently the pathway of  $\vec{E}_{\text{B}}$  is longer by twice the tip-sample distance plus a constant distance  $d$  which includes both the distance  $d'$  to the scattering region and the thickness of an (optional) glass layer on top of the high reflective layer that reflects  $\vec{E}_{\text{R}}$  (compare chapter ). Thus,  $\vec{E}_{\text{B}}$  acquires a phase shift

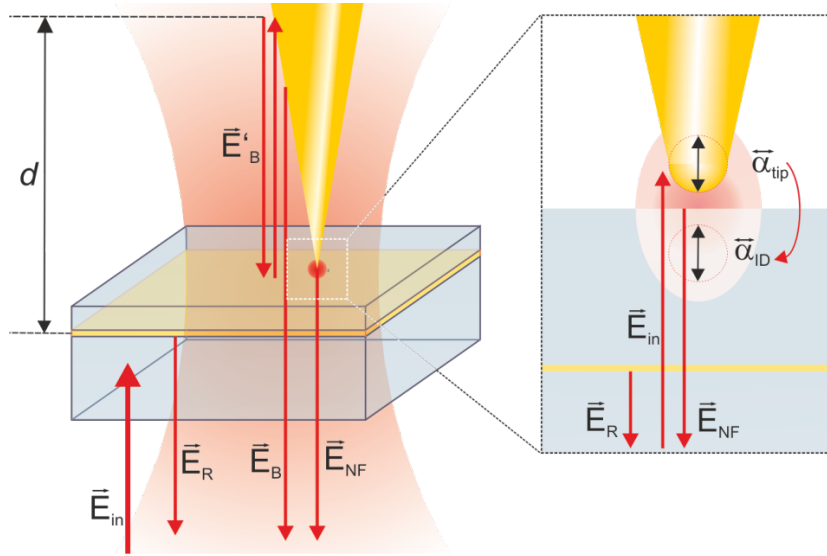


**Figure 5.5:** Graphical depiction of the sample, the origin of the interacting fields, and the tip-sample interaction region. The incident light field  $\vec{E}_{in}$  illuminates sample and tip in a diffraction-limited spot. A part  $\vec{E}_R$  is reflected off the semitransparent gold film, and a part  $\vec{E}_B$  is scattered back from the shaft of the gold tip, possibly after multiple reflections ( $\vec{E}'_B$ ). The inset on the right depicts the enhancement of the tip dipole with polarizability  $\vec{\alpha}_{tip}$  by its image dipole. The electric field radiated from the tip dipole and propagating back towards the illuminating microscope objective is the origin of the near-field contribution  $\vec{E}_{NF}$ .

with respect to the reference field and can be written as

$$\vec{E}_B(z) = \vec{E}_{B,0} \cdot e^{2ik(z+d)+\phi_B} \quad (5.2)$$

with an additional phase shift  $\phi_B$  due to the reflection.

Moreover, multiple reflections between the layer and the tip can occur. The number of reflections that alter the resulting optical signal depends on the reflectivity of the most reflective layer in the multilayer system close to the tip. By comparison with experimental data we found that even for a gold layer with 30-50% reflectivity one additional reflection is sufficient to describe the measurement. Equation (5.2) therefore has to be modified to

$$\vec{E}'_{B,0}(z) = \vec{E}_{B,0} \cdot \left( e^{2ik(z+d)+\phi_{B1}} + r \cdot e^{4ik(z+d)+\phi_{B2}} \right) \quad (5.3)$$

with a parameter  $r$  that combines the reflection coefficient of the tip shaft and the reflective layer. An additional factor two in the exponent of the second term accounts for the doubled path difference between the reflective layer and the origin of the background scattering.

However, for simplicity we will use equation (5.2) in the following notation. The additional reflection will be included at a later point.

Finally, the near-field  $\vec{E}_{\text{NF}}$  holds the desired information about the sample properties and is therefore the desired quantity, however its amplitude is mostly the smallest of all the three considered fields. As already discussed in chapter 4.2.3 we use a description of the near-field in a framework of the coupled tip dipole with a sample image dipole. This means the electric fields at the tip apex are enhanced because of the image dipole induced in the sample that is acting back on the tip:

$$\vec{p}_{\text{tip}} = \overset{\leftrightarrow}{\alpha}_{\text{tip}} \left( \vec{E}_{\text{in}} + \vec{E}_{\text{ID}} \right) \quad (5.4)$$

The electric field by the enhanced tip dipole radiated out into the far field is described by the dyadic Green's function  $\overset{\leftrightarrow}{G}_{\text{out}}$ :

$$\vec{E}_{\text{out}}(\vec{r}) = \overset{\leftrightarrow}{G}_{\text{out}}(\vec{r}, \vec{r}') \vec{p}_{\text{tip}} = \overset{\leftrightarrow}{G}_{\text{out}}(\vec{r}, \vec{r}') \overset{\leftrightarrow}{\alpha}_{\text{tip}} \left( \vec{E}_{\text{in}} + \vec{E}_{\text{ID}} \right) \quad (5.5)$$

In the case of strong coupling of the incident field and the excited dipoles, potentially more than two consecutive scattering events have to be considered in a similar fashion as described above. Here, a self-consistent model can be applied to yield an effective polarizability [15]. In our experimental scheme, however, the tip dipole moment is dominant over the image dipole in the sample, and the main contribution to fields radiated out of the tip-sample interaction region stems from the tip dipole enhanced by the image dipole. We treat the conical tip as a small metal sphere with radius  $R$  and with the polarizability  $\alpha_{\text{tip}} = 4\pi R^3 (\varepsilon_{\text{tip}} - 1) (\varepsilon_{\text{tip}} + 2)^{-1}$ , where  $\varepsilon_{\text{tip}}$  is the complex dielectric constant of the tip material [15]. In this case, Eq. (5.5) is sufficient to describe the radiated field. This radiated field  $\vec{E}_{\text{out}}(\vec{r})$  consists of two terms; the first,  $\overset{\leftrightarrow}{G}_{\text{out}}(\vec{r}, \vec{r}') \overset{\leftrightarrow}{\alpha}_{\text{tip}} \vec{E}_{\text{in}}$  results in a constant field contribution due to the tip dipole alone. As the tip-sample distance is changed, the amplitude of this first term does not change, but the phase changes with respect to the background field in the same fashion as was found before for the background field  $\vec{E}_B(z)$ . Hence this first term can simply be considered a contribution to the background field. The second term  $\overset{\leftrightarrow}{G}_{\text{out}}(\vec{r}, \vec{r}') \overset{\leftrightarrow}{\alpha}_{\text{tip}} \vec{E}_{\text{ID}}$ , in contrast, depends strongly on the tip-sample distance and approaches zero for large  $z$ . If Eq. (5.5) was evaluated for the position  $\vec{r}_{\text{Det}}$  given by the cross section of beam path and detector plane, and the constant first term was subtracted, the resulting field would yield the near-field contribution to the measured signal, i. e.,

$$\vec{E}_{\text{NF}} = \vec{E}_{\text{out}}(\vec{r}_{\text{Det}}) - \overset{\leftrightarrow}{G}_{\text{out}}(\vec{r}_{\text{Det}}, \vec{r}') \overset{\leftrightarrow}{\alpha}_{\text{tip}} \vec{E}_{\text{in}}. \quad (5.6)$$

Due to the strong distance-dependence of the dipole-dipole coupling, the near field intensity measured in the detector plane decreases exponentially with increasing tip-sample distance,

and a phase shift  $\varphi_{\text{NF}}$  due to the dipole-dipole coupling is taken into account:

$$\vec{E}_{\text{NF}}(z) = \vec{E}_{\text{NF},0} \cdot e^{-\frac{z}{z_0}} \cdot e^{i\varphi_{\text{NF}}} \quad (5.7)$$

Here  $z_0$  is the near-field decay length, which depends on the tip radius of curvature and lies typically in the range of 5 to 10 nm.

The latter two fields,  $\vec{E}_B$  and  $\vec{E}_{\text{NF}}$  are varying as a function of the tip-sample distance  $z$ , which itself is a periodic function with period  $T$ :  $z = z(t) = z(t + T)$ , where  $T = f^{-1} = 2\pi\Omega^{-1}$  is the inverse of the tip modulation frequency. The distance can be written as a sinusoidal function with the modulation amplitude  $M$ , centered at the average tip-sample distance  $\bar{z}$ :

$$z(t) = \bar{z} + M \cdot \cos(\Omega t). \quad (5.8)$$

Thus also  $\vec{E}_B$  and  $\vec{E}_{\text{NF}}$  are temporally periodic functions with the same period  $T$ :

$$\vec{E}_B(z) = \vec{E}_B(\bar{z}, t) = \vec{E}_{B,0} \cdot e^{i2k(\bar{z}+d)+i\varphi_B} \cdot e^{i2kM \cos(\Omega t)} \quad (5.9)$$

$$\vec{E}_{\text{NF}}(z) = \vec{E}_{\text{NF}}(\bar{z}, t) = \vec{E}_{\text{NF},0} \cdot e^{i\varphi_{\text{NF}}} \cdot e^{\frac{-\bar{z}}{z_0}} \cdot e^{\frac{-M}{z_0} \cos(\Omega t)} \quad (5.10)$$

To simplify the comparison with the experimental signals, which are measured at different harmonics of  $f$ , we approximate the explicitly time-dependent factors of these two fields by Fourier sums, following the idea of previous works [15]:

$$\vec{E}_B(\bar{z}, t) \approx \vec{E}_{B,0} \cdot e^{i2k(\bar{z}+d)+i\varphi_B} \cdot \sum_{n=-\infty}^{\infty} b^{(n)} \cdot e^{in\Omega t} \quad (5.11)$$

$$\vec{E}_{\text{NF}}(\bar{z}, t) \approx \vec{E}_{\text{NF},0} \cdot e^{i\varphi_{\text{NF}}} \cdot e^{\frac{-\bar{z}}{z_0}} \cdot \sum_{n=-\infty}^{\infty} c^{(n)} \cdot e^{in\Omega t} \quad (5.12)$$

Here we have introduced the complex Fourier coefficients  $b^{(n)}$  and  $c^{(n)}$  of the background field  $\vec{E}_B$  and the near field  $\vec{E}_{\text{NF}}$ , respectively, where  $n$  is the harmonic order of the tip modulation frequency. The Fourier coefficients can be easily calculated:

$$b^{(n)} = \frac{1}{T} \int_0^T e^{i2kM \cos(\Omega t)} \cdot e^{-in\Omega t} dt = (i)^n \cdot J_n(2kM) \quad (5.13)$$

$$c^{(n)} = \frac{1}{T} \int_0^T e^{\frac{-M}{z_0} \cos(\Omega t)} \cdot e^{-in\Omega t} dt = (-1)^n \cdot I_n\left(\frac{M}{z_0}\right) \quad (5.14)$$

The Fourier coefficients for the background field are given by Bessel functions of the first kind and of order  $n$ ,  $J_n$ . The Fourier coefficients  $b^{(n)}$  of even order are real values, while those of odd orders are imaginary. This means that the phase of the background field shifts with each modulation order, which causes the distance dependent interference pattern to alternate

between cosine and sine functions. The Fourier coefficients of the near field are modified Bessel functions of the first kind and of order  $n$ ,  $I_n$ , and are all real.

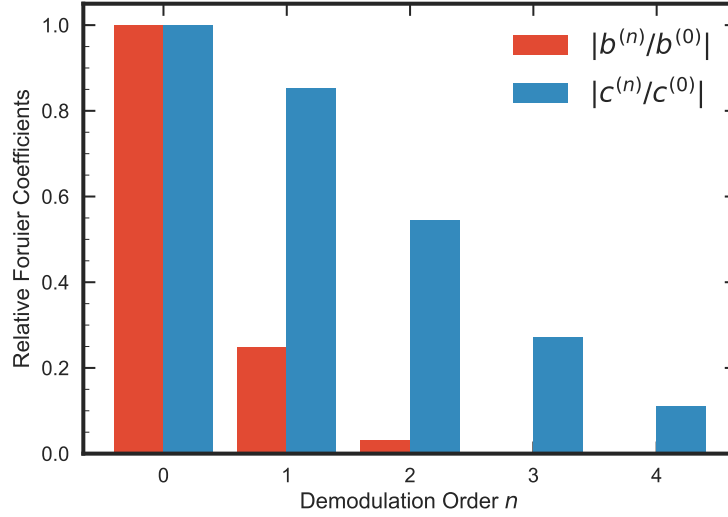


**Figure 5.6:** Relative amplitude of the Fourier coefficients  $b^{(0)}$  to  $b^{(4)}$  (red bars) and  $c^{(0)}$  to  $c^{(4)}$  (blue bars) normalized to  $b^{(0)}$  and  $c^{(0)}$ , respectively, as a function of demodulation order  $n$ . The amplitude of both decreases with demodulation order, but the background-field coefficients  $b^{(n)}$  decreases much more rapidly than the near-field coefficients  $c^{(n)}$ .

Figure 5.6 shows the absolute of the Fourier coefficients for our experimental parameters as a function of demodulation order  $n$  in a bar diagram. The red bars are the background-field coefficients normalized to the zeroth order coefficient, i. e.,  $|b^{(n)}/b^{(0)}|$ , and the blue bars the according near-field coefficients  $|c^{(n)}/c^{(0)}|$ . It is noteworthy that not only do both coefficients decrease with demodulation order, but that the relative strength of the background decreases much more rapidly than that of the near field. This is in agreement with the measurements presented in Fig. 5.4, where the near-field contribution becomes more clearly visible as the demodulation order increases, as well as with observations in earlier works. The increase of the near-field-to-background-ratio with demodulation order forms the basis for higher-order demodulation SNOM [50, 151].

Any signal that is measured in the detector plane is proportional to the absolute square of the total field  $\vec{E}_{\text{total}}(\vec{z}, t) = \vec{E}_R + \vec{E}_B(\vec{z}, t) + \vec{E}_{\text{NF}}(\vec{z}, t)$ . Inserting Eqs. (5.1), (5.11) and (5.12) and executing the absolute square gives

$$\begin{aligned}
 \left| \vec{E}_{\text{total}}(\vec{z}, t) \right|^2 &= \left| \vec{E}_R + \vec{E}_B(\vec{z}, t) + \vec{E}_{\text{NF}}(\vec{z}, t) \right|^2 \\
 &= \left| \vec{E}_R + \vec{E}_{B,0} e^{i2k(\vec{z}+d)+i\varphi_B} \cdot \sum_{n=-\infty}^{\infty} b^{(n)} e^{in\Omega t} + \vec{E}_{\text{NF},0} e^{i\varphi_{\text{NF}}} e^{\frac{-\vec{z}}{z_0}} \cdot \sum_{n=-\infty}^{\infty} c^{(n)} e^{in\Omega t} \right|^2
 \end{aligned} \tag{5.15}$$

$$\begin{aligned}
\left| \vec{E}_{\text{total}}(\bar{z}) \right|^2 &= \left| \vec{E}_R \right|^2 + \left( \vec{E}_R^* \vec{E}_{B,0} e^{i2k(\bar{z}+d)+i\varphi_B} \cdot \sum_{n=-\infty}^{\infty} b^{(n)} e^{in\Omega t} + c.c. \right) \\
&+ \left( \vec{E}_R^* \vec{E}_{\text{NF},0} e^{i\varphi_{\text{NF}}} e^{\frac{-2\bar{z}}{z_0}} \cdot \sum_{n=-\infty}^{\infty} c^{(n)} e^{in\Omega t} + c.c. \right) \\
&+ \left| \vec{E}_{B,0} \right|^2 \sum_{n=-\infty}^{\infty} \sum_{m=-\infty}^{\infty} b^{(n)} b^{(m)*} e^{i(n-m)\Omega t} \\
&+ \left| \vec{E}_{\text{NF},0} \right|^2 e^{\frac{-2\bar{z}}{z_0}} \sum_{n=-\infty}^{\infty} \sum_{m=-\infty}^{\infty} c^{(n)} c^{(m)*} e^{i(n-m)\Omega t} \\
&+ \left( \vec{E}_{B,0} \vec{E}_{\text{NF},0}^* e^{i(2k(\bar{z}+d)+\varphi_B-\varphi_{\text{NF}})} e^{\frac{-2\bar{z}}{z_0}} \sum_{n=-\infty}^{\infty} \sum_{m=-\infty}^{\infty} b^{(n)} c^{(m)*} e^{i(n-m)\Omega t} + c.c. \right)
\end{aligned} \tag{5.16}$$

where *c.c.* denotes the complex conjugate.

The power impinging on the photodiode is

$$P(z, t) = \frac{1}{2} \varepsilon_0 c A \cdot \left| \vec{E}_{\text{total}} \right|^2 \tag{5.17}$$

where  $\varepsilon_0$  is the electric field constant of the vacuum,  $c$  is the velocity of light, and  $A$  is the area of the detector. Multiplication with the detector efficiency  $\eta$  yields the output voltage  $U(\bar{z}, t) = \eta \cdot P(\bar{z}, t)$ . The unmodulated signal  $S_{0f}$ , which is measured using the photodiode without lock-in detection, is in fact the lowest order Fourier component of this voltage, which is a function only of the tip-sample distance and not of time:

$$S_{0f}(\bar{z}) = U^{(0)}(\bar{z}) = \eta \cdot P^{(0)}(\bar{z}) \tag{5.18}$$

In other words,  $S_{0f}$  is the mean value over the measurement. For the first and higher-order demodulated signals, the lock-in output signal can be written as:

$$S_{\text{nf}}(\bar{z}) = \gamma \frac{1}{T} \int_{t'-T}^{t'} \cos[n\Omega t + \theta] \cdot U(\bar{z}, t) dt, |n| \geq 1 \tag{5.19}$$

Here, the index *nf* denotes the demodulation frequency,  $\gamma$  is the gain parameter of the lock-in detector, and  $\theta$  is the phase between modulation waveform and detected signal. When measuring  $S_{\text{nf}}(\bar{z})$  with the lock-in detector, the influence of this phase is eliminated by actually recording the amplitude, i. e., the geometrical average of  $S_{\text{nf}}(\bar{z}, \theta_1)$  measured for one phase setting  $\theta_1$  and  $S_{\text{nf}}(\bar{z}, \theta_2)$  measured for a second phase setting  $\theta_2 = \theta_1 + \frac{\pi}{2}$ . In our calculations the same effect is achieved easily by evaluating the integral of Eq. (5.19) for  $\theta = 0$ . The integral,

performed over time intervals  $T \gg 2\pi\Omega^{-1}$ , is zero unless the demodulation frequency matches the angular frequency  $n\Omega$  of the Fourier component under consideration.

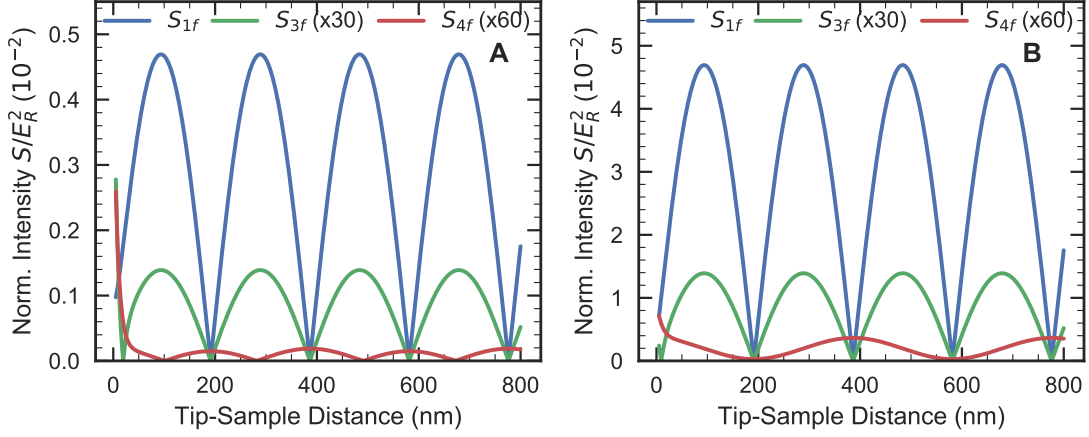


**Figure 5.7:** Simulated approach curve detector signal at 1st, 3rd and 4th harmonic ( $S_{1f}, S_{3f}, S_{4f}$ ) following equation (5.22)-(5.25) for (A) a ratio  $ER:EB=50$  and (B) a ratio  $ER:EB=5$ . The remaining variables are the same for both figures, namely the ratio  $ER:ENF=1000$ , the wavelength  $\lambda = 780$  nm, the near-field decay length  $z_0 = 8$  nm, a modulation amplitude  $M = 30$  nm and the phase terms  $\phi_B = -0.3$  and  $\phi_{NF} = 1.5$ .

The respective combinations of  $\vec{E}_R$ ,  $\vec{E}_{B,0}b^{(n)}$ , and  $\vec{E}_{NF,0}c^{(n)}$  that contribute to the measured signals  $S_{nf}$  can easily be extracted from the expression for  $|\vec{E}_{total}|^2$  given in Eq. (5.15). Because the highest order demodulation that can be measured with our 210 kHz line camera is the fourth order, we consider only Fourier coefficients up to this order, i. e., we restrict the sums in Eq. (5.17) to  $-4 \leq n, m \leq 4$ . The unmodulated signal then becomes:

$$\begin{aligned}
 S_{0f}(\bar{z}) \approx \frac{1}{4}\eta\epsilon_0cA \cdot & \left[ |\vec{E}_R|^2 + |\vec{E}_{B,0}|^2 \sum_{n=-4}^4 b^{(n)}b^{(n)*} + |\vec{E}_{NF,0}|^2 e^{\frac{-2\bar{z}}{z_0}} \sum_{n=-4}^4 c^{(n)}c^{(n)*} \right. \\
 & + 2Re \left\{ \vec{E}_R \vec{E}_{B,0} b^{(0)} \right\} \cos(2k(\bar{z} + d) + \varphi_B) + 2Re \left\{ \vec{E}_R \vec{E}_{NF,0} c^{(0)} \right\} e^{\frac{-\bar{z}}{z_0}} \cos(\varphi_{NF}) \\
 & \left. + \left( \vec{E}_{B,0} \vec{E}_{NF,0}^* e^{i(2k(\bar{z}+d)+\varphi_B-\varphi_{NF})} e^{\frac{-\bar{z}}{z_0}} \sum_{n=-4}^4 b^{(n)}c^{(n)*} + c.c. \right) \right] \quad (5.20)
 \end{aligned}$$

In the DC signal  $S_{0f}$  the directly reflected fields  $\vec{E}_R$  and  $\vec{E}_B$  have field strengths several orders of magnitude higher than the near field contribution:  $|\vec{E}_{NF,0,j}| \ll |\vec{E}_{R,j}|, |\vec{E}_{B,0,j}|$  for all  $n$  and for each vector component  $j = x, y, z$  individually. Furthermore, the calculation of the Fourier coefficients showed that the background contribution decreases rapidly with increasing demodulation order, such that  $|\vec{E}_{B,0,j}b^{(n)}| \ll |\vec{E}_{R,j}|, |\vec{E}_{B,0,j}b^{(0)}|$  for  $|n| > 0$ . With these

assumptions Eq. (5.20) can be simplified:

$$S_{0f}(\bar{z}) \approx \frac{1}{4}\eta\varepsilon_0cA \cdot \left[ \left| \vec{E}_R \right|^2 + \left| \vec{E}_{B,0}b^{(0)} \right|^2 + 2\vec{E}_R\vec{E}_{B,0}b^{(0)} \cos(2k(\bar{z} + d) + \varphi_B) \right] \quad (5.21)$$

Eq. (5.21) describe the interference of two fields with a phase varying as the distance between tip and sample increases, and with a contrast given by the respective field strengths of background and reference field.

Similarly, the signals measured at the first and higher harmonic demodulation frequencies,  $S_{1f}$  to  $S_{4f}$ , can be extracted from Eq. (5.15). After applying the same approximations as enumerated above for the example of  $S_{0f}$ , the less dominant terms are neglected, and we obtain the following four approximated expressions for  $S_{1f}$  to  $S_{4f}$ :

$$\begin{aligned} S_{1f}(\bar{z}) \approx \gamma\nu\varepsilon_0cA \cdot & \left| -\operatorname{Re} \left\{ \vec{E}_R\vec{E}_{B,0} \right\} \left| b^{(1)} \right| \sin(2k(\bar{z} + d) + \varphi_B) \right. \\ & - \operatorname{Re} \left\{ \vec{E}_R\vec{E}_{\text{NF},0} \right\} \left| c^{(1)} \right| e^{\frac{-\bar{z}}{z_0}} \cos \varphi_{\text{NF}} \\ & \left. - \operatorname{Re} \left\{ \vec{E}_{B,0}\vec{E}_{\text{NF},0} \right\} \left| b^{(0)} \right| \left| c^{(1)} \right| \cdot e^{\frac{-\bar{z}}{z_0}} \cos(2k(\bar{z} + d) + \varphi_B - \varphi_{\text{NF}}) \right| \end{aligned} \quad (5.22)$$

$$\begin{aligned} S_{2f}(\bar{z}) \approx \gamma\nu\varepsilon_0cA \cdot & \left| -\operatorname{Re} \left\{ \vec{E}_R\vec{E}_{B,0} \right\} \left| b^{(2)} \right| \cos(2k(\bar{z} + d) + \varphi_B) \right. \\ & + \operatorname{Re} \left\{ \vec{E}_R\vec{E}_{\text{NF},0} \right\} \left| c^{(2)} \right| e^{\frac{-\bar{z}}{z_0}} \cos \varphi_{\text{NF}} - \left| \vec{E}_{B,0} \right|^2 \left| b^{(0)} \right| \left| b^{(2)} \right| \\ & \left. + \operatorname{Re} \left\{ \vec{E}_{B,0}\vec{E}_{\text{NF},0} \right\} \left| b^{(0)} \right| \left| c^{(2)} \right| \cdot e^{\frac{-\bar{z}}{z_0}} \cos(2k(\bar{z} + d) + \varphi_B - \varphi_{\text{NF}}) \right| \end{aligned} \quad (5.23)$$

$$\begin{aligned} S_{3f}(\bar{z}) \approx \gamma\nu\varepsilon_0cA \cdot & \left| \operatorname{Re} \left\{ \vec{E}_R\vec{E}_{B,0} \right\} \left| b^{(3)} \right| \sin(2k(\bar{z} + d) + \varphi_B) \right. \\ & - \operatorname{Re} \left\{ \vec{E}_R\vec{E}_{\text{NF},0} \right\} \left| c^{(3)} \right| e^{\frac{-\bar{z}}{z_0}} \cos \varphi_{\text{NF}} \\ & \left. - \operatorname{Re} \left\{ \vec{E}_{B,0}\vec{E}_{\text{NF},0} \right\} \left| b^{(0)} \right| \left| c^{(3)} \right| \cdot e^{\frac{-\bar{z}}{z_0}} \cos(2k(\bar{z} + d) + \varphi_B - \varphi_{\text{NF}}) \right| \end{aligned} \quad (5.24)$$

$$\begin{aligned} S_{4f}(\bar{z}) \approx \gamma\nu\varepsilon_0cA \cdot & \left| \operatorname{Re} \left\{ \vec{E}_R\vec{E}_{B,0} \right\} \left| b^{(4)} \right| \cos(2k(\bar{z} + d) + \varphi_B) \right. \\ & + \operatorname{Re} \left\{ \vec{E}_R\vec{E}_{\text{NF},0} \right\} \left| c^{(4)} \right| e^{\frac{-\bar{z}}{z_0}} \cos \varphi_{\text{NF}} + \left| \vec{E}_{B,0} \right|^2 \left| b^{(2)} \right|^2 \\ & \left. + \operatorname{Re} \left\{ \vec{E}_{B,0}\vec{E}_{\text{NF},0} \right\} \left| b^{(0)} \right| \left| c^{(4)} \right| \cdot e^{\frac{-\bar{z}}{z_0}} \cos(2k(\bar{z} + d) + \varphi_B - \varphi_{\text{NF}}) \right| \end{aligned} \quad (5.25)$$

The relevant Eqs. (5.21)-(5.25) describe the signal detection after the interference of vectorial fields. They are simplified to terms of products of two fields each, with only the three field amplitudes and phases and the near-field decay length as input parameters. Typically, not all three vector components contribute with comparable strengths, such that a full vectorial

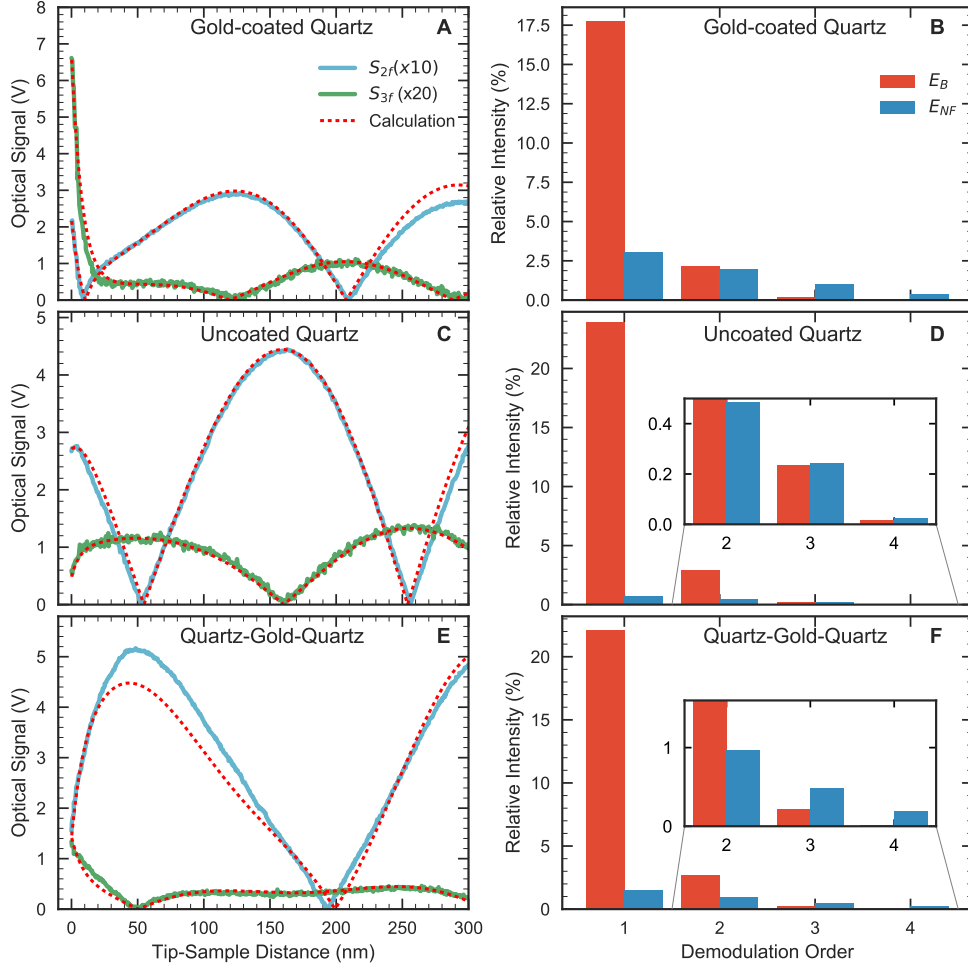
treatment is not required. In our experiment, the incident light is linearly polarized in the plane parallel to the table, corresponding to the  $y$ -direction given in Fig. 3.1. The reference field  $\vec{E}_R$  consists of light directly reflected from the semi-transparent gold film or from the uncoated surface of the substrate, which in both cases results in a purely  $y$ -polarized reference field. The background field  $\vec{E}_B$ , which is reflected off the cone-shaped surface of the gold tip, is expected to be mainly polarized along the  $y$ -direction, but to carry also a weak  $x$ -component. The near field  $\vec{E}_{NF}$  is constituted of light that is scattered out of the near-field interaction region of sample and tip into the detected far field, as described above (Eqs. (5.4) and (5.5)). Earlier measurements have shown that this light is radially polarized with a high degree of polarization [94]. In the in-line homodyne detection scheme that is employed here, however, the near field contribution is only detected by mixing with the  $y$ -polarized reference field or with the mainly  $y$ -polarized background field, which restricts the near-field detection to its  $y$ -component. For this reason, a scalar description of the interference is sufficient. This is achieved by substituting  $\vec{E}_R$  with  $E_R = \vec{E}_R \cdot \hat{y}$ ,  $\vec{E}_{B,0}$  with  $E_{B,0} = \vec{E}_{B,0} \cdot \hat{y}$ , and by substituting  $\vec{E}_{NF,0}$  with  $E_{NF,0} = \vec{E}_{NF,0} \cdot \hat{y}$  in Eqs. (5.21)-(5.25).

Figure 5.7 shows an exemplary calculation of the  $S_{0f}$  to  $S_{4f}$  signals using a ratio of near-field to background of once 50 and once 5 that clearly demonstrates the importance of the ratio. In the next section we will use the derived equations to fit them to our measurement data and disentangle the real near-field and background contributions.

## 5.4 Near-Field Contributions in the Measurements

The reference field strength  $E_R$  is measured directly as the unmodulated signal  $S_{0f}$  with the tip removed from the setup, setting  $E_{B,0} = 0$  in Eq. (5.21). For the gold-coated quartz sample, the power measured with the photodiode is  $P = 2.8 \mu\text{W}$ , which, assuming a beam cross section of  $A = 1 \text{ mm}^2$ , corresponds to the reference field strength  $E_R = 46 \text{ V/m}$ . The background field strength  $E_{B,0} \cdot |b^{(0)}|$  can be estimated rather precisely from the modulation depth on the signal  $S_{0f}$  in Fig. 5.4A, which originates from the cosine-term in Eq. (5.21), with the result  $E_{B,0} \cdot |b^{(0)}| = 1.1 \text{ V/m}$  and the ratio  $E_R : E_{B,0} \cdot |b^{(0)}| = 43 : 1$ . It should be noted that it is not possible to directly obtain a value for  $E_{NF,0} \cdot |c^{(0)}|$  from the unmodulated signal since it is by far dominated by the background and reference fields. No near-field contribution is discernible in the measurement shown in Fig. 5.4A. This is the case for all three substrates.

The derived expressions (5.22)-(5.25) for the optical signals  $S_{1f}$  to  $S_{4f}$  are compared to the measured approach curves, using the values  $E_R = 46 \text{ V/m}$  and  $E_{B,0} \cdot |b^{(0)}| = 1.1 \text{ V/m}$  obtained from the measured signal  $S_{0f}$  in Fig. 5.4A, and using the phase for the near field,  $\varphi_{NF}$ , and the phase for the background field,  $\varphi_{B1}$ , to manually adapt the shape of the calculated curves to the measured signal. Furthermore, for the gold-coated quartz substrate the effect of multiple



**Figure 5.8:** Disentangled background and near-field signals. The left hand side graphs show the measured optical signals  $S_{2f}$  (blue curves) and  $S_{3f}$  (green curves) as a function of the tip-sample distance together with calculated approach curves (dashed red curves) for A, the gold-coated quartz substrate, C, the uncoated quartz substrate, and E, the quartz substrate coated with a semitransparent gold film and  $\sim 200$  nm quartz on top of the gold film. Adapting the theoretically derived expressions for  $S_{0f}$  to  $S_{4f}$  allows determination of the electric field strengths  $E_R$ ,  $E_{B,0}$ , and  $E_{NF}$ , and, together with the Fourier coefficients  $b^{(n)}$  and  $c^{(n)}$  disentangling background and near-field contributions to the measured signals. The right hand side graphs show the ratio of background and near-field contribution to the measured signals as red and blue bars, respectively, as function of the demodulation order for B, the gold-coated quartz substrate, D, the uncoated quartz substrate, and F, the quartz substrate coated with a semitransparent gold film and  $\sim 200$  nm quartz on top of the gold film. The bars are normalized to  $\text{Re}\{E_R E_{B,0}\} |b^{(0)}| = 100\%$  on the gold-coated quartz substrate. For the substrates with a gold film (B and F), the background signal decays much faster with increasing demodulation frequency than the near-field signal, such that when demodulating at  $f_{\text{demod}} = 4 \cdot f_{\text{mod}}$ , basically only the near-field signal is measured. For the uncoated quartz substrate, even at fourth-order demodulation, the background signal surmounts the near-field signal.

reflections can be seen clearly from the deviation of especially  $S_{1f}$  from a single-sinusoidal behavior (Fig. 5.4B). This is taken into account by using Eq. (5.3) to describe the background field, adding the reflection coefficient  $r$  and the second phase  $\varphi_{B2}$  as adaptation parameters. For the gold-coated quartz substrate, the reflection coefficient is between  $r = 0.15$  and  $0.45$ . As an example, Fig. 5.4A shows the calculated curves  $S_{2f}$  and  $S_{3f}$  (dashed red curves) together with the experimentally measured approach curves ( $S_{2f}$ : blue curve,  $S_{3f}$ : green curve). With the above mentioned adjustable parameters, the derived expressions reproduce the measured curves quite closely. As a result of comparing the measurement to the derived expressions, we obtain on the one hand  $\text{Re} \{E_R E_{\text{NF},0}\} \cdot |c^{(n)}|$  for  $n = 1, 2, 3, 4$ , which represents a direct measure for the near-field contributions to the measured signals, and on the other hand the contributions that arise due to the background light scattered from the tip shaft, i. e.,  $\text{Re} \{E_R E_{B,0}\} \cdot |b^{(n)}|$ ,  $|E_{B,0}|^2 \cdot |b^{(n)}| |b^{(m)}|$ , and  $\text{Re} \{E_{B,0} E_{\text{NF},0}\} \cdot |b^{(n)}| \cdot |c^{(m)}|$ . In Fig. 5.4B, these values are plotted as bar diagrams as a function of demodulation order, normalized to  $\text{Re} \{E_R E_{B,0}\} |b^{(0)}| = 100\%$ . Both signal contributions decrease exponentially with increasing demodulation order, and as expected for a gold surface, the background signal decreases much faster than the near-field signal, such that for  $S_{3f}$  the near-field contribution already surmounts the background, and that for  $S_{4f}$  the background contribution amounts to only  $\sim 2.5\%$ .

With a similar measurement of the pure reference power, we find for the uncoated quartz substrate the much smaller reference field strength  $E_R = 12 \text{ V/m}$  and the background field strength  $E_{B,0} \cdot |b^{(0)}| = 2.3 \text{ V/m}$ , i. e.,  $E_R : E_{B,0} \cdot |b^{(0)}| = 5 : 1$ . The absence of a semitransparent gold film results in more light reaching the tip and hence increased scattering from the tip shaft, while the reference field is created only by a relatively weak reflection from the glass surface. As before, there is no near-field contribution  $E_{\text{NF},0} \cdot |c^{(0)}|$  discernible. Again, the derived expressions Eq. (5.22)-(5.25) are adapted to the measurements by manually varying the phases of background and near-field light,  $\varphi_{B1}$ ,  $\varphi_{B2}$ , and  $\varphi_{\text{NF}}$ . The reflectivity of the uncoated quartz is reduced to about half that of the gold-coated quartz samples, but due to the high background-to-reference ratio multiple reflections between tip and sample again have a high influence on the over-all signal (Fig. 5.4C). Compared to the gold-coated quartz substrate, the high background-to-reference ratio of the uncoated quartz substrate results in a much stronger influence of the background-related signal components even at high demodulation orders: up to the fourth order near-field- and background-related signal components are of comparable strength (see Fig. 5.4D). From this measurement it is clear that the reference signal needs to be increased in order to measure predominantly the near-field signal at demodulation frequencies that are experimentally easily accessible.

As the last substrate, we evaluate the approach curves for the in-line homodyne interferometer, i. e., for the gold- and glass-coated quartz substrate. Here the reference is again increased due to the semitransparent gold film, with  $E_R = 66 \text{ V/m}$  and  $E_{B,0} \cdot |b^{(0)}| = 1.9 \text{ V/m}$ , i. e.,

$E_R : E_{B,0} \cdot |b^{(0)}| = 36 : 1$ . The derived expressions Eqs. (5.22)-(5.25) are adapted to the measurements like described before, and as examples,  $S_{2f}$  and  $S_{3f}$  are plotted in Fig. 5.4E. In this case, there is still a small deviation between the measured and the calculated curves for  $S_{2f}$  apparent, and the curvature of  $S_{3f}$  at small tip-sample distances of  $< 50$  nm could also not be entirely reproduced. This observation points towards somewhat more complicated multiple reflections than accounted for by our simple model, e. g., reflections not only between the tip and gold film but also between tip and substrate surface. The near-field and background contributions to the measured optical signals are plotted as a function of the demodulation order in the bar diagram in Fig. 5.4F, where one can see that both signal contributions decrease exponentially with increasing demodulation order. Similar to the gold-coated substrate, also for our in-line interferometer, the background signal decreases faster than the near-field signal. For  $S_{3f}$  the near-field contribution surmounts the background, and at  $S_{4f}$  the background contribution amounts to only  $\sim 7\%$ .

In conclusion, for the uncoated quartz substrate the reference and the background field are of comparable strength. Hence, for this case, cross terms not only between any higher order near-field terms and the reference field contribute to the measured signals, but also between higher order near-field terms and the background term  $E_{B,0} \cdot |b^{(0)}|$  have considerable influence. For uncoated glass substrates, a measurement exploiting near-field contrast will be possible only for higher demodulation orders than accessible to us in this work. For both metal-coated quartz substrates, in contrast,  $E_{B,0} \cdot |b^{(0)}| \ll E_R$ , such that the cross terms between higher-order coefficients  $E_{B,0} \cdot |b^{(n)}|$  and  $E_{NF,0} \cdot |c^{(n)}|$ ,  $n \neq 0$  and the reference field dominate. The faster decay of  $E_{B,0} \cdot |b^{(n)}|$  with increasing demodulation order then nearly completely removes the dependence on the unknown background field. The dominance of the near-field signal  $\text{Re} \{E_R E_{NF,0}\} \cdot |c^{(n)}|$  is a result of mixing the near field with a strong reference field, i. e. of the in-line homodyne interferometer formed by the buried gold film.

## 5.5 Summary

In this work, we have analyzed the signal in scattering-type scanning near-field optical microscopy on the field level, and we have identified and designed a layered structure that allows disentangling near-field and background-related signal contributions by mixing the near field with a strong reference field. The layered structure was realized by depositing a thin gold film on the sample substrate and covering it with a thin dielectric layer and forms an inherently phase-stable in-line interferometer. We have shown that this efficiently amplifies the near field and suppresses the background light, such that when demodulating the signal with the third or fourth harmonic of the tip modulation frequency mainly the near field is detected.

Our measured and calculated optical signals verify and demonstrate the challenging effect

of background signals in scattering-type SNOM. Interference between light that is reflected from the sample and light that is scattered from the tip shaft dominates the measured signal, in the case of an uncoated sample even if the signal is demodulated at the fourth harmonic of the tip modulation frequency. For broad-bandwidth spectroscopy, this results in spectral interference that basically determines the shape of the measured spectra. In this work, we have shown that a reference field of sufficient amplitude, namely of roughly 50-fold amplitude of the background field, can achieve efficient background suppression. The reference field then amplifies the near field such that at demodulation at the third or fourth harmonic of the tip modulation frequency results in the very precise detection of the near field. Specifically, we have created the reference field within the substrate of the sample, thereby realizing an inherently stable in-line interferometer. In this work, a reference field with suitable amplitude is provided by 30-50% reflection of the incident laser field off a  $\sim 20$  nm thick gold film. Alternatively, one may use a substrate made of a dielectric material with high refractive index. A somewhat lower reflectivity between 10 and 20% could be realized in a trade-off between ease of substrate production and near-field amplification.

While we have concentrated on overriding the background-related signal contributions with an amplified near-field related signal, it would be even more advantageous to reduce the detrimental effect of the background field. Reduction of light scattered from the tip shaft would greatly improve the potential of s-SNOM. Such a reduction of background light would require changing the dielectric function of the tip material, i. e., making the tip in essence transparent to the incident laser light. Creating a near-field signal, however, requires a strong tip dipole. Both requirements could be combined, for example, by placing a metal sphere on a transparent mount such as a dielectric taper [185]. A metal sphere offers a large dipole moment, but has a narrow resonance. Thus, while such a tip on the one hand could hold great potential to improve the signal-to-background ratio in s-SNOM, it would, on the other hand, considerably reduce the bandwidth for spectroscopy. There is a trade-off between background reduction, tip dipole moment, and spectral bandwidth. In our experience, the gold nanotapers that were used in this work optimize dipole moment and spectral bandwidth, but introduce a relatively large background signal that requires additional measures for background suppression.

In summary we have realized an inherently phase-stable in-line interferometer for mixing the near field with a strong reference field by depositing a thin gold film on the sample substrate and covering it with a thin dielectric layer. We have shown that this efficiently amplifies the near field and suppresses the background light. Moreover, the in-line interferometer is not only limited to monochromatic measurements but can be used for broad-band s-SNOM spectroscopy as well. This will be shown in the following chapters.

# Local Spectroscopy 6

---

In the previous chapter I've demonstrated the in-line interferometer to record near-field signals for one specific wavelength.

However, a complete spectral evaluation is crucial to better understand the sample's material response to light-matter interaction.

Hence, first, in chapter 6.1, I demonstrate a simple extension of the monochromatic measurements by substituting the monochromatic laser source with a broad-band Ti:Sa laser source and the detection photodiode with a monochromator and a fast line camera. Using a similar evaluation as for the monochromatic measurements, this approach already reveals a lot of spectral information, but lacks a complete description of the recorded data. <sup>1</sup>

For SNOM spectra not only the sample properties, but also the interaction with the tip plays an important role. In fact, a resonance of the tip can alter the spectral features of the sample under investigation in the SNOM spectra. A tip influence was for example demonstrated by García-Etxarri et al. [143] by mapping the near-fields of a gold-nanodisk at a single wavelength of 633 nm for both a metallic and a dielectric SNOM tip. It was found that for the dielectric tip and thus weak coupling between tip and sample, the plasmonic mode of this antenna structure could be mapped. In contrast, with the metallic nanotip, the mode profile could not be mapped, but was highly distorted due to the strong coupling between the antenna mode and the nanotip mode and a resulting spectral shift of the antenna resonance. The experiments from García-Etxarri et al. emphasize the importance of understanding the tip influence and especially the tip-sample interaction on SNOM spectra.

In the literature, mainly infrared SNOM spectra measurements are presented. In this wavelength range, the spectral influence of a tip resonance is mostly negligible as was shown by Aizupura et al. [70], Novotny et al., Romanov et al. [186] and others [187]. This is because the tip resonance always lies in the visible or UV range and thus the spectral response of the tip is

---

<sup>1</sup>Parts of section 6.1 are taken from the peer-reviewed publication "Brauer, J., Zhan, J., Chimeh, A., Korte, A., Lienau, C., & Gross, P. (2017). In-line interferometer for broadband near-field scanning optical spectroscopy. *Optics Express*, 25(13), 15504". My part was the planning of the experiment, measurement of the data, literature research, setting up the equations as well as simulating and plotting of the results. The paper is attached in appendix D.

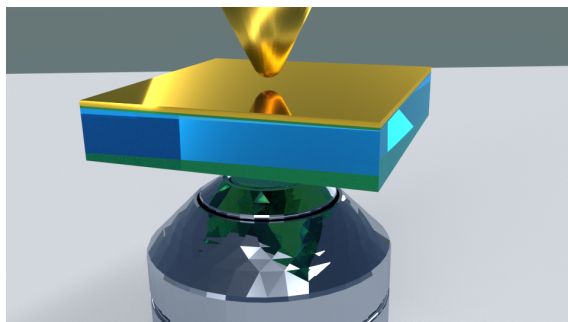


**Figure 6.1:** 3D visualization of the measurement geometry that shows the SNOM gold tip over the gold-coated quartz substrate. A microscope objective is focusing the light onto the taper apex. Due to small tip-sample distances, the interaction of tip and sample can be complex and it is important to understand the influence of the tip in the spectral domain.

nearly constant for longer wavelengths. Here, we are however interested in measurements in the visible to near-infrared wavelength range and the actual spectral response of the tip can have a significant influence on the SNOM spectra and the interaction needs to be determined.

Hence, in chapter 6.2, I use a new evaluation of the data, taking into account the full vectorial properties of tip and sample, i.e., considering tip and sample polarizability tensors, as well as the polarization of the excitation light. This chapter is structured in 4 parts: first the influence of the polarization of the excitation light on the distance and wavelength dependent effective polarizability is shown for a flat gold film. Next, the influence of the focus fields as well as the impact of the tip position within the focus area is investigated. Then a new method to extract distance dependent near-field spectra from the measurement via Fourier-composition of near field spectra is presented. Using this it is not necessary to record distance-dependent spectra by slowly retracting the tip, but due to the large modulation amplitude of the tip, approach spectra can be reconstructed directly and are basically recorded "on the fly". In the last part of that chapter, different measured spectra on flat films, here on a gold film and on a  $\text{Sb}_2\text{S}_3$  film, are discussed.

The following two sections, 6.3 and 6.4, then present measurements on an anisotropic squaraine dye material, as well as spectroscopic imaging of strong coupling of the SNOM tip with nano-rod antennas.

## 6.1 Simple expansion of quasi-monochromatic model to broad-bandwidth measurements

As a first approach to broadband near-field spectroscopy we investigate the same gold sample as in the monochromatic measurements described before, i. e., an evaporated gold film on top of the BK-7 glass substrate with a thickness of about 20 nm. Such a thin semi-transparent gold layer with a transmission of around 50% is needed in order to be able to still detect the weak near-field signals scattered from the gold tip of the SNOM. In contrast to chapter 5, the quasi-monochromatic light source is substituted by a spectrally broad Ti:Sa laser and for detection we use a monochromator and a fast line camera.

Specifically, SNOM spectra on the gold film are recorded with a Ti:Sa laser with a bandwidth exceeding 100 nm and centered at 780 nm (figure 6.2A). Figure 6.2B shows the tuning fork amplitude as a function of the tip-sample distance  $z_0$ . The tuning fork amplitude acts as a control parameter and a decreasing amplitude indicates a damped oscillation caused by short ranging Van-der-Waals forces. Colored circles mark the positions at which spectra are recorded. For a fixed tip-sample distance we recorded 60000 spectra with a rate of 210 kHz. The recorded spectra are then post-processed to extract the resulting spectra demodulated at the  $n$ th order of the tip modulation frequency  $\Omega$ . This means we apply a Fourier transform for each pixel of the line camera and extract the value at the  $n$ th order (compare chapter 3.1). This results in demodulated spectra  $S_{n,f}(\lambda)$  which are exemplary shown for  $n = 1, n = 2$  and  $n = 4$  in figure 6.2C, E and G. The color of each curve corresponds to the color of the dots in figure 6.2B. Hereby, the darkest blue indicates a very small tip-sample distance, whereas the light blue colored spectra are measured further away. The red line corresponds to a measurement at a large tip-sample distance, where the near-field contribution is vanishingly small.

By comparison of the demodulated spectra with the laser spectrum we find a very different spectral shape of the first and second order demodulated spectra. The spectral shape additionally varies with tip-sample distance, which is most apparent for the spectrum measured at large distances (red curve) but is also observed for tip-sample distance variations on a small scale of  $< 20$  nm. To understand these results we expanded the derived equations (eq. (5.22)-(5.25)) for the demodulated signals  $S_{1f}$  to  $S_{4f}$  to also include the wavelength dependency, i.e.  $S_{1f}$ ,  $S_{2f}$ ,  $S_{3f}$  and  $S_{4f}$  are now a function of  $\lambda$ :

$$\begin{aligned}
 S_{1f}(\bar{z}, \lambda) \approx \gamma \nu \varepsilon_0 c A \cdot & \left| - \operatorname{Re} \left\{ \vec{E}_R(\lambda) \vec{E}_{B,0}(\lambda) \right\} \left| b^{(1)}(\lambda) \right| \sin(2k(\lambda)(\bar{z} + d) + \varphi_B) \right. \\
 & - \operatorname{Re} \left\{ \vec{E}_R(\lambda) \vec{E}_{\text{NF},0}(\lambda) \right\} \left| c^{(1)} \right| e^{\frac{-\bar{z}}{z_0}} \cos \varphi_{\text{NF}} \\
 & \left. - \operatorname{Re} \left\{ \vec{E}_{B,0}(\lambda) \vec{E}_{\text{NF},0}(\lambda) \right\} \left| b^{(0)}(\lambda) \right| \left| c^{(1)} \right| \cdot e^{\frac{-\bar{z}}{z_0}} \cos(2k(\lambda)(\bar{z} + d) + \varphi_B - \varphi_{\text{NF}}) \right|
 \end{aligned} \tag{6.1}$$

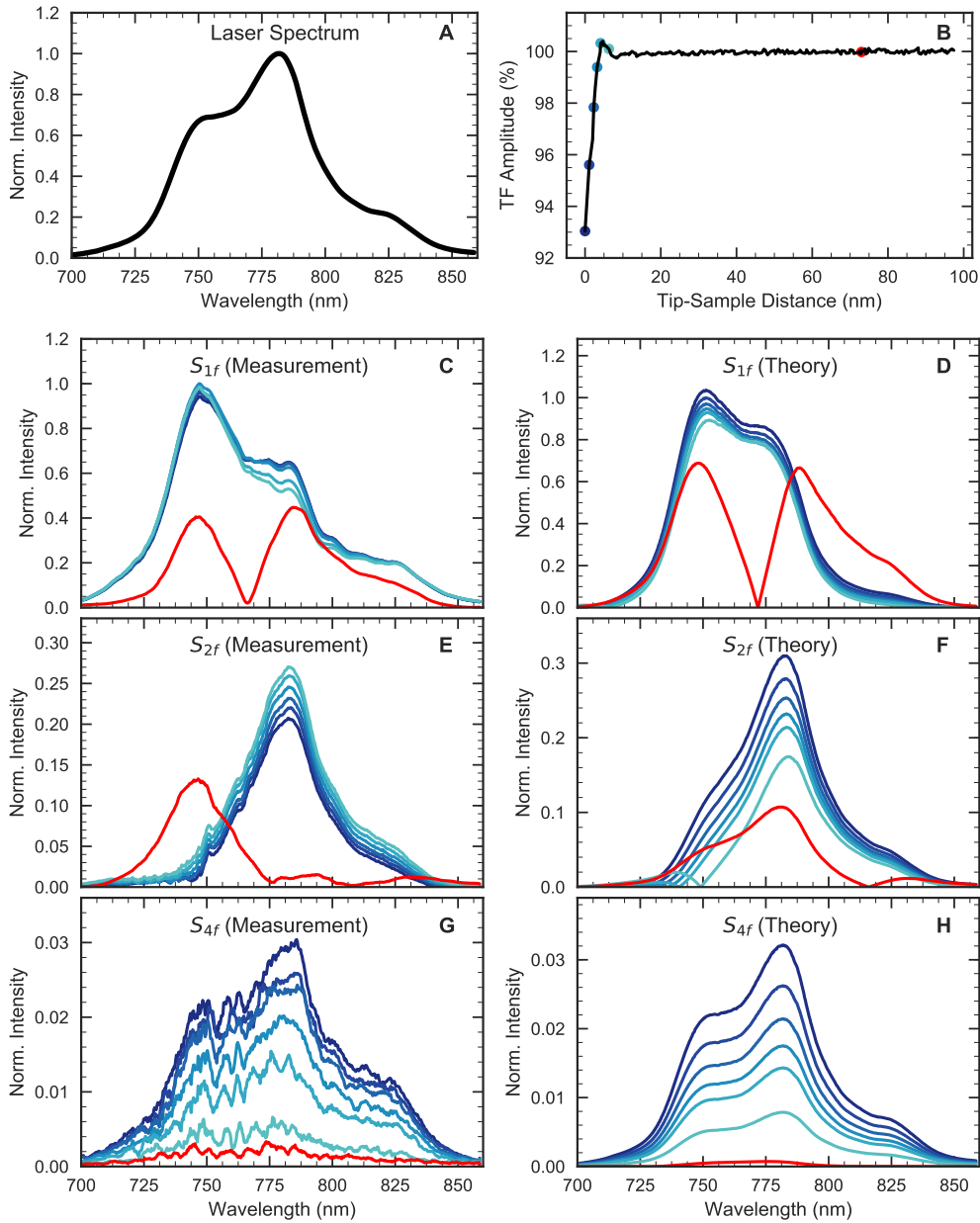


**Figure 6.2:** Broad-bandwidth near-field spectroscopy. **A**, Input laser spectrum. **B**, Tuning fork amplitude as a function of tip-sample distance. The positions where spectra are measured are marked by colored circles. **C**, The measured spectra  $S_{1f}(\lambda)$ , demodulated at the fundamental tip modulation frequency, do not resemble the input spectrum, but are prominently modulated by interference between reference and background fields. **D**, The calculated spectra  $S_{1f}(\lambda)$  model the main characteristics of the measured spectra very well. **E**, The measured as well as **F**, the calculated spectra  $S_{2f}$  also differ from the input laser, and due to different field components interfering they also strongly differ from  $S_{1f}$ . **G**, In contrast, the measured spectra  $S_{4f}(\lambda)$ , demodulated at the fourth harmonic, mainly resemble the input laser spectrum and strongly decrease with increasing tip-sample distance. **H**, The calculated spectra  $S_{4f}$  show the same behavior.

$$\begin{aligned}
 S_{2f}(\bar{z}, \lambda) \approx \gamma \nu \varepsilon_0 c A \cdot & \left| - \operatorname{Re} \left\{ \vec{E}_R(\lambda) \vec{E}_{B,0}(\lambda) \right\} \left| b^{(2)}(\lambda) \right| \cos(2k(\lambda)(\bar{z} + d) + \varphi_B) \right. \\
 & + \operatorname{Re} \left\{ \vec{E}_R(\lambda) \vec{E}_{\text{NF},0}(\lambda) \right\} \left| c^{(2)} \right| e^{\frac{-\bar{z}}{z_0}} \cos \varphi_{\text{NF}} - \left| \vec{E}_{B,0}(\lambda) \right|^2 \left| b^{(0)}(\lambda) \right| \left| b^{(2)}(\lambda) \right| \\
 & \left. + \operatorname{Re} \left\{ \vec{E}_{B,0}(\lambda) \vec{E}_{\text{NF},0}(\lambda) \right\} \left| b^{(0)}(\lambda) \right| \left| c^{(2)} \right| \cdot e^{\frac{-\bar{z}}{z_0}} \cos(2k(\lambda)(\bar{z} + d) + \varphi_B - \varphi_{\text{NF}}) \right| \\
 & \tag{6.2}
 \end{aligned}$$

$$\begin{aligned}
 S_{3f}(\bar{z}, \lambda) \approx \gamma \nu \varepsilon_0 c A \cdot & \left| \operatorname{Re} \left\{ \vec{E}_R(\lambda) \vec{E}_{B,0}(\lambda) \right\} \left| b^{(3)}(\lambda) \right| \sin(2k(\lambda)(\bar{z} + d) + \varphi_B) \right. \\
 & - \operatorname{Re} \left\{ \vec{E}_R(\lambda) \vec{E}_{\text{NF},0}(\lambda) \right\} \left| c^{(3)} \right| e^{\frac{-\bar{z}}{z_0}} \cos \varphi_{\text{NF}} \\
 & \left. - \operatorname{Re} \left\{ \vec{E}_{B,0}(\lambda) \vec{E}_{\text{NF},0}(\lambda) \right\} \left| b^{(0)}(\lambda) \right| \left| c^{(3)} \right| \cdot e^{\frac{-\bar{z}}{z_0}} \cos(2k(\lambda)(\bar{z} + d) + \varphi_B - \varphi_{\text{NF}}) \right| \\
 & \tag{6.3}
 \end{aligned}$$

$$\begin{aligned}
 S_{4f}(\bar{z}, \lambda) \approx \gamma \nu \varepsilon_0 c A \cdot & \left| \operatorname{Re} \left\{ \vec{E}_R(\lambda) \vec{E}_{B,0}(\lambda) \right\} \left| b^{(4)}(\lambda) \right| \cos(2k(\lambda)(\bar{z} + d) + \varphi_B) \right. \\
 & + \operatorname{Re} \left\{ \vec{E}_R(\lambda) \vec{E}_{\text{NF},0}(\lambda) \right\} \left| c^{(4)} \right| e^{\frac{-\bar{z}}{z_0}} \cos \varphi_{\text{NF}} + \left| \vec{E}_{B,0}(\lambda) \right|^2 \left| b^{(2)}(\lambda) \right|^2 \\
 & \left. + \operatorname{Re} \left\{ \vec{E}_{B,0}(\lambda) \vec{E}_{\text{NF},0}(\lambda) \right\} \left| b^{(0)}(\lambda) \right| \left| c^{(4)} \right| \cdot e^{\frac{-\bar{z}}{z_0}} \cos(2k(\lambda)(\bar{z} + d) + \varphi_B - \varphi_{\text{NF}}) \right| \\
 & \tag{6.4}
 \end{aligned}$$

Hereby,  $\vec{E}_R$ ,  $\vec{E}_{B,0}$ ,  $\vec{E}_{\text{NF},0}$ ,  $k$  and the Bessel coefficients  $b^{(n)}$  are wavelength dependent. As the spectral response of both the gold film and the glass substrate is rather flat in the spectral region investigated here (cmp. chapter 4.2.3), we assume it to be constant. The reference field  $\vec{E}_R$  then takes the spectral shape of the laser input field, and the spectral phase is flat and can be set to  $\varphi_R = 0$ .

The background field has the same spectral shape of the laser spectrum, i.e., the same amplitude, but its phase takes a more complex form. In particular the background field is governed by two phase terms, one is from the light scattered back from the tip that acquires the phase  $2k(z + d) + \varphi_B = 4\pi(z + d)\lambda^{-1} + \varphi_B$  with respect to the reference field. This phase is due to the extra distance  $(2(z + d))$  traveled by the background field and further depends on the wavelength via  $k \propto \lambda^{-1}$ . The offset phase  $\varphi_B$  is taken to be constant. Furthermore, in the monochromatic experiments (section 5.3) we had shown that we need to take into account one more reflection between substrate and tip to describe the curves. Hence the background field is expanded by a factor  $r \cos(4k(z + d) + \varphi_{B,2})$ , also depending on the wavelength.

Finally the near-field  $\vec{E}_{\text{NF},0}$  is given by the product of the reference field and an effective tip-sample polarizability, which is proportional to the tip polarizability. For this first test we assume a tip polarizability described by a gold sphere with 10 nm radius, which results in a non-resonant characteristic of the tip in this spectral region, with changes of  $\sim 6\%$  of the real part and negligible imaginary part of the polarizability (cmp. also Fig. 4.21B). Thus, the tip polarizability can also be estimated to be spectrally flat.

The simulated spectra are plotted at the right side next to the measurements (panel D,F and G in figure 6.2). For signals with a high background contribution, such as the  $S_{1f}$  and  $S_{2f}$  signals, we find that the wavelength dependent phase shifts between reference and background field lead to spectral interferences. Compared to the phase terms, the bessel coefficients have a much weaker influence on the spectra. Overall, this simple wavelength expansion to the previous quasi monochromatic model can explain the spectra already quite well. In the  $S_{1f}$  simulation, the distance dependency and especially the spectral interference, that are most prominent for large distances, could very well be reproduced. Also we found that the shape of the spectra depends sensitively on the wavelength independent phase offsets,  $\varphi_{B1}$  and  $\varphi_{B2}$ . By adjusting these phases, some spectral components can even vanish completely from the calculated spectra. This demonstrates clearly that spectral interference is the dominant effect that shapes the spectra and quantitative statements about the sample response are difficult to make from the  $S_{1f}$  signal. The signal  $S_{2f}$  from figure 6.2E and F exposes this effect even more. Here the spectrum in contact is much narrower than the input spectrum and is changing its shape with each new tip-sample distance. Additionally, the spectral shape is very different from the  $S_{1f}$  spectrum as well. However, knowing that the signal  $S_{2f}$  is composed of different terms of interfering fields than  $S_{1f}$  (compare the equations above), it becomes clear that spectral interference between the fields should lead to quite different measured and calculated spectra and shows once more that spectral interference can easily obscure true near-field spectral information.

On the contrary to these results, the spectrum demodulated at the 4th order ( $S_{4f}$ ) from figure 6.2G and H does not show any spectral interferences. In fact, the simulated curves follow the shape of the laser input spectrum, because the dominant part in the  $S_{4f}$  signal is the cross term of reference field and near-field. Due to the flat spectral response of sample and tip the cross term is proportional to the input spectrum.

In total, the overall shape in the  $S_{4f}$  signal is maintained for larger tip-sample distances and the amplitude of the spectrum is decreasing to nearly 0 within less than 20 nm from the closest point, indicating once more a main contribution from the short-ranging near-field. Similar to the quasi monochromatic measurements presented earlier, we can conclude that a background contribution and thus spectral interferences are suppressed at this demodulation order, verified by the simulated results. Hence, meaningful statements about the sample properties can be made.

However, a closer comparison of the simulated spectrum with the measured spectrum shown in figure 6.3 reveals a discrepancy, manifesting specifically in the lower wavelength region up to 740 nm and the higher wavelength region from around 800-830 nm. Deviations larger than 5% are marked as either a grey area in the low wavelength region and a green area for the longer wavelengths. These two increased shoulders of both the  $S_{1f}$  and  $S_{4f}$  spectra are further analyzed in the next sections by analyzing the tip-sample interaction with the tip polarizability described by a tensor.

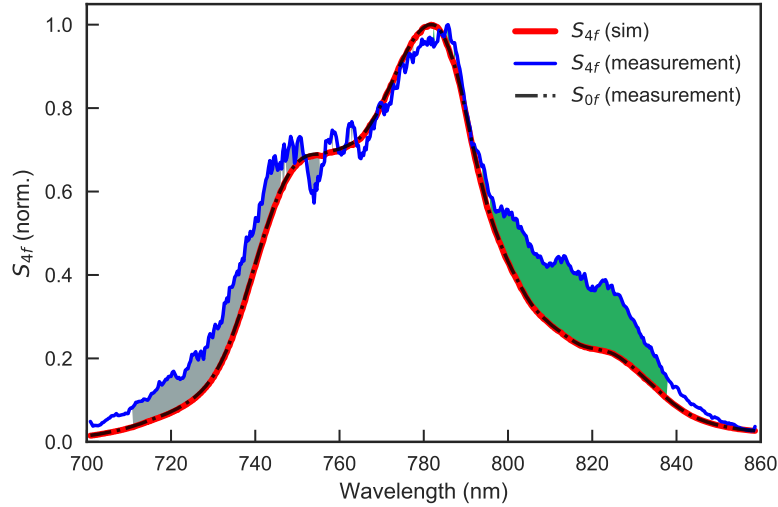


**Figure 6.3:** Simulated  $S_{4f}$  spectra (red) plotted together with the measured  $S_{4f}$  spectra (blue) and the laser input spectrum (dotted black curve). The simulated spectrum has the same shape as the input spectrum, whereas the measured spectrum shows a significant difference. Deviations to the simulation by more than 5% are marked as a filled area. Two distinct areas (green and grey area) can be distinguished.

## 6.2 Tip-sample interaction

The spectral discrepancies observed in 6.1 may arise from dipole-dipole coupling between tip and sample. For small distances, one expects to observe changes in the center wavelength, line width and phase of the measured spectra. The simple model used in 6.1 cannot describe such changes. Instead, this requires taking into account the complete vectorial tip and sample dipoles. Depending on their relative orientation and on their distance, the coupling of different components becomes dominant. Hence, it is important to consider tip and sample polarizability tensors, as well as the polarization of the excitation light.

In the following, I will lay out these couplings and demonstrate some resulting experimental observations with sample dipoles whose dipole moments vary in strength as well as spectral shape. In order to rapidly record distance-dependent near-field spectra, I have developed a novel experimental scheme, namely broadband near-field spectroscopy followed by Fourier-composition of near field spectra.

In my experimental geometry, it is not necessary to record distance-dependent spectra by slowly retracting the tip. Instead, by modulating the tip-sample distance at  $\sim 25$  kHz frequency with a peak-to-peak modulation amplitude  $2A$  of around 30 nm, and by recording spectra with the monochromator and fast line camera with a line-readout rate of roughly 8 times that frequency, spectra are continuously recorded at different distances spanning twice the modulation amplitude. Thus, approach-curves are practically recorded "on the fly". The

measured spectra are sorted to their respective tip-sample distance in post-processing.

### 6.2.1 Tip polarizability and effective polarizability

In Ch. 4.2, I have already given an overview over different tip polarizability models. In our experiments, it has proven realistic to describe the tip polarizability as a tensor

$$\alpha = \begin{pmatrix} \alpha_{tip,xx} & 0 & 0 \\ 0 & \alpha_{tip,yy} & 0 \\ 0 & 0 & \alpha_{tip,zz} \end{pmatrix} \quad (6.5)$$

where  $\alpha_{tip,xx}$  is described well by the polarizability of a sphere with the radius of the tip, and where  $\alpha_{tip,zz}$  is matched better by a Lorentzian oscillator with a center energy of  $\hbar\omega = 1.55$  eV and a damping energy of 0.33 eV [93]. In the following, I want to point out the consequence of these tip polarizabilities on the effective polarizability especially for the spectral range that is used in the following sections. Also I show the resulting relative effective polarizability that can be compared to our demodulation measurements. The overall consequence of the field enhancement of the tip on the spectra is already demonstrated in Ch. 4.2.3.

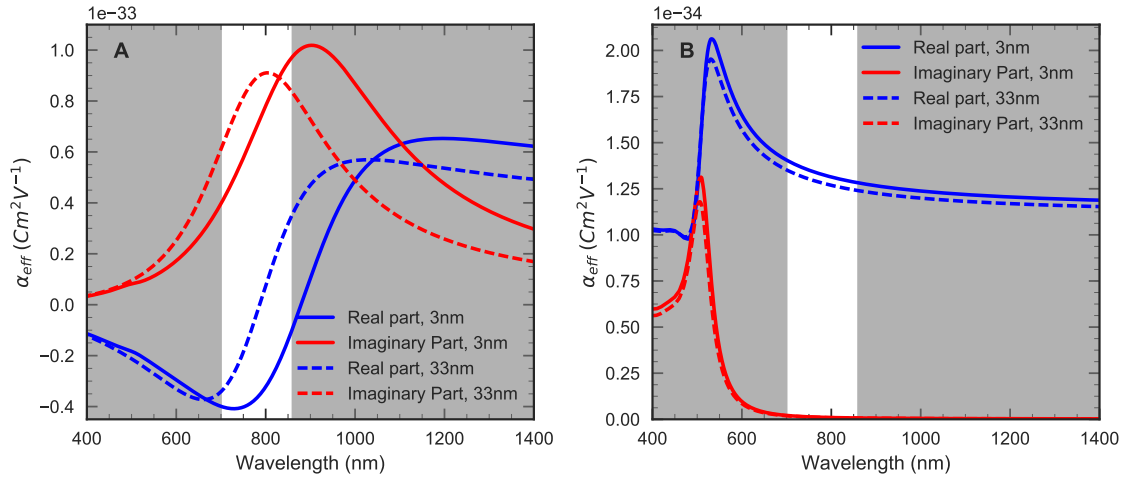


**Figure 6.4:** A: Calculated  $\alpha_{eff}$  for a gold surface and the electric field polarized perpendicular to the surface. In this case the tip dipole was modeled by a Lorentzian resonance. Real and imaginary part of  $\alpha_{eff}$  are shown for two tip sample distances of 3 nm and 33 nm respectively. B: The same calculation, but for an electric field polarized parallel to the surface. For this case, the polarizability of the tip dipole was modeled by a gold sphere with 10 nm radius.

Figure 6.4 shows a replot of the effective polarizability that was already shown in chapter 4.2. Note that the effective polarizability reflects the tip-sample interaction where both the tip polarizability as well as the sample dependent factor  $\beta = (\epsilon_{Au} - 1)/(\epsilon_{Au} + 1)$  enter the equation.

Both, the tip polarizability for a gold sphere as well as for a broad Lorentzian resonance and the sample dependent factor  $\beta$  are shown in Fig. 4.21.

For Fig. 6.4 I've calculated the effective polarizability for a gold film once for excitation of the tip x (and y-) dipole, i.e., for the incident electric field polarized parallel to the surface, and once for excitation of the tip z-dipole (electric field polarized perpendicular to the surface). The data for the dielectric function was taken from Olmon et al. [129]. For comparison, each figure shows two calculations for a tip dipole in a distance of 3 nm and 33 nm from the sample surface. A large spectral range was taken so that all possible resonances can be observed. The area not superimposed with a semi-transparent gray area is what we can reasonably well cover with the spectral bandwidth of the experiment.

Clearly, we can observe a very broad resonance in  $\alpha_{eff}$  for the excitation of the z-dipole, i.e. the tip polarizability modeled by a Lorentzian resonance in Fig. 6.4A. This resonance is within our spectral range and the amplitude strongly increases as the tip-sample distance decreases. Furthermore, a resonance shift towards longer wavelengths and a spectral broadening of the resonance can be observed. The resonance is much broader than our detection region, such that our measurements will always reflect only a part of it.

For excitation of the x-dipole in Fig. 6.4B a resonance far below our spectral detection range is excited. As a recap from chapter 4.2 the resonance is reached when the denominator of the sphere resonance for the tip polarizability is zero, i.e.  $\epsilon_{tip} + 2\epsilon_{air} = 0$ , or when the real part of the dielectric function of the tip material equals -2. This results in a sharp resonance of  $\alpha_{eff}$  at 532 nm. In the spectral range covered by the laser in this experiment, however,  $\alpha_{eff}$  is rather flat, a little higher at shorter wavelengths, and increases evenly and only slightly as the tip-sample distance decreases.

For better comparison with the experiment, I have plotted the real part of  $\alpha_{eff}$  as a function of tip-sample distance in the accessible spectral range from 700 nm to 860 nm in figure 6.5. Here, the values are color-coded and the distance decreases from bottom to top. As we measure only the demodulated signal, we probe only the difference of the effective polarizability with respect to the tip distance to the sample, because at one time the tip is closer to the sample than half a modulation period later. Thus, for this figure the effective polarizability at distance 50 nm has been subtracted from each of the linewise calculated  $\alpha_{eff}(d, \lambda)$ .

In this comparison we can see that the amplitude of  $Re(\alpha_{eff})$  is steadily increasing as the distance decreases. For the excitation of the x-dipole (Fig. 6.5B) only a weak wavelength dependency can be observed, i.e. slightly larger values of the polarizability for shorter wavelength can be observed, which are basically flat otherwise. For the excitation of the z-dipole the spectral shift and especially the strong increase with decreasing distance can clearly be seen and the

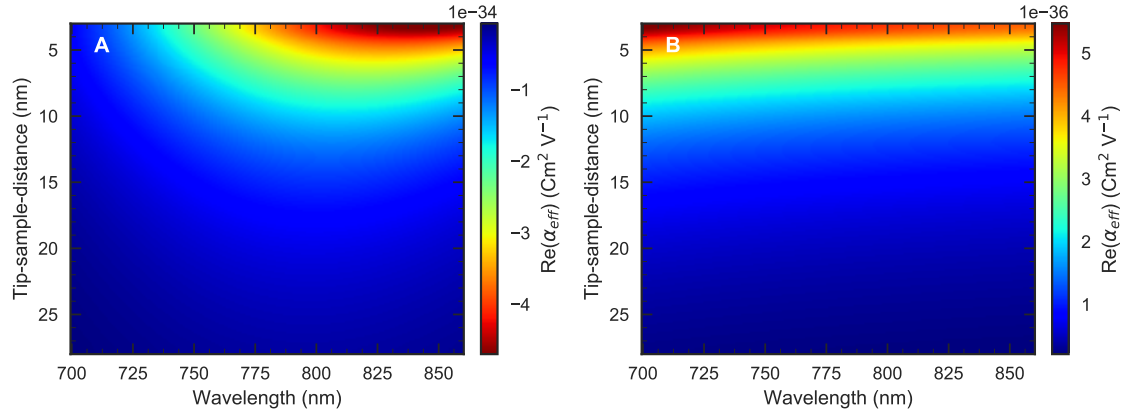


**Figure 6.5:** A: Calculated  $\alpha_{eff}$  for a gold surface and the electric field polarized perpendicular to the surface as a function of tip-sample-distance. B: The same calculation, but for an electric field polarized parallel to the surface.

part of the Lorentzian resonance can be recognized.

Hereby, I would like to note that we never clearly observe a spectral shift in the measurements that are presented in the following sections. Hence, in our case probably the tip-sample distance is always larger than we previously assumed, or the tip was not always as sharp as the assumed 10 nm tip radius, or the field enhancement of the tip was smaller than the factor of 7 used in the simulation. In either way, we can abstract that we measure always in the regime of a weak coupling where spectral shifts do not play a big a role. Still, the presented coupling to the different components of the tip polarizability tensor will affect the spectra measurement and has to be considered in the data evaluation.

### 6.2.2 Illumination of tip and sample: electric field distribution in the laser focus

The field in the focus region needs to be calculated as the full vectorial field: first, the response of the tip to an electric field will be different for coupling to the z-component of the field rather than to the in-plane components, and second, some samples may show an anisotropic response. In this first example, we only consider a gold film, which we describe with a scalar dielectric function and thus assume the sample to be isotropic. Later (in Ch. 6.3), however, we will investigate a film of strongly ordered organic molecules, which show a significant difference between the in-plane and out-of-plane dielectric function.

For propagation of the focused field through the sample, the field is therefore decomposed in an s- and a p-polarized component. Both field components propagate through the sample, but only the p-polarized beam generates a component  $E_z$  of the electric field in the focus. However, both s- and p-polarized waves contribute to the x-component of the focus field. The equation for

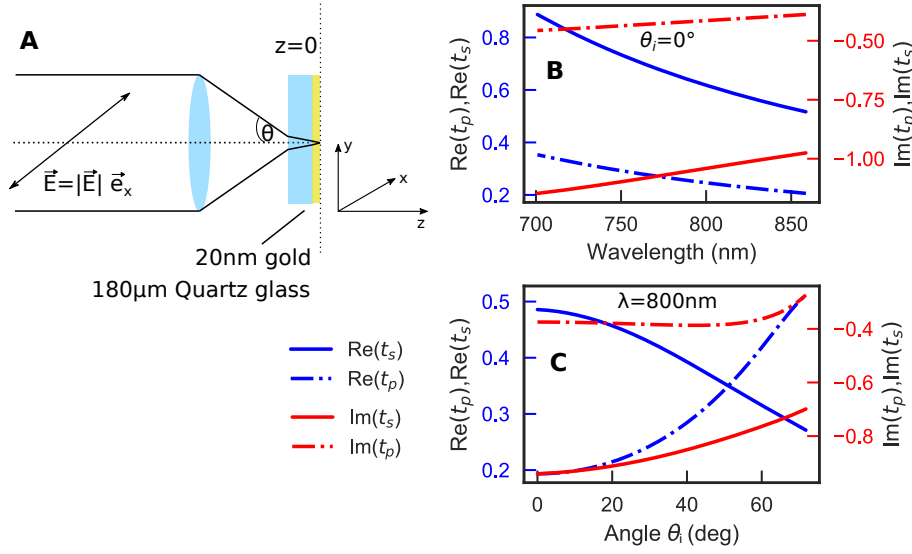


**Figure 6.6:** Visualization of the simulation geometry (A) and the complex transmission coefficients through the sample for different wavelengths and at a fixed angle of  $0^\circ$  (B), and for different incident angles  $\theta$  at a fixed wavelength of 800 nm (C).

the focus field as a function of spatial coordinates  $(x,y,z)$  is then given by (cmp. chapter 4.2)

$$\vec{E}(x, y, z) = \frac{if e^{-ikf}}{2\pi} \iint_{k_x^2 + k_y^2 < k^2} [t^s(k_x, k_y) \vec{E}_s^\infty(k_x, k_y) + t^p(k_x, k_y) \vec{E}_p^\infty(k_x, k_y)] \times \sqrt{k_z/k} e^{i[k_x x + k_y y]} e^{ik_z z} \frac{1}{k_z} dk_x dk_y \quad (6.6)$$

Here  $\vec{E}_{p,s}^\infty(k_x, k_y)$  is the electric field after the lens, but before entering the sample, as described in chapter 4.2,  $k$  is the modulus of the wavevector,  $f$  the focal length of the microscope objective and  $t^s$  and  $t^p$  are the complex transmission coefficients for the 20 nm gold film on top of a glass substrate calculated by the transfer matrix method. Hereby the gold layer of thickness  $d$  introduces a phase shift  $\exp(ik_z d)$  that is included in the transfer matrix calculation. However, in the focus field expression only the phase difference to propagation in air has to be considered. Consequently, the transfer matrix calculation has been changed to only include the phase  $\exp(i\delta)$  with  $\delta = (k_z - k_{z,0})d = (k_z - \frac{2\pi}{\lambda} \cos(\theta_i))d$  for an incident angle  $\theta_i$ . The calculated transmission coefficients are shown in figure 6.6B and C, once as a function of wavelength for a fixed angle, and once as a function of angle of incidence for a fixed wavelength. Hereby the dielectric function of gold was taken from measurements by Olmon et al. [150]. A decreasing amplitude of real and imaginary part of both s- and p-polarized transmission coefficients with larger wavelengths can be observed. On the other hand increasing the incident angle leads to an increase in the real value of the p-polarized transmission amplitude, but a decrease in the real valued s-polarized transmission amplitude. This will slightly change the spectrum in the

focus with respect to the incident laser spectrum, as we will see later in this section.

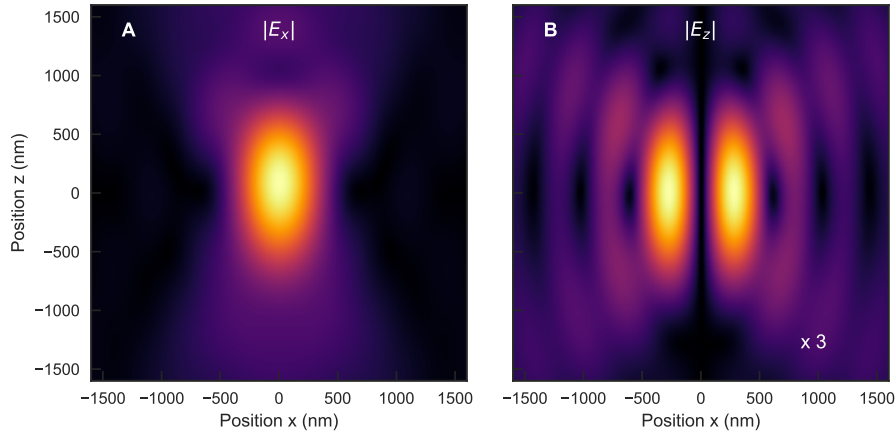


**Figure 6.7:** 2D focal field components  $|E_x|$  in (A) and  $|E_z|$  in (B) after transmission through a gold film of 20 nm thickness. The fields are plotted in the  $xz$  plane, at  $y=0$ . The simulation was carried out for a numerical aperture of 0.95.

The result of the 2D calculation using equation (6.6) is shown in Fig. 6.7 for a numerical aperture of 0.95, thus  $k_x, k_y \leq k_{max} = k \cdot 0.95$ . Plotted are the field components  $|E_x|$  and  $|E_z|$  in the  $xz$  plane at  $y=0$  for a wavelength of 780 nm. One can see that the  $E_x$ -field has a single maximum with a FWHM in the focus plane of 680 nm. The  $z$ -field has zero field strength on the  $z$ -axis with  $x=y=0$  and two maxima in the  $xz$ -plane, one on each side. The  $E_y$  component is nearly zero for the plane with  $y = 0$ , but is considered in the simulation as well. In the experiment we align the tip position within this focus region by maximizing a higher order signal ( $S_{3f}$  or  $S_{4f}$ ), with the tip in close proximity (around 3 nm) to the sample. Coupling of the  $E_z$  component to the tip dominates if the point of high intensity is found in one of the two maxima of the  $E_z$  field. If only one maximum is measured this indicates a strong coupling to the  $x$ -component. In general however, both  $z$ -fields and  $x$ -fields can mix in the measured tip-scattered intensity signal. Even if only one maximum is measured in a beam scan, the point of maximum intensity could still be ascribed to a coupling of both the  $x$ - and  $z$ -component. This is due to a mixing of both components that results in a shift of the point of maximum intensity, as is visualized in figure 6.8. Hence, only when placing the tip at  $x=0$  the field  $E_z$  is close to zero and solely coupling to the  $x$ -component has to be considered. When the two lobes of the  $E_z$  field are strong enough to alter the total measured intensity, the point of maximum intensity can shift away from the  $x=0$  position and the focus field contains both  $x$ - and  $z$ - components. In that case the ratio of the two field components highly depend on the exact position of the tip and is typically hard to establish. For the following simulation we choose the right maximum of  $|E_z|$  (at  $x=320$  nm,  $z=0$ ,  $y=0$ ), because here both components contribute and the influence of

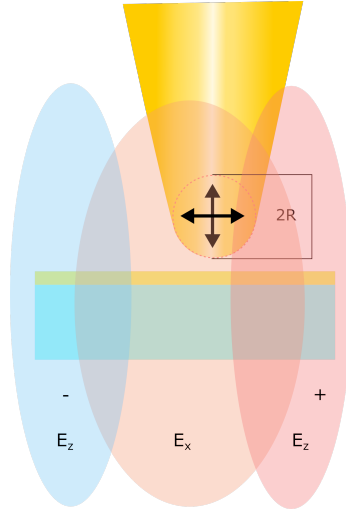


**Figure 6.8:** Sketch of the tip inside the focus field. Depending on the exact tip position the tip can couple to either the  $x$  component of the focus field centered in the middle, the  $z$ -component of the focus field shown as the two lobes with different sign or a combination of both field components.

them can be analyzed.

Furthermore, introducing a sample into the beam path will shift the focus in  $z$ -direction. In the experiment the focus is always aligned on the tip apex. For small tip-sample distances this is equivalent to placing the focus on the last interface between sample and air, facing the tip. Therefore, we denote the  $xy$ -plane with  $z = 0$ . To accomplish this in the simulation one way is to consider the phase shift due to the curved wavefront that is introduced by the lens or focusing unit. In the parabolic approximation, assuming the radius of curvature of the lens is much larger than the beam size near the sample interface, the additional phase can be expressed by

$$\phi_{comp} = -\frac{2\pi}{\lambda} \frac{x^2 + y^2}{2f_{wf}} = -\frac{2\pi}{\lambda} \frac{f_{wf} \tan(\theta_i)^2}{2} \quad (6.7)$$

with  $f_{wf}$  the focal length of the wavefront that can be chosen to compensate the  $z$ -shift. In figure 6.7 the factor  $\exp(i\phi_{comp})$  is already considered and the focus is shifted to  $z = 0$  by suitable choice of  $f_{wf}$ .

The transmission function for the focal fields  $|E_x|$  and  $|E_z|$  evaluated in the single spot at  $x=320$  nm,  $z=0$  and  $y=0$  is shown in figure 6.9C. The curves shown in Fig. 6.9C correspond to the spectrum that would be seen by the tip at this position if the input spectrum was completely flat. The large decrease of the field amplitude towards longer wavelength is the result of three effects. One is that the focus is aligned on the gold-sample interface for a wavelength of 780 nm which was displayed in figure 6.7. For other wavelengths the focus will slightly shift out of the evaluated focal plane. Furthermore, only a single pixel out of the focus area is considered. As the focus spot diameter scales with wavelength  $\lambda$ , the focus area scales with  $\lambda^2$ . Evaluating

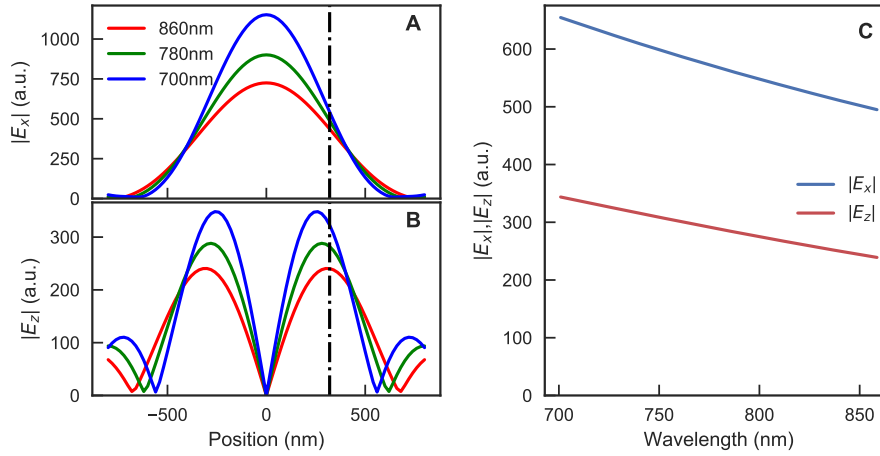


**Figure 6.9:** (A) and (B) show cuts through the focus area (fig. 6.7) along the x-axis for  $y=z=0$ , showing A, the  $|E_x|$  and B, the  $|E_z|$  component of the field, for three different wavelengths. (C) Field strength in one pixel ( $x=320 \text{ nm}, y=0, z=0$ ) given as a function of wavelength.  $|E_y|$  is 0 in this particular point.

only a single pixel thus results in a decrease proportional to  $\lambda^{-2}$ . This is illustrated in figure 6.9A and B by plotting a cross section through the 2D image of figure 6.7 for  $z=0$  and for three different wavelengths. With increasing wavelength the focus spot gets broader and the amplitude decreases. Finally, we already found that the transmission coefficients show the same decrease with wavelength and play a significant role in this calculation as well (compare figure 6.6C).

As I have shown before, in our measurements the  $S_{4f}$  signal is in good approximation proportional to the product of near field and reference field, while a background contribution can be neglected. To simulate the  $S_{4f}$  signal, we thus need to know the near field and the reference field. In the following, we will first derive the reference field  $\vec{E}_R$ , before turning to the near-field scattered by the tip interaction.

### The reference field

The reference field is simply constituted by light that is reflected off the gold layer in the focus area and collimated by the focusing lens. As we evaluate the reference field  $\vec{E}_R$  far away from the focus region we can treat the field within the laws of geometrical ray optics. Each ray is characterized by a particular plane wave of the angular spectrum representation. The signal that we are measuring on the photodiode is then an integral over all ray vectors with corresponding angles from  $\theta = 0^\circ$  to  $\theta_{max}$  and  $\phi = 0$  to  $360^\circ$ . We first calculate the light field that is focused by the lens and is incident on the glass-gold interface. As before, the action of the lens can be seen as a transformation from the x-y coordinate system to the spherical system. We express

the field by

$$\vec{E}^s = [\vec{E}_{inc}\vec{n}_\phi]\vec{n}_\phi, \quad \vec{E}^p = [\vec{E}_{inc}\vec{n}_\rho]\vec{n}_\theta. \quad (6.8)$$

with the normal vectors given in chapter 4.2. The reference field can now be written as a function of the k-vector as

$$\vec{E}_R(k_x, k_y) = [r_s(k_x, k_y) \cdot \vec{E}^s + r_p(k_x, k_y)\vec{E}^p]\sqrt{k_z/k}, \quad (6.9)$$

with  $r^s$  and  $r^p$  denoting the complex reflection coefficients of the gold layer as calculated by the transfer matrix method shown in chapter 4.1.2. We can see from these equations that even if our incident field is polarized only along x-direction ( $\vec{E}_{inc} = E_{inc}\vec{n}_x$ ) focusing the fields will generate a y-component also in the back-reflected collimated beam. With the normal vectors  $\vec{n}_\phi = -\sin(\phi)\vec{n}_x + \cos(\phi)\vec{n}_y$  and  $\vec{n}_\rho = \cos(\phi)\vec{n}_x + \sin(\phi)\vec{n}_y$  we get for the s-polarized field

$$\vec{E}^s = E_{inc} \left( \sin(\phi)^2 \vec{n}_x - \sin(\phi) \cos(\phi) \vec{n}_y \right) \quad (6.10)$$

and thus, larger azimuthal angles will increase the y-component of the s-polarized field. For the p-polarized field we get

$$\vec{E}^p = E_{inc} \left( \cos(\phi)^2 \cos(\theta) \vec{n}_x + \cos(\phi) \sin(\phi) \cos(\theta) \vec{n}_y - \cos(\phi) \sin(\theta) \vec{n}_z \right). \quad (6.11)$$

The p-polarized field furthermore depends on the angle  $\theta$ . Hence, both the s-and p-polarized field components, as well as the reflection coefficients are different and the ratio of s-and p-polarized components can change for the reflected fields. This is included in the simulation. In order to determine  $E_R$ , we have measured the spectrum reflected off the sample in our setup in the absence of the tip. This signal is given by

$$S_{w/o\ tip} \propto \iint_{(k_x^2 + k_y^2 \leq k^2)} |\vec{E}_R|^2 dk_x dk_y \quad (6.12)$$

In the case that the reference field is much stronger than the background field we can also neglect the background influence in the measured, non-demodulated spectra (previously labeled as  $S_{0f}$ ) and write  $S_{w/o\ tip} \approx S_{0f}$ . Figure 6.10A shows the simulated  $S_{w/o\ tip}$  signal for a flat input spectrum ( $E_{inc}(\lambda) = 1$ ). We can observe a slight decrease of the intensity for larger wavelengths. For the case that the incident laser beam is polarized along the x-direction and the spectrum has some arbitrary wavelength dependency, the incident spectrum can be factored out and the  $S_{w/o\ tip} \approx S_{0f}$  signal is directly proportional to the input spectrum  $E_{inc}^2$ . Since we have measured the  $S_{0f}$  signal, we can also calculate the intensity spectrum of the incoming laser beam by  $|E_{inc}|^2 = S_{0f,meas}/S_{0f,sim}$ , dividing the measured signal with the simulated response

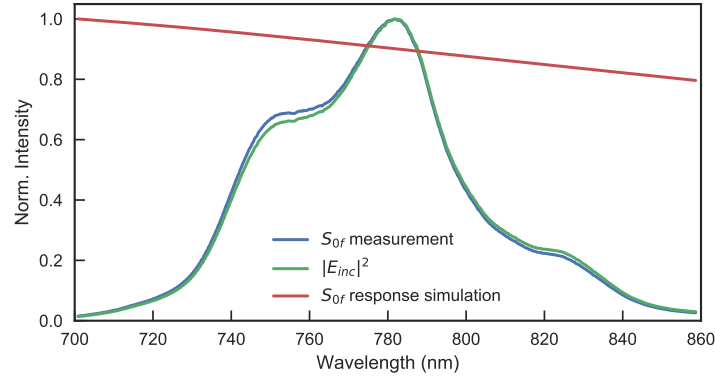


**Figure 6.10:** Simulated  $S_{0f}$  response for a flat incident spectrum (red), measured  $S_{0f}$  signal (blue) and retrieved  $|E_{inc}|^2$  (green)

due to the reflection off the gold film. The result is shown in figure 6.10B as the green curve. Clearly, the difference of the input spectrum to the  $S_{0f}$  spectrum is very small, such that in good approximation the  $S_{0f}$  spectrum could also be used as the input spectrum.

### 6.2.3 Extraction of distance-dependent near field spectra from measurements

The spectra that are recorded by the fast camera are, in first approximation, periodic with the tip modulation period and can be approximated by a Fourier series  $I_{\lambda}^F(t) = \sum_{n=-\infty}^{\infty} c_{n,\lambda} \cdot e^{in\Omega t}$ , where we in practice extract the complex Fourier coefficients  $c_{n,\lambda} = c_{n,\lambda}^*$  up to order  $n = 4$  from the measurements (compare 3.2).

The index  $\lambda$  designates the pixels of the camera.

In the following I present approach curves that are extracted from the spectra measured with the fast line camera. The steps are documented for one measurement exemplary in Figs. 6.11 to 6.12.

The recorded dataset consists of 60.000 consecutively recorded spectra. The integration time was  $4.6 \mu\text{s}$ , and the line readout rate was slightly slower, at  $f_{cam} = \frac{1}{4.6 \mu\text{s}} = 210 \text{ kHz}$ . With a tip modulation frequency of  $f_{mod} = 4.6 \text{ kHz}$ , this means that approximately 8 spectra are recorded per tip modulation period.

Fig. 6.11A shows the spectral region from 740 to 800 nm of the first 100 spectra, recorded during the first 480  $\mu\text{s}$ . The spectra are plotted linewise, as the time increases from top to bottom. The color code gives the count on each camera pixel. In these spectra the signal increase at the times the tip is approaching the gold film is already visible as a stripe pattern in this image, even without any further signal processing. This is, however, very rare and can be seen only in this particular example of a sharp gold tip with large near-field enhancement above a gold film

as the sample.

Averaging over the spectra results in the DC spectrum or the unmodulated spectrum, which we call the  $S_{0f}(\lambda)$  spectrum (Fig. 6.11B). The Fourier coefficients  $c_n$  with  $n = 1..4$  are extracted by evaluating equation (3.4), resulting in the higher-order demodulated spectra

$$S_{nf}(\lambda) = c_{n,\lambda} = \frac{1}{T_{mod}} \int_{-T_{mod}/2}^{T_{mod}/2} I_{\lambda}(t) e^{in\Omega t} dt. \quad (6.13)$$

With  $N=60.000$  measured spectra and the time span between measurements  $T_{cam} = f_{cam}^{-1} = 4.8 \mu s$  the integral transfers into a sum over  $k$ , where  $k$  indicates the  $k^{th}$  measurement:

$$S_{nf}(\lambda) = \frac{1}{N} \sum_{k=1}^N I_{\lambda,k} e^{in\Omega k T_{cam}} dt. \quad (6.14)$$

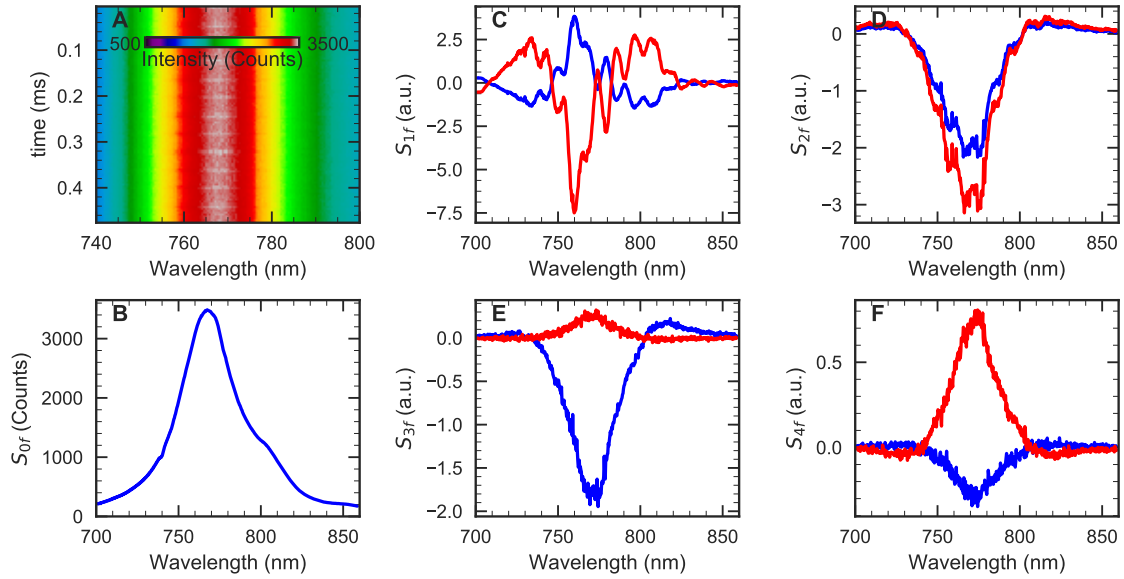


**Figure 6.11:** A: Color coded raw data of the first 100 recorded spectra on a gold surface over time. At specific times the tip is closer to the sample resulting in an increased intensity signal. The modulation of the tip is here already clearly visible as dark stripes in the intensity signal. B: The  $S_{0f}$  signal, which is defined as the sum over all 60.000 recorded spectra. C-F: The demodulated  $S_{1f}$  to  $S_{4f}$  spectra respectively. The blue curves show the real part, the red curves the imaginary part of the  $S_{nf}$  signals

The demodulated spectra  $S_{1f}$  to  $S_{4f}$  for a tip in close contact to a 30 nm gold surface are shown in Figs. 6.11C to 6.11F, respectively. The four spectra are complex, with the real part plotted as the blue curve and the imaginary part plotted as the red curve. As explained in Ch. 3.2, the angle  $\phi$  in the complex plane ( $\tan(\phi_{n,\lambda}) = \frac{Im(S_{nf}(\lambda))}{Re(S_{nf}(\lambda))}$ ) is determined by the starting condition,

i.e. the phase of the tip modulation cycle at the first camera recording. This implies the relation

$$\phi_{n,\lambda} = n \cdot \phi_{1,\lambda} \quad (6.15)$$

In the current example one finds an angle  $\phi = -62.3^\circ$ , which is independent of wavelength. In order to reconstruct the approach curve, we set the angle to zero by rotating the demodulated spectra in the complex plane

$$S_{nf}(\lambda) \rightarrow S_{nf}(\lambda) \cdot e^{-in\phi_1} \quad (6.16)$$

Furthermore, one can see that there is a strong modulation apparent on the  $S_{1f}$  signal, which can be found to much lesser extent also on the  $S_{2f}$  signal, but which is almost absent from the  $S_{3f}$  and  $S_{3f}$  signal. This modulation has its origin in the background signal. As the monochromatic measurements on a gold film have shown, for first order demodulation, the signal  $S_{1f}$  is dominated by the interference of reference and background signal. For second order demodulation,  $S_{2f}$ , we expect about equal contribution of background field and near field, and only for orders  $n > 2$  the near field significantly dominates the background field (compare Fig. 5.4F).

This is clearly reflected in Fig. 6.11. We have applied a low-pass filter to reduce the interference (by a Fourier transform on the k-axis, then applying a filter and transforming back to the wavelength axis). The result can be seen in Fig. 6.12. All four spectra are now rotated in the complex plane such that the resulting spectra are predominantly real with negligible imaginary part. Due to filtering, the spectra are now smooth. However, in Fig. 6.12A the modulation has not been completely removed. This is because the modulation frequency is so low that after Fourier transformation its signature overlaps with that of the spectral shape on the spatial axis. The approach curve can now be assembled by adding the Fourier components, i.e., the demodulated spectra:

$$I_\lambda(d) = \sum_{n=-4}^4 c_{n,\lambda} e^{in\Omega t(d)}, \quad (6.17)$$

with  $c_{-n} = c_n^*$ , and where the time and distance are connected by equation (3.5).

Since we always measure the relative spectral change  $\frac{I_\lambda(d) - I_\lambda(2A)}{S_{0f}}$  with the modulation amplitude  $A$ , we here introduce the near-field signal

$$N(\lambda, d) = \frac{I_\lambda(d) - I_\lambda(2A)}{S_{0f}} \quad (6.18)$$

that is used in the following sections.

Fig. 6.12E shows the assembled approach curve  $N(\lambda, d)$  for the measurement on the gold film.

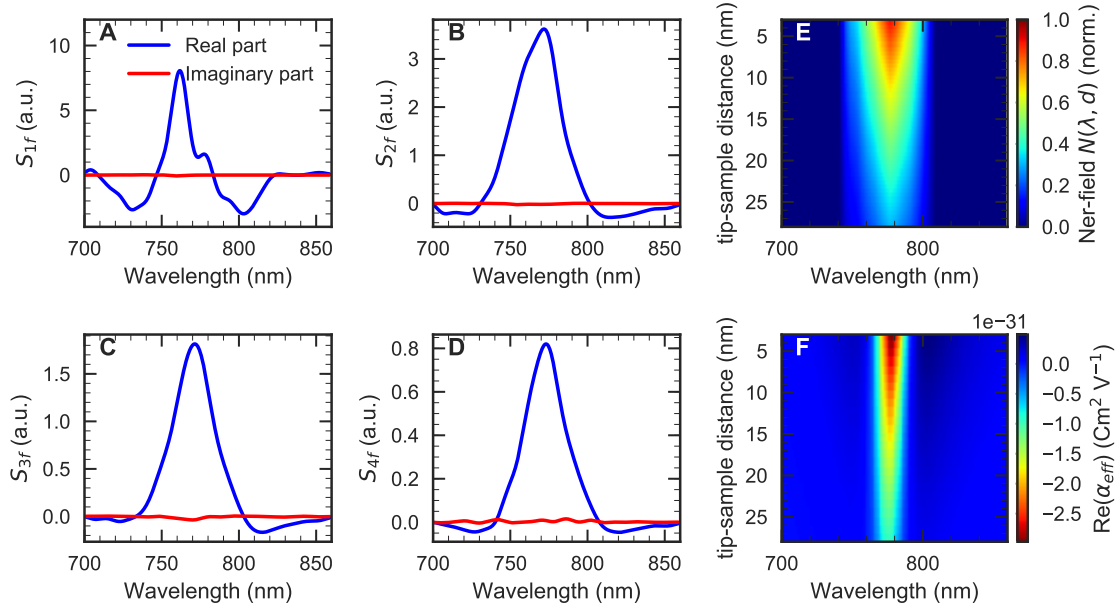


**Figure 6.12:** A-D: The reconstructed  $S_{1f}$  to  $S_{4f}$  spectra from the measurements close to the 30 nm gold film after phase correction and filtering in the Fourier domain. E: Calculated approach  $N(\lambda, d)$  from the reconstructed data. F: Simulated approach with an incident field polarized perpendicular to the sample and modeling the tip polarizability by an ellipse to mimic a blunt tip that was probably used in the measurement.

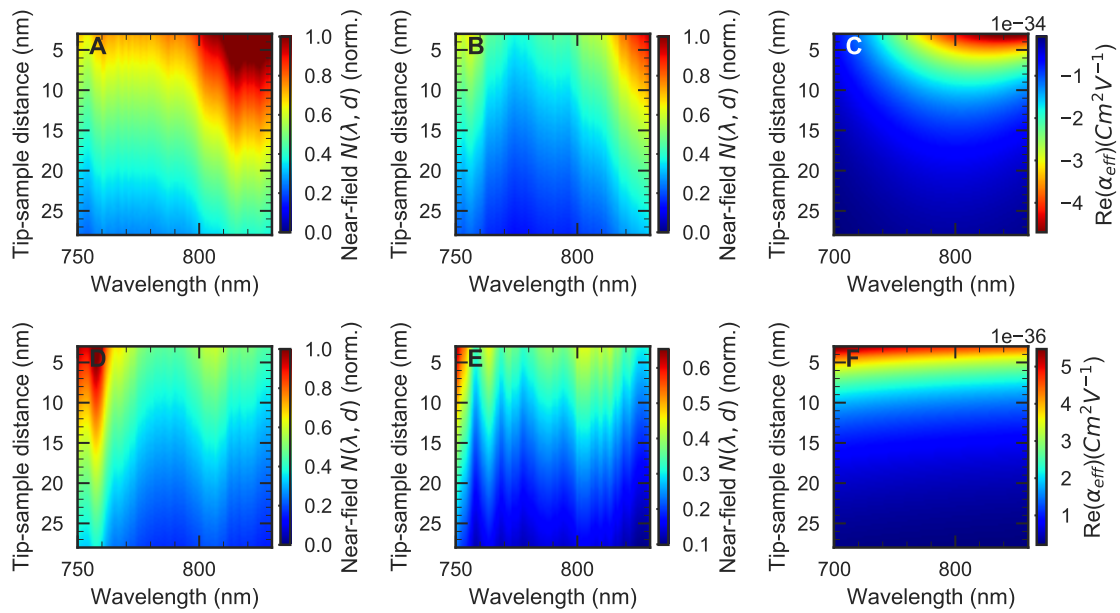
One can see a strong increase for small tip sample distances in a roughly 40 nm broad spectral band centered at 780 nm. The plotted signal is expected to resemble the real part of the effective polarizability  $\alpha_{eff}$  that was shown in Fig. 6.5(cmp. Ch. 6.2.1). In agreement with the previous simulation, the calculated effective polarizability from the measurement in this case also shows a signal increase in a limited spectral range. There are, however two major discrepancies: firstly, the measured increase is over a much narrower spectral range (roughly one fourth), and it is at a slightly different center wavelength (about 60 nm shorter). Secondly, the measured approach shows a much weaker distance dependence than the calculated one. Its decay length is about 15 nm, whereas the near field decay length of very sharp gold tips has been shown to be <5 nm [154]. This indicates that the tip I used was rather blunt when this measurement was recorded. It seems that for a blunt tip, the tip polarizability is better described by an ellipse (cmp. Ch. 4, especially equation (4.111)). As was shown already in Fig. 4.16, the polarizability of an ellipse reflects that of a resonance with a rather small spectral width and the center position depends on the parameters of the ellipse. A higher aspect ratio of the radius  $R_z$  to the radius  $R_x$  of the ellipse shifts the resonance more towards longer wavelengths. The sphere was in this case just a special case with  $R_x = R_y = R_z$  and showed the resonance around 500 nm. To test if an elliptical tip can explain the measurement, I have calculated the approach curve for a blunt tip with radius of  $R_x = R_y = 20$  nm and an aspect ratio  $R_z/R_x$  of 5.3, shown in

Fig. 6.12F. As we can see, in this case this simulated approach fits the approach data from the measurement much better, as now the decay length matches and the resonance is located at the right wavelength. Overall, only the bandwidth of the resonance seems to be a factor 2 narrower, which could be caused by a non-uniformly damaged tip with respect to the simulation. This also demonstrates how the tip shape can highly affect the measured spectrum. In next section I will show additional measurements on a gold surface, but this time with a tip that is not that blunt. In that case, the previously shown simulations for the tip-sample interaction can be reproduced.

#### 6.2.4 Near-field spectra on flat films

Here we show the previously simulated and discussed approach spectra reproduced from measurements recorded over a flat gold film. Each of the measurements was recorded with the same tip and the same gold film, but with the tip placed at a different position within the focus. Unfortunately, we do not know where in the focus the tip was placed, the focus alignment was simply changed between two measurements.

Figs. 6.13 A,B,D, and E show four such approach spectra  $N(\lambda, d)$  retrieved over the gold film



**Figure 6.13:** A, B, D, E: 4 measured approaches on the gold film. For each measurement the approach spectrum was reconstructed from the measurement data. A and B show a different spectral characteristic as D and E. For A and B probably coupling to the z-component of the tip ( $\alpha_{tip,zz}$ ) was predominant and is comparable to the simulated  $Re(\alpha_{eff})$  for coupling to the z-component shown in C. For D and E the spectral approach is rather flat and resembles the result of coupling to the in-plane component of the tip shown in the simulated result of F.

(cmp. Eq. (6.18)). From their appearance, they can be grouped in two pairs: The approach spectra shown in Figs. 6.13 A and B display for small tip-sample distances a signal increase

at longer wavelengths, from  $\lambda > 780$  nm to the long-wavelength end of the measurement interval. This resembles the real part of  $\alpha_{eff}$  assuming that mainly the z-polarizability of the tip was excited (simulation shown for comparison in Fig. 6.13C). The other two approach spectra, in Figs. 6.13 D and E, in contrast, show a rather spectrally flat increase, over the whole spectral range of the measurement. The signal increase with decreasing tip-sample distance appears stronger at shorter wavelengths. This resembles the expected behavior for the case that predominantly the x-polarizability  $\alpha_{tip,xx}$  was excited during this measurement.

In conclusion, I have shown that with our measurement geometry, depending on the position of the tip in the focus, either the z-oriented tip dipole or the x-oriented tip dipole can be excited, or a superposition of the two. For both cases the near-field signal is completely different to that of a blunt tip shown in the previous section that was better modelled by an ellipse. Thus great care has to be taken when aligning this setup to excite tip and sample in the desired way. Otherwise evaluation of the data can become quite challenging.

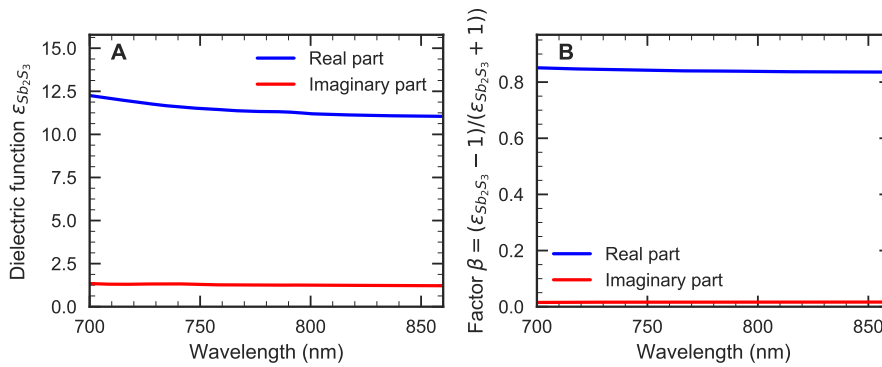


**Figure 6.14:** (A) Dielectric function  $\epsilon_{Sb_2S_3}$  for our wavelength range. (B) Sample dependent factor  $\beta = (\epsilon_{Sb_2S_3} - 1)/(\epsilon_{Sb_2S_3} + 1)$ . Both the dielectric function as well as the factor  $\beta$  used for the calculation of an effective polarizability are spectrally flat in the wavelength region supported by our laser source.

This difficulty is lessened in the second side-illumination setup (which was introduced in Sec. 3.4). In that case, where the tip and sample are illuminated from the side (in the xz-plane, under  $20^\circ$  from the x axis), the polarization of the light field at the tip can be controlled to a much higher degree. Here, for comparison, we show a measurement of local spectra recorded above a flat Sb<sub>2</sub>S<sub>3</sub> film, where the electric field vector was aligned along the y-axis, i.e., perpendicular to the tip axis and within the sample plane. The laser beam was focused with an 0.4 NA reflective microscope objective. This means that also in the focus the light was predominantly polarized along the y axis. We can therefore safely assume that excitation of  $\alpha_{tip,zz}$  was negligible in comparison with  $\alpha_{tip,yy}$ . Furthermore, the illuminating laser beam does not travel through the sample, such that unwanted reflections from substrate and sample surfaces are suppressed.

Instead of using a strong reflection off the sample surface as a reference, a reference beam is generated in a reference arm with adjustable delay and reference field strength. The general working principle for evaluation of the so recorded spectral interferograms was described in Sec. 3.4. The sample was a flat  $\text{Sb}_2\text{S}_3$  film (the same as in Sec. 3.4.).  $\text{Sb}_2\text{S}_3$  is a semiconductor with a band gap of 1.7 eV, such that our laser light excitation is well below the band gap. This means that, in the spectral range accessible in our experiment, it behaves like a dielectric with a quite flat dielectric function that is shown in Fig. 6.14A.

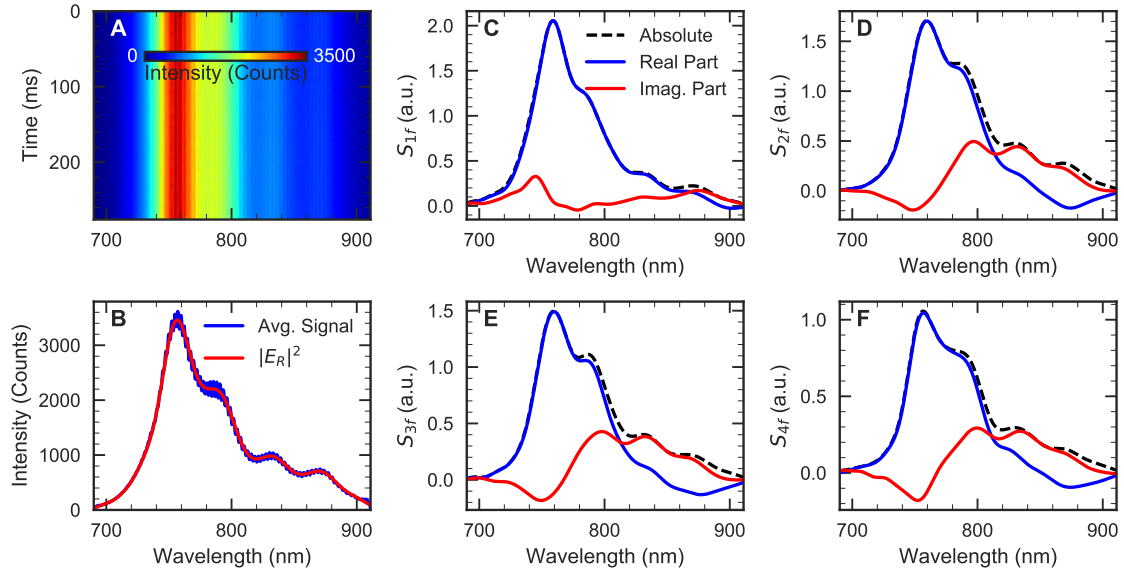


**Figure 6.15:** (A) The first 276 ms of the recorded SNOM intensity dataset  $I_{\lambda,t}$  on the  $\text{Sb}_2\text{S}_3$  film. (B) The squared reference spectrum  $|E_R|^2$  (red) and the average signal of the measurement (blue). (C-F) Real, imaginary and absolute value of the calculated  $S_{1f}$  to  $S_{4f}$  spectra.

Figure 6.15 shows an example of recorded local spectra above  $\text{Sb}_2\text{S}_3$  with the side-illumination setup. The data shown in Fig. 6.15 are from the same measurement series as those shown in Fig. 5B of ref. [117]. The recorded spectra are shown in Fig. 6.15A as a function of time and wavelength, with the count on each CCD pixel denoted by the color-code. Fig 6.15B shows the average spectrum in blue, and the reference spectrum extracted the same way as described in Sec. 3.3 in red.

Then the  $S_{1f}$  to  $S_{4f}$  spectra are extracted by (i) demodulating the original data pixel-wise with  $1f$ ,  $2f$ ,  $3f$ ,  $4f$ ; (ii) converting from the wavelength to the  $k$ -axis, (iii) Fourier transform to the spatial axis, (iv) filtering with the reference arm length, (v) transforming back to the  $k$ -axis and (vi) back to wavelength axis, and finally (vii) correcting the phase. The result is shown in Fig. 6.15C-F. One can see that the correction of the phase was not fully successful in this case either: the resulting  $S_{1f}$  to  $S_{4f}$  spectra are not purely real. This means that the phase was not constant over the spectral region. This is probably due to a non-ideal tip shape, since

the sample was an unstructured film with a flat spectral response. Here we correct for the tip-shape-caused deviation by simply setting the  $S_{1f}$  to  $S_{1f}$  spectra to real values (or by using a wavelength-dependent rotation angle in the complex plane to correct the phase to  $\varphi = 0$ ).

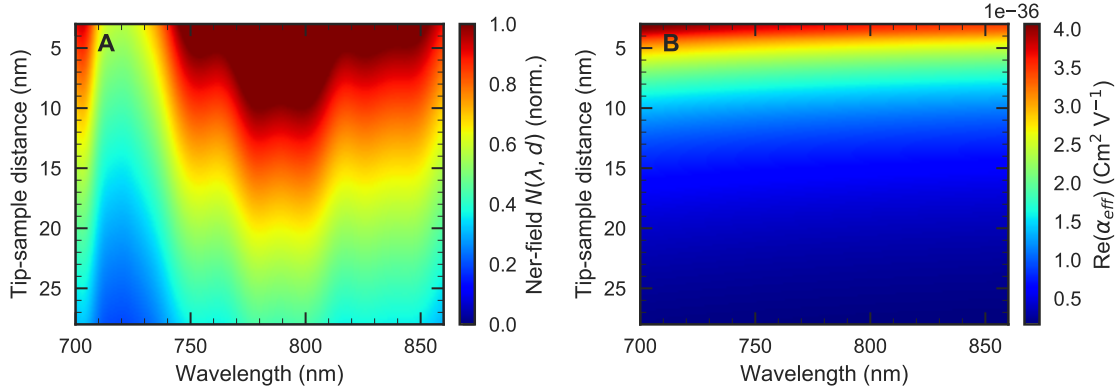


**Figure 6.16:** (A) Reconstructed spectral near-field approach data  $N(\lambda, d)$  from the SNOM measurement on the  $\text{Sb}_2\text{S}_3$  film. (B) Simulated real part of the effective polarizability for a  $\text{Sb}_2\text{S}_3$  film and excitation of the tip along the  $y$ -axis.

The approach curve assembled from the  $S_{1f}$  to  $S_{4f}$  spectra is shown in Fig. 6.16A (cmp. Eq. (6.18)) together with the  $\text{Re}(\alpha_{eff})$  calculated for a tip excited along the  $y$  direction as a function of tip-sample distance in Fig. 6.16B. For the simulation the dielectric function enters in the sample dependent coefficient  $\beta = (\epsilon_{\text{Sb}_2\text{S}_3} - 1)/(\epsilon_{\text{Sb}_2\text{S}_3} + 1)$  that is used for the calculation of the effective polarizability.  $\beta$  is also spectrally flat, as is demonstrated in Fig. 6.14B. The tip polarizability  $\alpha_{tip,yy}$  that enters the simulation is again modelled by a gold sphere with 10 nm radius.

Overall, the results show a signal increase over a rather wide spectral range, in good agreement to what is expected for this illumination geometry. However, where the calculated  $\text{Re}(\alpha_{eff})$  steadily increases towards short wavelengths, the measured curve decreases to both spectral sides, the long- as well as the short-wavelength side resulting in a broad maximum (or rather a dip around 720 nm in Fig. 6.16A). Even though the measured approach curve shown in Fig. 6.16A has been normalized by the reference spectrum  $|E_{ref}|^2$ , this decrease towards both sides may be caused by the finite bandwidth of the laser spectrum. Altogether, the approach curve measured with the side-illumination setup shows strongly reduced noise and a much improved image quality, and its spectral shape is in better agreement with the theoretical behavior. The former is probably due to the increased reference field strength, while the latter may be due to the improved control of the vectorial field composition in the laser focus in the side-illumination setup.

### 6.3 Local spectra on Squaraine dye molecules

In previous sections local spectroscopy on flat surfaces was discussed. In the following I want to apply the understanding of SNOM signals that we have achieved there to a more complex sample, an anisotropic dye material named ProSQ-C16. The anisotropic dielectric function of this dye has a drastic impact on the interaction between tip and sample. In particular, the orientation of the dye molecules in space will influence the amount of tip-sample interaction for a given field polarization.

The measurements presented in this chapter contribute to the understanding of the still relatively new dye material on a nanoscale level and may help in future experiments, e.g. regarding the use of the dye as a promising new organic solar cell material.

In the first subsection, 6.3.1, a short introduction to the dye material is given.

To be able to compare measured local SNOM spectra to simulated results the dielectric function of the dye must be known. In subsection 6.3.2 therefore angle dependent transmission measurements are presented from which the dielectric function can be extracted by modeling the dye monomers as two-level systems in a quantum mechanical model.

The last subsection presents local SNOM spectra on the dye material. Supported by beam scans and near-field simulations these results demonstrate the ability to record and understand SNOM signals even for highly anisotropic samples. Finally, measurements on a non-uniform sample demonstrate chemical specificity on a sub-diffraction-limited length scale.

### 6.3.1 Introduction to squaraine dyes

Squaraine dyes are a class of dye molecules that show strong fluorescence in the red or infrared region and could be used as molecular thin film material for energy generation (e.g. as a thin-film solar cell) or energy storage (thin-film batteries). A four-membered ring is the central core of the squaraines that is derived from squaric acid [188]. This ring behaves as a strong electron-acceptor group. The four-membered ring is further linked to two electron-donating side groups either in a symmetric (same side groups) or asymmetric (different side groups) manner [188]. Thus, squaraines can be described as small molecular quadrupolar donor-acceptor-donor (D-A-D) chromophores. They can be synthesized through environmentally friendly reactions and thus are a promising material for organic solar cells or semiconductors or find use as NIR probes [189–192].

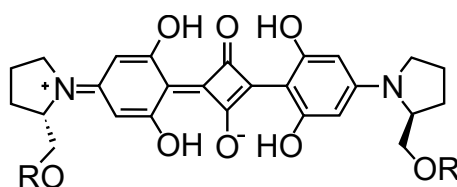


Figure 6.17: ProSQ-C16 molecular structure with  $R = C_{16}H_{33}$

We investigate the dye ProSQ-C16 recently used for organic photodiodes by Schulz et al. [193]. Figure 6.17 shows the molecular structure.

To understand the optical properties of the relatively unknown dye, we employ transmission spectroscopy and finally local nanoscale SNOM spectroscopy. These methods will help us to get insight into material properties. Essentially, the different methods combined help us to gain a better understanding of the measured sSNOM spectra and the tip-sample coupling process. The new findings may be applied to all kinds of samples in future works.

### 6.3.2 The Dielectric function of squaraine dyes

In all light-induced coupling processes the dielectric function of the sample plays a crucial role, as it describes the extent to which the medium concentrates the electric flux. Having access to this material property is a prerequisite to predicting and simulating spectra e.g. for the sSNOM tip-sample interaction process.

The sample we measure is spincoated on either a glass substrate or the in-line interferometer substrate used for SNOM measurements and is annealed at a temperature of 300 °C. The annealing process leads to an (self-) aggregation of adjacent monomers resulting in an excitonic coupling of two (or more) chromophores [193, 194]. As a consequence of the coupling, the two excited states of the two dipoles split into two levels separated by an energy  $2V$ , which is

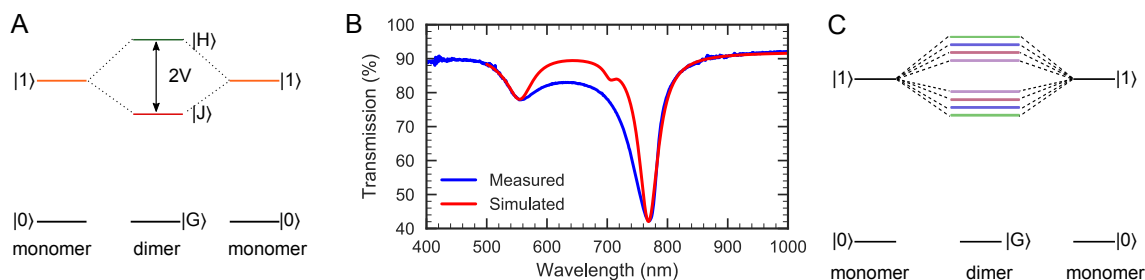


**Figure 6.18:** A: Energy levels for two two-level systems coupling to each other. B: Measured transmission spectrum at  $0^\circ$  incidence (blue curve), together with the first quantum mechanical simulation (red curve). C: Energy levels like in A, but taking into account a splitting in different energy levels, e.g. by taking into account a variation of the alignment of the dye molecules to their neighbors.

also known as Davydov splitting [194, 195] (compare figure 6.18A). Hereby, the red shifted band is called the J-Band or the J-aggregate, named after Edwin Jelly, whereas the blue shifted (hypsochromic shifted) band is called the H-Band or H-Aggregate [196–201]. ProSQ-C16 has two branched side-chains that reportedly lead to Davydov splitting [191]. In comparison, squaraines with linear alkyl side that show triclinic crystal structures do not support Davydov splitting but are instead described by charge transfer interactions along the chain [202, 203]. The measured spectrum recorded at an incident angle of  $0^\circ$  shown as the blue curve in Figure 6.18B supports these findings: we observe two absorption peaks located at 769 nm (or 1.61 eV) and 555 nm (or 2.23 eV), resulting in a splitting energy  $2V$  slightly above 600 meV. The monomer energy of 1.9 eV, probed by a photon with a wavelength of 652 nm, can be directly deduced from the transmission spectra as arithmetic mean of the J- and H-band resonances.

From the structure of the molecule we can furthermore already see that the molecule is not rotationally symmetric and hence it is expected to result in a packing that supports optical anisotropy, i.e. a different dielectric response to light polarized perpendicular to the sample plane (out-of-plane component) and light polarized parallel to the sample plane (in-plane component).

We now simulate the dielectric function by modeling the dye molecules as a 2-level system in a quantum mechanical model. This model is then compared to measured transmission spectra. Here, we firstly start with the already mentioned spectrally resolved transmission measurement at an incident angle of  $0^\circ$  shown in figure 6.18B. In this case we allow only an interaction with the in-plane component of the dielectric function of the dye. In a second step we will analyze spectra recorded under higher incident angles.

Within a quantum mechanical model as outlined in chapter 4.1.1 we now describe each monomer molecule as a dipole.

Thus, for the ProSQ-C16 dye, we describe the coupling of the two dipoles with the same energy  $E_1 = \hbar\omega_1 = E_2 = \hbar\omega_2 = 1.9$  eV in a quantum mechanical model governed by the Hamilton operator

$$\begin{aligned} \hat{H}_0 = & \hbar\omega_0 |0\rangle\langle 0| + \hbar\omega_1 |1\rangle\langle 1| + \hbar\omega_2 |2\rangle\langle 2| \\ & + \sum_{n=0}^2 \hbar\omega_{vib} (\hat{n}_n + \frac{1}{2}) \\ & + \sum_{n=1}^2 \hbar\omega_{vib} \left[ \lambda \cdot (\hat{a}_n^\dagger + \hat{a}_n) + \lambda^2 \right] |n\rangle\langle n| \\ & + V(|1\rangle\langle 2| + |2\rangle\langle 1|) \end{aligned} \quad (6.19)$$

Here  $\hat{a}_n^\dagger$  and  $\hat{a}_n$  are the phonon creation and annihilation operators and  $\hat{n}_n = \hat{a}_n^\dagger \hat{a}_n$  is the number operator that counts the number of vibronic states (cmp. chapter 4.1.1.2). The first three terms in equation (6.19) then describe energies of the electronic states, the fourth term is the Hamiltonian of the non-shifted harmonic oscillator describing the vibrational modes and the last two terms describe an additional shift of the oscillator along the nuclear coordinate and an electronic coupling of the two states. Here the shift of the potential energy surface (PES) is determined by the Huang Rhys factor  $\lambda$ . The last term describes a coupling between the two dipoles with a coupling energy  $V = \hbar\omega_c$ . From the already estimated maximum coupling energy we found  $V = \hbar\omega_c = 325$  meV to give the best match to the measurement.

For the vibrational energy, a typical coupling energy of the ring breathing mode found in molecules is around  $1000\text{-}1400$   $\text{cm}^{-1}$  or  $130\text{-}160$  meV [203, 204]. We found that a vibrational energy of  $E_{vib} = \hbar\omega_{vib} = 130$  meV fits very well to our experimental measurements.

The Huang-Rhys factor  $\lambda$  is a measure for the shift of the potential energy surface and hence a magnitude of the vibronic coupling [203]. With increasing  $\lambda$  more sidepeaks around each eigenfrequency  $\omega_n$  will appear in the spectra. We do not see any obvious sidepeaks in our spectra and hence only allow for a weak vibronic coupling with a value of  $\lambda = 0.2$ . A weak vibronic coupling might be justified, if we assume a fast energy transfer along the aggregate length of the squaraine dyes with a relatively long coherent length, as was reported by Higgins et al. for a pseudoisocyanine J-aggregate with a coherent length of around 50 nm [92, 205]. In that case the energy cloud around the nuclei would not be affected much at the time of the excitation, resulting in only weak coupling to the nuclear degree of freedoms and therefore a small Huang Rhys factor.

The response of the sample to light excitation can then be expressed by a typical Lorentzian

line shape by

$$\chi(\omega) = \frac{n_0}{\hbar\epsilon_0} \sum_n |\mu_n|^2 \cdot \left[ \frac{1}{\omega - \omega_n - i\gamma} + \frac{1}{\omega + \omega_n + i\gamma} \right], \quad (6.20)$$

with  $\omega_n$  the energy states that solve the Schrödinger equation  $\hat{H}_0\psi = \hbar\omega\psi$  and  $\mu_n$  the magnitudes of the dipole moments.  $n_0 = 2.9 \times 10^{27} \text{ m}^{-3}$  is the fixed dipole density that we estimated from the crystal structure of similar squaraines from Balzer et al. [191]. The damping factor  $\gamma$  defines the linewidth of the Lorentzian. Here, we used a value for  $\gamma$  of  $4 \times 10^{13} \text{ s}^{-1}$  (or  $t = 25 \text{ fs}$ ) for the J-aggregate and  $10 \times 10^{13} \text{ s}^{-1}$  (or  $t = 10 \text{ fs}$ ) for the H-aggregate peak. In the simulation we left the dipole density fixed and used an effective dipole moments used which were found to be around 4.2 D for the monomer and 5.6 D for the J-aggregate as well as 3.7 D for the H-Aggregate.

To finally simulate the transmission spectrum we use a transfer matrix formalism as described in chapter 4.1.2 and the dielectric susceptibility is used to calculate the refractive index by

$$n(\omega) = \sqrt{1 + \chi(\omega)}. \quad (6.21)$$

The resulting simulated transmission spectrum is shown as the red line in Fig. 6.18B. Hereby the lower energy side of the J-aggregate resonance and the higher energy side of the H-aggregate resonance can be well reproduced. The small peak at around 705 nm originates from the weak phonon coupling and could be removed by decreasing the Huang-Rhys factor to 0. However, in general a weak coupling to phonon modes is more meaningful and is used in the next simulations as well, therefore we kept it in this simulation. In total however, the parameters for this model can never be chosen so that the calculated spectrum describes the measurement sufficiently well. In particular, we can observe that the two resonances are broader than in the simulation, but only to one side: the H-aggregate band is broader on the low energy side and the J-aggregate band is broader on the high energy side. This is not surprising, because the spincoating process will hardly lead to smoothly aligned monomers, but will distribute them over the sample resulting in defined angles between two coupling dipoles. A different alignment will alter the coupling energy. Hence, a specific distribution of aggregate alignment and thus of different energy splittings must be taken into account. This is illustrated by the energy scheme in figure 6.18C.

Following this discussion, we take into account the orientation of the dipoles describing each monomer and thus allow for an additional degree of freedom. Figure 6.19 illustrates two dipoles with dipole moment  $\vec{\mu}_1$  and  $\vec{\mu}_2$  spanning an angle  $\theta$  to each other.

The potential energy of such a coupled two dipole system can be classically described as

$$V = \frac{1}{4\pi\epsilon_0} \frac{\vec{\mu}_1 \cdot \vec{\mu}_2 - 3(\vec{\mu}_1 \cdot \vec{n})(\vec{\mu}_2 \cdot \vec{n})}{r^3} \quad (6.22)$$

with  $r$  the distance between two dipoles and  $\vec{n} = \vec{r}/r$ .

Consequently, it follows that the coupling energy is given by the angle between the two dipoles with a potential maximum

$$V_{max} = \frac{\mu_1 \cdot \mu_2}{4\pi\epsilon_0 r^3} \quad (6.23)$$

for an angle of  $\theta = 0^\circ$  or dipoles aligned in a head-to-head configuration. From this equation, we can further approximate the distance  $r$  between two dipoles by the previously found dipole moment and maximum coupling energy to a value of around 1-2 nm. Hence, for the squaraine dye the distance between the two dipoles is on the same order as the dipole lengths. In this case the direction of the dipoles must be distinguished. In the following we consider the potential energy of both a head-to-head and head-to-tail orientation separately. Hereby we assume that the angle to the z-axis is the same for both dipole moments so that each of them spans an angle  $\theta/2$  to the z-axis as illustrated in figure 6.19.

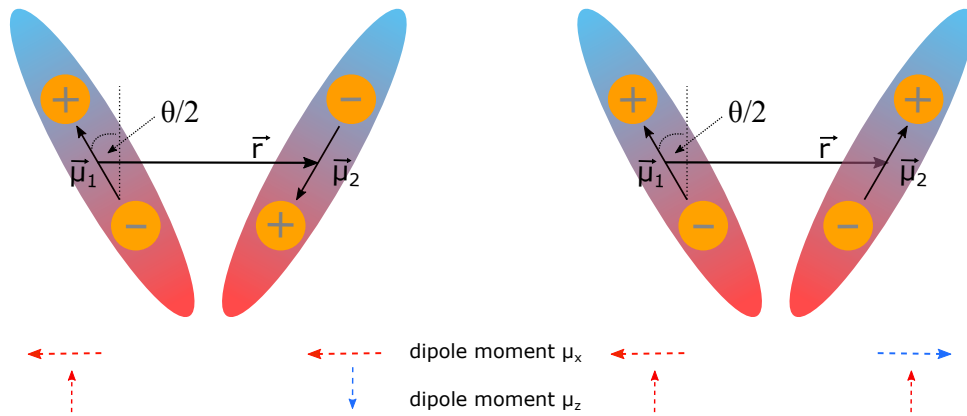


**Figure 6.19:** Head to tail and head to head orientation of the two dipoles

For a head-to-tail configuration the dipole of both monomers share the same x-direction (along the dipoles or parallel to the vector  $\vec{r}$ ), but have an opposite z-direction. In this case we can write

$$\mu_{1,ht} = \mu_1 \begin{pmatrix} -\sin \frac{\theta}{2} \\ 0 \\ \cos \frac{\theta}{2} \end{pmatrix}, \quad \mu_{2,ht} = \mu_2 \begin{pmatrix} -\sin \frac{\theta}{2} \\ 0 \\ -\cos \frac{\theta}{2} \end{pmatrix} \quad (6.24)$$

When we further define the direction of the distance vector  $\vec{r}$  to be positioned along the positive

x-axis ( $\vec{r} = (1, 0, 0)$ ) this leads to a potential energy

$$\begin{aligned}
 V_{ht} &= \frac{1}{4\pi\epsilon_0} \frac{\vec{\mu}_1 \cdot \vec{\mu}_2 - 3(\vec{\mu}_1 \cdot \vec{n})(\vec{\mu}_2 \cdot \vec{n})}{r^3} \\
 &= \frac{1}{4\pi\epsilon_0 r^3} \mu_1 \mu_2 \left( -\cos(\theta/2)^2 - 2\sin(\theta/2)^2 \right) \\
 &= \frac{1}{4\pi\epsilon_0 r^3} \mu_1 \mu_2 \left( -\frac{1}{2}(\cos(\theta) - 3) \right)
 \end{aligned} \tag{6.25}$$

For the case of a head-to-head configuration the vectors share the same z-direction but are opposite in x-direction. Hence, we can deduce

$$\mu_{1,\vec{hh}} = \mu_1 \begin{pmatrix} -\sin \frac{\theta'}{2} \\ 0 \\ \cos \frac{\theta'}{2} \end{pmatrix}, \quad \mu_{2,\vec{hh}} = \mu_2 \begin{pmatrix} \sin \frac{\theta'}{2} \\ 0 \\ \cos \frac{\theta'}{2} \end{pmatrix} \tag{6.26}$$

and

$$\begin{aligned}
 V_{hh} &= \frac{1}{4\pi\epsilon_0 r^3} \mu_1 \mu_2 \left( \cos(\theta/2)^2 + 2\sin(\theta/2)^2 \right) \\
 &= \frac{1}{4\pi\epsilon_0 r^3} \mu_1 \mu_2 \left( -\frac{1}{2}(3 - \cos(\theta)) \right)
 \end{aligned} \tag{6.27}$$

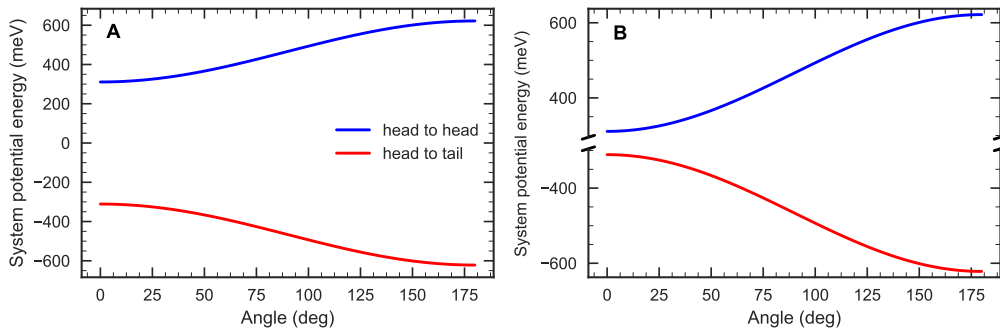


**Figure 6.20:** Potential energy  $V$  of the head to head and head to tail model for different angles  $\theta$

Figure 6.20A shows the potential energy for both the head-to-head and head-to-tail configuration. Within this description the absorption bands of the squaraine dye can be understood as a strong coupling of aggregated monomers that split the energy level in two new energy levels  $|E_H\rangle$  and  $|E_J\rangle$  which leads to the J-band with a negative potential energy and the H-Band with a positive potential energy. Hence, both bands correspond to two kinds of oscillatory motion in either a head to tail (J-band) or head to head (H-band) dipole configuration. With increasing angle  $\theta$  the potential energy of the of J-Band decreases, whereas the energy of the H-Band increases (compare figure 6.20B). Further we can infer that the head-to-tail orientation results in an

increased dipole moment along the x-direction whereas the z-component of the dipole vectors cancels out. For a head-to-head orientation the dipole moment in z-direction is increased and the component along x-direction cancels out.

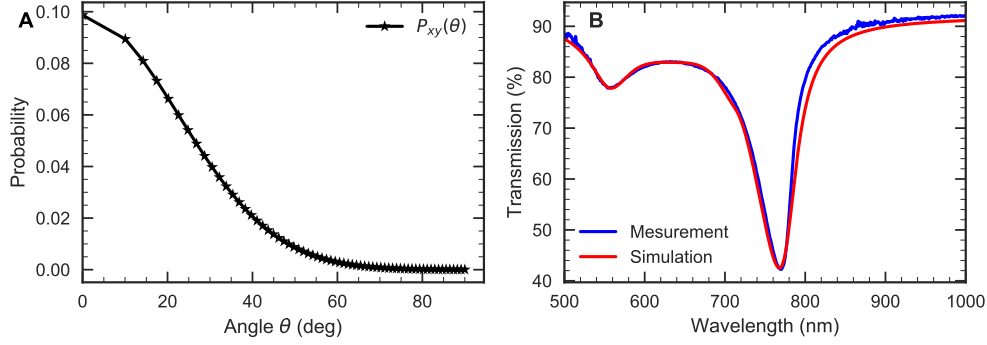


**Figure 6.21:** A: Distribution  $P(\theta)$  of in-plane angles used for the simulation. B: 0deg incident spectrum and simulated spectrum using the distribution  $P(\theta)$ .

When illuminating the sample with a diffraction-limited laser spot a large number of molecules is excited, which means in total we have an angular distribution of dipoles at the laser spot. In our model this can be included by calculating the electric susceptibility  $\chi(\omega)$  by averaging over molecular dimer oscillators with different coupling energies. Or in other words, we consider an angle dependent probability distribution of the dipoles in our sample and accordingly change the density  $n_0$  to

$$n_0(\theta) = n_0 \cdot P(\theta), \quad \sum_{\theta > 0} P(\theta) = 1 \quad (6.28)$$

A light beam incident on the sample at  $0^\circ$  incidence angle has only electric field components parallel to the surface. Hence, a transmission measurement at  $0^\circ$  incidence is only sensitive to in-plane dipole moments. That means the dipole moment probed by such a measurement is that of the projection onto the xy plane:

$$\mu_{xy}(\theta) = 2\mu_0 \cos(\theta/2) \quad (6.29)$$

In terms of coupling energies with  $\hbar\omega_c = \hbar\omega_{c,max} \cos(\theta)$  we can write

$$\mu_{xy}(\theta) = \frac{\mu_0 P(\theta) \omega_c(\theta)}{\omega_{c,max}} \quad (6.30)$$

Also, as the right side of the J-agg resonance and the left side of the H-agg resonance can already be well described by two coupled dipoles without an angular distribution, we can infer that higher coupling energies (or small angles) are more likely to be found than smaller coupling

energies. To match the simulation with the experimental results we used a Gaussian distribution centered around  $0^\circ$  given by

$$P(\theta) = e^{-\frac{\theta^2}{2\sigma^2}} \cdot \frac{2}{\sqrt{2\pi}\sigma} \quad (6.31)$$

with  $\sigma = 22.6$ , which is shown in Fig. 6.21A. The distribution is symmetric in  $\theta$  around  $\theta = 0$ , i.e. negative angles have the same probability as their positive counterpart. Hence, we only considered positive angles to normalize the sum in eq. 6.28.

With this angle distribution we then simulated the transmission spectrum. This is shown in Fig. 6.21B as the red line together with the measurement shown as the blue line. Hereby, we used an effective dipole moment for the low energy side (J-agg) of  $\mu_{0,1} = 7.6D$  and the high energy side (H-agg) of  $\mu_{0,2} = 3.9D$ . To get a better match with the measurement we additionally increased the factor  $\gamma$  for the case of no coupling by a factor of 3 compared to the H-aggregate band, which is related to a part of non-aggregated monomers and results in a broader line width for the monomer peak. As we can observe from Fig. 6.21B the simulated result matches the measurement very well. Thus, the angular distribution of dipole angles solves the discrepancy of the simulation using only one fixed coupling energy and gives us a good intuitive picture of the microscopical distribution of the dye molecules.

The dielectric function used to produce the transmission spectrum in Fig.6.21A as the red line is shown in Fig. 6.22A as the red line.

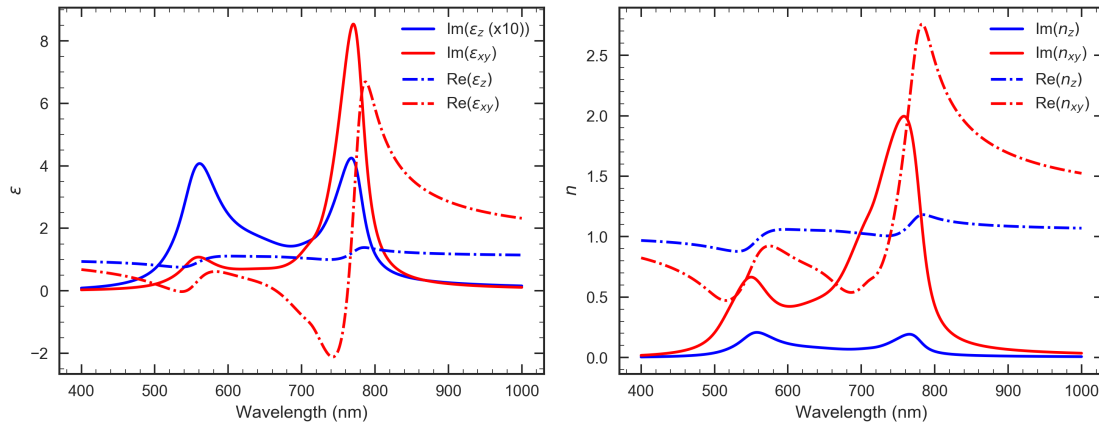


**Figure 6.22:** Dielectric function (left) and refractive index (right) of the anisotropic sample.

Now we want to analyze angular dependent spectra. Here, the sample surface with the dye material is not perpendicular to the laser beam anymore, but is tilted by an angle. Hence, a p-polarized light beam incident on the sample under a non-zero angle contains both electric field components parallel and perpendicular to the surface. The measurement was performed with an s- and p-polarized input beam under 4 different angles  $0^\circ$ ,  $30^\circ$ ,  $60^\circ$  and  $75^\circ$ . The recorded

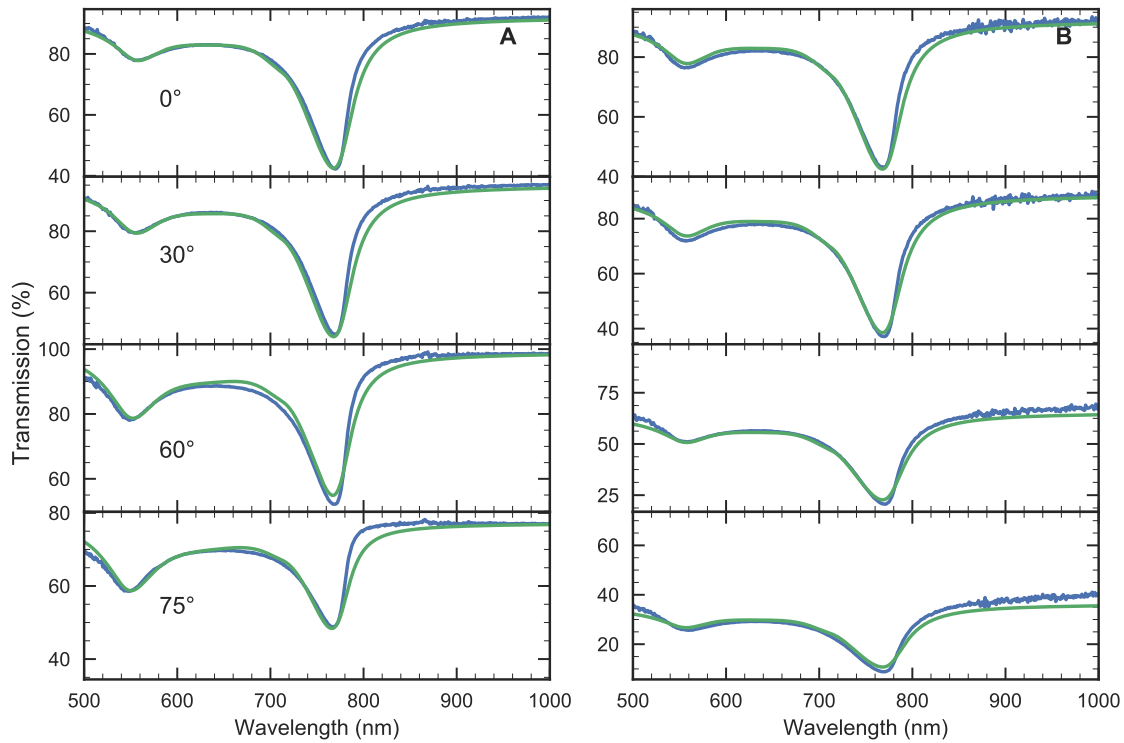


**Figure 6.23:** Angular dependent measurements for p-pol light (A) and s-polarized light (B). The blue curves show the measurement, the green curve the simulated transmission.

spectra are shown as the blue lines in Fig. 6.23A for the p-polarized input light and in 6.23B for the s-polarized input light.

From the measurement using the p-polarized light we can see that the ratio of the two resonances changes for higher angles: For 0° incidence, the absorption of the H-band is very low with respect to the absorption of the J-Band, whereas for 75° incidence and the absorption for the H-band drastically increases and is now nearly on a comparable level to that of the J-band.

For transmission spectra measured with s-polarized light, the ratio of the J-band and H-band does not change noticeably as can be seen in Fig. 6.23B.

These findings in the spectra cannot be reproduced with an isotropic refractive index and are a proof for anisotropic behavior of the squaraine dye. Hence, the full tensor of the dielectric function must be considered. To account for this, we used an uniaxial anisotropic model of the Fresnel coefficients as derived in chapter 4.1.3 and exploit a different refractive index for the in-plane ( $n_x = n_y = n_o$ ) and the z component  $n_z = n_e$ . The difference between p-polarized and s-polarized light is expected as well, because only the p-polarized light produces a z-component and here the effective refractive index of the medium is a superposition of both the ordinary and extraordinary refractive index. On the contrary, for s-polarized light the effective refractive

index of the medium is the same as the ordinary refractive index.

From geometrical considerations, the dipole moment for the z-components is then given by  $\mu_z(\theta) = \mu_0 \cdot (\sin(\theta) + \nu \cos(\theta)) \cdot c$ . The term  $\nu \cos(\theta)$  accounts for the rotation of the two coupled dipoles in space. That means the dipoles can span an angle  $\theta$  to each other, but can still be rotated in space. Hence, the z-component can be higher, for example when one of the molecules is aligned along the xy plane and the other molecule points out of the plane. The maximum allowed contribution to the z direction is thus  $(\sin(\theta) + \nu \cos(\theta))$ . The actual projection to the z-plane has to be equal or smaller than the maximum allowed values. This is regulated by the factor  $c$  with  $c < 1$ .

We found that for  $c=0.074$  and  $\nu = 2.46$  our simulation shows a good match to the measurement as is shown in Fig. 6.23A as the green line. The complete resulting dielectric function is shown in figure 6.22. Hereby the new component for the z-direction is plotted as the blue line. In total the transmission spectra calculated with this dielectric function match both the measurement for s- and p-polarized input light for all measured angles to a large extent.

From these results, it becomes clear that for larger angles and p-polarized light stronger coupling to the z-component of the electric field takes place. As we can see from  $\varepsilon_z$ , in this case the H-Band is increased with respect to the J-Band: The in-plane component of the dielectric function  $\varepsilon_{xy}$  shows a ratio of around 8 between the J-Band and the H-band, whereas the out-of plane component  $\varepsilon_z$  shows a ratio of nearly 1. At the same time we observe that the maximum value of the dielectric function for the H-aggregate is decreasing by a factor of 2.6 with respect to the in-plane component, whereas the J-aggregate peak is decreased by a factor of around 20. Hence, the J-aggregated dipoles are mainly aligned within the xy plane and only show a weak z-component.

These findings and the acquired dielectric function are used in the following section to simulate and understand SNOM near-field spectra measured on the sample.

### 6.3.3 Nanoscale spectroscopy

For local spectra measurements we use the same SNOM setup as outlined in previous chapters. We are using the in-line interferometer that was described in chapter 5 as a substrate to enhance the near-field contrast by homodyne mixing, and the squaraine dye is spincoated on top of it. Additionally, gold particles are placed on top of the dye to demonstrate spectral contrast, i.e. we are able to compare the local near-field on the dye with the near-field on a gold nanoparticle. The squaraine dye itself was prepared by M. Schieck of the energy and semiconductor research group of the university of Oldenburg. The exact procedure is documented in [193]. In total the sample then consists of 4 layers that are visualized in figure 6.24: a 180  $\mu\text{m}$ -thick glass substrate (BK7), a 20 nm-thick gold film, a 107 nm-thick  $\text{SiO}_2$  glass layer and the spincoated

layer of the squaraine dye with about 17 nm thickness. Finally, we spincoated the gold-particles on top of the squaraine layer. The solution originally contained monodispers particles with nominally 30 nm diameter, but after spincoating we typically found larger clusters of particles with sizes of around 200 nm diameter. These bigger particles are far off-resonant with respect to the spectral range of our laser system and thus the local measurement on top of such a particle is comparable with a measurement on a flat gold film that was analyzed in previous sections.

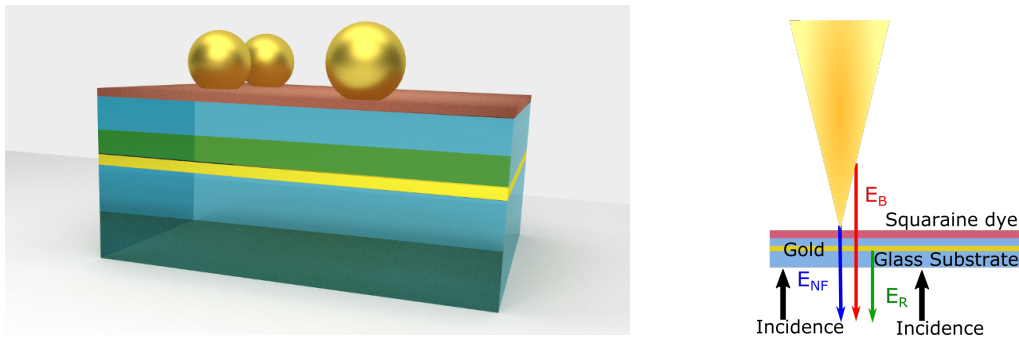


**Figure 6.24:** Left: Visualization of the layered sample used in the SNOM: a BK7 glass substrate, a thin 17 nm gold layer, a SiO<sub>2</sub> glass layer (107 nm), the spincoated squaraine dye (17 nm) and around 100 nm gold particles on top. Right: Illustration of the fields that propagate through the layered system.

In a first step we now analyze the spectra measured on the squaraine material far away from any gold particle. In a second step we compare the spectra measured on the dye material with one measured on the gold particle.

To analyze the the SNOM spectra measured on the dye material we need knowledge of the reference field as well as the focus field. The reference field is already known as the laser spectrum reflected at the gold layer (cmp. the right image in Fig. 6.24). The focus field however is the field after transmitting through the complete 4 layer system for different angles, which then interacts with the tip. After interaction the field is then propagating through the sample a second time. To calculate the focus field we thus need the TMM model to calculate angle dependent transmission coefficients and the refractive index of the dye material which was the result of the previous subsection.

The focus fields can then be calculated as outlined in chapter 4.1.4. Fig. 6.25A shows the result of such a calculation: the spectrally resolved focus field components  $|E_x|$  and  $|E_z|$  after passing all layers, and assuming a spectrally flat input spectrum of  $E_{in}(\lambda) = 1 \text{ V/m}$ . Hereby all allowed k-vectors for a microscope objective with an NA=0.95 are considered. The electric field magnitudes are shown for two positions inside the focus field, namely at  $x = 0$ , where the  $x$ -component has its single maximum, and  $x=320 \text{ nm}$ , at one of the two maxima of the  $z$ -component (at  $\pm 320 \text{ nm}$ ). The resulting figure 6.25A shows that the  $x$ -component of the focus

field has a larger electric field strength than the  $z$ -component. This is true even for the case that the tip is placed on the right-hand spot at  $x = 320$  nm for a maximum of the  $|E_z|$  component. Furthermore, the  $z$ -component is almost 0 when the tip is placed in the focus area at  $x = 0$ . This coincides with the findings from the previous transmission measurements, that the dielectric function for the in-plane component of the J-aggregate resonance is increased by a factor of around 20 in comparison to the out-of-plane component and suggests that even with a high field enhancement factor of the tip, coupling to the  $xy$  component of the tip polarizability matrix will probably outweigh the coupling to the  $z$ -component.

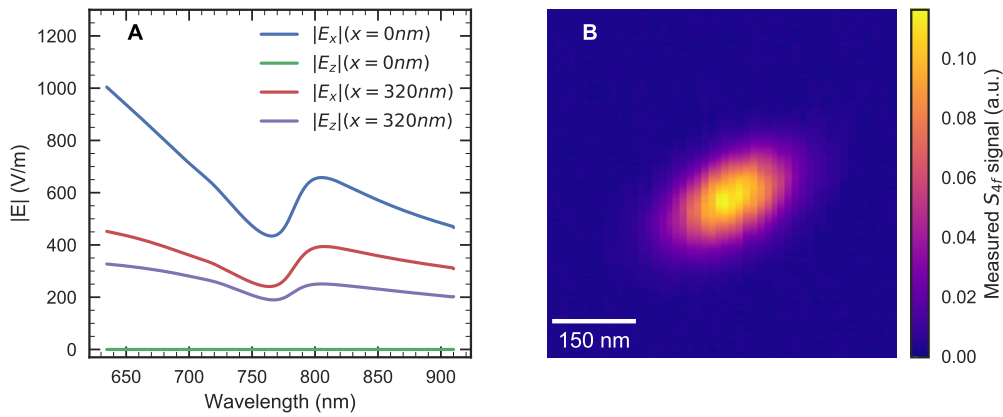


**Figure 6.25:** A: Focus fields  $|E_x|$  and  $|E_z|$  through the in-line interferometer with squaraine dye for either placing the tip on the maximum spot of  $|E_x|$  ( $x=0$  nm) or  $|E_z|$  ( $x=320$  nm). The dielectric function used to describe the squaraine dye layer is the same that was found previously and is plotted in Fig. 6.22. B: Typical measured beam scan demodulated at the 4th harmonic around the tip apex shows just one maximum, indicating a higher coupling to the in-plane component of the tip than to the  $z$ -component.

Additionally, Fig. 6.25B shows a measured beam scan with the tip in close contact, i.e. the tip is on a fixed position close to the sample surface and the piezo mirror in front of the  $4f$  lens system is moved such that the beam scans an area around the tip. Here, the signal from the APD demodulated at the 4<sup>th</sup> harmonic of the tip frequency is shown. The beam scan can be seen as a measure for the focus field that interacts with the tip dipole. From this measurement we can see that the scan reveals just a single maximum and not the two maxima expected for the  $E_z$  focus field component. As pointed out in earlier chapters this does not necessarily mean that there is no  $z$ -component at all, as they could still be mixed together, but a single maximum is nevertheless a strong indication that coupling to the in-plane component plays an important role for this tip-sample system. Together with the focus field simulations we conclude that in-plane coupling is the dominant factor. In the following we therefore focus our attention on the in-plane coupling.

It should be noted though, that for other 2D materials the coupling could be even manipulated

by the tilt angle of the tip. K.D. Park and M. Raschke for example recently showed that a tilted tip can be used to break the axial symmetry in tip enhanced near-field microscopy. A tilted tip can then systematically be used to probe 2D materials as it leads to a localized plasmonic antenna effect. This means the optical field vectors are enhanced and the amount of in-plane and out-of-plane components can be controlled by the tilt-angle [206].

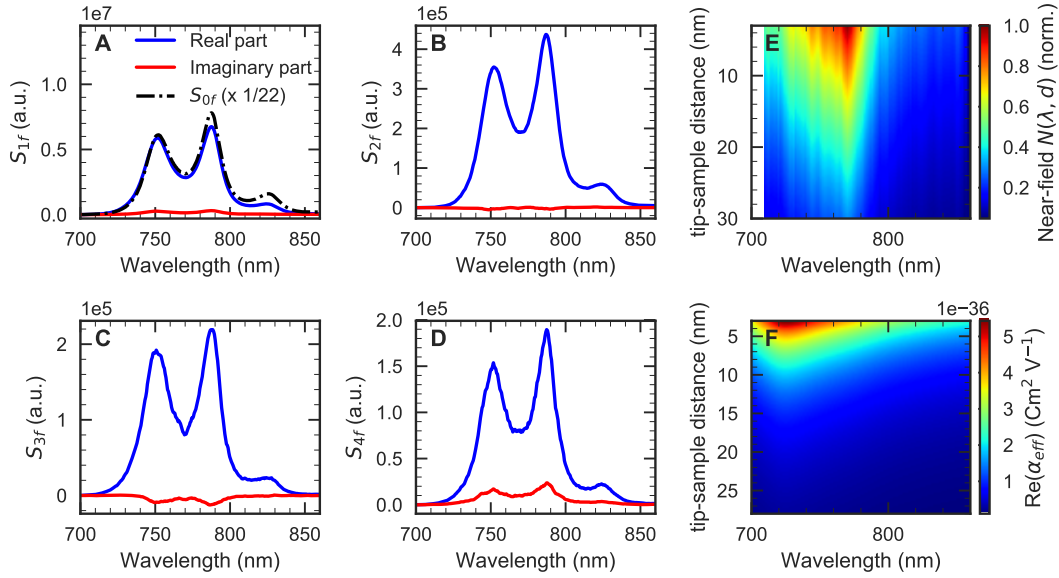


**Figure 6.26:** (A-D) Signals  $S_{1f}$  to  $S_{4f}$  respectively. The blue curve always shows the real part, whereas the red curve shows the imaginary part. The black dotted line in A additionally shows the  $S_{0f}$  spectrum. The applied phase correction led to an almost negligible imaginary part. (E) The reconstructed near-field approach  $N(\lambda, d)$  from the measured data. (F) Simulated effective polarizability for the material and the incoming field polarized along the  $x$ -direction

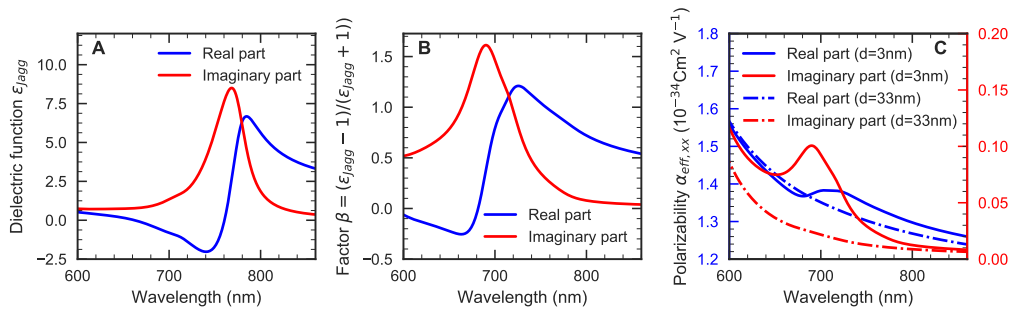


**Figure 6.27:** A: Dielectric function for the J-aggregate of the squaraine dye (cmp. Fig. 6.22). B: The sample dependent factor  $\beta = (\epsilon_{Jagg} - 1)/(\epsilon_{Jagg} + 1)$  that enters calculation of the effective polarizability. C: Effective polarizability  $\alpha_{eff,xx}$  with the tip polarizability modeled by a sphere with 10 nm radius for two distances  $d=3$  nm and  $d=33$  nm.

Figure 6.26 now shows a typical SNOM spectrum recorded on the dye material with the tip in close contact. Here, Fig. 6.26A-D show the complex  $S_{1f}$  to  $S_{4f}$  signals. The blue curve shows the real part and the red curve the imaginary part of the signals. Analogous to the previous chapters the initial phase was corrected in a post-processing step, which leads to an almost negligible imaginary part. The spectra look very similar in all  $S_{nf}$  signals. Especially the fact that the shape of the  $S_{1f}$  signal is not different from the other ones indicates a small background field contribution. As expected from previous measurements, the overall signal strength is decreasing for higher harmonics of the tip frequency.

Using these signals we can now recreate the spectral approach. To account for the transmission through the multiple layer system in both the excitation and back-scattered signal, we normalized the calculated near-field by  $(E_{ref})^2$  instead of only  $E_{ref}^2$ . Hereby we define  $t = |E_x|/E_{in}$  with the simulated electric field in the focus  $E_x$  at  $x = 0$  shown in Fig. 6.25A and  $E_{in}$  the constant, wavelength independent field along x-direction.

The recreated approach curve data  $N(\lambda, d)$  (cmp. Eq. (6.18)) is shown in Fig. 6.26E. Here, an obvious difference to the results on spectrally flat surfaces of the previous chapters is visible. In fact, we can observe a maximum signal around 760 nm and almost no signal at larger wavelength. This maximum is located around the wavelength of the J-aggregate absorption maximum, slightly shifted towards shorter wavelengths due to the coupling with the tip. This means we presumably probe the local interaction of the tip with the J-aggregate. An interaction with the H-aggregate can't be seen, because the expected peak is outside our laser spectrum.

Fig. 6.25F shows a comparable simulation of the effective polarizability for the squaraine dye material. Following the results on the focus field simulations, we hereby used an incident field polarized along the  $x$ -direction and the tip polarizability was modeled by a sphere with 10 nm radius. The parameters entering this simulation, such as the factor  $\beta$  and the dielectric function of the J-aggregate in the wavelength range between 600 nm and 860 nm are plotted in Fig. 6.27A and B. The dielectric function was hereby taken from the previous transmission spectra calculations. By comparing the simulated effective polarizability with the reconstructed approach spectra from the measurement, we can find that both the measurement and simulation show a resonance of around the same width in the spectral range. For the simulation however, the maximum intensity of this resonance is shifted towards shorter wavelengths, which can also be observed in the factor  $\beta(\lambda)$  in Fig. 6.27B and in  $\alpha_{eff,xx}(\lambda)$  at a distance of  $d=3$  nm in Fig. 6.27C. The shape of the near-field approach  $N(\lambda, d)$  hence differs considerably from the calculated effective polarizability. This could be due to an erroneous assumption for the absorption of the electric field in the substrate, e.g., due to a locally varying film thickness. Furthermore, the decay length is much shorter in the simulation. This difference in decay length is typically caused by a larger tip radius than we assumed for the simulation.

Hence, we believe both the resonance in the simulation as well as in the reconstructed near-field

from the measurement represent the same influence of the J-aggregate resonance.

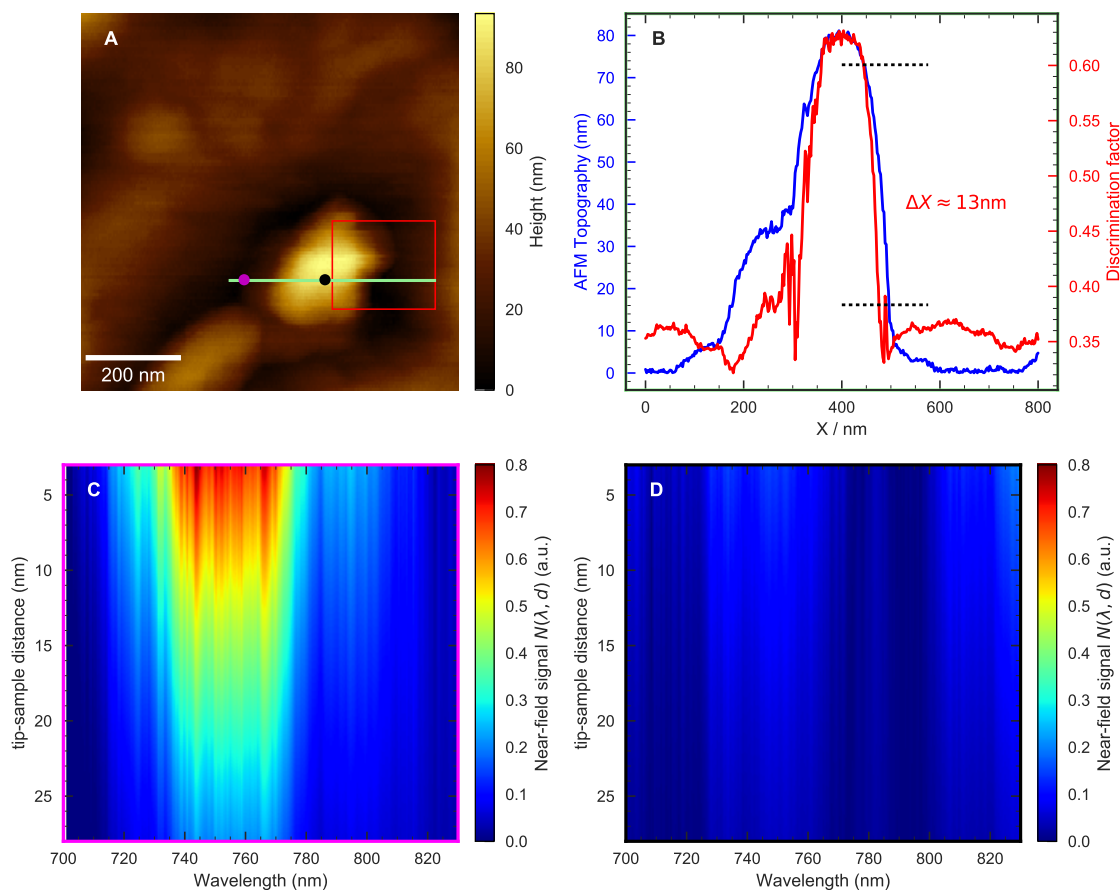


**Figure 6.28:** A: AFM scan of gold particles on top of the spincoated squaraine dye, B: Line scan over the gold particle and dye as indicated by the green line in A. The blue curve shows the topography change from AFM, the red curve shows the discrimination factor which is defined as the division of the mean values of the spectrum from 781 nm to 866 nm to the mean values of the spectrum from 662 nm to 753 nm. The dotted lines show the values taken to measure a optical resolution of around 14 nm in the 10-90% interval. C & D: Graphical 2D representation of the reconstructed near-field approach signal  $N(\lambda, d)$  with the tip positioned at  $x \approx 5$  nm and  $x \approx 400$  nm of the linescan in B, i.e. once on the dye material and once on the nanoparticle as indicated by the magenta and cyan dot in (A).

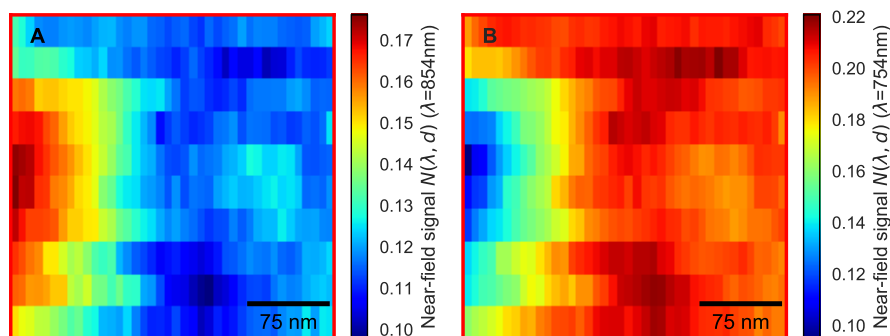
To demonstrate that the observed spectral shape of the near-field measurement indeed is a first indication of spectrally resolved near-field measurements with chemical specificity, we recorded AFM and optical near-field maps for a region with both the squaraine dye material and a gold particle on top.

Figure 6.28A shows the AFM scan of such an area. The spincoated dye exhibits a rather flat surface topography with a surface roughness of less than 10 nm. We can identify a larger cluster of gold particles in the lower right-hand quadrant of around 200 nm diameter and 100 nm height. We measured spectra in a 2D area marked by the red box and a linescan as indicated by

the green line.

We know already that the SNOM spectra on the dye material show a pronounced resonance, whereas spectra on flat films show a rather flat spectral response. To quantify this spectral behavior for a complete linescan we introduce a discrimination factor, which is defined by the ratio of the mean value of the reconstructed, normalized near-field signal at a tip-sample distance of around 3 nm between 781 nm to 866 nm to the mean value between 662 nm to 753 nm. This discrimination factor is closer to unity for relatively flat near-field spectra and deviates more from unity, the stronger the spectral variation between these two spectral ranges is.

Figure 6.28B shows the AFM topography for the linescan as the blue curve together with a plot of the discrimination factor as the red curve. On the AFM topography we can clearly identify the nanoparticle starting from position  $x \approx 300$  nm to  $x \approx 500$  nm and reaching a height of 80 nm. The discrimination factor roughly follows the topography curve and has its maximum, closest to unity, on top of the gold particle. The discrimination factor is much smaller,  $\sim 0.35$ , to the sides of the nanoparticle, where the tip was above the J-aggregate film. The height profile further shows that the particle has a rather sharp edge. The height decreases from 80 nm to nearly 0 nm over a distance of around 20 nm in the 10-90% interval. The discrimination parameter follows this trend, but decreases even faster. Here, the factor decreases from 0.62 to around the baseline of 0.35. In the 10-90% interval marked by the dotted lines this happens on a scale of around  $\Delta X \approx 13$  nm. This gives an upper limit for our optical resolution and shows that the tip was quite sharp at the time of this measurement.



**Figure 6.29:** Near-field signal at a wavelength of 854 nm in (A) and 754 nm in (B). The area of this scan is illustrated by the red box in Fig. 6.28A.

To emphasize the importance of the discrimination between measuring near-fields on the gold particle and on the dye material, Figure 6.28C and D now show two reconstructed near-field approach curves from the measured data. Fig. 6.28C shows the near-field for a position on the dye material as indicated by the magenta point on the AFM image (at  $x \approx 5$  nm) and Fig. 6.28D for a position on top of the nanoparticle (at  $x \approx 400$  nm) as indicated by the black point on

the AFM image. The colorbar of both figures is scaled to the overall maximum of both datasets. In comparison we find a well pronounced resonance on the dye material, similar to the one we observed before in Fig. 6.26E, On the gold particle however, the near-field signal is almost flat and much weaker. The gold particle shields the tip from the dye material resulting in a flat spectral response. This is also the reason for the steep increase of the discrimination factor in Fig. 6.28B and means the spectrum measured on the gold particle has a shape similar to the input spectrum, whereas on the dye material a clear deviation from the input spectrum can be observed.

Finally, we have used the spectral contrast to create two maps that show the chemical specificity for the areas indicated by the red box in Fig. 6.28, which is demonstrated in Fig. 6.29 for two wavelengths. Here, the optical near-field signal is shown in a 2D plot for a wavelength of  $\lambda = 854$  nm in Fig. 6.29A and for  $\lambda = 754$  nm in Fig. 6.29B. The map at 845 nm shows a high near-field signal on the gold particle and a lower near-field signal on the dye, whereas the map at 754 nm shows a strongly increased near-field signal on the dye material. In fact, the near-field signal on the dye in this case is increased by a factor of around 1.3 against the highest near-field signal on the gold particle at 854 nm. Hence, the image looks like the inverted version of the near-field signal for 845 nm.

The difference here can be ascribed again to the dielectric function: the gold particle is far off-resonant for both wavelengths and hence the dielectric function is very small and so is the interaction with the tip. At the wavelength of 854 nm also the dielectric function of the dye is very small, as this wavelength is far away from the J-aggregate resonance at around 760 nm. Here, the dye is nearly transparent for the wavelength of 854 nm and the interaction with the tip is less pronounced than for the off-resonant gold particle. The measurement on the dye is then comparable to a glass substrate which typically has a smaller near-field than a gold surface. The wavelength around 754 nm is near the J-aggregate of the dye and the dielectric function is much higher than that of gold and hence the tip-sample interaction is pronounced, resulting in a higher effective polarizability.

Overall these measurements demonstrate the possibility to measure near-field signals even on a highly anisotropic material where mainly coupling to in-plane component can occur. In the next section we demonstrate exemplary for a nanorod antenna that we can even observe and decouple an interaction to both in-plane and out-of-plane component in the same measurement.

## 6.4 Spectroscopic imaging of nanorod antenna modes

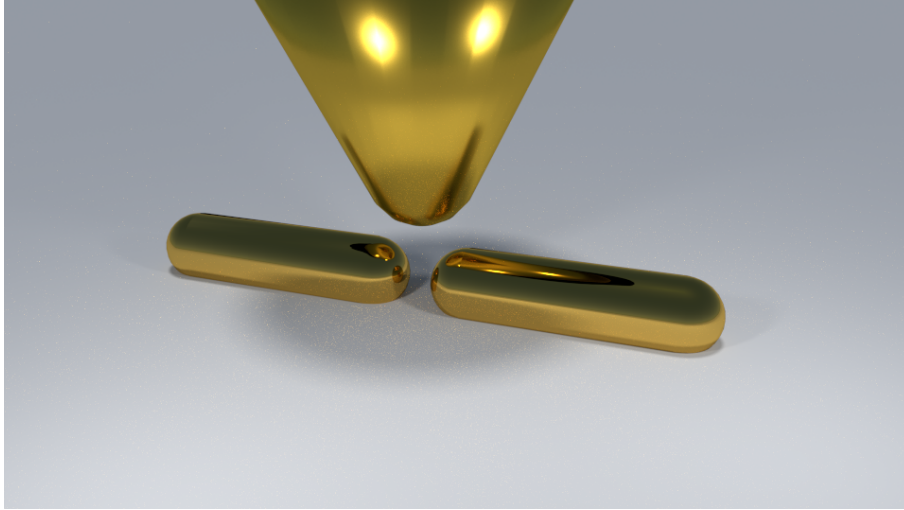


**Figure 6.30:** Visualization of a SNOM tip over a nanorod dimer antenna

As a final example, we show how the non-trivial polarizability of a nanotip can be used for vectorial near-field studies. In this example, we study a nanorod dimer antenna as visualized in Fig. 6.30.

Optical nano antennas can be seen as the counterpart to microwave and radio frequency antennas that find use in our everyday life. Nano antennas however show some interesting new physical phenomena, one of them is to provide a highly localized and enhanced field inside the gap between the two antenna structures. The strong fields can be explained by a lightning rod effect resulting in a large electric field near the sharpest end of the structure. This happens both in the gap and at the ends of the rods. The ability to provide an interface between highly localized informations, due to the excitation of surface plasmon polaritons, and free space wireless information in the form of electromagnetic waves [179, 182], makes nano antennas an extremely important tool in the research area of plasmonics. So far optical nano antennas have been used for higher harmonic generation [207, 208], optical imaging, biological and chemical sensing of single molecules [209, 210] and other applications that use light in the visible or near-infrared region [211, 212]. Overall, the remarkable advance in nanotechnology led to a high interest in nano antennas to manipulate optical properties on the nanoscale by changing antenna parameters, such as gap size, structure size and antenna material.

In order to design and optimize such plasmonic resonators, a detailed knowledge of the nanoscopic light field becomes essential. For the case of investigating strongly scattering plasmonic structures, SNOM is arguably the method that comes close to the ideal of measuring electric and magnetic fields on a sub-wavelength scale, without perturbing the fields [213].

As we have seen in previous chapters this is of course not the case for samples without strong scattering properties, where the SNOM tip highly perturbs the system. Even though a full vectorial field characterization at the nanoscale remains challenging, some successful attempts can be found. For example, using two-channel detection, two of the field components (usually both in-plane components) of both electric and magnetic fields can be unraveled and the remaining components (usually the out-of plane component) can be subsequently derived from Maxwell's equations. Such approaches have been demonstrated for both collection-mode [214] and scattering-type SNOM [215]. Using a bent near-field probe, the scheme can be altered such as to measure directly one in-plane and the out-of-plane component [216]. Here, we demonstrate a different solution to this long-standing problem, where we measure the in-plane and out-of-plane electric field component simultaneously and by employing our near-field spectroscopy technique. This is possible because one component is spectrally shifted with respect to the other due to a different tip-sample coupling.

Fig. 6.31 shows a typical simulation of the fields around such nanorod antennas. Considering the strong coupling behavior of the antenna structure each nanorod is hereby modeled as a chain of individual dipoles. The electric field  $\vec{E}_i$  at the position of the dipole is then a superposition of the excited fields of all other dipoles (compare chapter 4.2.2).

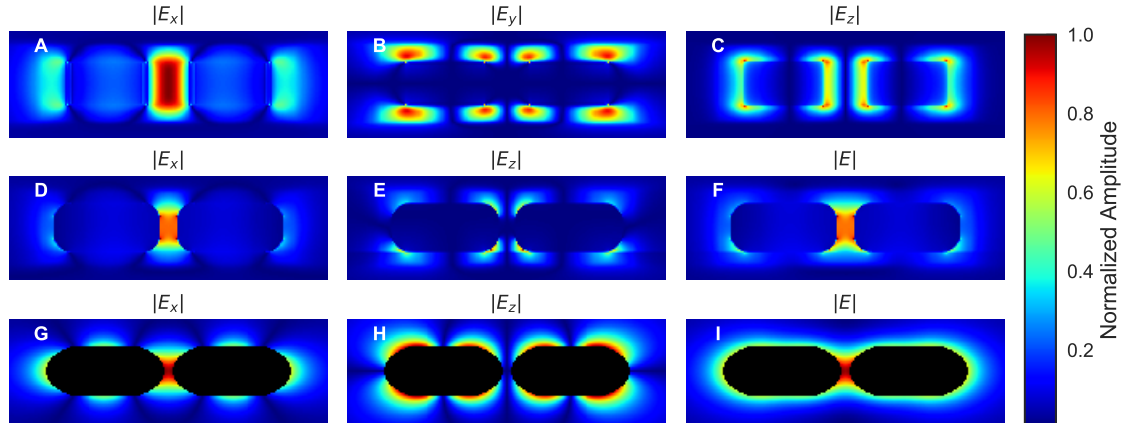


**Figure 6.31:** Rod antenna mode. A-C: FEM simulations for a wavelength of 707 nm of the fields  $E_x, E_y$  and  $E_z$  in the  $xy$  plane with  $z=30$  nm evaluated at the top of the antenna structure. D-F: FEM simulations of the fields  $E_x, E_z$  and  $|E|$  in the  $xy$  plane with  $z=0$ . At the bottom of the antenna, a glass substrate was assumed. G-I: Simulations of the fields  $E_x, E_y$  and  $E_z$  in the  $xy$  plane with  $z=0$  by the Green's function approach that show a comparable result..

Since for a nanorod essentially the component along the rod-axis plays a role, the polarizability tensor of each of the rod dipoles can be reduced to only one nonzero component, the x-component  $\alpha_{xx}$ . Compare chapter 4.2.2 for the phase relation and calculation of the fields around the nanorod.

The polarizability (as derived in chapter 4.2.2) is now multiplied with a spectral lineshape  $S(\omega, \omega_r, \gamma_r)$  that describes the nanorod antenna mode by a Lorentzian with a resonance energy of  $\hbar\omega_r = 1.74$  eV and a linewidth of  $\hbar\gamma_r = 0.05$  eV. The nanorod itself is modeled by a cylinder of length  $2L = 30$  nm and the ends are closed by a hemisphere of radius  $R = 5$  nm. Similar parameters were recently used to describe the vectorial near-field coupling of a SNOM tip to a nanorod as shown in [93, 95].

The field around the nanorod calculated by  $\vec{E}(\vec{r}) = \mu_0\omega_0^2 \sum_i \overleftrightarrow{G}(\vec{r}, \vec{r}_i) \vec{p}_i$  with  $\vec{p}_i = \overleftrightarrow{\alpha}(\vec{r}, \vec{r}_i, \omega) \vec{E}_{exc}$  (cmp. equation (4.125)) is then shown in Fig. 6.31G-I for a wavelength of 707 nm. The excitation field  $\vec{E}_{exc}$  was set to  $\vec{E}_{exc} = (1, 0, 0)$ , hence an excitation field polarized along the long antenna axis. This is in analogy with the experimental scheme, which is described below. Figures 6.31A-F show the fields calculated for the the xz and xy plane with a FEM simulation. For the FEM simulation, the nanoantenna was placed on a glass substrate and excitation is from the bottom with an excitation wavelength of 707 nm and the input field is polarized parallel to the long axis of the antenna, as well. Clearly, both the Greens function approach as well as the FEM simulation show comparable results. Both show the strong fields in the antenna gap and a weaker field around the nanorod edges.

Next, I want to focus on the SNOM measurement. Also hereby, the nanorod dimer antenna is illuminated by broad-bandwidth laser pulses from below, i.e., through the glass substrate, with the polarization set parallel to the nanorod's long axis (along the x-direction in our geometry). This way, the fundamental mode is excited globally, and since the nanorod is a much stronger scatterer than the near-field probe, we can, in this experiment, view the tip simply as a local probe brought into the near field of the nanorod. The tip is then polarized by the local electric field around the nanorod dimer and emits dipole radiation to the detector. In order to disentangle the in-plane and out-of-plane components of the electric field, we chose a relatively blunt tip, which should show the polarizability of an elliptical tip. We expect the in-plane- (x and y) components of the tip polarizability to be flat, corresponding to the polarizability of a sphere, such that the detected near field in-plane components should spectrally closely resemble the resonance of the nanorod dimer.

The z-component of the tip polarizability, however, should correspond to the polarizability of an ellipse and should display a resonance in the spectral region of our experiment. Hence we expect out-of-plane (z-polarized) near field components to be spectrally shifted to the ellipse's resonance. As a result, we should be able to distinguish between the in-plane and the out-of-plane electric field components of the near field in spectrally resolved measurements.

Figures 6.32A-C show 3 randomly chosen SEM images of nanorod antenna structures. They were produced out of a 30 nm thick, flat gold film on a BK7 glass substrate. A gallium ion beam was then used to remove the gold layer in a box around the desired gold nanorod structure,

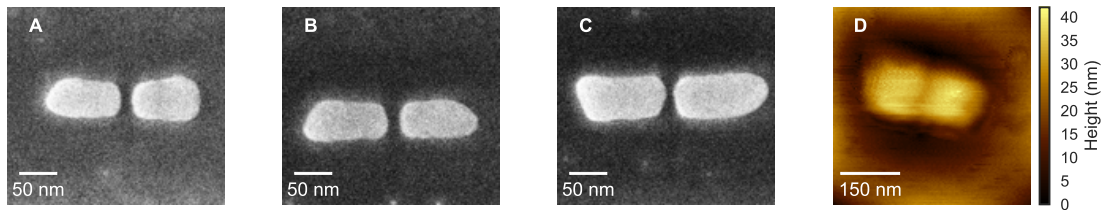


**Figure 6.32:** (A)-(C) SEM images of different nanorod antenna structures produced by focussed ion beam milling. Both the gap size and the rod dimensions differ for each structure, thus the exact resonance frequency of the antennas may change as well. (D) AFM height image scanned with a blunt tip.

i.e. only the glass substrate is left around the structure. The gap in the middle was finally produced by focused Helium ion beam milling. The antennas were designed to have a resonance around 780 nm. The SEM images however clearly indicate a change in both gap size and rod dimensions for different structures. Thus, the actual resonance frequency will differ for different antennas and can only be estimated, e.g. by FEM simulations and comparison to previous works of similar shapes.

In other works we found that resonances of nanorod dimer antennas are redshifted with respect to the resonance of a single nanorod and typically antenna resonances of around 800 nm or even longer wavelengths are reported. For example Biagioni et al. [179] showed that the resonance for a 100 nm long single nanorod is around 770 nm which shifts to 830 nm when going from a single-wire structure to a 10-nm-gap two-wire structure. Gittinger et al. measured darkfield and scattering spectra for nanorod antennas with sizes of  $90 \times 35 \times 30$  nm that are only slightly longer than the ones we used. They observed a resonance around 750 nm for gap sizes larger than 20 nm and also a red-shift up to 900 nm for very small gap sizes of less than 5 nm [212]. All these works however use longer and more asymmetrical nanorods in comparison to our structures.

In general a single rod already has its own two surface plasmon resonances for polarization along the nanorod and perpendicular to it. Muskens et al. showed, that for nanorods with increasing lengths, the longitudinal mode shifts to longer wavelengths, but the transverse resonance is unaffected and is located around 600 nm for nanorods of 60 nm width and 20 nm height [217]. When two nanorods are brought in close proximity, there is a coupling of the longitudinally polarized surface plasmon resonance resulting in a red-shifted, delocalized bonding mode [212]. In our case, the ratio of width versus length of the single nanorods is close to 1, a few of the produced nanorods are even more square than elongated. In this case, the two resonances for a single nanorod are very similar and the longitudinal mode is more blue-shifted than in the previous mentioned works for more elongated rod-structures. Here, Muskens et al. predict a resonance below 700 nm for a nearly quadratic nanorod with sizes of around  $70 \times 60$  nm

positioned in each antenna arm. For slightly longer nanorods of 80 nm length the resonance of the dimer antenna shifts to a wavelength of around 700 nm. Following these results, we think the resonance of our nanorod dimer antenna structure could be located in the lower 700 nm region, between 700 nm and 750 nm, as well.

The nanorod antenna that we measured with the SNOM has dimensions of around 85x60x30 nm and a gap size of around 10-15 nm. An AFM image of this structure is shown in Fig. 6.32D. In this scan the edges of the nanorod are not very clear and the structure looks slightly larger than in the SEM images. Also, in contrast to the SEM image, the height in the gap barely reaches 0. This discrepancy is due to the larger size of our tip, that was most probably exceeding the gap size, i.e. our tip was relatively blunt which now results in a convolution of the tip shape with the rod structure. From the edge steepness we estimate the tip radius to be around 25-30 nm.

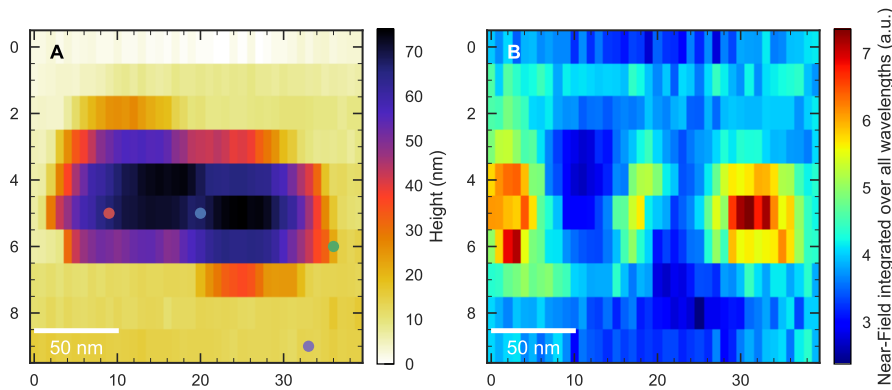


**Figure 6.33:** (A) AFM image of the coarse scan with fewer points. (B) Corresponding optical near-field signal integrated over all wavelengths.

The spectrally resolved SNOM scan was then carried out with fewer points on a smaller area around the same nanorod to avoid too much mechanical drift during the measurement. The coarse AFM image together with an optical near-field signal is shown in Fig. 6.33. The optical signal in this case is the calculated near-field from the measurement integrated over the complete wavelength range. Already here we can see that mainly the edges and the gap of the nanorod antenna have a reasonable high near-field signal. In the following we want to investigate the spectrally resolved near-field at 4 points of interest as indicated by the 4 points in Fig. 6.33A: in the antenna gap, on the edge of one nanorod, in the center of one nanorod and outside the nanostructure on the glass substrate.

Fig. 6.34 shows the near-field spectra  $N(\lambda, d)$  (cmp. eq. (6.18)) as a function of tip-sample distance for these 4 points indicated in the AFM image.

The results clearly demonstrate that we have a very strong near-field enhancement in the gap

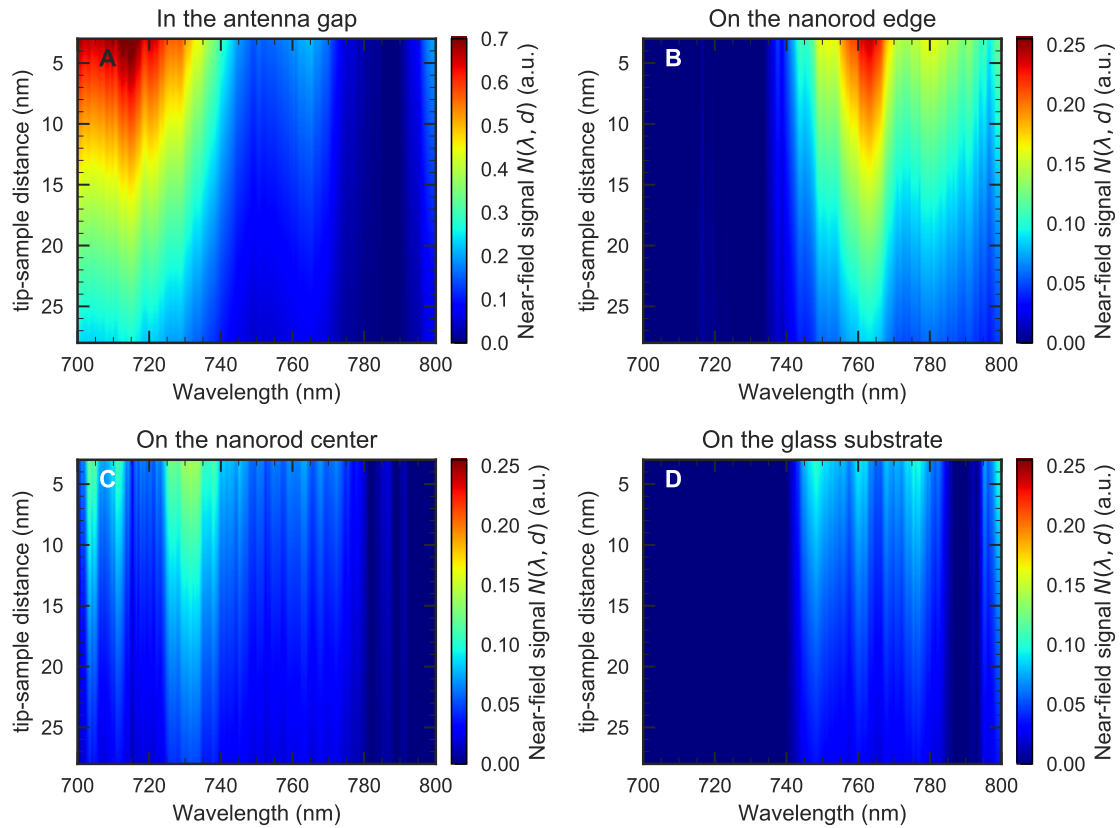


**Figure 6.34:** Local near-field spectra recorded inside the gap (A), at the edge of the nanorod (B) in the middle of one rod (C) and outside the nanostructure (D) as visualized by the colored dots in Fig. 6.33A.

in Fig. 6.34A. Only there we observe a resonance around 710 nm and a total near-field at least twice as high compared to any other position on the scan area. Here, we believe, the x-component of the electric field is dominant, which couples to the x-component of the tip polarizability. A more accurate determination of the tip-induced shift would require an analysis of the eigenmodes of the nanorod antenna dimer, e.g. using FDTD simulations, and a comparison with spectrally resolved near-field maps at different wavelengths. This was, however, not possible within the timeframe of this thesis and is left for future works.

The near-field on the edge of the nanorod in Fig. 6.34B mainly shows a second resonance around 760 nm, whereas the strong near-field we observed at 710 nm is almost completely vanished. We believe that this reflects the resonance of an elliptic tip for polarization in z-direction. This is in agreement with the measurement position on the edge, where a strong z-component of the electric field is expected. A similar resonance could be demonstrated for a blunt tip over a gold surface as well (cmp. Ch. 6.2.3).

The measurement on the nanorod middle position in Fig. 6.34C is comparable to a measurement

outside the antenna structure in Fig. 6.34D: here we see almost no resonances anymore and the overall spectral response is rather flat and the near-field strength is comparable to that of a near-field measurement on a glass substrate.

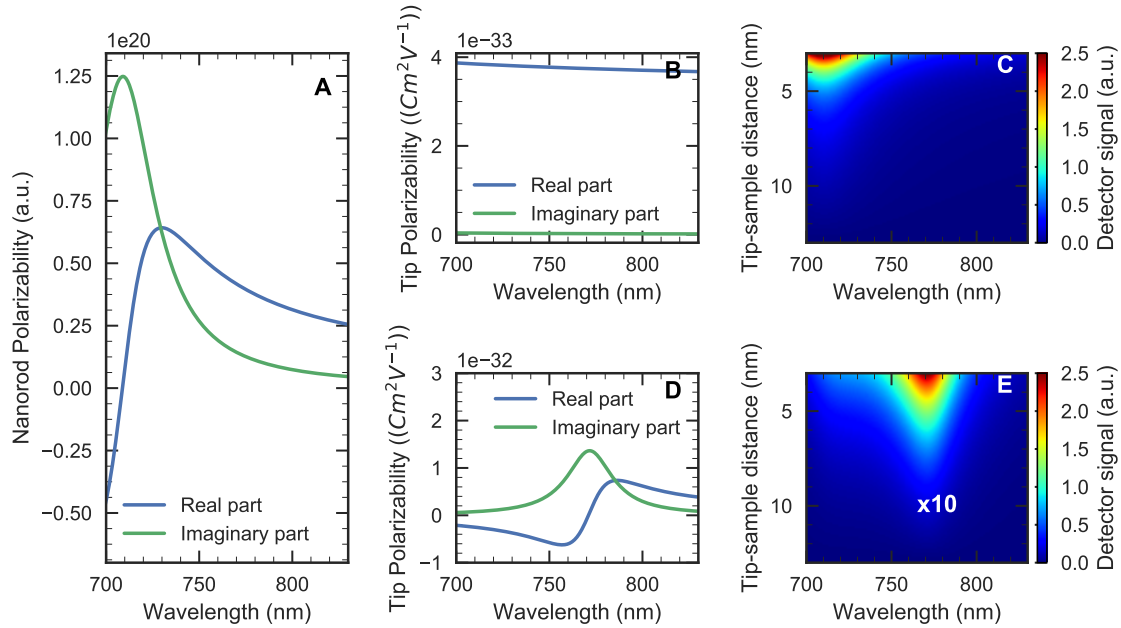


**Figure 6.35:** Simulation of the near-field around the nanorod antenna. (A) shows the assumed spectral lineshape of the nanorod antenna resonance. (B) is the assumed tip polarizability  $\alpha_{tip,xx}$ . (C) show the simulated near-field spectra as a function of wavelength and tip-sample distance for the tip polarizability shown in (B). (D) is the assumed tip polarizability  $\alpha_{tip,zz}$  and (E) shows the corresponding near-field signal for this tip resonance.

In order to verify our intuitive understanding of the SNOM data, we now simulate the four presented spectrally resolved approach curves, which were measured at the four selected tip positions. Here we consider a simple second-order scattering event that should reflect the experimental situation quite well: We take the nanorod to have a strong dipole moment, induced by the laser illumination from the back, and the gold nanotip to act as a much weaker dipole that is excited by the nanorod's near field and emits dipole radiation towards the detector. For this simple simulation, we model the rod antenna as a chain of  $2 \times 11$  dipoles  $\vec{p}_i$ , with  $i = 1..22$  and with polarizabilities  $\alpha_{i,xx}(\omega) = w_i \alpha_{rod,xx}(\omega)$  of the rod polarizability, as described in Ch. 4.2.2. The polarizabilities of the dipole chain elements all have only one non-zero component,  $\alpha_{i,xx}$ , with identical spectral shape  $S_{rod}(\omega) = \alpha_{rod,xx}(\omega)$  of the nanorod resonance. This spectral shape is taken as a Lorentzian function centered at 1.75 eV (710 nm) and with a width  $\gamma = 0.08$  eV. The real part and the imaginary part of this spectral function are plotted in Fig. 6.35A as the green and the blue curve, respectively. We here assume global excitation with

a spectrally flat electric field strength polarized along the rod axis,  $\vec{E}(\omega) = E_0\hat{x}$ , resulting in a dipole moment oriented along x-direction. The spatial distribution of the vectorial electric field around the nanorod,  $\vec{E}_{rod}(\vec{r})$  is then calculated applying the Green's function formalism to the chain of 22 dipoles, as described in Ch.4. The spatial function of the three vector components around the nanorod antenna dimer was shown in Fig. 6.31G-I. The complete electric field at position  $\vec{r}$  is then  $\vec{E}_{rod}(\vec{r}, \omega) = \vec{E}_{rod}(\vec{r}) \cdot S_{rod}(\omega)$ .

Now let's consider the polarization of the tip due to the electric field  $\vec{E}_{rod}(\vec{r}, \omega)$ . Here we used an elliptical tip, which is well described by

$$\overset{\leftrightarrow}{\alpha}_{tip} = \begin{pmatrix} \alpha_{tip,xx} & 0 & 0 \\ 0 & \alpha_{tip,yy} & 0 \\ 0 & 0 & \alpha_{tip,zz} \end{pmatrix}. \quad (6.32)$$

$\alpha_{tip,jj}$  with  $j = x, y, z$  are approximated as the polarizabilities for an ellipse (following Eqs. (4.111) and (4.112)) with  $R_x = R_y = 20$  nm and  $R_z = 100$  nm.

The spectral difference between the  $x, y$  and the  $z$ -polarizability is very strong, as is shown in Figs. 6.35B and D. The  $x$  and  $y$  polarizability are relatively flat in the spectral region covered by our experiment, while the  $z$ -polarizability shows a clear resonance centered at 770 nm.

The vector dipole moment induced in the tip placed at position  $\vec{r}_{tip}$  is given by

$$\vec{p}_{tip}(\vec{r}_{tip}, \omega) = \overset{\leftrightarrow}{\alpha}_{tip} \vec{E}_{rod}(\vec{r}, \omega) \quad (6.33)$$

and the electric field at the detector placed at position  $\vec{R}_{det}$  on the negative z-axis by

$$\vec{E}(\vec{R}_{det}) = \overset{\leftrightarrow}{G}(\vec{R}_{det}, \vec{r}_{tip}, \omega) \vec{p}_{tip}(\vec{r}_{tip}, \omega). \quad (6.34)$$

Figures 6.35 C and E show, for demonstration purposes, two spectrally resolved approach curves measured at the detector for two artificial cases: one, where only the  $x$ -component of the electric field is allowed and the  $y$  and  $z$ -components are set to zero, and one where the  $z$ -component of the electric field is allowed and the  $x$  and  $y$ -components are set to zero. In both cases, the maximum electric field strength at the resonance frequency and at a distance of 3 nm to the surface was set to 1 V/nm. The two approach curves show two spectrally well-separated maxima, clearly demonstrating that our choice of a strongly elliptic tip allows spectral separation of  $x/y$  and  $z$ -polarized electric field components.

Similar, we can now evaluate the near-field for the 4 tip positions. The result is shown in Fig. 6.36A-D.

It is important to note that in this simulation we consider the tip as a weak scatterer that scatters the already very strong near-field of the antenna. As we can see, the simulated near-field approach curves in Fig. 6.36 then match our measurement with good accuracy: We find a

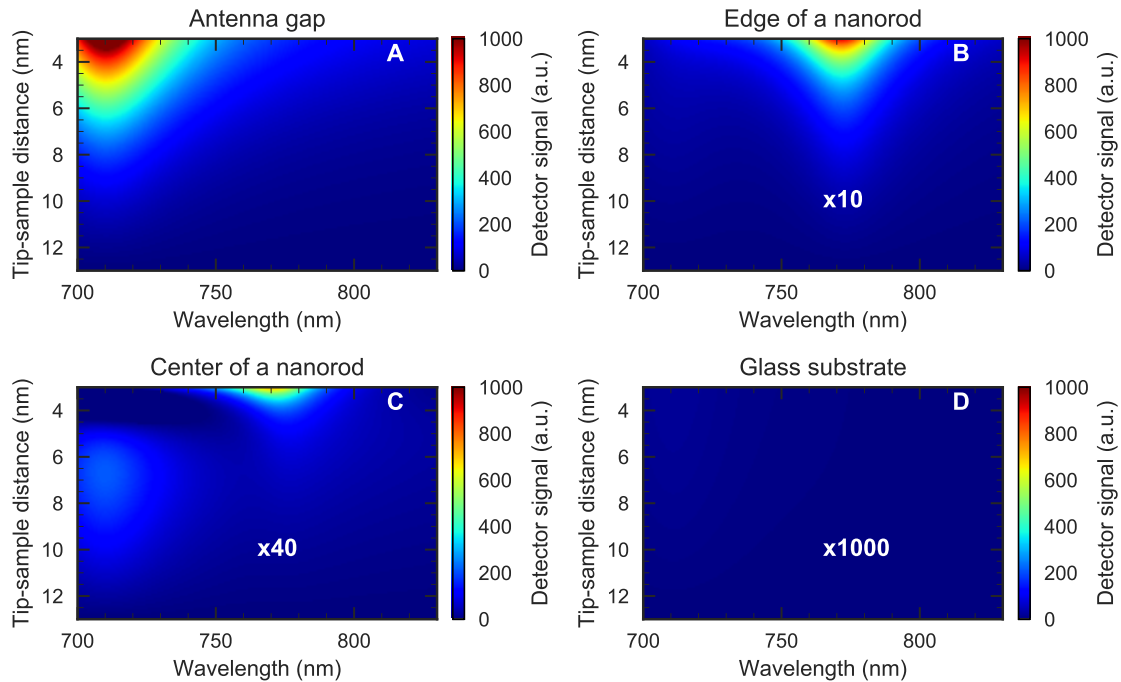


**Figure 6.36:** Simulation of the near-field around the nanorod antenna as a function of wavelength and tip-sample distance for tip positions: in the antenna gap, at the nanorod edge, at the nanorod middle and outside the structure. Note the factor  $\times 10$  and  $\times 100$  in (C) and (D) showing that the near-field signal strength is much weaker in the nanorod middle and outside the structure.

strong resonance in the gap centered around 710 nm that is stronger than all other near-field signals, a resonance around 760 nm mainly at the nanorod edges and a very small near-field signal at the nanorod middle and even less at the outside of the structure.

Finally, I present the optical near-field signal from our measurement in a 2D plot at the two wavelengths of 710 nm and 760 nm that were previously found to show a resonance. Due to the reduced amount of only  $40 \times 10$  scan points a bilinear interpolation filter was used to better visualize the near-fields around the structure. Similar to the previous analysis we observe a high near-field signal in the gap at the wavelength of 710 nm and only a small near-field signal near the middle or the edge of the nanorods. With the larger wavelength of 760 nm the near-field signal in the gap is highly reduced and now the edges of the nanorod show the highest near-field signal at this wavelength. In these results we also observe a strong near-field on the right nanorod for both wavelengths. We believe this is caused by an undesired strong scatterer on top of the nanorod. In total, the results are in agreement with our expectations: the tip scatters both x- and z-field components, whereas the z-component can be mostly observed around the nanorod edges at around 760 nm and the x-component is mostly scattered from the nano antenna gap at 710 nm. Thus, not only the local spectra evaluated at a few picked

positions indicate a wavelength dependent coupling to the tip polarizability tensor, but we can see this directly in a 2D SNOM scan around the antenna structure. This is an important result as it shows that we are able to easily measure and interpret vectorial near-field around nanostructures by demodulated SNOM spectra measurements and knowledge about the tip polarizability. This opens up the possibility optimize the design of these structures with respect to their desired optical properties.

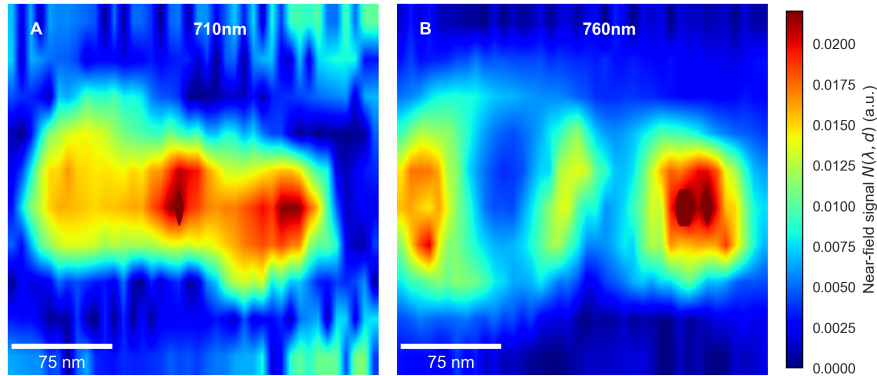


**Figure 6.37:** (A) and (B) show the optical near-field signal for a wavelength of 710 nm and 760 nm respectively. For better visualization the results were interpolated with a bilinear interpolation filter.

In our group, it is for example important for future studies to have antennas with a good field enhancement. SNOM measurements could be a very to characterize the actual near-fields and to optimize antenna designs.

Additionally, the analysis shown in this section emphasizes the high importance of nano antennas. The enhanced fields between tip and antenna in the gap or at the rim of the nano rod are ideal to probe strong coupling of individual nano materials. For example one could spincoat the squaraine dye on top of the antenna and should observe an energy splitting of the two single resonance from both the antenna and the dye. Similarly, one could probe the strong coupling characteristics of a single quantum dot by position the quantum dot in the gap of such an antenna structure. This could for example be done by following and moving the quantum dot with a atomic force microscope. Such experiments are already worked on and will be analyzed in future works.



# Summary & Outlook

# 7

In this thesis I addressed nanoscale local spectroscopy with a scanning near-field microscope with an experimental approach supported by theoretical considerations for the evaluation of the acquired SNOM spectra. A SNOM setup in back-reflection geometry was realized in such way, that it could be easily extended by new devices, e.g. a fast line camera. Throughout the thesis the setup was applied to a new way of performing direct local spectroscopy. Additionally, the tip-sample interaction for both isotropic and anisotropic media as well as for nanostructures was investigated.

To my knowledge for the first time an aperture-less SNOM setup was used with a monochromator and a fast line camera. This opens up many opportunities as it allows for a direct approach to measure locally resolved SNOM spectra, by combining the tip modulation technique with the acquisition of complete spectra. Nanoscale spectroscopy with SNOM was up to now mostly performed indirectly by Fourier Transform interferometry or a selective wavelength tuning of the laser source. These options both have their drawbacks, as the measurements are typically very slow, resulting in a long recording time for a SNOM map or in a very limited spectral resolution with only very few spectral positions probed. Other direct SNOM spectra measurements have only be obtained by more complex setups, e.g. by using the effect of adiabatic nanofocussing, which offers a low background signal but also a very limited near field strength.

The presented approach of direct spectra measurement with a fast line camera and a monochromator opens up the possibility to perform spectroscopic measurements as an extension to already existing aperture less setups, as well.

To finally be able to measure meaningful and understandable spectra various steps had to be solved beforehand. Two main issues were addressed in this thesis: the possibility to eliminate or weaken an always present optical background field for monochromatically as well as for spectrally resolved measurements and the data evaluation considering the tip-sample interaction that influences the measured spectra.

Hence, one chapter in this thesis addresses the problem of field interferences between a background field, a reference field and the desired near-fields from the nanotip used in SNOM measurements. Typically, higher order demodulation of the tip-to-sample distance modulation frequency is used to suppress the background interferences. However, we found for samples on a glass substrate, the ratio of the background field amplitude to the reference field is on the same order. Even with higher order demodulation the background field plays a significant role and cannot be neglected in the data discussion. Hence, in this thesis an in-line interferometer was presented that can be used to replace the standard glass substrate. The in-line interferometer consists of a gold-coated glass substrate, which is again coated with a 100-300 nm SiO<sub>2</sub> glass layer. This way the near-field is enhanced by a reference field reflected from a gold film and the near-field to background ratio increases. As there are no moving parts, the interference is intrinsically stable. Furthermore, the last layer is glass, which is often desired for various samples that may arrange differently or have changed properties on a bare gold film.

Finally, this new local spectroscopy technique involving higher order demodulation was applied to several different samples. Here, in a first step spectra measurements on less complex, flat samples that show no resonance in the investigated spectral region were used in order to study the tip-sample interaction in more detail and demonstrate the data evaluation, such as a 30 nm-thick gold film. The overall interpretation of the measured SNOM spectra revealed the complexity of the tip-sample interaction and showed that the tip influence can drastically alter the SNOM spectra. The field enhancement of the individual tip as well as the sample properties dictate the final outcome and even a blunt or deformed tip can result in a new spectral resonance. An extensive simulation model has been worked out to gain a better understanding of the effects that take place. By analyzing multiple measurements we found that both a coupling to the in-plane component as well as to the z-component of the tip polarizability tensor can occur. Their relative coupling strength depends on the tip position in the focus field as well as on the sample properties and the tip shape. By measuring spectrally resolved spectra around a nanorod antenna we could even demonstrate a coupling to both components in a single measurement by placing the tip inside the gap of the antenna structure where coupling to the x-component exceeds and placing the tip at the edge of nanorod where coupling to the z-component exceeds.

With the gained understanding, a local absorption spectrum measurement of a squaraine dye material was performed. The squaraine dye is currently a promising candidate to be used as organic photodiode or solar cell material. Since only little was known about this new dye material, we firstly used far field transmission spectroscopy to investigate the light-matter interaction. For this purpose a quantum mechanical description by modeling the dye as a 2-level system was developed. Far-field transmission spectra could then be explained by an angular distribution

of coupling squaraine monomer dipoles. Using nanoscale spectroscopy an actual difference in spectra on the nanoscale could be reported and supported this model. Our measurements further indicate that the squaraine dyes were mostly oriented in the sample plane and hence a coupling to the tip's xy-component of the polarizability tensor highly outweighs coupling to the z-component. Thus, these measurements also demonstrated the possibility to measure near-field signals even on a strongly anisotropic materials.

The presented SNOM setup with a fast line camera could easily be extended to enable measuring polarization resolved SNOM spectra, more specifically, spectra as a function of the laser input polarization. This could be used for investigating the orientation of nanostructures as well as of organic materials with long molecules that are capable of forming aggregates. Polarization-resolved measurements with nanometer-spatial resolution could shed light on the orientation and nanometer-range order of such samples and could thus be of great importance for developing fabrication methods supporting specific structure-function relations.

Some early results of measurements on a polymer sample are presented in appendix C as an outlook. Long polymer chains show higher absorption for light polarized parallel to the polymer chain direction than for light polarized perpendicular to it and are the ideal candidate for such measurements. Local SNOM absorption measurements for different laser input polarizations presented in the appendix already indicate that spincoating of the polymers onto a glass substrate results in multiple domains of ordered polymer chain directions with sizes on the order of  $<1\ \mu\text{m}$  whereas a blade-coating method can produce polymer films with a far longer-ranged alignment. In total, polarization dependency adds another layer of complexity to the already non-trivial tip-sample interaction. For a quantitative statement more measurements and a more in-depth analysis is needed, which is left to future works.

All in all, this thesis presents various experiments that were carried out to measure local spectra on a nanometer scale and to study the tip-sample interaction for nanostructures as well as for (anisotropic) organic sample materials in the visible to near-infrared spectral region. Together with the simulations presented in this thesis, this serves as a first attempt of a near-field spectroscopy overview by using a direct demodulation-based approach and can be used as the groundwork for understanding and interpreting local spectroscopy data in future works.



# Matlab/Python Programming of SNOM controls

---



## A.1 Program Interface

The interface to control the SNOM and all attached devices was written from scratch. For that task mainly MatLab and Python were used.

This appendix section gives an overview of how the controls were written and provides details about the hardware and software to help future researcher maintaining and extending the SNOM setup used throughout this thesis.

The following main components had to be controlled:

- PI XYZ Stage / Rotation Stages / Linear Actuators / 5-AXis Coarse Stage
- Zürich Instruments Lockin Amplifier / IO device
- Data Translation AI/AO Converter Card
- Aviiva 210kHz LineCamera (over Framegrabber card)

The connection of these devices was either over USB/ parallel connection, serial connection or in the case of the LineCamera with an addtinal FrameGrabber Card inbetween.

The software was written using object oriented programming. Each device has it's own Matlab class that can connect with other classes as well.

We made use of the package folders created by a plus sign as the first character of the folder name <sup>1</sup>.

---

<sup>1</sup>Compare the MathWorks help: [https://de.mathworks.com/help/matlab/matlab\\_oop/scoping-classes-with-packages.html](https://de.mathworks.com/help/matlab/matlab_oop/scoping-classes-with-packages.html)

The folder structure then divides into sub-package-folders with:

+devices

... +stage

... Axis.m

... E7XX\_Stage.m

... Rotation\_Stage.m

... Stage.m (Super Class)

... APT\_Stage.m

... MO\_actuator.m

... +spectrometer

... Spectrometer.m (Super Class)

... Ocean\_Optics\_Spectrometer.m

... +io

... IOBoard.m

... DTOL.m

... +some subclasses

... FunctionGeneratorZi.m

... e2VCamera.m

+fcns

... ApproachCurve.m

... ResonanceCurve.m

... BeamScan.m

+tools

... Tools to saving as gsf files or send push messages for finished measurements

The main control is done via a separate file "SNMOM.m" and control of the complete SNOM can then easily be done with simple commands like

```
NSOM = SNOM();
NSOM.setStage('E7XX_x64');
ret = NSOM.init_all();
NSOM.Stage.setServoStatus(z, true);
...
data_tmp = NSOM.scan(NSOM.Stage.xAxis, ...
NSOM.Stage.yAxis, ...
[startx, starty], [endx, endy], [numstepsx numstepsy], ...
timeperline, scandirection);
```

An additional GUI was available as well.

As we can see each device is individually controllable by its own class functions and can easily be extended. A git version control software was used on top to track changes, allow multi-user collaboration and ensure safe operation at any time.

Most of these classes were simultaneously written in Python and a few rare used programs like the coarse control of a 5-Axis stage were decoupled from the main Matlab/Python interface and have been compiled into a standalone application with a GUI for an easy controllability using PyInstaller.



# Refractive index and Snell's law for anisotropic materials

# B

This appendix supplements chapter 4.1.3 and shows the derivations for the refractive index as well as the Snell's law for anisotropic media to obtain an equation for the angle  $\theta$  in the anisotropic medium as a function of the incident angle  $\theta_i$ .

## B.1 Derivation 1: The refractive index

Starting from equation (4.64)

$$\frac{1}{n^2} = \frac{s_x^2}{n^2 - n_x^2} + \frac{s_y^2}{n^2 - n_y^2} + \frac{s_z^2}{n^2 - n_z^2} \quad (\text{B.1})$$

we can multiply both sides by  $(n^2 - n_x^2)(n^2 - n_y^2)(n^2 - n_z^2)$ :

$$\frac{1}{n^2} \cdot (n^2 - n_x^2)(n^2 - n_y^2)(n^2 - n_z^2) = s_x^2(n^2 - n_y^2)(n^2 - n_z^2) + s_y^2(n^2 - n_x^2)(n^2 - n_z^2) + s_z^2(n^2 - n_x^2)(n^2 - n_y^2) \quad (\text{B.2})$$

Since  $\vec{s} = \vec{k}/k$  is the unit vector in the direction of  $\vec{k}$  we also have  $1 = s_x^2 + s_y^2 + s_z^2$ . By replacing the nominator of  $1/n^2$  with that expression and multiplying both sides by  $n^2$  we get

$$\begin{aligned} (s_x^2 + s_y^2 + s_z^2) \cdot (n^2 - n_x^2)(n^2 - n_y^2)(n^2 - n_z^2) &= n^2[s_x^2(n^2 - n_y^2)(n^2 - n_z^2) \\ &+ s_y^2(n^2 - n_x^2)(n^2 - n_z^2) \\ &+ s_z^2(n^2 - n_x^2)(n^2 - n_y^2)] \end{aligned} \quad (\text{B.3})$$

As the equation gets very long, we will focus only on one term for the sake of simplicity. Expanding the  $s_x^2$  term on the left side reads:

$$s_x^2 n^2 (n^2 - n_y^2)(n^2 - n_z^2) - s_x^2 n_x^2 (n^2 - n_y^2)(n^2 - n_z^2) + \dots = n^2 [s_x^2 n_x^2 (n^2 - n_y^2)(n^2 - n_z^2) + \dots] \quad (\text{B.4})$$

Subtracting all terms from the left hand side of the equation yields

$$0 = n^2[s_x^2(n^2 - n_y^2)(n^2 - n_z^2) - s_y^2(n^2 - n_x^2)(n^2 - n_z^2)] + s_x^2 n_x^2 (n^2 - n_y^2)(n^2 - n_z^2) + \dots \quad (\text{B.5})$$

or

$$0 = s_x^2 n_x^2 (n^2 - n_y^2)(n^2 - n_z^2) + \dots \quad (\text{B.6})$$

The same procedure can be done for the other two terms which are multiplied by either  $s_y$  or  $s_z$ . So in total we get equation (4.65):

$$s_x^2 n_x^2 (n^2 - n_y^2)(n^2 - n_z^2) + s_y^2 n_y^2 (n^2 - n_x^2)(n^2 - n_z^2) + s_z^2 n_z^2 (n^2 - n_x^2)(n^2 - n_y^2) = 0 \quad (\text{B.7})$$

Now for uniaxial media with  $n_x = n_y = n_o$  and  $n_z = n_e$  the term  $(n^2 - n_o^2)$  can be found multiple times in the above equation and can be factored out:

$$(n^2 - n_o^2)[n_o^2(s_x^2 + s_y^2)(n^2 - n_e^2) + s_z^2 n_e^2 (n^2 - n_o^2)] = 0 \quad (\text{B.8})$$

This means either  $n^2 - n_o^2 = 0$  or

$$n_o^2(s_x^2 + s_y^2)(n^2 - n_e^2) + s_z^2 n_e^2 (n^2 - n_o^2) = 0 \quad (\text{B.9})$$

Factoring out then gives

$$n^2 n_o^2 (s_x^2 + s_y^2) - n_e^2 n_o^2 (s_x^2 + s_y^2) - n_e^2 n_o^2 s_z^2 + s_z^2 n_e^2 n^2 = 0 \quad (\text{B.10})$$

and can be written as

$$n^2(n_o^2(s_x^2 + s_y^2) + n_e^2 s_z^2) - n_e^2 n_o^2 (s_x^2 + s_y^2 + s_z^2) = 0 \quad (\text{B.11})$$

Like before  $s_x^2 + s_y^2 + s_z^2$  is the squared value of the length of the unit vector  $\vec{s}$  and can be set to 1. Addition of  $n_e^2 n_o^2$  to both sides now yields

$$n^2(n_o^2(s_x^2 + s_y^2) + n_e^2 s_z^2) = n_e^2 n_o^2 \quad (\text{B.12})$$

Finally by dividing by  $(n_o^2(s_x^2 + s_y^2) + n_e^2 s_z^2)$  and taking the reciprocal value of the whole equation we get equation (4.67):

$$\frac{1}{n^2} = \frac{s_x^2 + s_y^2}{n_e^2} + \frac{s_z^2}{n_o^2}. \quad (\text{B.13})$$

## B.2 Derivation 2: The angle in the medium

We start from Snell's law in anisotropic media for p-polarized light:

$$n_i \sin(\theta_i) = n(\theta) \sin(\theta) \quad (\text{B.14})$$

Substituting  $n(\theta)$  yields:

$$n_i \sin(\theta_i) = \frac{n_o n_e}{\sqrt{n_o^2 \sin^2(\theta) + n_e^2 \cos^2(\theta)}} \sin(\theta) \quad (\text{B.15})$$

By dividing by  $n_o$  and introducing  $a = n_i/n_o \sin(\theta)$  and  $b = n_o^2/n_e^2$  we get

$$a = \frac{\sin(\theta)}{\sqrt{b \sin^2(\theta) + \cos^2(\theta)}} \quad (\text{B.16})$$

With  $\cos^2(\theta) = 1 - \sin^2(\theta)$  and squaring the equation we then get

$$a^2 = \frac{\sin^2(\theta)}{b \sin^2(\theta) + 1 - \sin^2(\theta)} \quad (\text{B.17})$$

$$a^2 = \frac{\sin^2(\theta)}{(b-1) \sin^2(\theta) + 1} \quad (\text{B.18})$$

$$(\text{B.19})$$

Multiplying by the denominator  $(b-1) \sin^2(\theta) + 1$

$$a^2(b-1) \sin^2(\theta) + a^2 = \sin^2(\theta) \quad (\text{B.20})$$

and factoring out  $\sin^2(\theta)$

$$\sin^2(\theta)(a^2(b-1) - 1) = -a^2 \quad (\text{B.21})$$

gives us finally the relationship between the angle  $\theta$  in the medium and the angle of the incident medium  $\theta_i$ :

$$\sin^2(\theta) = \frac{-a^2}{(a^2(b-1) - 1)} \quad (\text{B.22})$$

$$\sin(\theta) = \frac{a}{\sqrt{1 - a^2(b-1)}} \quad (\text{B.23})$$

$$\sin(\theta) = \frac{n_i/n_o \sin(\theta_i)}{\sqrt{1 - (n_i/n_o \sin(\theta_i))^2 (n_o^2/n_e^2 - 1)}} \quad (\text{B.24})$$

$$\theta = \arcsin \left( \frac{n_i/n_o \sin(\theta_i)}{\sqrt{1 - (n_i/n_o \sin(\theta_i))^2 (n_o^2/n_e^2 - 1)}} \right) \quad (\text{B.25})$$



# Outlook: Local orientations of polymers by polarization resolved SNOM



We have already outlined the importance of local spectroscopy to understand the relationship between structure and functionality of a squaraine dye spincoated on top of a glass substrate. From these measurements we learned about the local change of coupling energies that are contributed to a variation in relative dipole-dipole orientation. Another way of studying local orientations by SNOM is presented here as an outlook by making use of the polarization dependent absorption of long polymer chains attached on a substrate. In particular, the presented polymer chains show a higher absorption when light is polarized along the chains, rather to light that is polarized perpendicular to the chains.

We investigated the polymer P(NDI2OD-T2) synthesized in the group of Prof. Dr. S.Ludwigs from the institute of polymer chemistry of the university of Stuttgart [218]. The structure formula is shown in Fig. C.1A. These kind of conjugated polymers have gathered a lot of interest in many research areas as they show very promising semiconducting properties which make them ideal for flexible electronic devices or organic solar cells. In particular also their light weight and corrosion resistance make them a very appealing alternative to inorganic semiconductors [219].

The spectral absorption of the polymer has been previously measured by Trefz et.al. for polarization parallel (denoted  $I_{\parallel}$ ) and perpendicular (denoted  $I_{\perp}$ ) to the chain axis for a bulk sample [220] and is shown in figure C.1C. Two absorption maxima are directly visible, one spectrally very broad absorption maximum around 700 nm spanning nearly 200 nm and another one with a smaller spectral width of around 40 nm centered at around 400 nm. Our laser system can only operate in the wavelength range covering the broad resonance. Here, the absorption for light polarized parallel and perpendicular to the polymer chains differs drastically and we can read out a reduction in absorption by a factor of at least 10 for a wavelength of 700 nm.

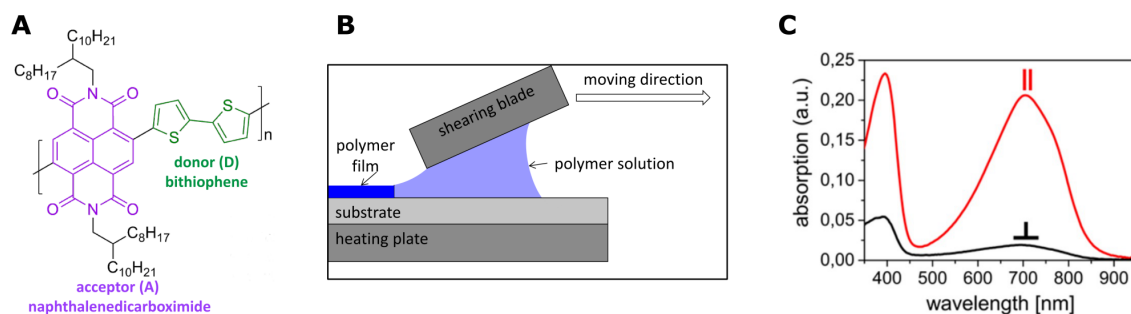


**Figure C.1:** (A) Structure formula (B) Illustration of the blade coating process (cmp. [220]), (C) Absorption spectra measured for two orthogonal polarizations (taken from [220])

For smaller or larger wavelength the difference decreases. Thus, for a sample with differently aligned polymers we expect to see a wavelength dependent change in contrast in a local SNOM scan.

At first, we investigate the polarization dependency by using a linearly polarized Titanium:Sapphire laser operated at a fixed wavelength of 740 nm in cw-mode with the previously described SNOM setup. This means the laser is focused through the sample onto a sharp gold tip and scattered near-field signal from the tip is collected by an avalanche photodiode in a backscattering geometry. The signal is demodulated at the first harmonic frequency, thus a large background field contribution is included. Still, some early conclusions can be drawn already. In order to measure SNOM signals dependent on the input polarization of the linearly polarized laser source, a zero order half-wave-plate was mounted in a motorized rotation holder after the laser source and in front of the actual SNOM setup. Changing the direction of the linearly polarized laser source now enables us to measure polarization dependent absorption on a local, nanometer scale and may help us to determine polymer orientation differences. The motorized rotation holder is furthermore connected to a computer, such that it can be rotated automatically. This way it does not generate disturbing vibrations and can even be used when the SNOM tip is in close contact to the sample.

In the following we evaluate two different samples that were produced with the same polymer material, but with two different techniques: For one sample the polymer was spincoated on top of a BK7 glass substrate, in the other case a blade-coating technique was used to attach the polymer to the substrate. The blade-coating technique is visualized in figure C.1B: while heating the substrate at a degree of 220 to 320 deg a shearing blade is held at an angle of around 40° over the substrate with the polymer solution beneath it. This process is meant to produce highly aligned polymers on the substrate. Control over the alignment is one important goal of current organic semiconductor film fabrication, since the structure and alignment on an

nm- to  $\mu\text{m}$  length scale is decisive for charge transport in these materials [221]. The spincoated sample is expected to be less ordered and may even produce groups of clustered polymer chains, with the polymer molecules inside these groups having a preferred alignment direction. These groups are in the following denoted as domains.

A typical AFM and two SNOM images for two polarizations of the incoming laser beam (visualized by the white arrows) are shown in Fig. C.2A-C for the spincoated polymer sample and in Fig.C.2D-F for the blade-coated sample.

The AFM image of the spincoated polymer film shows large domains with sizes of 100 nm and height changes of up to 70 nm. On a closer look, one can even recognize a filament-like structure inside these domains. These filaments may be attributed to clustered polymer strings. Each domain seems to have slightly different directions of these strings, the majority however is pointing mostly from south to north direction.

Depending on the polarization of the incoming beam, the SNOM scans in Fig. C.2B and C differ in intensity at specific positions. Analogous to the different areas in the AFM image, also in the optical image different domains of high intensity can be recognized. They have similar domain sizes of around 100 nm. Furthermore one can see areas that have a particular high optical signal in one image often have a low signal strength in the other, obtained with perpendicular polarization. These differences between the two images with different polarizations suggest that the method is sensitive to the alignment of the polymers and means the optical images probably carry new information.

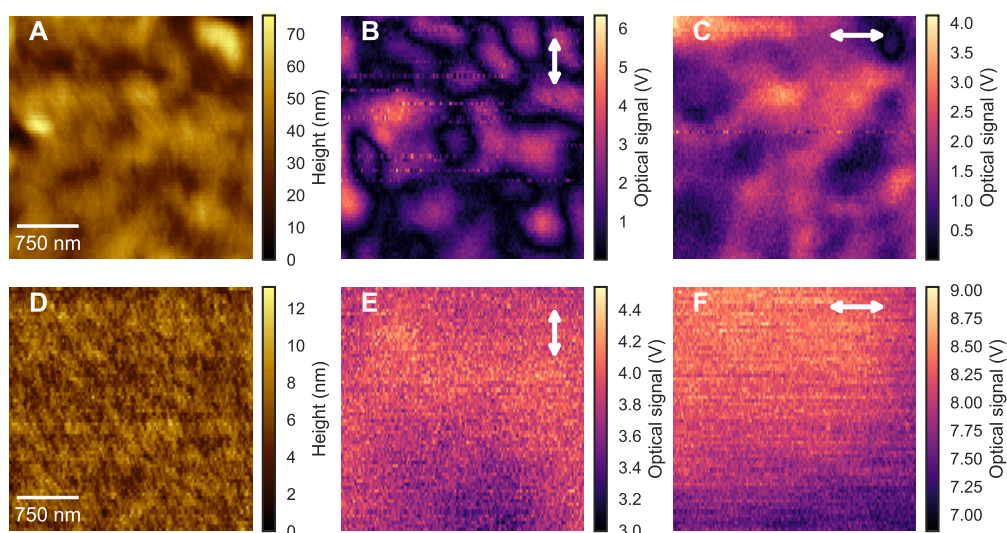


**Figure C.2:** AFM scan and optical signals of a spincoated (A-C) and blade-coated (D-F) thin film of the polymer P(NDI2OD-T2). The white arrows in the optical images denote the polarization direction of the linearly polarized laser source.

For the case of the blade-coated sample shown in Fig. C.2D-F, already the AFM scan shows

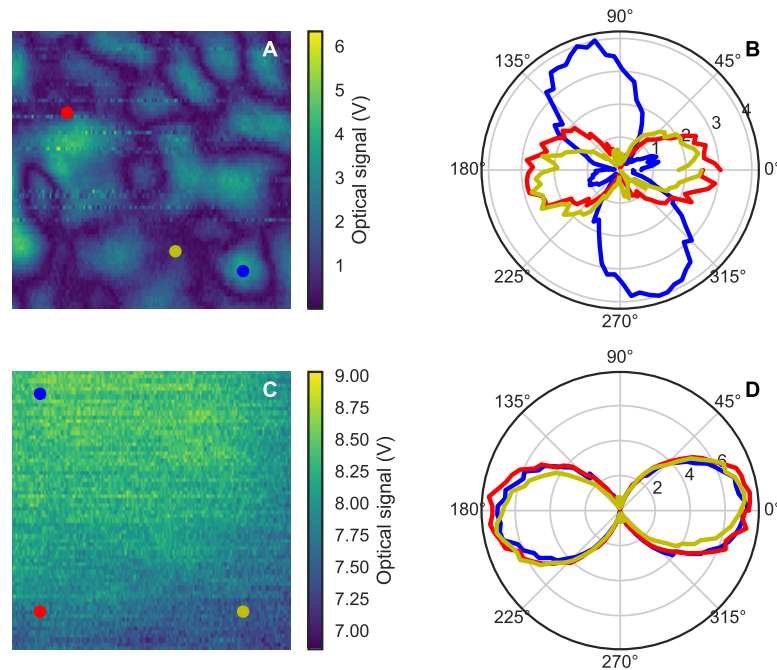


**Figure C.3:** (A) shows again the optical signal from spincoated sample presented in Fig. C.2 together with 3 points. At these points the laser input polarization dependent scans were carried out, which are shown in (B). The line colors match the colors of the points in (A). (C) shows the optical signal of the blade-coated sample together with 3 points of polarization dependent scans shown in (D).

a much smoother polymer thin film. Height changes of less than 12 nm are observed and no obvious large domains are forming anymore. The optical signal still shows differences in intensity between the two polarizations, but shows otherwise a nearly constant signal over the given area of  $2 \times 2 \mu\text{m}$ . This is a clear difference to the optical signal of the spincoated sample and is already a promising indication for better aligned polymers.

For a more detailed analysis, we now recorded a laser input polarization dependent SNOM signal for different spots on both the unordered and the ordered sample. These polarization dependent scans are presented in figure C.3. Hereby, the scan positions are visualized by the colored dots in the optical images in Fig. C.3A for the spincoated sample and in C.3C for the blade-coated sample.

On the sample with the spincoated polymers Fig.C.3B clearly indicates a change of the direction with maximum intensity: the yellow and red curve were recorded at a low intensity point in Fig.C.3A and show the highest signals at a polarization direction of about 0 and 180 deg. They both show a signal proportional to  $\cos^2(\theta)$  with  $\theta$  describing the angle of input polarization direction. The blue curve was recorded at a point of high optical signal and the polar plot shows a cloverleaf structure. The smaller lobes of this structure have a maximum for a direction of a

few degrees, but are of much lower intensity than the measurements on the other two points. The larger lobes have a maximum in the optical signal at around 120 deg. This maximum is around 4/3 stronger than the maximum for the other two measurements.

In contrast, we can observe almost no change in direction for different points in the polarization dependent scans of the optical signals for the blade-coated sample shown in Fig. C.3D . The polarization scans are nearly the same for each measurements and all show a typical  $\cos^2(\theta)$  curve.

The measured SNOM signal depends on the relative orientation of electric field and molecular dipole moment, and hence can indicate the molecule alignment. We believe that the variation of the polar plots for the spin-coated sample is due to differently aligned domains, while for the shear-blade fabricated sample the spatial unaltered polar plot indicates a much more uniform alignment. Moreover, we propose that the applied polarization-resolved near-field microscopy does contain information on the actual polymer orientation within the tip-sample interaction area of  $\sim 10$  nm diameter.

Extracting the real polymer orientation from the polarization measurements and explaining the observed polar plot shapes however is non-trivial and requires a more quantitative analysis, for example by using the Green's function approach, applying a biaxial anisotropic model and pre-characterizing the spectral response of the tip. In general, many factors are entering in the polarization description. Besides the interference and the tip-sample distance also focusing of the fields and the angle of the tip with respect to the sample and thus the coupling to the in-plane and z-component of the tip plays a role. Hence, for now only conclusions about the relative change of the measured polar plot for different points across the sample can be made. A quantitative analysis is left for future works.

Finally, we want to solidify our assumption that the observed polarization-dependent patterns are indeed due to a polarization-dependent absorption of the polymer. For this we expand our study by spectrally resolved measurements around the absorption maximum determined in the far-field measurements (Fig. C.1C). From the measured absorption spectrum in Fig. C.1 we already know that the difference in absorption is highest at a wavelength of 700 nm and decreases for larger wavelengths. Thus, if our setup is sensitive to the polymer orientation we would expect a spectrally dependent contrast in SNOM maps recorded in the same way as Fig. C.3A for a spincoated sample. For a wavelength of 800 nm the difference in absorption is already decreased by a factor of around 5 in comparison to the factor of at least 10 for the wavelength of 700 nm and should lead to a blurry SNOM image.

Figure C.4 shows the results of recording the optical signal  $S_{1f}$  in an area on this sample with five different wavelengths by tuning the narrow-band wavelength of a Titanium:Sapphire laser in cw-mode. We measured scans at wavelengths of 740 nm, 775 nm, 810 nm, 840 nm and 860 nm.

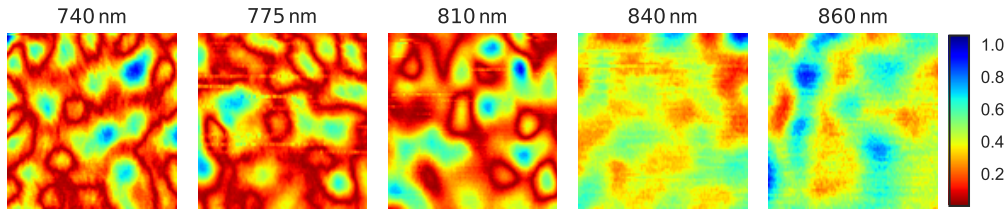


**Figure C.4:** Recorded  $S_{1f}$  signal on the spincoated polymer sample for different wavelengths by tuning the wavelength of a Ti:Sa laser in cw mode. Due to drift of the sample during the scan time, the area may not be the same in all scans.

As the output beam from the laser slightly changed with each new wavelength, the setup was optimized for a maximum signal each time. This means a new beam scan was performed for each wavelength to ensure the focus is always on the tip apex. During that time the sample may have experienced drift and thus it is not ensured that the area in all images is completely the same. This shows at the same time the major drawback of such a method and one important motivation to perform direct local spectroscopy as presented in previous chapters. Yet, the measurements nicely reveal the expected reduction in contrast for higher wavelengths: for a wavelength of 740 nm, near the absorption maximum, we can observe various domains which are clearly separated. For longer wavelengths the absorption at both polarizations becomes less distinguishable and the measurement results in the expected blurry optical image. At a wavelength 860 nm only very little contrast between what presumably are different domains is visible anymore.

In total, the presented results already show that we indeed can measure polarization resolved local absorption by SNOM. For a quantitative discussion however, a more in-depth analysis is needed. In particular for an ordered polymer string, the dielectric function will be different in all three dimensions  $x, y$  and  $z$  and thus the sample is called a biaxial anisotropic medium. Furthermore, a pre-characterization of the polarization dependency of the tip response is needed. Also, one could consider to tilt the tip under an angle. As recently shown by Park & Raschke [206] a tilted tip with respect to the sample can help to vary the ratio of in-plane to out-of plane coupling and hence increase the coupling efficiency of the tip and the mostly in-plane aligned polymers. These measurements and simulations are not covered here but are suggested for future works. The analytical models presented in this thesis can be used as a good starting point.

**Paper attachment: In-line  
interferometer for  
broadband near-field  
scanning optical  
spectroscopy**

**D**

---

The following pages contain the original paper with the title "In-line interferometer for broadband near-field scanning optical spectroscopy", from Jens Brauer, Jinxin Zhan, Abbas Chimeh, Anke Korte, Christoph Lienau, and Petra Gross, published in *Opt. Express* 25, 15504-15525 (2017).

Parts of this paper were used in chapter 5 and 6.1 of this thesis.



# In-line interferometer for broadband near-field scanning optical spectroscopy

JENS BRAUER,<sup>1</sup> JINXIN ZHAN,<sup>1</sup> ABBAS CHIMEH,<sup>1</sup> ANKE KORTE,<sup>1</sup>  
CHRISTOPH LIENAU,<sup>1,2,3</sup> AND PETRA GROSS<sup>1,\*</sup>

<sup>1</sup>Carl von Ossietzky Universität, Institut für Physik and Center for Interface Science, Carl-von-Ossietzky-Str. 9, 26129 Oldenburg, Germany

<sup>2</sup>Forschungszentrum Neurosensorik, Carl von Ossietzky Universität, Carl-von-Ossietzky-Str. 9, 26129 Oldenburg, Germany

<sup>3</sup>christoph.lienau@uni-oldenburg.de

\*petra.gross@uni-oldenburg.de

**Abstract:** We present and investigate a novel approach towards broad-bandwidth near-field scanning optical spectroscopy based on an in-line interferometer for homodyne mixing of the near field and a reference field. In scattering-type scanning near-field optical spectroscopy, the near-field signal is usually obscured by a large amount of unwanted background scattering from the probe shaft and the sample. Here we increase the light reflected from the sample by a semi-transparent gold layer and use it as a broad-bandwidth, phase-stable reference field to amplify the near-field signal in the visible and near-infrared spectral range. We experimentally demonstrate that this efficiently suppresses the unwanted background signal in monochromatic near-field measurements. For rapid acquisition of complete broad-bandwidth spectra we employ a monochromator and a fast line camera. Using this fast acquisition of spectra and the in-line interferometer we demonstrate the measurement of pure near-field spectra. The experimental observations are quantitatively explained by analytical expressions for the measured optical signals, based on Fourier decomposition of background and near field. The theoretical model and in-line interferometer together form an important step towards broad-bandwidth near-field scanning optical spectroscopy.

© 2017 Optical Society of America

**OCIS codes:** (180.4243) Near-field microscopy; (240.6490) Spectroscopy, surface; (240.6380) Spectroscopy, modulation; (240.6680) Surface plasmons; (350.4238) Nanophotonics and photonic crystals.

## References and links

1. W. Bao, M. Melli, N. Caselli, F. Riboli, D. S. Wiersma, M. Staffaroni, H. Choo, D. F. Ogletree, S. Aloni, J. Bokor, S. Cabrini, F. Intonti, M. B. Salmeron, E. Yablonovitch, P. J. Schuck, and A. Weber-Bargioni, "Mapping local charge recombination heterogeneity by multidimensional nanospectroscopic imaging," *Science* **338**(6112), 1317–1321 (2012).
2. S. Berweger, J. M. Atkin, R. L. Olmon, and M. B. Raschke, "Light on the tip of a needle: plasmonic nanofocusing for spectroscopy on the nanoscale," *J. Phys. Chem. Lett.* **3**(7), 945–952 (2012).
3. R. Chikkaraddy, B. de Nijs, F. Benz, S. J. Barrow, O. A. Scherman, E. Rosta, A. Demetriadou, P. Fox, O. Hess, and J. J. Baumberg, "Single-molecule strong coupling at room temperature in plasmonic nanocavities," *Nature* **535**(7610), 127–130 (2016).
4. S. Yampolsky, D. A. Fishman, S. Dey, E. Hulkko, M. Banik, E. O. Potma, and V. A. Apkarian, "Seeing a single molecule vibrate through time-resolved coherent anti-Stokes Raman scattering," *Nat. Photonics* **8**(8), 650–656 (2014).
5. A. Anderson, K. S. Deryckx, X. G. Xu, G. Steinmeyer, and M. B. Raschke, "Few-femtosecond plasmon dephasing of a single metallic nanostructure from optical response function reconstruction by interferometric frequency resolved optical gating," *Nano Lett.* **10**(7), 2519–2524 (2010).
6. T. Guenther, C. Lienau, T. Elsaesser, M. Glanemann, V. M. Axt, T. Kuhn, S. Eshlaghi, and A. D. Wieck, "Coherent nonlinear optical response of single quantum dots studied by ultrafast near-field spectroscopy," *Phys. Rev. Lett.* **89**(5), 057401 (2002).
7. R. Hildner, D. Brinks, J. B. Nieder, R. J. Cogdell, and N. F. van Hulst, "Quantum coherent energy transfer over varying pathways in single light-harvesting complexes," *Science* **340**(6139), 1448–1451 (2013).
8. E. Betzig, J. K. Trautman, T. D. Harris, J. S. Weiner, and R. L. Kostelak, "Breaking the diffraction barrier: optical microscopy on a nanometric scale," *Science* **251**(5000), 1468–1470 (1991).

9. W. E. Moerner, T. Plakhotnik, T. Irgartinger, U. P. Wild, D. W. Pohl, and B. Hecht, "Near-field optical spectroscopy of individual molecules in solids," *Phys. Rev. Lett.* **73**(20), 2764–2767 (1994).
10. L. Novotny and S. J. Stranick, "Near-field optical microscopy and spectroscopy with pointed probes," *Annu. Rev. Phys. Chem.* **57**(1), 303–331 (2006).
11. W. Bao, M. Staffaroni, J. Bokor, M. B. Salmeron, E. Yablonovitch, S. Cabrini, A. Weber-Bargioni, and P. J. Schuck, "Plasmonic near-field probes: a comparison of the campanile geometry with other sharp tips," *Opt. Express* **21**(7), 8166–8176 (2013).
12. T. Taubner, R. Hillenbrand, and F. Keilmann, "Performance of visible and mid-infrared scattering-type near-field optical microscopes," *J. Microsc.* **210**(3), 311–314 (2003).
13. J. M. Gerton, L. A. Wade, G. A. Lessard, Z. Ma, and S. R. Quake, "Tip-enhanced fluorescence microscopy at 10 nanometer resolution," *Phys. Rev. Lett.* **93**(18), 180801 (2004).
14. S. F. Becker, M. Esmann, K. Yoo, P. Groß, R. Vogelgesang, N. Park, and C. Lienau, "Gap-Plasmon-Enhanced Nanofocusing Near-Field Microscopy," *ACS Photonics* **3**(2), 223–232 (2016).
15. R. Zhang, Y. Zhang, Z. C. Dong, S. Jiang, C. Zhang, L. G. Chen, L. Zhang, Y. Liao, J. Aizpurua, Y. Luo, J. L. Yang, and J. G. Hou, "Chemical mapping of a single molecule by plasmon-enhanced Raman scattering," *Nature* **498**(7452), 82–86 (2013).
16. E. Bailo and V. Deckert, "Tip-enhanced Raman spectroscopy of single RNA strands: towards a novel direct-sequencing method," *Angew. Chem. Int. Ed. Engl.* **47**(9), 1658–1661 (2008).
17. A. J. Babadjanyan, N. L. Margaryan, and K. V. Nerkararyan, "Superfocusing of surface polaritons in the conical structure," *J. Appl. Phys.* **87**(8), 3785–3788 (2000).
18. M. I. Stockman, "Nanofocusing of optical energy in tapered plasmonic waveguides," *Phys. Rev. Lett.* **93**(13), 137404 (2004).
19. V. Kravtsov, R. Ulbricht, J. M. Atkin, and M. B. Raschke, "Plasmonic nanofocused four-wave mixing for femtosecond near-field imaging," *Nat. Nanotechnol.* **11**(5), 459–464 (2016).
20. S. Schmidt, B. Piglosiewicz, D. Sadiq, J. Shirdel, J. S. Lee, P. Vasa, N. Park, D.-S. Kim, and C. Lienau, "Adiabatic nanofocusing on ultrasmooth single-crystalline gold tapers creates a 10-nm-sized light source with few-cycle time resolution," *ACS Nano* **6**(7), 6040–6048 (2012).
21. M. Esslinger, J. Dorfmueller, W. Khunsin, R. Vogelgesang, and K. Kern, "Background-free imaging of plasmonic structures with cross-polarized apertureless scanning near-field optical microscopy," *Rev. Sci. Instrum.* **83**(3), 033704 (2012).
22. R. Hillenbrand, B. Knoll, and F. Keilmann, "Pure optical contrast in scattering-type scanning near-field microscopy," *J. Microsc.* **202**(1), 77–83 (2001).
23. B. Knoll and F. Keilmann, "Enhanced dielectric contrast in scattering-type scanning near-field optical microscopy," *Opt. Commun.* **182**(4–6), 321–328 (2000).
24. N. Ocelic, A. Huber, and R. Hillenbrand, "Pseudoheterodyne detection for background-free near-field spectroscopy," *Appl. Phys. Lett.* **89**(10), 101124 (2006).
25. Y. Sasaki and H. Sasaki, "Heterodyne detection for the extraction of the probe-scattering signal in scattering-type scanning near-field optical microscope," *Jpn. J. Appl. Phys.* **39**(4A), L321–L323 (2000).
26. A. V. Zayats and V. Sandoghdar, "Apertureless scanning near-field second-harmonic microscopy," *Opt. Commun.* **178**(1–3), 245–249 (2000).
27. E. A. Ash and G. Nicholls, "Super-resolution aperture scanning microscope," *Nature* **237**(5357), 510–512 (1972).
28. R. Hillenbrand and F. Keilmann, "Complex optical constants on a subwavelength scale," *Phys. Rev. Lett.* **85**(14), 3029–3032 (2000).
29. M. B. Raschke and C. Lienau, "Apertureless near-field optical microscopy: Tip-sample coupling in elastic light scattering," *Appl. Phys. Lett.* **83**(24), 5089–5091 (2003).
30. M. Esmann, S. F. Becker, B. B. da Cunha, J. H. Brauer, R. Vogelgesang, P. Groß, and C. Lienau, "k-space imaging of the eigenmodes of sharp gold tapers for scanning near-field optical microscopy," *Beilstein J. Nanotechnol.* **4**(1), 603–610 (2013).
31. L. Lepetit, G. Cheriaux, and M. Joffre, "Linear techniques of phase measurement by femtosecond spectral interferometry for applications in spectroscopy," *J. Opt. Soc. Am. B* **12**(12), 2467–2474 (1995).
32. P. Anger, P. Bharadwaj, and L. Novotny, "Enhancement and quenching of single-molecule fluorescence," *Phys. Rev. Lett.* **96**(11), 113002 (2006).

## 1. Introduction

One of the aims of optical near-field spectroscopy is to study the optical properties of nanostructures by resonant light scattering, localized to a nanometric volume far below the diffraction limit [1–4]. Ideally, near-field spectroscopy should enable broadband spectroscopic investigation at the single emitter level and may, in combination with ultrafast pump-probe measurement schemes [5–7], shed light on the dynamics of primary light-induced processes such as light harvesting and photo-catalytic surface reactions.

Such sub-diffraction-limit spectroscopy can be accomplished by focusing light into a diffraction-limited spot on the sample and by scattering light from the near field around a

quantum emitter into the far field, either using an aperture-based probe or an aperture-less, pointed probe [8–10]. While light-guiding probes require a trade-off between throughput and lateral resolution [1,11], a principally smaller resolution is achieved when a solid metal or dielectric probe is brought near the emitter. In this aperture-less or scattering-type SNOM (s-SNOM), light from the near field is scattered into the far field, where it can be collected by a detector. The lateral resolution of tip-enhanced near-field spectroscopy is determined by the size of the probe apex of down to 10 nm [12,13], and can be even smaller, if the processes under observation depend on the field strength in a nonlinear fashion or when light localization by means of gap modes is used [3,14–16].

Typically in s-SNOM, a diffraction-limited laser focus simultaneously illuminates both the sample and the probe, a sharp metal or dielectric tip. Light is scattered from the near field of emitters in the vicinity of the tip, but also directly from the tip shaft as well as the sample. This directly scattered light usually causes a large background signal, obscuring the orders of magnitude smaller near-field signal. In principle, the background signal can be largely avoided by employing adiabatic nanofocusing to SNOM [17,18]. This technique is an active topic of current research and first applications in broadband light scattering and time-resolved spectroscopy are currently pursued in different laboratories [19,20]. Regular s-SNOM is already much better understood. Specifically, some effort has been devoted in the past to distinguishing the near-field signal from the background in s-SNOM [21–26]. In a very common approach, the tip-sample distance is modulated with a frequency typically in the 10-kHz-range [27]. Due to the highly nonlinear dependence of the scattered near-field signal on the tip-sample distance, higher harmonics of the modulation frequency are found in the signal. Demodulating at higher harmonics improves the near-field to background ratio and leads to improved contrast [23].

However, even with demodulation at higher harmonic frequencies, a complete suppression of the unwanted background is challenging. Generally, the light field components that are scattered from the near field, from the diffraction-limited spot on the sample and from the tip shaft interfere and lead to the detection of a mixed intensity signal that cannot be disentangled, because mixing occurs at the electric field level [22,25,28]. In order to enable such discrimination of the different contributions to the signal and to eliminate the background signal, amplification of the near-field signal by mixing of the scattered signal with a well-controlled reference wave was introduced. In principle, the simplest way to achieve such amplification is by homodyne mixing via a Michelson interferometer [23]. This interference, however, requires a highly stable interferometer. In particular at visible wavelengths, active stabilization is generally unavoidable, while in the infrared wavelength region high mechanical stability may be sufficient. A more robust approach is heterodyne mixing with a reference wave that was frequency-shifted with an acousto-optic modulator (AOM) [25,28]. The same principle can be realized without the need for an AOM in a pseudo-heterodyne mixing scheme, where a reference light wave is supplied with a sinusoidal phase modulation via a vibrating mirror in a Michelson interferometer [24].

This poses two considerable experimental challenges to broadband s-SNOM spectroscopy in the visible spectral range. Firstly, the background signal has to be suppressed efficiently and over a broad spectral range by mixing with a broad-bandwidth reference field. Secondly, this reference field is required to remain phase-stable with respect to the optical field scattered from the tip apex over a sufficiently long time to scan a sample.

Here we propose and experimentally demonstrate an efficient and easy-to-implement solution to both challenges. We deposit the sample under investigation on a homogeneous, semitransparent gold layer covered with a thin dielectric sheet. When illuminating the tip-sample region with a broadband light source transmitted through the gold film, this creates an inherently phase-stable in-line interferometer. The reflection from the gold film provides a reference field with an amplitude that largely exceeds that of spurious background fields. Near-field spectra recorded at higher modulation orders of the periodic modulation of the tip-

sample distance thus predominantly probe the spectrum of the local near-field scattered from the tip-sample interaction region. In contrast, spectra recorded at lower modulation orders are governed by background fields scattered from the tip shaft. These spectra reveal a highly complex spectral modulation resulting from multiple-field interferences. Our results open up a new approach towards quantitative, ultrahigh resolution, broadband near-field scattering spectroscopy.

## 2. Experimental setup and measurement principle

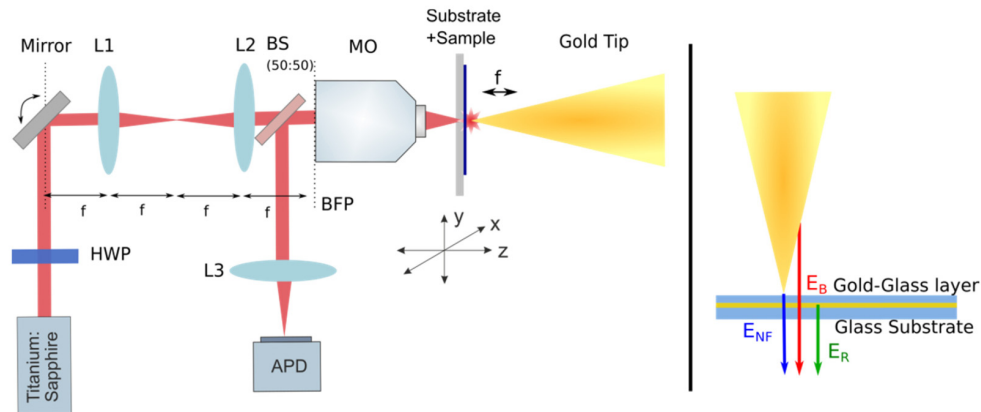


Fig. 1. Experimental setup (left) and the fields that contribute to the measured signal (right). Left: Light from a Titanium:Sapphire laser is focused on a sample. The polarization is controlled by a half-wave plate (HWP), and the position of the focus is corrected by a steering mirror followed by a 4f-system (lenses L1 and L2), which image the beam tilt to the back focal plane (BFP) of the microscope objective (MO). A sharply etched gold tip is brought closely to the sample to scatter light from the near-field region to the far field. The scattered light is split off the incident beam path by a 50:50 beam splitter (BS), collected by a lens (L3) and detected by an avalanche photodiode (APD). Right: The sample is coated onto a thin glass-covered gold layer. The signal detected by the APD comprises contributions of electric fields from the near field ( $\vec{E}_{NF}$ ), of the field scattered from the tip shaft ( $\vec{E}_B$ ), as well as the reference field that is reflected off the semi-transparent gold film ( $\vec{E}_R$ ).

Our experimental setup is in principle a back-scattering type SNOM, depicted schematically in Fig. 1. In order to study the near-field optical properties of our in-line interferometer, we first performed quasi-monochromatic measurements using a narrow-bandwidth laser, and later equipped the setup with a broad-bandwidth laser source and a spectrally resolving detector.

First, for quasi-monochromatic measurements, light from a Titanium:Sapphire laser (Spectra Physics, Tsumani) supplying pulses with a relatively narrow spectral bandwidth of around 20 nm centered at a wavelength of 780 nm is used to illuminate the sample. The light is linearly polarized, and the direction of the electric field vector is controlled by a half-wave plate (HWP) in a motorized rotation holder. To adjust the position of the focus precisely, a steering mirror equipped with two piezo actuators is employed in a 4f imaging system, consisting of two lenses with the same focal length of 50 mm. The tilt of the beam induced by the steering mirror is imaged onto the back focal plane of the microscope objective (MO) with a numerical aperture (NA) of 0.95. This results in a displacement of the beam in the MO focal plane, without distorting the focus. The light passes a 50:50 beam splitter (BS) and is then focused onto the far side of the sample, i.e., through a 150- $\mu\text{m}$  thick quartz microscope slide onto the exit side of the slide. In this study we compare three different samples, for which the far side of the sample is either an uncoated quartz surface, the quartz surface covered with a

semitransparent (~20-nm thick) gold film, or a semitransparent gold film covered with a ~200-nm thick SiO<sub>2</sub> film. Positioning the focus position along the *z*-axis, perpendicular to the sample surface, is achieved by piezo-controlling the MO position.

A sharply etched gold taper is brought in close proximity to the sample surface in order to interact with and scatter light out of the near-field region. The laser focus is adjusted on the taper apex by maximizing the back-scattered light. Note that when scanning or when varying the tip-sample distance, the focus position remains on the apex of the gold nanotaper, while the sample is moved towards or away from the tip. The light that is scattered from the focus region is collected in backwards direction by the same MO, and the part reflected by the BS is collected by a lens (L3) and detected using an avalanche photodiode (APD, Hamamatsu C5331-02).

The single-crystalline gold nanotips are produced from polycrystalline, 99.99%-gold wire with a diameter of 125 μm. The gold wire is annealed and electrochemically etched as described in [20]. The process typically results in tapers with a very smooth surface, with an opening angle of around 30°, and in a sharp apex with a radius of curvature of about 10 nm. Such a sharp gold tip is glued onto a tuning fork, which is driven by an AC voltage at its resonance frequency  $f \approx 26$  kHz. The tuning fork amplitude is set such that the tip moves back and forth along the taper axis over a distance of about 30 nm. The tip is then brought in close proximity to the sample, such that the tip is aligned with its axis perpendicular to the sample surface. The tip-sample distance is controlled by adjusting the sample *z*-position using the tuning fork oscillation amplitude as the feedback signal in a tapping-mode atomic force microscope. The signal detected in back reflection by the APD is processed using a lock-in amplifier (Zurich Instruments HFLI) and using the tip modulation frequency as the reference signal. In this work, typically the signal demodulated at the fundamental tip modulation frequency ( $S_{1f}$ ,  $1f \approx 26$  kHz), as well as the signals demodulated at its second, third, and fourth harmonic ( $S_{2f}$ ,  $S_{3f}$ ,  $S_{4f}$ ) are recorded. To determine the DC field strength, the APD is substituted by a silicon photodiode (SiPD, Thorlabs PDA36A) and its signal is recorded without lock-in detection, which basically yields the unmodulated signal ( $S_{0f}$ ).

Finally, for broad-bandwidth spectroscopic measurements the narrow-bandwidth laser is substituted with a titanium:sapphire laser (Femtolasers Rainbow) with a spectral bandwidth exceeding 100 nm. Instead of measuring with the APD and lock-in detector the light is spectrally dispersed using a monochromator (Princeton Instruments, Acton SP2150i with 300-lines/mm grating) equipped with a fast line camera (e2V Aviiiva EM4 with 512 pixels). This line camera enables acquisition of spectra with a rate of 210 kHz, such that by post-processing the data pixel-wise we can extract complete spectra demodulated up to the fourth harmonic.

In the following sections describing the measurements and the analysis of the signals  $S_{0f}$  to  $S_{4f}$  we assume the detected signal to consist of the following electric field components (see the right-hand side of Fig. 1): First, light is directly reflected off the far side surface of the microscope slide. This direct reflection is rather weak in the case of the uncoated quartz sample and up to ~50% of the incident light in the case that the quartz substrate is coated with a semitransparent gold film, and is used as our reference field  $\vec{E}_R$ . The light that is transmitted through the substrate is partly scattered from the tip shaft, causing a background light contribution  $\vec{E}_B$ . If the tip is in close proximity to the sample surface, it interacts with the sample's near field region, scattering light to the far field. This interaction contributes the near-field component  $\vec{E}_{NF}$  to the detected signal.

### 3. Quasi-monochromatic measurements

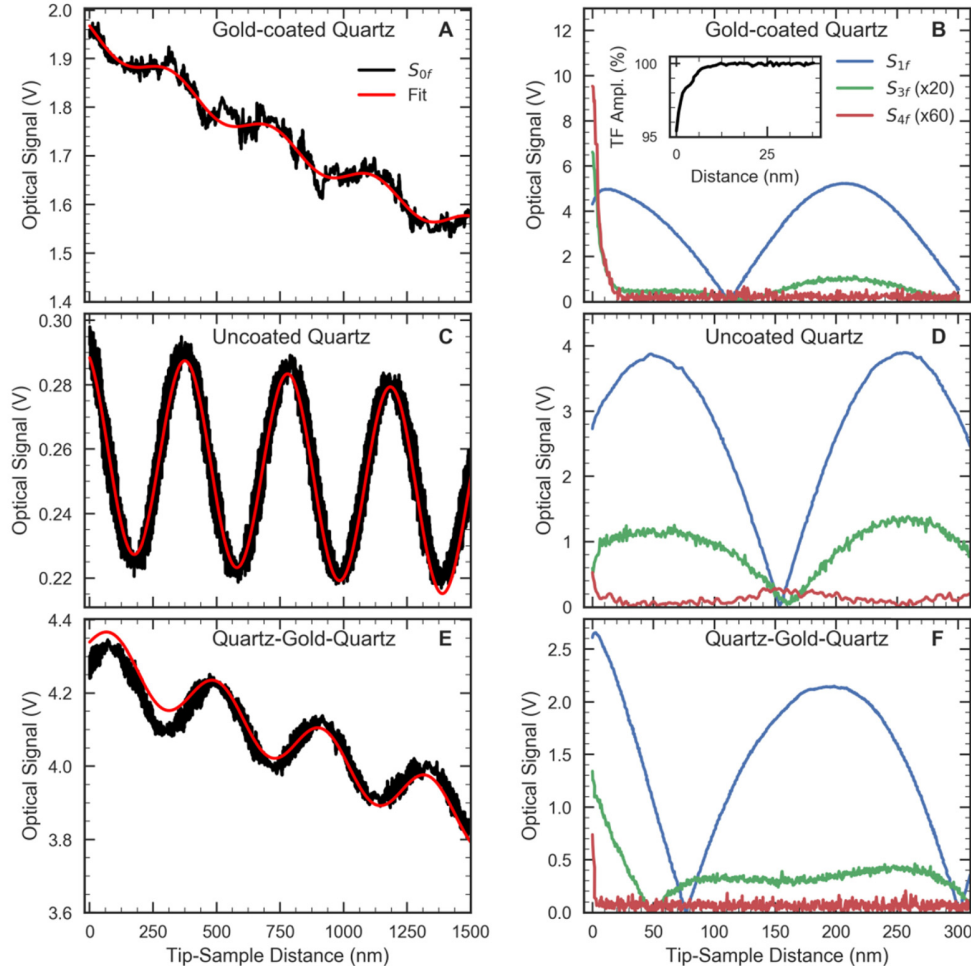


Fig. 2. The measured optical signals  $S_{0f}$  plotted together with a sinusoidal fit (black and red curves in the left hand graphs) and  $S_{1f}$ ,  $S_{3f}$ , and  $S_{4f}$  (blue, green and red curves, respectively, in the right hand graphs) recorded during the approach of the three different substrates towards the gold nanotip. A, B: Approach of a gold-coated quartz microscope slide to the nanotip. A, The DC signal  $S_{0f}$  is weakly modulated and B, there is a strong near-field signal when the gold surface is in close proximity to the tip. The inset shows the tuning fork amplitude; the point of contact is defined as the position when the tuning fork amplitude is decreased by 5%. C, D: Approach of an uncoated quartz substrate to the nanotip. C, The DC signal is strongly modulated, and D, the near-field signal is very weak on the glass surface. E, F: Approach of the in-line interferometer to the gold tip, i. e., a quartz surface covered with a  $\sim 200$ -nm thick  $\text{SiO}_2$  film on top of the  $\sim 20$ -nm thick semitransparent gold film. E, The DC signal is moderately modulated, and F, when bringing the glass surface in close proximity to the tip, a near-field contribution is clearly visible. The in-line interferometer enables homodyne measurement of a weak near-field signal, such as on a glass surface in vicinity to a gold nanotip.

We record the signals  $S_{0f}$  to  $S_{4f}$  with the setup as described above as a function of the distance between tip and sample. The tip-sample distance is controlled by adjusting the sample  $z$ -position. The approach is stopped when the tuning fork oscillation amplitude is

reduced by 5%, which we take as the point of contact or zero distance. We record such approach curves for three different samples, namely for a quartz surface covered with a semitransparent ( $\sim 20$ -nm thick) gold film, for an uncoated quartz surface, and for a quartz surface covered with a  $\sim 200$ -nm thick  $\text{SiO}_2$  film on top of the  $\sim 20$ -nm thick semitransparent gold film.

Figures 2(a) and 2(b) show the optical signals when the sample with the semi-transparent gold film is approached to the tip. The unmodulated signal  $S_{0f}$ , which is measured using the SiPD and without lock-in detection, displays a weak modulation with a period of  $\sim 390$  nm, corresponding to half the wavelength of the excitation laser [see the red fit curve of a sinusoidal function on top of a linear function, plotted together with the experimentally measured black curves in Fig. 2(a)]. This modulation is a result of the interference of the light reflected from the tip shaft,  $\vec{E}_B$ , and from the gold-coated surface of the substrate facing the tip,  $\vec{E}_R$ . This modulation is weak, because the electric field strength of  $\vec{E}_B$  is only a small fraction of that of  $\vec{E}_R$ . Furthermore,  $\vec{E}_R$  decreases steadily as the reflecting gold surface is moved out of the laser focus, causing the constant slope underneath the modulation. As expected, a near-field contribution cannot be discerned in the DC optical signal.

The experiment is repeated with the APD and lock-in detector, and the demodulated signals  $S_{1f}$  to  $S_{4f}$  are recorded as a function of tip-sample distance. Figure 2(b) shows the amplitude of the lock-in-detector signal during the approach at the respective demodulation frequency, for the gold-coated sample. The optical signal demodulated at the fundamental tip modulation frequency,  $S_{1f}$  [blue curve in Fig. 2(b)], still shows a strong modulation for both samples, now at a period of a quarter wavelength due to plotting the amplitude of the lock-in signal. The optical signal demodulated at the second harmonic,  $S_{2f}$  (not shown in Fig. 2 for the sake of clarity), shows a similar behavior and has an amplitude comparable to that of  $S_{1f}$ . When demodulating at the third harmonic, however,  $S_{3f}$  (green curve) still shows some modulation, but the amplitude is reduced by roughly a factor 4. Finally, demodulating at the fourth harmonic (red curve), the amplitude of  $S_{4f}$  is not above noise level.

In close vicinity to the gold surface [compare the steep decrease of the tuning fork amplitude, i. e., the black curve in the inset in Fig. 2(b)], a weak deviation from the sinusoidal curve by less than 15% is discernible on the first-harmonic optical signal  $S_{1f}$ , and there is a clear near-field contribution apparent of both  $S_{3f}$  and  $S_{4f}$ . The near-field signal resembles a strong exponential signal increase with a  $1/e$ -decay length of 8 nm. On the fourth-harmonic optical signal,  $S_{4f}$ , this near-field signal strength is more than 20 times above the noise level. Such a near-field enhancement is similar to what has been observed in earlier work and what is expected from the interaction of a gold tip and a gold surface [23,29].

For comparison, the measurements of the optical signals  $S_{0f}$  and  $S_{1f} - S_{4f}$  are repeated with the uncoated quartz substrate and are shown in Figs. 2(c) and 2(d), respectively. The DC signal  $S_{0f}$  for the uncoated quartz microscope slide is much stronger modulated than in the case of the gold-coated sample [Fig. 2(c)], showing that the interfering fields reflected from the tip shaft and from the quartz surface are well balanced. There is no near-field contribution to  $S_{0f}$  discernible in Fig. 2C. Even when demodulating the photodiode signal, the effect when approaching the uncoated sample to the gold tip is weak:  $S_{1f}$  does not display any deviation from the behavior far from contact [blue curve in Fig. 2(d)]. The signal  $S_{3f}$  shows a small roll-off near contact, of less than one third of its maximum amplitude, and  $S_{4f}$

simultaneously displays an increase of slightly less than its signal amplitude out of contact [green and red curves in Fig. 2(d)]. Thus, there is evidence of a near-field signal when demodulating at the third or fourth harmonic, but it seems still overrun by background signal ( $S_{3f}$ ) or is on the order of the background signal ( $S_{4f}$ ).

Finally, we turn to the optical signals measured when approaching the in-line interferometer, i. e., a quartz substrate coated with a  $\sim 20$ -nm thick gold film and a  $\sim 200$ -nm thick  $\text{SiO}_2$  film on top of the gold film, to the gold nanotip. The modulation depth of the DC signal  $S_{0f}$  is in between that of the gold-coated and the uncoated sample [Fig. 2(e)], indicating a lower reflectivity of the in-line interferometer gold film than that of the gold-coated substrate. However, the modulation is clearly sufficiently strong to facilitate using  $\vec{E}_R$  as a reference field in our in-line interferometer homodyne scheme. This can be seen more clearly in the approach curves shown in Fig. 2(f): There is a near-field contribution discernible in all three signals  $S_{1f}$ ,  $S_{3f}$ , and  $S_{4f}$ . The near-field increase is less pronounced than in the case that the tip is directly in contact with the gold film; the fourth-harmonic signal  $S_{4f}$  shows an increase of 7 times the noise level (compared to 20 times observed for the gold film). Considering that the near field signal that is measured when the gold tip is in contact with a glass surface [Fig. 2(d)] is just on the order of the noise level, we conclude that the enhancement by a factor 7 is due to interference of the near field  $\vec{E}_{NF}$  and the field reflected from the semi-transparent gold film,  $\vec{E}_R$ .

Thus, on the one hand the multi-layer structure of the in-line interferometer indeed seems to enable the measurement of rather small near-field contributions, which can hardly be detected otherwise. On the other hand, the measured signals are a result of mixing on the field level, and knowledge of the electric field strengths of  $\vec{E}_R$  and  $\vec{E}_B$  is required in order to determine the actual near-field strength. In the next section we derive expressions that allow disentangling the contributions of the fields to each of the measured signals  $S_{0f}$  to  $S_{4f}$ .

#### 4. Analysis of the interfering fields

In all cases investigated experimentally in Sec. 3, we consider the measured signal as the result of interference of the three electric fields  $\vec{E}_{NF}$ ,  $\vec{E}_B$ , and  $\vec{E}_R$ , as already briefly mentioned above. This section aims at disentangling the experimentally measured signals in order to discriminate the near field signal from the background contribution. For this, we first derive an analytic expression for the measured signals up to the fourth order of the tip modulation frequency, based on approximating the individual electric field strengths  $\vec{E}_B$  and  $\vec{E}_{NF}$  by Fourier sums.

After the expressions are derived in Sec. 4.1, in the following Sec. 4.2 we compare them to the measured signals. Together, they will allow us to estimate the experimental conditions necessary for an “artefact-free” measurement of the near-field signal, i.e., the optimum sample properties and the demodulation order that enable to obtain a pure near-field signal with negligible influence of the background field.

##### 4.1 Analytical expressions for the measured signals

The signals are measured with integration times much longer than the inverse of the light carrier frequency and even of the pulse repetition frequency; hence we can restrict the following considerations to temporal variations on the order of the tip modulation period. The measurement takes place at the detector, which is placed at a distance of several tens of cm from the light-sample-interaction region. At this position, we can describe the light as plane

waves and neglect any lateral variation of the electric field strength. The considered electric fields are quasi-monochromatic and quasi-static plane waves, the only dependencies considered in this section are the tip-sample distance  $z$ , and the three different samples we investigated. This translates into changes of the field amplitudes or the relative phases of the three interfering fields, which manifest as variations of the measured signal.

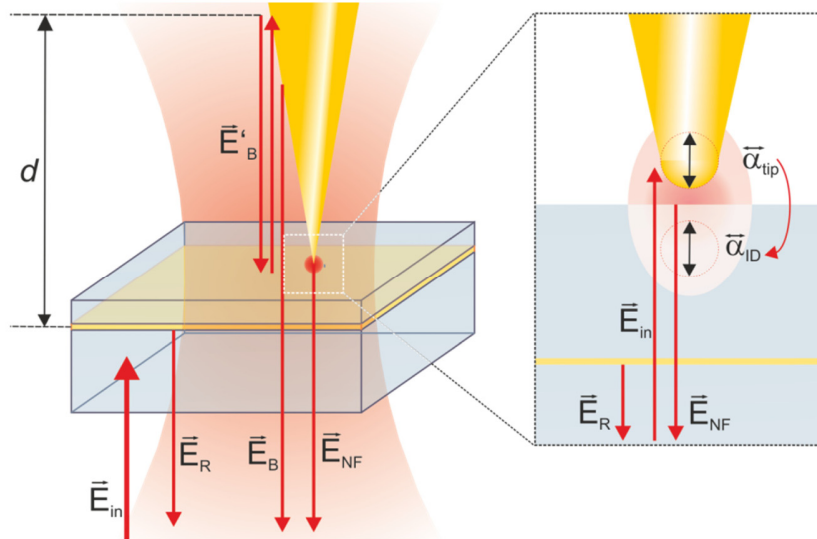


Fig. 3. Graphical depiction of the sample, the origin of the interacting fields, and the tip-sample interaction region. The incident light field  $\vec{E}_{in}$  illuminates sample and tip in a diffraction-limited spot. A part  $\vec{E}_R$  is reflected off the semitransparent gold film, and a part  $\vec{E}_B$  is scattered back from the shaft of the gold tip, possibly after multiple reflections ( $\vec{E}'_B$ ). The inset on the right depicts the enhancement of the tip dipole with polarizability  $\tilde{\alpha}_{tip}$  by its image dipole. The electric field radiated from the tip dipole and propagating back towards the illuminating microscope objective is the origin of the near-field contribution  $\vec{E}_{NF}$ .

The sample and the origin of the interfering fields are depicted in Fig. 3. The reference field  $\vec{E}_R$  is the part of the incident light that is reflected before reaching the nanotip and the tip-sample-interaction region and does not depend on the tip-sample distance. Furthermore, we chose  $\vec{E}_R$  to carry the reference phase,  $\varphi_R = 0$ , such that  $\vec{E}_R$  becomes a constant in our frame of reference:

$$\vec{E}_R(z) = \vec{E}_R = \text{const.} \quad (1)$$

The background signal  $\vec{E}_B$  is scattered back from the gold nanotip. Hence it acquires a phase shift with respect to the reference field, according to the pathway difference of the two. The pathway of  $E_B$  is longer by twice the tip-sample distance  $z$  plus a constant distance  $d$ , which combines the distance from the apex, at which the backscattering from the shaft occurs, and the thickness of the glass layer in the case of the in-line interferometer. The pathway multiplied with the wave vector  $k = 2\pi/\lambda$  determines the phase of  $\vec{E}_B$ , together with a phase shift  $\varphi_B$  that can occur due to the reflection:

$$\vec{E}_B(z) = \vec{E}_{B,0} \cdot e^{2ik(z+d)+i\varphi_B} \quad (2)$$

Depending on the reflectivity of the sample, i. e., of the semitransparent gold layer, multiple reflections between this layer and the tip can alter the distance dependence of the background field. For the samples investigated here, we found that one additional reflection is sufficient to describe the measured curves:

$$\vec{E}'_B(z) = \vec{E}_{B,0} \cdot \left( e^{2ik(z+d)+i\varphi_{B1}} + r \cdot e^{4ik(z+d)+i\varphi_{B2}} \right) \quad (3)$$

Here,  $r$  is the combined reflection coefficient of the tip shaft and gold layer and is typically between 0.1 and 0.4, and the path difference of the back-and-forth reflected light is doubled with respect to the main part of the background light. Equation (3) is used later to disentangle background and near-field contributions to the measured signals. Furthermore, for the monochromatic measurements that are analyzed first, it is sufficient to treat the phase shift due to the fixed distance  $d$  as a constant and to combine it with the phase  $\varphi_B$ . This distance becomes important, however, for the spectral measurements presented in Sec. 5. For broad spectra the wavelength dependence of  $k$  results in a spectral phase and hence the interference of the three fields must show spectral modulation. In the following derivation of an expression for the measured signals, for the sake of simplicity, we use the Eq. (2) to describe the background field and will expand the derived expressions to include an additional reflection later.

Finally, as the near field we denote light that is scattered from the tip-sample-interaction region into the far field, after at least one interaction with the tip dipole and a dipole in the sample (see inset on the right of Fig. 3). The process can be described in the framework of dipole-dipole-coupling between sample and tip as introduced by B. Knoll and F. Keilmann [23] and propagation of the point-dipole-like excitation via the dyadic Green's function [30]. The incident electric field  $\vec{E}_{in}$  excites the z-oriented tip dipole and creates a polarization  $\vec{p}_1 = \vec{\alpha}_{ip} \vec{E}_{in}$  with the tip polarizability tensor  $\vec{\alpha}_{ip}$ . The polarization is the source of a point-dipole-like excitation at the tip position and emits a secondary field, which in turn induces an image dipole in the sample, if the tip-sample-distance is roughly equal to or smaller than the apex radius of curvature. This image dipole, whose dipole moment is determined by the complex dielectric function of the sample material, emits an electric field  $\vec{E}_{ID}$ , which enhances the incident field at the tip position, such that the tip dipole moment becomes:

$$\vec{p}_{ip} = \vec{\alpha}_{ip} (\vec{E}_{in} + \vec{E}_{ID}) \quad (4)$$

The so enhanced tip dipole leads to the radiation of an electric field  $\vec{E}_{out}$ , which is described by the dyadic Green's function  $\vec{G}_{out}$ :

$$\vec{E}_{out}(\vec{r}) = \vec{G}_{out}(\vec{r}, \vec{r}') \vec{p}_{ip} = \vec{G}_{out}(\vec{r}, \vec{r}') \vec{\alpha}_{ip} (\vec{E}_{in} + \vec{E}_{ID}) \quad (5)$$

In the case of strong coupling of the incident field and the excited dipoles, potentially more than two consecutive scattering events have to be considered in a similar fashion as described above. Here, a self-consistent model can be applied to yield an effective polarizability [23]. In our experimental scheme, however, the tip dipole moment is dominant over the image dipole in the sample, and the main contribution to fields radiated out of the tip-sample interaction region stems from the tip dipole enhanced by the image dipole. We treat the conical tip as a small metal sphere with radius  $R$  and with the polarizability  $\alpha_{ip} = 4\pi R^3 (\epsilon_{ip} - 1) (\epsilon_{ip} + 2)^{-1}$ , where  $\epsilon_{ip}$  is the complex dielectric constant of the tip material [23]. In this case, Eq. (5) is sufficient to describe the radiated field. This radiated

field  $\vec{E}_{out}(\vec{r})$  consists of two terms; the first,  $\vec{G}_{out}(\vec{r}, \vec{r}') \vec{\alpha}_{tip} \vec{E}_{in}$  results in a constant field contribution due to the tip dipole alone. As the tip-sample distance is changed, the amplitude of this first term does not change, but the phase changes with respect to the background field in the same fashion as was found before for the background field  $\vec{E}_B(z)$ . Hence this first term can simply be considered a contribution to the background field. The second term  $\vec{G}_{out}(\vec{r}, \vec{r}') \vec{\alpha}_{tip} \vec{E}_{ID}$ , in contrast, depends strongly on the tip-sample distance and approaches zero for large  $z$ . If Eq. (5) was evaluated for the position  $\vec{r}_{Det}$  given by the cross section of beam path and detector plane, and the constant first term was subtracted, the resulting field would yield the near-field contribution to the measured signal, i. e.,

$$\vec{E}_{NF} = \vec{E}_{out}(\vec{r}_{Det}) - \vec{G}_{out}(\vec{r}_{Det}, \vec{r}') \vec{\alpha}_{tip} \vec{E}_{in} \quad (6)$$

Due to the strong distance-dependence of the dipole-dipole coupling, the near field intensity measured in the detector plane decreases exponentially with increasing tip-sample distance, and a phase shift  $\varphi_{NF}$  due to the dipole-dipole coupling is taken into account:

$$\vec{E}_{NF}(z) = \vec{E}_{NF,0} \cdot e^{-z/z_0} \cdot e^{i\varphi_{NF}} \quad (7)$$

Here  $z_0$  is the near-field decay length, which depends on the tip radius of curvature and lies typically in the range of 5 to 10 nm. For the tip used in the experiment described here, Figs. 2(b), 2(d), and 2(f) yield a near-field decay length of 8 nm.

The latter two fields,  $\vec{E}_B$  and  $\vec{E}_{NF}$  are varying as a function of the tip-sample distance  $z$ , which itself is a periodic function with period  $T$ :  $z = z(t) = z(t+T)$ , where  $T = f^{-1} = 2\pi\Omega^{-1}$  is the inverse of the tip modulation frequency. The distance can be written as a sinusoidal function with the modulation amplitude  $M$ , centered at the average tip-sample distance  $\bar{z}$ :

$$z(t) = \bar{z} + M \cdot \cos(\Omega t) \quad (8)$$

Thus also  $\vec{E}_B$  and  $\vec{E}_{NF}$  are temporally periodic functions with the same period  $T$ :

$$\vec{E}_B(z) = \vec{E}_B(\bar{z}, t) = \vec{E}_{B,0} \cdot e^{i2k(\bar{z}+d)+i\varphi_B} \cdot e^{i2kM \cos(\Omega t)} \quad (9)$$

$$\vec{E}_{NF}(z) = \vec{E}_{NF}(\bar{z}, t) = \vec{E}_{NF,0} \cdot e^{i\varphi_{NF}} \cdot e^{-\bar{z}/z_0} \cdot e^{-M/z_0 \cos(\Omega t)} \quad (10)$$

To simplify the comparison with the experimental signals, which are measured at different harmonics of  $f$ , we approximate the explicitly time-dependent factors of these two fields by Fourier sums, following the idea of previous works [23]:

$$\vec{E}_B(\bar{z}, t) \approx \vec{E}_{B,0} \cdot e^{i2k(\bar{z}+d)+i\varphi_B} \cdot \sum_{n=-\infty}^{\infty} b^{(n)} \cdot e^{in\Omega t} \quad (11)$$

$$\vec{E}_{NF}(\bar{z}, t) \approx \vec{E}_{NF,0} \cdot e^{i\varphi_{NF}} \cdot e^{-\bar{z}/z_0} \cdot \sum_{n=-\infty}^{\infty} c^{(n)} \cdot e^{in\Omega t} \quad (12)$$

Here we have introduced the complex Fourier coefficients  $b^{(n)}$  and  $c^{(n)}$  of the background field  $\vec{E}_B$  and the near field  $\vec{E}_{NF}$ , respectively, where  $n$  is the harmonic order of the tip modulation frequency. The Fourier coefficients can be easily calculated:

$$b^{(n)} = \frac{1}{T} \int_0^T e^{i2kM \cos(\Omega t)} \cdot e^{-in\Omega t} dt = (i)^n \cdot J_n(2kM) \quad (13)$$

$$c^{(n)} = \frac{1}{T} \int_0^T e^{-M/z_0 \cos(\Omega t)} \cdot e^{-in\Omega t} dt = (-1)^n \cdot I_n\left(\frac{M}{z_0}\right) \quad (14)$$

The Fourier coefficients for the background field are given by Bessel functions of the first kind and of order  $n$ ,  $J_n$ . The Fourier coefficients of even order are real values, while those of odd orders are imaginary. This means that the phase of the background field shifts with each modulation order, which causes the interference pattern we observed in the approach curves to alternate between cosine ( $S_{0f}, S_{2f}, S_{4f}$ ) and sine ( $S_{1f}, S_{3f}$ ) functions. The Fourier coefficients of the near field are modified Bessel functions of the first kind and of order  $n$ ,  $I_n$ , and are all real.

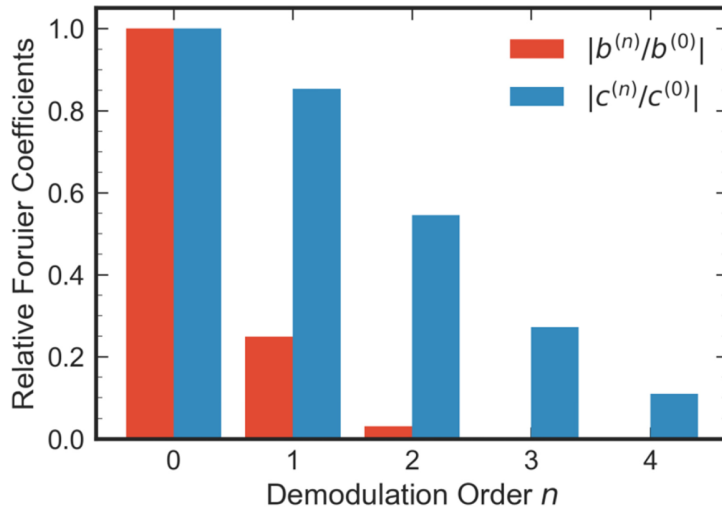


Fig. 4. Relative amplitude of the Fourier coefficients  $b^{(0)}$  to  $b^{(4)}$  (red bars) and  $c^{(0)}$  to  $c^{(4)}$  (blue bars) normalized to  $b^{(0)}$  and  $c^{(0)}$ , respectively, as a function of demodulation order  $n$ . The amplitude of both decreases with demodulation order, but the background-field coefficients  $b^{(n)}$  decreases much more rapidly than the near-field coefficients  $c^{(n)}$ .

Figure 4 shows the absolute of the Fourier coefficients for our experimental parameters, specifically for a wavelength  $\lambda = 780$  nm and the tuning fork modulation amplitude  $M = 30$  nm, as a function of demodulation order  $n$  in a bar diagram. The red bars are the background-field coefficients normalized to the zeroth order coefficient, i. e.,  $|b^{(n)}/b^{(0)}|$ , and the blue bars the according near-field coefficients  $|c^{(n)}/c^{(0)}|$ . It is noteworthy that not only do both coefficients decrease with demodulation order, but that the relative strength of the background decreases much more rapidly than that of the near field. This is in agreement with the measurements presented in Fig. 2, where the near-field contribution becomes more clearly visible as the demodulation order increases, as well as with observations in earlier works. The increase of the near-field-to-background-ratio with demodulation order forms the basis for higher-order demodulation SNOM [23,29].

Any signal that is measured in the detector plane is proportional to the absolute square of the total field  $\vec{E}_{total}(\bar{z}, t) = \vec{E}_R + \vec{E}_B(\bar{z}, t) + \vec{E}_{NF}(\bar{z}, t)$ . Inserting Eqs. (1), (11) and (12) and executing the absolute square gives

$$\left| \vec{E}_{total}(\bar{z}, t) \right|^2 = \left| \vec{E}_R + \vec{E}_{B,0} e^{i2k(\bar{z}+d)+i\varphi_B} \cdot \sum_{n=-\infty}^{\infty} b^{(n)} e^{in\Omega t} + \vec{E}_{NF,0} e^{i\varphi_{NF}} e^{-\bar{z}/z_0} \cdot \sum_{n=-\infty}^{\infty} c^{(n)} e^{in\Omega t} \right|^2 \quad (15)$$

$$\begin{aligned} \left| \vec{E}_{total}(\bar{z}) \right|^2 = & \left| \vec{E}_R \right|^2 + \left( \vec{E}_R^* \vec{E}_{B,0} e^{i2k(\bar{z}+d)+i\varphi_B} \cdot \sum_{n=-\infty}^{\infty} b^{(n)} e^{in\Omega t} + c.c. \right) + \left( \vec{E}_R^* \vec{E}_{NF,0} e^{i\varphi_{NF}} e^{-\bar{z}/z_0} \cdot \sum_{n=-\infty}^{\infty} c^{(n)} e^{in\Omega t} + c.c. \right) \\ & + \left| \vec{E}_{B,0} \right|^2 \sum_{n=-\infty}^{\infty} \sum_{m=-\infty}^{\infty} b^{(n)} b^{(m)*} e^{i(n-m)\Omega t} + \left| \vec{E}_{NF,0} \right|^2 e^{-2\bar{z}/z_0} \sum_{n=-\infty}^{\infty} \sum_{m=-\infty}^{\infty} c^{(n)} c^{(m)*} e^{i(n-m)\Omega t} \\ & + \left( \vec{E}_{B,0} \vec{E}_{NF,0}^* e^{i(2k(\bar{z}+d)+\varphi_B-\varphi_{NF})} e^{-\bar{z}/z_0} \sum_{n=-\infty}^{\infty} \sum_{m=-\infty}^{\infty} b^{(n)} c^{(m)*} e^{i(n-m)\Omega t} + c.c. \right) \end{aligned} \quad (16)$$

where *c.c.* denotes the complex conjugate.

The power impinging on the photodiode is

$$P(z, t) = \frac{1}{2} \varepsilon_0 c A \cdot \left| \vec{E}_{total} \right|^2 \quad (17)$$

where  $\varepsilon_0$  is the electric field constant of the vacuum,  $c$  is the velocity of light, and  $A$  is the area of the detector. Multiplication with the detector efficiency  $\eta$  yields the output voltage  $U(\bar{z}, t) = \eta \cdot P(\bar{z}, t)$ . The unmodulated signal  $S_{0f}$ , which is measured using the SiPD and without lock-in detection, is in fact the lowest order Fourier component of this voltage, which is a function only of the tip-sample distance and not of time:

$$S_{0f}(\bar{z}) = U^{(0)}(\bar{z}) = \eta \cdot P^{(0)}(\bar{z}) \quad (18)$$

For the first and higher-order demodulated signals, the lock-in output signal can be written as:

$$S_{nf}(\bar{z}) = \gamma \frac{1}{T} \int_{t'-T}^{t'} \cos[n\Omega t + \theta] \cdot U(\bar{z}, t) dt, \quad |n| \geq 1\sqrt{b^2 - 4ac} \quad (19)$$

Here, the index *nf* denotes the demodulation frequency,  $\gamma$  is the gain parameter of the lock-in detector, and  $\theta$  is the phase between modulation waveform and detected signal. When measuring  $S_{nf}(\bar{z})$  with the lock-in detector, the influence of this phase is eliminated by actually recording the amplitude, i. e., the geometrical average of  $S_{nf}(\bar{z}, \theta_1)$  measured for one phase setting  $\theta_1$  and  $S_{nf}(\bar{z}, \theta_2)$  measured for a second phase setting  $\theta_2 = \theta_1 + \frac{\pi}{2}$ . In our calculations the same effect is achieved easily by evaluating the integral of Eq. (19) for  $\theta = 0$ . The integral, performed over time intervals  $T \gg 2\pi \Omega^{-1}$ , is zero unless the demodulation frequency matches the angular frequency  $n\Omega$  of the Fourier component under consideration.

The respective combinations of  $\vec{E}_R$ ,  $\vec{E}_{B,0} b^{(n)}$ , and  $\vec{E}_{NF,0} c^{(n)}$  that contribute to the measured signals  $S_{nf}$  can easily be extracted from the expression for  $\left| \vec{E}_{total} \right|^2$  given in Eq. (16). Because the highest order demodulation that can be measured with our 210-kHz line camera is the fourth order, we consider only Fourier coefficients up to this order, i. e., we restrict the sums in Eq. (17) to  $-4 \leq n, m \leq 4$ . The unmodulated signal then becomes:

$$\begin{aligned}
S_{0f}(\bar{z}) \approx & \frac{1}{4} \eta \epsilon_0 c A \cdot \left[ \left| \bar{E}_R \right|^2 + \left| \bar{E}_{B,0} \right|^2 \sum_{n=-4}^4 b^{(n)} b^{(n)*} + \left| \bar{E}_{NF,0} \right|^2 e^{-\bar{z}/z_0} \sum_{n=-4}^4 c^{(n)} c^{(n)*} \right. \\
& + 2 \operatorname{Re} \left\{ \bar{E}_R \bar{E}_{B,0} b^{(0)} \right\} \cos(2k(\bar{z} + d) + \varphi_B) + 2 \operatorname{Re} \left\{ \bar{E}_R \bar{E}_{NF,0} c^{(0)} \right\} e^{-\bar{z}/z_0} \cos(\varphi_{NF}) \quad (20) \\
& \left. + \left( \bar{E}_{B,0} \bar{E}_{NF,0}^* e^{i(2k(\bar{z} + d) + \varphi_B - \varphi_{NF})} e^{-\bar{z}/z_0} \sum_{n=-4}^4 b^{(n)} c^{(n)*} + c.c. \right) \right]
\end{aligned}$$

In the DC signal  $S_{0f}$  the directly reflected fields  $\bar{E}_R$  and  $\bar{E}_B$  have field strengths several orders of magnitude higher than the near field contribution:  $|\bar{E}_{NF,0,j}| \ll |\bar{E}_{R,j}|, |\bar{E}_{B,0,j}|$  for all  $n$ , and for each vector component  $j = x, y, z$  individually. Furthermore, the calculation of the Fourier coefficients showed that the background contribution decreases rapidly with increasing demodulation order, such that  $|\bar{E}_{B,0,j} b^{(n)}| \ll |\bar{E}_{R,j}|, |\bar{E}_{B,0,j} b^{(0)}|$  for  $|n| > 0$ . With these assumptions Eq. (20) can be simplified:

$$S_{0f}(\bar{z}) \approx \frac{1}{4} \eta \epsilon_0 c A \cdot \left[ \left| \bar{E}_R \right|^2 + \left| \bar{E}_{B,0} b^{(0)} \right|^2 + 2 \bar{E}_R \bar{E}_{B,0} b^{(0)} \cos(2k(\bar{z} + d) + \varphi_B) \right] \quad (21)$$

It is easy to see that Eq. (21) replicates the measured curves  $S_{0f}$  in Figs. 2(a), 2(c), and 2(e) quite well: they describe the interference of two fields with a phase varying as the distance between tip and sample increases, and with a contrast given by the respective field strengths of background and reference field.

Similarly, the signals measured at the first and higher harmonic demodulation frequencies,  $S_{1f}$  to  $S_{4f}$ , can be extracted from Eq. (16). After applying the same approximations as enumerated above for the example of  $S_{0f}$ , the less dominant terms are neglected, and we obtain the following four approximated expressions for  $S_{1f}$  to  $S_{4f}$ :

$$\begin{aligned}
S_{1f}(\bar{z}) \approx & \eta \epsilon_0 c A \cdot \left| -\operatorname{Re} \left\{ \bar{E}_R \bar{E}_{B,0} \right\} b^{(1)} \sin(2k(\bar{z} + d) + \varphi_B) - \operatorname{Re} \left\{ \bar{E}_R \bar{E}_{NF,0} \right\} c^{(1)} e^{-\bar{z}/z_0} \cos \varphi_{NF} \right. \\
& \left. - \operatorname{Re} \left\{ \bar{E}_{B,0} \bar{E}_{NF,0} \right\} b^{(0)} c^{(1)} \cdot e^{-\bar{z}/z_0} \cos(2k(\bar{z} + d) + \varphi_B - \varphi_{NF}) \right| \quad (22)
\end{aligned}$$

$$\begin{aligned}
S_{2f}(\bar{z}) \approx & \eta \epsilon_0 c A \cdot \left| -\operatorname{Re} \left\{ \bar{E}_R \bar{E}_{B,0} \right\} b^{(2)} \cos(2k(\bar{z} + d) + \varphi_B) + \operatorname{Re} \left\{ \bar{E}_R \bar{E}_{NF,0} \right\} c^{(2)} e^{-\bar{z}/z_0} \cos \varphi_{NF} \right. \\
& \left. - \left| \bar{E}_{B,0} \right|^2 |b^{(0)}| |b^{(2)}| + \operatorname{Re} \left\{ \bar{E}_{B,0} \bar{E}_{NF,0} \right\} b^{(0)} c^{(2)} \cdot e^{-\bar{z}/z_0} \cos(2k(\bar{z} + d) + \varphi_B - \varphi_{NF}) \right| \quad (23)
\end{aligned}$$

$$\begin{aligned}
S_{3f}(\bar{z}) \approx & \eta \epsilon_0 c A \cdot \left| \operatorname{Re} \left\{ \bar{E}_R \bar{E}_{B,0} \right\} b^{(3)} \sin(2k(\bar{z} + d) + \varphi_B) - \operatorname{Re} \left\{ \bar{E}_R \bar{E}_{NF,0} \right\} c^{(3)} e^{-\bar{z}/z_0} \cos \varphi_{NF} \right. \\
& \left. - \operatorname{Re} \left\{ \bar{E}_{B,0} \bar{E}_{NF,0} \right\} b^{(0)} c^{(3)} \cdot e^{-\bar{z}/z_0} \cos(2k(\bar{z} + d) + \varphi_B - \varphi_{NF}) \right| \quad (24)
\end{aligned}$$

$$\begin{aligned}
S_{4f}(\bar{z}) \approx & \eta \epsilon_0 c A \cdot \left| \operatorname{Re} \left\{ \bar{E}_R \bar{E}_{B,0} \right\} b^{(4)} \cos(2k(\bar{z} + d) + \varphi_B) + \operatorname{Re} \left\{ \bar{E}_R \bar{E}_{NF,0} \right\} c^{(4)} e^{-\bar{z}/z_0} \cos \varphi_{NF} \right. \\
& \left. + \left| \bar{E}_{B,0} \right|^2 |b^{(2)}|^2 + \operatorname{Re} \left\{ \bar{E}_{B,0} \bar{E}_{NF,0} \right\} b^{(0)} c^{(4)} \cdot e^{-\bar{z}/z_0} \cos(2k(\bar{z} + d) + \varphi_B - \varphi_{NF}) \right| \quad (25)
\end{aligned}$$

The relevant Eqs. (21)-(25) describe signal detection after the interference of vectorial fields. They are simplified to terms of products of two fields each, with only the three field amplitudes and phases and the near-field decay length as input parameters. Typically, not all three vector components contribute with comparable strengths, such that a full vectorial treatment is not required. In our experiment, the incident light is linearly polarized in the

plane parallel to the table, corresponding to the  $y$ -direction given in Fig. 1. The reference field  $\vec{E}_R$  consists of light directly reflected from the semi-transparent gold film or from the uncoated surface of the substrate, which in both cases results in a purely  $y$ -polarized reference field. The background field  $\vec{E}_B$ , which is reflected off the cone-shaped surface of the gold tip, is expected to be mainly polarized along the  $y$ -direction, but to carry also a weak  $x$ -component. The near field  $\vec{E}_{NF}$  is constituted of light that is scattered out of the near-field interaction region of sample and tip into the detected far field, as described above [Eqs. (4) and (5)]. The emission pattern of the coupled system of tip dipole and its image dipole in the sample is transformed by the high-NA objective into a radiation pattern that propagates back along the illumination path. Earlier measurements have shown that this light is radially polarized with a high degree of polarization [30]. In the in-line homodyne detection scheme that is employed here, however, the near field contribution is only detected by mixing with the  $y$ -polarized reference field or with the mainly  $y$ -polarized background field. This restricts the near-field detection to approximately half the signal, namely the near field's  $y$ -component. For this reason, a scalar description of the interference is sufficient. This is achieved by substituting  $\vec{E}_R$  with  $E_R = \vec{E}_R \cdot \hat{y}$ ,  $\vec{E}_{B,0}$  with  $E_{B,0} = \vec{E}_{B,0} \cdot \hat{y}$ , and by substituting  $\vec{E}_{NF,0}$  with  $E_{NF,0} = \vec{E}_{NF,0} \cdot \hat{y}$  in Eqs. (21)-(25).

#### 4.2 Near-field contribution in the measurements

The reference field strength  $E_R$  is measured directly as the unmodulated signal  $S_{0f}$  with the tip removed from the setup, setting  $E_{B,0} = 0$  in Eq. (21). For the gold-coated quartz sample, the power measured with the SiPD is  $P = 2,8 \mu\text{W}$ , which, assuming a beam cross section of  $A = 1 \text{ mm}^2$ , corresponds to the reference field strength  $E_R = 46 \text{ Vm}^{-1}$ . The background field strength  $E_{B,0} \cdot |b^{(0)}|$  can be estimated rather precisely from the modulation depth on the signal  $S_{0f}$  in Fig. 2(a), which originates from the cosine-term in Eq. (21), with the result  $E_{B,0} \cdot |b^{(0)}| = 1,1 \text{ Vm}^{-1}$  and the ratio  $E_R : E_{B,0} \cdot |b^{(0)}| = 43:1$ . It should be noted that it is not possible to directly obtain a value for  $E_{NF,0} \cdot |c^{(0)}|$  from the unmodulated signal since it is by far dominated by the background and reference fields. No near-field contribution is discernible in the measurement shown in Fig. 2(a). This is the case for all three substrates.

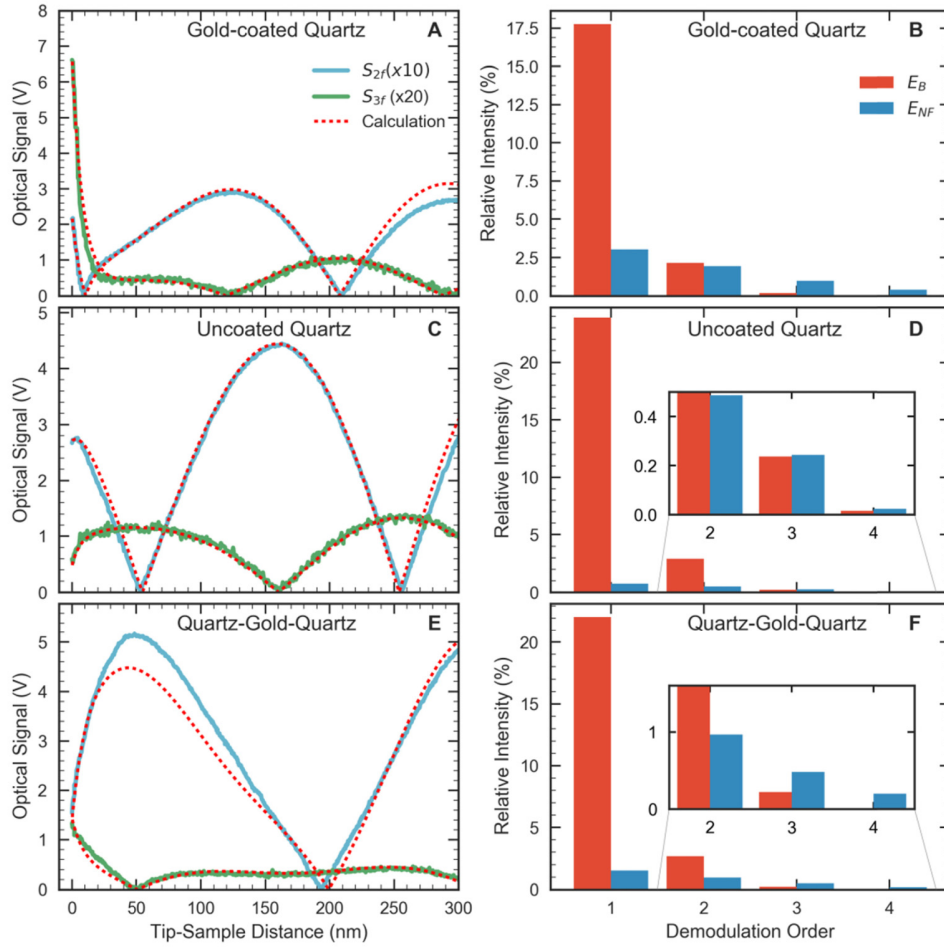


Fig. 5. Disentangled background and near-field signals. The left hand side graphs show the measured optical signals  $S_{2f}$  (blue curves) and  $S_{3f}$  (green curves) as a function of the tip-sample distance together with calculated approach curves (dashed red curves) for A, the gold-coated quartz substrate, C, the uncoated quartz substrate, and E, the quartz substrate coated with a semitransparent gold film and  $\sim 200$  nm quartz on top of the gold film. Adapting the theoretically derived expressions for  $S_{0f}$  to  $S_{4f}$  allows determination of the electric field strengths  $E_R$ ,  $E_{B,0}$ , and  $E_{NF}$ , and, together with the Fourier coefficients  $b^{(n)}$  and  $c^{(n)}$  disentangling background and near-field contributions to the measured signals. The right hand side graphs show the ratio of background and near-field contribution to the measured signals as red and blue bars, respectively, as function of the demodulation order for B, the gold-coated quartz substrate, D, the uncoated quartz substrate, and F, the quartz substrate coated with a semitransparent gold film and  $\sim 200$  nm quartz on top of the gold film. The bars are normalized to  $\text{Re}\{E_R E_{B,0}\} |b^{(0)}| = 100\%$  on the gold-coated quartz substrate. For the substrates with a gold film (B and F), the background signal decays much faster with increasing demodulation frequency than the near-field signal, such that when demodulating at  $f_{\text{demod}} = 4 \cdot f_{\text{mod}}$ , basically only the near-field signal is measured. For the uncoated quartz substrate, even at fourth-order demodulation, the background signal surmounts the near-field signal.

The derived expressions 22-25 for the optical signals  $S_{1f}$  to  $S_{4f}$  are compared to the measured approach curves, using the values  $E_R = 46 \text{ Vm}^{-1}$  and  $E_{B,0} \cdot |b^{(0)}| = 1,1 \text{ Vm}^{-1}$  obtained from the measured signal  $S_{0f}$  in Fig. 2(a), and using the phase for the near field,  $\varphi_{NF}$ , and the phase for the background field,  $\varphi_{B1}$ , to manually adapt the shape of the calculated curves to the measured signal. Furthermore, for the gold-coated quartz substrate the effect of multiple reflections can be seen clearly from the deviation of especially  $S_{1f}$  from a single-sinusoidal behavior [Fig. 2(b)]. This is taken into account by using Eq. (3) to describe the background field, adding the reflection coefficient  $r$  and the second phase  $\varphi_{B2}$  as adaptation parameters. For the gold-coated quartz substrate, the reflection coefficient is between  $r = 0.15$  and  $0.45$ .

As an example, Fig. 5(a) shows the calculated curves  $S_{2f}$  and  $S_{3f}$  (dashed red curves) together with the experimentally measured approach curves ( $S_{2f}$ : blue curve,  $S_{3f}$ : green curve). With the above mentioned adjustable parameters, the derived expressions reproduce the measured curves quite closely. As a result of comparing the measurement to the derived expressions, we obtain on the one hand  $\text{Re}\{E_R E_{NF,0}\} \cdot |c^{(n)}|$  for  $n = 1, 2, 3, 4$ , which represents a direct measure for the near-field contributions to the measured signals, and on the other hand the contributions that arise due to the background light scattered from the tip shaft, i. e.,  $\text{Re}\{E_R E_{B,0}\} \cdot |b^{(n)}|$ ,  $|E_{B,0}|^2 \cdot |b^{(n)}| |b^{(m)}|$ , and  $\text{Re}\{E_{B,0} E_{NF,0}\} \cdot |b^{(n)}| \cdot |c^{(m)}|$ . In Fig. 5(b), these values are plotted as bar diagrams as a function of demodulation order, normalized to  $\text{Re}\{E_R E_{B,0}\} |b^{(0)}| = 100\%$ . Both signal contributions decrease exponentially with increasing demodulation order, and as expected for a gold surface, the background signal decreases much faster than the near-field signal, such that for  $S_{3f}$  the near-field contribution already surmounts the background, and that for  $S_{4f}$  the background contribution amounts to only  $\sim 2.5\%$ .

With a similar measurement of the pure reference power, we find for the uncoated quartz substrate the much smaller reference field strength  $E_R = 12 \text{ Vm}^{-1}$  and the background field strength  $E_{B,0} \cdot |b^{(0)}| = 2,3 \text{ Vm}^{-1}$ , i. e.,  $E_R : E_{B,0} \cdot |b^{(0)}| = 5 : 1$ . The absence of a semitransparent gold film results in more light reaching the tip and hence increased scattering from the tip shaft, while the reference field is created only by a relatively weak reflection from the glass surface. As before, there is no near-field contribution  $E_{NF,0} \cdot |c^{(0)}|$  discernible. Again, the derived expressions Eq. (22)-(25) are adapted to the measurements by manually varying the phases of background and near-field light,  $\varphi_{B1}$ ,  $\varphi_{B2}$ , and  $\varphi_{NF}$ . The reflectivity of the uncoated quartz is reduced to about half that of the gold-coated quartz samples, but due to the high background-to-reference ratio multiple reflections between tip and sample again have a high influence on the over-all signal [Fig. 5(c)]. Compared to the gold-coated quartz substrate, the high background-to-reference ratio of the uncoated quartz substrate results in a much stronger influence of the background-related signal components even at high demodulation orders: up to the fourth order near-field- and background-related signal components are of comparable strength [see Fig. 5(d)]. From this measurement it is clear that the reference signal needs to be increased in order to measure predominantly the near-field signal at demodulation frequencies that are experimentally easily accessible.

As the last substrate, we evaluate the approach curves for the in-line homodyne interferometer, i. e., for the gold- and glass-coated quartz substrate. Here the reference is again increased due to the semitransparent gold film, with  $E_R = 66 \text{ Vm}^{-1}$  and

$E_{B,0} \cdot |b^{(0)}| = 1,9 \text{ Vm}^{-1}$ , i. e.,  $E_R : E_{B,0} \cdot |b^{(0)}| = 36 : 1$ . The derived expressions Eqs. (22)-(25) are adapted to the measurements like described before, and as examples,  $S_{2f}$  and  $S_{3f}$  are plotted in Fig. 5(e). In this case, there is still a small deviation between the measured and the calculated curves for  $S_{2f}$  apparent, and the curvature of  $S_{3f}$  at small tip-sample distances of  $< 50 \text{ nm}$  could also not be entirely reproduced. This observation points towards somewhat more complicated multiple reflections than accounted for by our simple model, e. g., reflections not only between the tip and gold film but also between tip and substrate surface. The near-field and background contributions to the measured optical signals are plotted as a function of the demodulation order in the bar diagram in Fig. 5(f), where one can see that both signal contributions decrease exponentially with increasing demodulation order. Similar to the gold-coated substrate, also for our in-line interferometer, the background signal decreases faster than the near-field signal. For  $S_{3f}$  the near-field contribution surmounts the background, and at  $S_{4f}$  the background contribution amounts to only  $\sim 7\%$ .

In conclusion, for the uncoated quartz substrate the reference and the background field are of comparable strength. Hence, for this case, cross terms not only between any higher order near-field terms and the reference field contribute to the measured signals, but also between higher order near-field terms and the background term  $E_{B,0} \cdot |b^{(0)}|$  have considerable influence. For uncoated glass substrates, a measurement exploiting near-field contrast will be possible only for higher demodulation orders than accessible to us in this work. For both metal-coated quartz substrates, in contrast,  $E_{B,0} \cdot |b^{(0)}| \ll E_R$ , such that the cross terms between higher-order coefficients  $E_{B,0} \cdot |b^{(n)}|$  and  $E_{NF,0} \cdot |c^{(n)}|$ ,  $n \neq 0$  and the reference field dominate. The faster decay of  $E_{B,0} \cdot |b^{(n)}|$  with increasing demodulation order then nearly completely removes the dependence on the unknown background field. The dominance of the near-field signal  $\text{Re}\{E_R E_{NF,0}\} \cdot |c^{(n)}|$  is a result of mixing the near field with a strong reference field, i. e. of the in-line homodyne interferometer formed by the buried gold film.

## 5. Broadband near-field spectroscopy

For broadband near-field spectroscopy we use a titanium:sapphire laser with a spectral bandwidth exceeding  $100 \text{ nm}$  as a broad-bandwidth excitation laser source [see laser input spectrum in Fig. 6(a)]. The APD and lock-in detector are replaced with a monochromator equipped with a fast line camera. Complete spectra are recorded at a rate of  $210 \text{ kHz}$  at fixed tip-sample distances. Figure 6(b) shows the tuning-fork amplitude that is used as the control parameter, as a function of tip-sample distance. Colored circles mark the positions at which spectra are recorded. For a first demonstration of spectrally resolved near-field measurements, we insert our in-line homodyne interferometer as the sample, i. e., a quartz substrate coated with a  $\sim 20\text{-nm}$  thick gold film and a  $\sim 200\text{-nm}$  thick  $\text{SiO}_2$  film on top of the gold film. As we have shown in Sec. 4.2, the reflection off the semitransparent gold film creates a reference field strong enough to amplify the near-field contributions above the background-related signal contributions. The near field, however, is created at the quartz surface, which in itself gives a weaker signal compared to a gold surface and is thus a more realistic test case for near-field spectroscopy of future samples. Furthermore, the spectral response of both a gold film and a quartz substrate is rather flat in the spectral range investigated here. The recorded spectra are post-processed to extract spectra demodulated at the  $n$ -th order of the modulation frequency  $\Omega$ : the signal recorded by each pixel as a function of time is multiplied by a factor  $\cos(n\Omega t)$  and integrated over time [emulating the effect of the lock-in detector, see Eq. (19)].

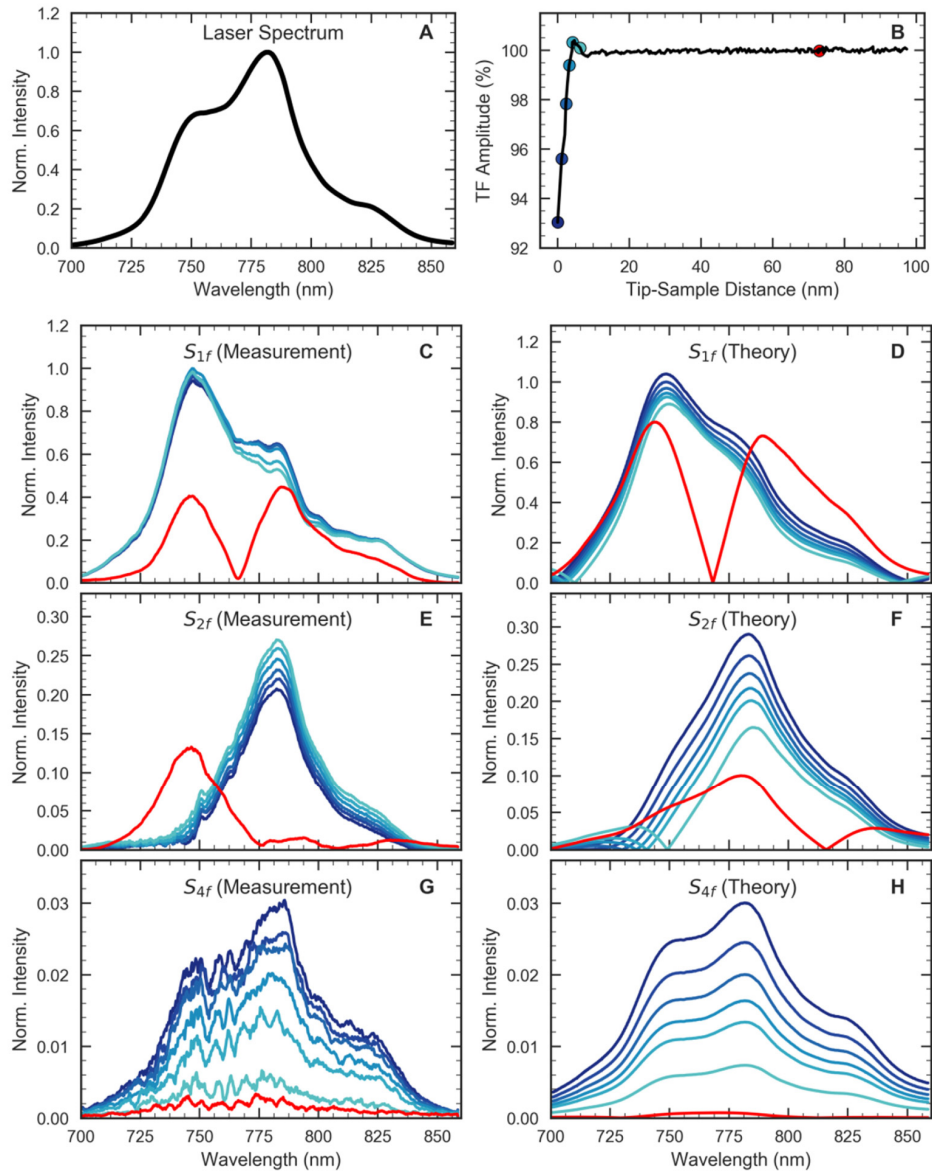


Fig. 6. Broad-bandwidth near-field spectroscopy. A, Input laser spectrum. B, Tuning fork amplitude as a function of tip-sample distance. The positions where spectra are measured are marked by colored circles. C, The measured spectra  $S_{1f}(\lambda)$ , demodulated at the fundamental tip modulation frequency, do not resemble the input spectrum, but are prominently modulated by interference between reference and background fields. D, The calculated spectra  $S_{1f}(\lambda)$  model the main characteristics of the measured spectra very well. E, The measured as well as F, the calculated spectra  $S_{2f}$  also differ from the input laser, and due to different field components interfering they also strongly differ from  $S_{1f}$ . G, In contrast, the measured spectra  $S_{4f}(\lambda)$ , demodulated at the fourth harmonic, mainly resemble the input laser spectrum and strongly decrease with increasing tip-sample distance. H, The calculated spectra  $S_{4f}$  show the same behavior.

This results in demodulated spectra  $S_{nf}(\lambda)$ , which are shown exemplary for the first- and the fourth-order demodulation in Figs. 6(c) and 6(d), respectively. The green-to-blue curves are measured in close proximity to the surface, with the darkest blue being the closest, and the red curve represents a spectrum that is recorded at a larger tip-sample distance, where the near-field contribution is vanishingly small.

The measured first-order demodulated spectra  $S_{1f}(\lambda)$  displayed in Fig. 6(c) have a spectral shape that generally differs from the input laser spectrum. Furthermore, this spectral shape varies with tip-sample distance, which is most apparent in the spectrum recorded at a large distance (red curve), but can also be seen in the other curves, where the tip-sample distance is varied only on a small scale of  $< 20$  nm .

In order to explain the measured spectra we have expanded the theory developed for quasi-monochromatic fields in Sec. 4.1 to include the wavelength dependence of the interfering electric fields. Since the dielectric functions of both gold and quartz are nearly constant in the investigated wavelength region between 700 and 860 nm, we have assumed a flat spectral response of the sample. The tip polarizability of the tip can be estimated assuming a spherical dipole as described above, which results in a non-resonant characteristic of the tip in this spectral region, with changes of  $\sim 6\%$  of the real part and negligible imaginary part of the polarizability. In good approximation,  $E_R(\lambda)$ ,  $E_{B,0}(\lambda)$  and  $E_{NF,0}(\lambda)$  have the spectral shape of the square root of the laser intensity spectrum and a flat spectral phase.

The phase shift between reference and background field,  $2k(\bar{z} + d) + \varphi_{B1} = 4\pi(\bar{z} + d)\lambda^{-1} + \varphi_{B1}$  now depends on the tip-sample distance and on the wavelength, leading to spectral interference in signals with sufficiently strong background contribution. The same is true for the background field that is reflected between the gold film and the tip a second time and carries the phase  $4k(\bar{z} + d) + \varphi_{B2} = 8\pi(\bar{z} + d)\lambda^{-1} + \varphi_{B2}$ . The Fourier coefficients  $b^{(n)}$  of the background field are also a function of the wavelength, but this has a much weaker influence on the observed spectra. With this simple expansion of the theory, the general behavior observed in the measured spectra  $S_{1f}(\lambda)$  is nicely reproduced: the calculated spectra  $S_{1f}(\lambda)$  shown in Fig. 6(d) show strong spectral modulation that varies considerably when the tip-sample distance is changed. We have observed that the shape of the spectra depends sensitively on the phase offset,  $\varphi_{B1}$  and  $\varphi_{B2}$ , such that some spectral components can vanish completely from the calculated spectra by adjusting these phases. Thus, spectral interference is the dominant effect that shapes the spectra. This makes it difficult to extract quantitative information on the sample response when ignoring those interferences.

This observation is emphasized, when comparing the measured and calculated spectra  $S_{2f}(\lambda)$  shown in Figs. 6(e) and 6(f), respectively. The second-order demodulated measured spectra also differ from the laser input spectrum, but they are also markedly different from the spectra  $S_{1f}(\lambda)$  in Figs. 6(c) and 6(d). Also within the spectra  $S_{2f}(\lambda)$ , each individual spectrum differs from those recorded at other tip-sample distance, which is most clearly visible for the spectrum recorded at the largest tip-sample distance (red curve). Knowing that the signal  $S_{2f}$  is composed of different terms of interfering fields than  $S_{1f}$  [compare Eqs. (22) and (23)], it is clear that spectral interference between the fields should lead to quite different measured and calculated spectra. From this, it is clear that such interference can easily obscure true near-field spectral information.

In contrast, the fourth-order demodulated spectra  $S_{4f}(\lambda)$  shown in Fig. 6(g) closely resemble the laser input spectrum, as expected for the sample with a flat spectral response,

and they retain their over-all shape when the tip-sample distance is changed. As observed in the quasi-monochromatic measurements, the background-related signal contribution and hence also spectral interference are mostly suppressed when demodulating at the fourth order. The amplitude of the spectra decreases strongly with increasing tip-sample distance, indicating that these spectra are mainly governed by the near field. This is verified by the calculated spectra shown in Fig. 6(h), which are governed by the cross term of near field and reference field, and which are in very good agreement with the measured spectra.

Note that, in near-field spectroscopy with this in-line homodyne interferometer, the amplitude and phase of the near field are easily obtained: Dividing the envelope of  $S_{4f}(\lambda)$  by the square root of the separately measured reference spectrum would yield the near field amplitude, and the phase difference  $\phi_{NF}$  would show as spectral modulation, as known from spectral interferometry [31]. The amplitude and phase of the near field will be determined by the complex dielectric function of the sample material via the effective polarizability of the probe (see Eqs. (5) and (6), and [23]).

## 6. Summary, discussion and outlook

In this work, we have analyzed the signal in scattering-type scanning near-field optical microscopy on the field level, and we have identified and designed a layered structure that allows disentangling near-field and background-related signal contributions by mixing the near field with a strong reference field. The layered structure was realized by depositing a thin gold film on the sample substrate and covering it with a thin dielectric layer and forms an inherently phase-stable in-line interferometer for. We have shown that this efficiently amplifies the near field and suppresses the background light, such that when demodulating the signal with the third or fourth harmonic of the tip modulation frequency mainly the near field is detected.

Both the interferometer and the gold nanotaper used as a near-field probe support broad-bandwidth spectroscopy over the visible and near-infrared wavelength range. Complete spectra were recorded in tip-modulated s-SNOM using a fast line camera that enables post-measurement extraction of spectra demodulated with up to the fourth-order harmonic frequency. With the developed multi-layer structure and with the fast line camera, we have measured pure near-field spectra over a broad bandwidth in the visible spectral region.

Our measured and calculated optical signals verify and demonstrate the challenging effect of background signals in scattering-type SNOM. Interference between light that is reflected from the sample and light that is scattered from the tip shaft dominates the measured signal, in the case of an uncoated sample even if the signal is demodulated at the fourth harmonic of the tip modulation frequency. For broad-bandwidth spectroscopy, this results in spectral interference that basically determines the shape of the measured spectra. In this work, we have shown that a reference field of sufficient amplitude, namely of roughly 50-fold amplitude of the background field, can achieve efficient background suppression. The reference field then amplifies the near field such that at demodulation at the third or fourth harmonic of the tip modulation frequency results in the very precise detection of the near field. Specifically, we have created the reference field within the substrate of the sample, thereby realizing an inherently stable in-line interferometer.

In this work, a reference field with suitable amplitude is provided by 30-50% reflection of the incident laser field off a ~20-nm thick gold film. This semitransparent gold film transmits sufficient light to create a near field, while at the same time supplying a reference field for amplification of the near field above the background contributions. Note that the optimum reflectivity of the gold layer of a few tens of percent is dictated not by the sample to be investigated but by the amount of background field that needs to be suppressed. A gold-dielectric interface however, supports surface plasmons, which could interact with the tip and with a sample applied to the gold surface. This could affect near-field spectra measured of the

sample. To avoid such disturbance, we have covered the gold film with a quartz layer of a 200-nm thickness. This is longer than the plasmon decay length, but also sufficiently thin to not result in spectral modulation of the measured  $S_{4f}$  spectra. Alternatively, one may use a substrate made of a transparent dielectric material with high refractive index. A somewhat lower reflectivity between 10 and 20% could be realized in a trade-off between ease of substrate production and near-field amplification.

While we have concentrated on overriding the background-related signal contributions with an amplified near-field related signal, it would be even more advantageous to reduce the detrimental effect of the background field. Reduction of light scattered from the tip shaft would greatly improve the potential of s-SNOM. Such a reduction of background light would require changing the dielectric function of the tip material, i. e., making the tip in essence transparent to the incident laser light. Creating a near-field signal, however, requires a strong tip dipole. Both requirements could be combined, for example, by placing a metal sphere on a transparent mount such as a dielectric taper [32]. A metal sphere offers a large dipole moment, but has a narrow resonance. Thus, while such a tip on the one hand could hold great potential to improve the signal-to-background ratio in s-SNOM, it would, on the other hand, considerably reduce the bandwidth for spectroscopy. There is a trade-off between background reduction, tip dipole moment, and spectral bandwidth. In our experience, the gold nanotapers that were used in this work optimize dipole moment and spectral bandwidth, but introduce a relatively large background signal that requires additional measures for background suppression.

In summary, we have made considerable progress towards broadband s-SNOM spectroscopy in the visible spectral range. We have realized an inherently phase-stable in-line interferometer for mixing the near field with a strong reference field by depositing a thin gold film on the sample substrate and covering it with a thin dielectric layer. We have shown that this efficiently amplifies the near field and suppresses the background light. Using a fast line camera we have recorded complete spectra in tip-modulated s-SNOM. By post-measurement extraction of spectra demodulated with the fourth-order harmonic frequency we have acquired pure near-field spectra in over a broad bandwidth of the visible spectral region.

Our results open up a new approach towards quantitative, ultrahigh resolution, broadband near-field scattering spectroscopy. Currently we are applying this new interferometric broadband near-field spectroscopy to observing the coupling in organic-metallic hybrid nanostructures.

## Funding

Deutsche Forschungsgemeinschaft (SPP1391, GRK1885); Niedersächsisches Ministerium für Wissenschaft und Kultur (LGRK “Nano-Energieforschung”); The Korea Foundation for International Cooperation of Science and Technology (K2081500003); The German-Israeli Foundation (1256).



# Bibliography

---

- [1] RICHARD P. FEYNMAN: **There's plenty of room at the bottom (transcript of a talk from 1959)**. In: *Journal of Microelectromechanical Systems*, **1:1** (Mar. 1992), pp. 60–66. DOI: [10.1109/84.128057](https://doi.org/10.1109/84.128057) (see p. 5).
- [2] RICHARD FEYNMAN: **Infinitesimal machinery**. In: *Journal of Microelectromechanical Systems*, **2:1** (Mar. 1993), pp. 4–14. DOI: [10.1109/84.232589](https://doi.org/10.1109/84.232589) (see p. 5).
- [3] TOBIAS A. MATTEI and AZEEM A. REHMAN: **“Extremely minimally invasive”**: recent advances in nanotechnology research and future applications in neurosurgery. In: *Neurosurgical Review*, **38:1** (Jan. 2015), pp. 27–37. DOI: [10.1007/s10143-014-0566-2](https://doi.org/10.1007/s10143-014-0566-2) (see p. 5).
- [4] L. R. HIRSCH, R. J. STAFFORD, J. A. BANKSON, et al.: **Nanoshell-mediated near-infrared thermal therapy of tumors under magnetic resonance guidance**. In: *Proceedings of the National Academy of Sciences*, **100:23** (Nov. 2003), pp. 13549–13554. DOI: [10.1073/pnas.2232479100](https://doi.org/10.1073/pnas.2232479100). arXiv: [0008204](https://arxiv.org/abs/0008204) [cond-mat] (see p. 5).
- [5] ERIC SHINN, ALFRED HÜBLER, DAVE LYON, et al.: **Nuclear energy conversion with stacks of graphene nanocapacitors**. In: *Complexity*, **18:3** (Jan. 2013), pp. 24–27. DOI: [10.1002/cplx.21427](https://doi.org/10.1002/cplx.21427) (see p. 5).
- [6] INTEL: **Intel's 10 nm Technology : Delivering the Highest Logic Transistor Density in the Industry Through the Use of Hyper Scaling**. In: (2017), pp. 8–11. URL: <https://newsroom.intel.com/newsroom/wp-content/uploads/sites/11/2017/09/10-nm-icf-fact-sheet.pdf> (see p. 5).
- [7] A J HUBER, J WITTBORN, and R HILLENBRAND: **Infrared spectroscopic near-field mapping of single nanotransistors**. In: *Nanotechnology*, **21:23** (2010), p. 235702. DOI: [10.1088/0957-4484/21/23/235702](https://doi.org/10.1088/0957-4484/21/23/235702) (see pp. 5, 16).
- [8] HEIKO KOLLMANN, XIANJI PIAO, MARTIN ESMANN, et al.: **Toward plasmonics with nanometer precision: Nonlinear optics of helium-ion milled gold nanoantennas**. In: *Nano Letters*, **14:8** (2014), pp. 4778–4784. DOI: [10.1021/nl5019589](https://doi.org/10.1021/nl5019589) (see pp. 5, 103).

- [9] HE YAN, ZHIHUA CHEN, YAN ZHENG, et al.: **A high-mobility electron-transporting polymer for printed transistors**. In: *Nature*, **457**:7230 (Feb. 2009), pp. 679–686. DOI: [10.1038/nature07727](https://doi.org/10.1038/nature07727) (see p. 5).
- [10] LUKAS NOVOTNY and STEPHAN J. STRANICK: **NEAR-FIELD OPTICAL MICROSCOPY AND SPECTROSCOPY WITH POINTED PROBES**. In: *Annual Review of Physical Chemistry*, **57**:1 (May 2006), pp. 303–331. DOI: [10.1146/annurev.physchem.56.092503.141236](https://doi.org/10.1146/annurev.physchem.56.092503.141236) (see pp. 6, 13–14).
- [11] SARAH MARIA FALKE, CARLO ANDREA ROZZI, DANIELE BRIDA, et al.: **Coherent ultrafast charge transfer in an organic photovoltaic blend**. In: *Science*, **344**: (2014), pp. 1001–1005. DOI: [10.1126/science.1249771](https://doi.org/10.1126/science.1249771) (see pp. 7, 15).
- [12] LE WANG and XIAOJI G. XU: **Scattering-type scanning near-field optical microscopy with reconstruction of vertical interaction**. In: *Nature Communications*, **6**: (2015), p. 8973. DOI: [10.1038/ncomms9973](https://doi.org/10.1038/ncomms9973) (see pp. 7, 16).
- [13] FLORIAN HUTH, ALEXANDER GOVYADINOV, SERGIU AMARIE, et al.: **Nano-FTIR Absorption Spectroscopy of Molecular Fingerprints at 20 nm Spatial Resolution**. In: *Nano Letters*, **12**:8 (Aug. 2012), pp. 3973–3978. DOI: [10.1021/nl301159v](https://doi.org/10.1021/nl301159v) (see pp. 7, 16–17).
- [14] M. BREHM, A. SCHLIESSER, and F. KEILMANN: **Spectroscopic near-field microscopy using frequency combs in the mid-infrared**. In: *Optics Express*, **14**:23 (2006), pp. 11222–11233. DOI: [10.1364/OE.14.011222](https://doi.org/10.1364/OE.14.011222) (see pp. 7, 16–17).
- [15] BERNHARD KNOLL and FRITZ KEILMANN: **Enhanced dielectric contrast in scattering-type scanning near-field optical microscopy**. In: *Optics Communications*, **182**:4 (2000), pp. 321–328. DOI: [10.1016/S0030-4018\(00\)00826-9](https://doi.org/10.1016/S0030-4018(00)00826-9) (see pp. 8, 88–89, 92, 96, 110–111).
- [16] B. KNOLL, F. KEILMANN, A. KRAMER, and R. GUCKENBERGER: **Contrast of microwave near-field microscopy**. In: *Applied Physics Letters*, **70**:20 (May 1997), pp. 2667–2669. DOI: [10.1063/1.119255](https://doi.org/10.1063/1.119255) (see p. 11).
- [17] E. ABBE: **Beiträge zur Theorie des Mikroskops und der mikroskopischen Wahrnehmung**. In: *Archiv für Mikroskopische Anatomie*, **9**:1 (Dec. 1873), pp. 413–418. DOI: [10.1007/BF02956173](https://doi.org/10.1007/BF02956173) (see p. 12).
- [18] M. BORN and EMIL WOLF: **Principles of optics: Electromagnetic Theory of Propagation, Interference and Diffraction of Light**. 1999, pp. 1–952. DOI: [10.1016/S0030-3992\(00\)00061-X](https://doi.org/10.1016/S0030-3992(00)00061-X). arXiv: [arXiv:1011.1669v3](https://arxiv.org/abs/1011.1669v3) (see p. 12).
- [19] EUGENE HECHT: **Optics**. Addison-Wesley, 2000. URL: <https://books.google.de/books/about/Optics.html?id=7aG6QgAACAAJ%7B%5C%7Dpgis=1> (see p. 12).

- [20] RAINER HEINTZMANN and GABRIELLA FICZ: **Breaking the Resolution Limit in Light Microscopy**. In: *Methods in Cell Biology*. Vol. 114. 4. 2013, pp. 525–544. DOI: [10.1016/B978-0-12-407761-4.00022-1](https://doi.org/10.1016/B978-0-12-407761-4.00022-1) (see p. 12).
- [21] L.C.J.M. OOMEN, R. SACHER, H.H.J. BROCKS, et al.: **Immersion oil for high-resolution live-cell imaging at 37°C: optical and physical characteristics**. In: *Journal of Microscopy*, **232**:2 (Oct. 2008), pp. 353–361. DOI: [10.1111/j.1365-2818.2008.02106.x](https://doi.org/10.1111/j.1365-2818.2008.02106.x) (see p. 12).
- [22] STEFAN W HELL: **Toward fluorescence nanoscopy**. In: *Nature Biotechnology*, **21**:11 (Nov. 2003), pp. 1347–1355. DOI: [10.1038/nbt895](https://doi.org/10.1038/nbt895) (see p. 12).
- [23] S. W. HELL: **Far-Field Optical Nanoscopy**. In: *Science*, **316**:5828 (May 2007), pp. 1153–1158. DOI: [10.1126/science.1137395](https://doi.org/10.1126/science.1137395) (see p. 12).
- [24] ULRIKE BÖHM, STEFAN W. HELL, and ROMAN SCHMIDT: **4Pi-RESOLFT nanoscopy**. In: *Nature Communications*, **7**: (Feb. 2016), p. 10504. DOI: [10.1038/ncomms10504](https://doi.org/10.1038/ncomms10504) (see p. 12).
- [25] S.W. HELL, S. LINDEK, C. CREMER, and E.H.K STELZER: **Measurement of the 4Pi confocal point spread function proves 75 nm axial resolution**. In: *Applied Physics Letters*, **64**:11 (Mar. 1994), pp. 1335–1337. DOI: [10.1063/1.111926](https://doi.org/10.1063/1.111926) (see p. 12).
- [26] NOBELPRIZE.ORG: **The Nobel Prize in Chemistry 2014 - Press Release**. URL: [http://www.nobelprize.org/nobel%7B%5C\\_%7Dprizes/chemistry/laureates/2014/press.htm](http://www.nobelprize.org/nobel%7B%5C_%7Dprizes/chemistry/laureates/2014/press.htm) (see p. 12).
- [27] EVA RITTWEGER, KYU YOUNG HAN, SCOTT E. IRVINE, CHRISTIAN EGGELING, and STEFAN W. HELL: **STED microscopy reveals crystal colour centres with nanometric resolution**. In: *Nature Photonics*, **3**:3 (2009), pp. 144–147. DOI: [10.1038/nphoton.2009.2](https://doi.org/10.1038/nphoton.2009.2) (see p. 12).
- [28] CHRISTIAN EGGELING, CHRISTIAN RINGEMANN, REBECCA MEDDA, et al.: **Direct observation of the nanoscale dynamics of membrane lipids in a living cell**. In: *Nature*, **457**:7233 (Feb. 2009), pp. 1159–1162. DOI: [10.1038/nature07596](https://doi.org/10.1038/nature07596) (see p. 12).
- [29] MICHAEL J RUST, MARK BATES, and XIAOWEI ZHUANG: **Sub-diffraction-limit imaging by stochastic optical reconstruction microscopy (STORM)**. In: *Nature Methods*, **3**:10 (Oct. 2006), pp. 793–796. DOI: [10.1038/nmeth929](https://doi.org/10.1038/nmeth929) (see p. 12).
- [30] E. BETZIG, G. H. PATTERSON, R. SOUGRAT, et al.: **Imaging Intracellular Fluorescent Proteins at Nanometer Resolution**. In: *Science*, **313**:5793 (Sept. 2006), pp. 1642–1645. DOI: [10.1126/science.1127344](https://doi.org/10.1126/science.1127344) (see p. 13).
- [31] W. E. MOERNER, TARAS PLAKHOTNIK, THOMAS IRNGARTINGER, et al.: **Near-Field Optical Spectroscopy of Individual Molecules in Solids**. In: *Physical Review Letters*, **73**:20 (Nov. 1994), pp. 2764–2767. DOI: [10.1103/PhysRevLett.73.2764](https://doi.org/10.1103/PhysRevLett.73.2764) (see p. 13).

- [32] E. BETZIG, J. K. TRAUTMAN, T. D. HARRIS, J. S. WEINER, and R. L. KOSTELAK: **Breaking the Diffraction Barrier: Optical Microscopy on a Nanometric Scale.** In: *Science*, **251**:5000 (Mar. 1991), pp. 1468–1470. DOI: [10.1126/science.251.5000.1468](https://doi.org/10.1126/science.251.5000.1468) (see p. 13).
- [33] E.H. SYNGE: **A suggested method for extending microscopic resolution into the ultra-microscopic region.** In: *The London, Edinburgh, and Dublin Philosophical Magazine and Journal of Science*, **6**:35 (Aug. 1928), pp. 356–362. DOI: [10.1080/14786440808564615](https://doi.org/10.1080/14786440808564615) (see p. 13).
- [34] D. W. POHL, W. DENK, and M. LANZ: **Optical stethoscopy: Image recording with resolution  $\lambda/20$ .** In: *Applied Physics Letters*, **44**:7 (Apr. 1984), pp. 651–653. DOI: [10.1063/1.94865](https://doi.org/10.1063/1.94865) (see p. 13).
- [35] A. LEWIS, M. ISAACSON, A. HAROOTUNIAN, and A. MURAY: **Development of a 500 Å spatial resolution light microscope.** In: *Ultramicroscopy*, **13**:3 (Jan. 1984), pp. 227–231. DOI: [10.1016/0304-3991\(84\)90201-8](https://doi.org/10.1016/0304-3991(84)90201-8) (see p. 13).
- [36] W. BAO, M. MELLI, N. CASELLI, et al.: **Mapping Local Charge Recombination Heterogeneity by Multidimensional Nanospectroscopic Imaging.** In: *Science*, **338**:6112 (Dec. 2012), pp. 1317–1321. DOI: [10.1126/science.1227977](https://doi.org/10.1126/science.1227977) (see p. 14).
- [37] WEI BAO, MATTEO STAFFARONI, JEFFREY BOKOR, et al.: **Plasmonic near-field probes: a comparison of the campanile geometry with other sharp tips.** In: *Optics Express*, **21**:7 (Apr. 2013), p. 8166. DOI: [10.1364/OE.21.008166](https://doi.org/10.1364/OE.21.008166) (see p. 14).
- [38] R. MULLER and C. LIENAU: **Three-dimensional analysis of light propagation through uncoated near-field fibre probes.** In: *Journal of Microscopy*, **202**:2 (May 2001), pp. 339–346. DOI: [10.1046/j.1365-2818.2001.00825.x](https://doi.org/10.1046/j.1365-2818.2001.00825.x) (see p. 14).
- [39] FRITZ KEILMANN and RAINER HILLENBRAND: **Near-field Nanoscopy by elastic light scattering from a tip - book chapter.** In: *Philosophical Transactions of the Royal Society A: Mathematical, Physical and Engineering Sciences*. Vol. 362. 1817. Apr. 2004, pp. 787–805. DOI: [10.1098/rsta.2003.1347](https://doi.org/10.1098/rsta.2003.1347) (see p. 14).
- [40] T. TAUBNER, R. HILLENBRAND, and F. KEILMANN: **Performance of visible and mid-infrared scattering-type near-field optical microscopes.** In: *Journal of Microscopy*, **210**:3 (June 2003), pp. 311–314. DOI: [10.1046/j.1365-2818.2003.01164.x](https://doi.org/10.1046/j.1365-2818.2003.01164.x) (see pp. 14, 16, 23–24).
- [41] JORDAN M. GERTON, LAWRENCE A. WADE, GUILLAUME A. LESSARD, Z. MA, and STEPHEN R. QUAKE: **Tip-Enhanced Fluorescence Microscopy at 10 Nanometer Resolution.** In: *Physical Review Letters*, **93**:18 (Oct. 2004), p. 180801. DOI: [10.1103/PhysRevLett.93.180801](https://doi.org/10.1103/PhysRevLett.93.180801) (see p. 14).

- [42] SIMON F. BECKER, MARTIN ESMANN, KYUNG WAN YOO, et al.: **Gap-Plasmon-Enhanced Nanofocusing Near-Field Microscopy**. In: *ACS Photonics*, **3**:2 (2016), pp. 223–232. DOI: [10.1021/acsphotonics.5b00438](https://doi.org/10.1021/acsphotonics.5b00438) (see p. 14).
- [43] ELENA BAILO and VOLKER DECKERT: **Tip-enhanced Raman scattering**. In: *Chemical Society reviews*, **37**: (2008), pp. 921–930. DOI: [10.1039/b705967c](https://doi.org/10.1039/b705967c) (see p. 14).
- [44] R. ZHANG, Y. ZHANG, Z. C. DONG, et al.: **Chemical mapping of a single molecule by plasmon-enhanced Raman scattering**. In: *Nature*, **498**:7452 (June 2013), pp. 82–86. DOI: [10.1038/nature12151](https://doi.org/10.1038/nature12151) (see p. 14).
- [45] ROHIT CHIKKARADDY, BART DE NIJS, FELIX BENZ, et al.: **Single-molecule strong coupling at room temperature in plasmonic nanocavities**. In: *Nature*, **535**:7610 (2016), pp. 127–130. DOI: [10.1038/nature17974](https://doi.org/10.1038/nature17974). arXiv: [NIHMS150003](https://arxiv.org/abs/150003) (see p. 14).
- [46] YASUSHI INOUE and SATOSHI KAWATA: **Near-field scanning optical microscope with a metallic probe tip**. In: *Optics Letters*, **19**:3 (Feb. 1994), p. 159. DOI: [10.1364/OL.19.000159](https://doi.org/10.1364/OL.19.000159) (see p. 14).
- [47] LUKAS NOVOTNY: **Chapter 5 The history of near-field optics**. In: *Progress in Optics*. Vol. 50. 2007, pp. 137–184. DOI: [10.1016/S0079-6638\(07\)50005-3](https://doi.org/10.1016/S0079-6638(07)50005-3) (see p. 14).
- [48] LUKAS NOVOTNY: **From near-field optics to optical antennas**. In: *Physics Today*, **64**:7 (July 2011), pp. 47–52. DOI: [10.1063/PT.3.1167](https://doi.org/10.1063/PT.3.1167) (see p. 14).
- [49] E. A. ASH and G. NICHOLLS: **Super-resolution Aperture Scanning Microscope**. In: *Nature*, **237**:5357 (June 1972), pp. 510–512. DOI: [10.1038/237510a0](https://doi.org/10.1038/237510a0) (see pp. 15, 32).
- [50] BERNHARD KNOLL and FRITZ KEILMANN: **Enhanced dielectric contrast in scattering-type scanning near-field optical microscopy**. In: *Optics Communications*, **182**:4 (Aug. 2000), pp. 321–328. DOI: [10.1016/S0030-4018\(00\)00826-9](https://doi.org/10.1016/S0030-4018(00)00826-9) (see pp. 15, 22, 107, 112).
- [51] R HILLENBRAND, B KNOLL, and F KEILMANN: **Pure optical contrast in scattering-type scanning near-field microscopy**. In: *Journal of microscopy*, **202**:Pt 1 (2001), pp. 77–83. DOI: [10.1046/j.1365-2818.2001.00794.x](https://doi.org/10.1046/j.1365-2818.2001.00794.x) (see p. 15).
- [52] JENS BRAUER, JINXIN ZHAN, ABBAS CHIMEH, et al.: **In-line interferometer for broadband near-field scanning optical spectroscopy**. In: *Optics Express*, **25**:13 (June 2017), p. 15504. DOI: [10.1364/OE.25.015504](https://doi.org/10.1364/OE.25.015504) (see pp. 15, 19, 21).
- [53] YASUO SASAKI and HIROKO SASAKI: **Heterodyne Detection for the Extraction of the Probe-Scattering Signal in Scattering-Type Scanning Near-Field Optical Microscope**. In: *Japanese Journal of Applied Physics*, **39**:Part 2, No. 4A (Apr. 2000), pp. L321–L323. DOI: [10.1143/JJAP.39.L321](https://doi.org/10.1143/JJAP.39.L321) (see p. 15).

- [54] R. HILLENBRAND and F. KEILMANN: **Complex Optical Constants on a Subwavelength Scale**. In: *Physical Review Letters*, **85**:14 (Oct. 2000), pp. 3029–3032. DOI: [10.1103/PhysRevLett.85.3029](https://doi.org/10.1103/PhysRevLett.85.3029) (see pp. 15, 21–22).
- [55] R. HILDNER, D. BRINKS, J. B. NIEDER, R. J. COGDELL, and N. F. VAN HULST: **Quantum Coherent Energy Transfer over Varying Pathways in Single Light-Harvesting Complexes**. In: *Science*, **340**:6139 (June 2013), pp. 1448–1451. DOI: [10.1126/science.1235820](https://doi.org/10.1126/science.1235820). arXiv: [1011.1669](https://arxiv.org/abs/1011.1669) (see p. 15).
- [56] TOBIAS GUENTHER, CHRISTOPH LIENAU, THOMAS ELSAESSER, et al.: **Coherent Non-linear Optical Response of Single Quantum Dots Studied by Ultrafast Near-Field Spectroscopy**. In: *Physical Review Letters*, **89**:5 (July 2002), p. 057401. DOI: [10.1103/PhysRevLett.89.057401](https://doi.org/10.1103/PhysRevLett.89.057401) (see p. 15).
- [57] ALEXANDRIA ANDERSON, KSENIYA S. DERYCKX, XIAOJI G. XU, GÜNTER STEINMEYER, and MARKUS B. RASCHKE: **Few-Femtosecond Plasmon Dephasing of a Single Metallic Nanostructure from Optical Response Function Reconstruction by Interferometric Frequency Resolved Optical Gating**. In: *Nano Letters*, **10**:7 (July 2010), pp. 2519–2524. DOI: [10.1021/nl101090s](https://doi.org/10.1021/nl101090s) (see p. 15).
- [58] ANTONIETTA DE SIO and CHRISTOPH LIENAU: **Vibronic coupling in organic semiconductors for photovoltaics**. In: *Phys. Chem. Chem. Phys.*, **19**:29 (2017), pp. 18813–18830. DOI: [10.1039/C7CP03007J](https://doi.org/10.1039/C7CP03007J) (see p. 15).
- [59] DONATAS ZIGMANTAS, ELIZABETH L. READ, TOMÁŠ MANČAL, et al.: **Two-dimensional electronic spectroscopy of the B800-B820 light-harvesting complex**. In: *Proceedings of the National Academy of Sciences*, **103**:34 (2006), pp. 12672–12677. DOI: [10.1073/pnas.0602961103](https://doi.org/10.1073/pnas.0602961103) (see p. 15).
- [60] DAVID M. JONAS: **Two Dimensional Femtosecond Spectroscopy**. In: *Annual Review of Physical Chemistry*, **54**:1 (Oct. 2003), pp. 425–463. DOI: [10.1146/annurev.physchem.54.011002.103907](https://doi.org/10.1146/annurev.physchem.54.011002.103907) (see p. 15).
- [61] TOBIAS BRIXNER, JENS STENGER, HARSHA M. VASWANI, et al.: **Two-dimensional spectroscopy of electronic couplings in photosynthesis**. In: *Nature*, **434**:7033 (Mar. 2005), pp. 625–628. DOI: [10.1038/nature03429](https://doi.org/10.1038/nature03429). arXiv: [1301.6970](https://arxiv.org/abs/1301.6970) (see p. 15).
- [62] R. POMRAENKE, C. ROPERS, J. RENARD, et al.: **Broadband optical near-field microscope for nanoscale absorption spectroscopy of organic materials**. In: *Journal of Microscopy*, **229**:2 (Feb. 2008), pp. 197–202. DOI: [10.1111/j.1365-2818.2008.01886.x](https://doi.org/10.1111/j.1365-2818.2008.01886.x) (see p. 16).

- [63] SERGEI KUEHN, PATRICK PINGEL, MARKUS BREUSING, et al.: **High-Resolution Near-Field Optical Investigation of Crystalline Domains in Oligomeric PQT-12 Thin Films**. In: *Advanced Functional Materials*, **21**:5 (Mar. 2011), pp. 860–868. DOI: [10.1002/adfm.201001978](https://doi.org/10.1002/adfm.201001978). arXiv: [0706.1062v1](https://arxiv.org/abs/0706.1062v1) (see p. 16).
- [64] D. VOBORNIK, G. MARGARITONDO, J. S. SANGHERA, et al.: **Spectroscopic infrared scanning near-field optical microscopy (IR-SNOM)**. In: *Journal of Alloys and Compounds*, **401**:1-2 (2005), pp. 80–85. DOI: [10.1016/j.jallcom.2005.02.057](https://doi.org/10.1016/j.jallcom.2005.02.057) (see p. 16).
- [65] JASBINDER S. SANGHERA, ISHWAR D. AGGARWAL, ANTONIO CRICENTI, et al.: **Infrared Scanning Near-Field Optical Microscopy Below the Diffraction Limit**. In: *IEEE Journal of Selected Topics in Quantum Electronics*, **14**:5 (2008), pp. 1343–1352. DOI: [10.1109/JSTQE.2008.928166](https://doi.org/10.1109/JSTQE.2008.928166) (see p. 16).
- [66] T. KLAR, M. PERNER, S. GROSSE, et al.: **Surface-Plasmon Resonances in Single Metallic Nanoparticles**. In: *Physical Review Letters*, **80**:19 (May 1998), pp. 4249–4252. DOI: [10.1103/PhysRevLett.80.4249](https://doi.org/10.1103/PhysRevLett.80.4249) (see p. 16).
- [67] MARKUS BREHM, THOMAS TAUBNER, RAINER HILLENBRAND, and FRITZ KEILMANN: **Infrared Spectroscopic Mapping of Single Nanoparticles and Viruses at Nanoscale Resolution**. In: *Nano Letters*, **6**:7 (July 2006), pp. 1307–1310. DOI: [10.1021/nl0610836](https://doi.org/10.1021/nl0610836) (see p. 16).
- [68] NEIL ANDERSON, ALEXANDRE BOUHELIER, and LUKAS NOVOTNY: **Near-field photonics: tip-enhanced microscopy and spectroscopy on the nanoscale**. In: *Journal of Optics A: Pure and Applied Optics*, **8**:4 (Apr. 2006), S227–S233. DOI: [10.1088/1464-4258/8/4/S24](https://doi.org/10.1088/1464-4258/8/4/S24) (see p. 16).
- [69] B KNOLL and F KEILMANN: **Near-field probing of vibrational absorption for chemical microscopy**. In: *Nature*, **399**:May (1999), pp. 7–10. DOI: [10.1038/20154](https://doi.org/10.1038/20154) (see p. 16).
- [70] JAVIER AIZPURUA, THOMAS TAUBNER, F JAVIER GARCÍA DE ABAJO, MARKUS BREHM, and RAINER HILLENBRAND: **Substrate-enhanced infrared near-field spectroscopy**. In: *Optics Express*, **16**:3 (2008), p. 1529. DOI: [10.1364/OE.16.001529](https://doi.org/10.1364/OE.16.001529) (see pp. 16, 121).
- [71] MELISSA PAULITE, ZAHRA FAKHRAAI, ISAAC T S LI, et al.: **Imaging Secondary Structure of Individual Amyloid Fibrils of a  $\beta$  2 -Microglobulin Fragment Using Near-Field Infrared Spectroscopy**. In: *Journal of the American Chemical Society*, **133**:19 (May 2011), pp. 7376–7383. DOI: [10.1021/ja109316p](https://doi.org/10.1021/ja109316p) (see p. 16).
- [72] MARC TOBIAS WENZEL, THOMAS HÄRTLING, PHILLIP OLK, et al.: **Gold nanoparticle tips for optical field confinement in infrared scattering near-field optical microscopy**. In: *Optics Express*, **16**:16 (Aug. 2008), p. 12302. DOI: [10.1364/OE.16.012302](https://doi.org/10.1364/OE.16.012302) (see p. 16).

- [73] J. M. STIEGLER, A. J. HUBER, S. L. DIEDENHOFEN, et al.: **Nanoscale free-carrier profiling of individual semiconductor nanowires by infrared near-field nanoscopy.** In: *Nano Letters*, **10**:4 (2010), pp. 1387–1392. DOI: [10.1021/nl100145d](https://doi.org/10.1021/nl100145d) (see pp. 16, 78).
- [74] JOHANNES M. STIEGLER, YOHANNES ABATE, ANTONIJA CVITKOVIC, et al.: **Nanoscale infrared absorption spectroscopy of individual nanoparticles enabled by scattering-type near-field microscopy.** In: *ACS Nano*, **5**:8 (2011), pp. 6494–6499. DOI: [10.1021/nn2017638](https://doi.org/10.1021/nn2017638) (see p. 16).
- [75] T. TAUBNER, R. HILLENBRAND, and F. KEILMANN: **Nanoscale polymer recognition by spectral signature in scattering infrared near-field microscopy.** In: *Applied Physics Letters*, **85**:21 (2004), pp. 5064–5066. DOI: [10.1063/1.1827334](https://doi.org/10.1063/1.1827334) (see p. 16).
- [76] R. HILLENBRAND, T. TAUBNER, and F. KEILMANN: **Phonon-enhanced light matter interaction at the nanometre scale.** In: *Nature*, **418**:6894 (2002), pp. 159–162. DOI: [10.1038/nature00899](https://doi.org/10.1038/nature00899) (see pp. 16, 80).
- [77] T. TAUBNER, F. KEILMANN, and R. HILLENBRAND: **Nanomechanical resonance tuning and phase effects in optical near-field interaction.** In: *Nano Letters*, **4**:9 (2004), pp. 1669–1672. DOI: [10.1021/nl0491677](https://doi.org/10.1021/nl0491677) (see p. 16).
- [78] H-G VON RIBBECK, M. BREHM, D. W. VAN DER WEIDE, et al.: **Spectroscopic THz near-field microscope.** In: *Optics Express*, **16**:5 (2008), p. 3430. DOI: [10.1364/OE.16.003430](https://doi.org/10.1364/OE.16.003430) (see p. 16).
- [79] SERGIU AMARIE, THOMAS GANZ, and FRITZ KEILMANN: **Mid-infrared near-field spectroscopy.** In: *Optics Express*, **17**:24 (Nov. 2009), p. 21794. DOI: [10.1364/OE.17.021794](https://doi.org/10.1364/OE.17.021794) (see pp. 16–17).
- [80] S. AMARIE and F. KEILMANN: **Broadband-infrared assessment of phonon resonance in scattering-type near-field microscopy.** In: *Physical Review B*, **83**:4 (Jan. 2011), p. 045404. DOI: [10.1103/PhysRevB.83.045404](https://doi.org/10.1103/PhysRevB.83.045404) (see p. 16).
- [81] FLORIAN HUTH, ANDREY CHUVILIN, MARTIN SCHNELL, et al.: **Resonant antenna probes for tip-enhanced infrared near-field microscopy.** In: *Nano Letters*, **13**:3 (2013), pp. 1065–1072. DOI: [10.1021/nl304289g](https://doi.org/10.1021/nl304289g) (see pp. 16–17).
- [82] SERGIU AMARIE, PAUL ZASLANSKY, YUSUKE KAJIHARA, et al.: **Nano-FTIR chemical mapping of minerals in biological materials.** In: *Beilstein Journal of Nanotechnology*, **3**:1 (2012), pp. 312–323. DOI: [10.3762/bjnano.3.35](https://doi.org/10.3762/bjnano.3.35) (see p. 16).
- [83] J.B. BATES: **Fourier transform spectroscopy.** In: *Computers & Mathematics with Applications*, **4**:2 (1978), pp. 73–84. DOI: [10.1016/0898-1221\(78\)90020-2](https://doi.org/10.1016/0898-1221(78)90020-2) (see p. 16).

- [84] ALBERT SCHLIESSER, MARKUS BREHM, FRITZ KEILMANN, and DANIEL W. VAN DER WEIDE: **Frequency-comb infrared spectrometer for rapid, remote chemical sensing**. In: *Optics Express*, **13**:22 (2005), p. 9029. DOI: [10.1364/OPEX.13.009029](https://doi.org/10.1364/OPEX.13.009029) (see p. 17).
- [85] T. GANZ, H.G. VON RIBBECK, M. BREHM, and F. KEILMANN: **Compact frequency-comb Fourier-transform infrared spectrometer**. In: *Optics Communications*, **281**:14 (July 2008), pp. 3827–3830. DOI: [10.1016/j.optcom.2008.03.071](https://doi.org/10.1016/j.optcom.2008.03.071) (see p. 17).
- [86] T. GANZ, M. BREHM, H. G. VON RIBBECK, D. W. VAN DER WEIDE, and F. KEILMANN: **Vector frequency-comb Fourier-transform spectroscopy for characterizing metamaterials**. In: *New Journal of Physics*, **10**: (2008). DOI: [10.1088/1367-2630/10/12/123007](https://doi.org/10.1088/1367-2630/10/12/123007) (see p. 17).
- [87] FRITZ KEILMANN, CHRISTOPH GOHLE, and RONALD HOLZWARTH: **Time-domain mid-infrared frequency-comb spectrometer**. In: *Optics Letters*, **29**:13 (July 2004), p. 1542. DOI: [10.1364/OL.29.001542](https://doi.org/10.1364/OL.29.001542) (see p. 17).
- [88] CRISTIAN MANZONI, DANIELE BRIDA, and GIULIO CERULLO: **Phase-locked pulses for two-dimensional spectroscopy by a birefringent delay line**. In: *2013 Conference on Lasers and Electro-Optics Europe and International Quantum Electronics Conference, CLEO/Europe-IQEC 2013*, **37**:15 (2013), pp. 3027–3029. DOI: [10.1109/CLEOE-IQEC.2013.6801061](https://doi.org/10.1109/CLEOE-IQEC.2013.6801061) (see p. 17).
- [89] JULIEN RÉHAULT, MARGHERITA MAIURI, AURELIO ORIANA, and GIULIO CERULLO: **Two-dimensional electronic spectroscopy with birefringent wedges**. In: *Review of Scientific Instruments*, **85**:12 (Dec. 2014), p. 123107. DOI: [10.1063/1.4902938](https://doi.org/10.1063/1.4902938) (see p. 17).
- [90] J. RÉHAULT, M. MAIURI, D. BRIDA, et al.: **2D IR spectroscopy with phase-locked pulse pairs from a birefringent delay line**. In: *Springer Proceedings in Physics*, **162**:8 (2015), pp. 462–465. DOI: [10.1007/978-3-319-13242-6\\_113](https://doi.org/10.1007/978-3-319-13242-6_113) (see p. 17).
- [91] ANTONIO LLOPIS, LIN JIE, ARUP NEOGI, et al.: **Near-field optical spectroscopy of Ga nanoparticles for plasmonics**. In: *Conference on Quantum Electronics and Laser Science (QELS) - Technical Digest Series*, (2008), pp. 3–4. DOI: [10.1109/QELS.2008.4552514](https://doi.org/10.1109/QELS.2008.4552514) (see p. 17).
- [92] ERIK J. SÁNCHEZ, LUKAS NOVOTNY, and X. SUNNEY XIE: **Near-Field Fluorescence Microscopy Based on Two-Photon Excitation with Metal Tips**. In: *Physical Review Letters*, **82**:20 (May 1999), pp. 4014–4017. DOI: [10.1103/PhysRevLett.82.4014](https://doi.org/10.1103/PhysRevLett.82.4014) (see pp. 17, 19, 147).
- [93] MARTIN ESMANN, SIMON FABIAN BECKER, JULIA WITT, et al.: **Vectorial near-field coupling**. In: *Nature Nanotechnology*, **14**:7 (July 2019), pp. 698–704. DOI: [10.1038/s41565-019-0441-y](https://doi.org/10.1038/s41565-019-0441-y). arXiv: [1801.10426](https://arxiv.org/abs/1801.10426) (see pp. 18, 82–83, 91, 128, 164).

- [94] MARTIN ESMANN, SIMON F BECKER, BERNARD B DA CUNHA, et al.: **k-space imaging of the eigenmodes of sharp gold tapers for scanning near-field optical microscopy**. In: *Beilstein Journal of Nanotechnology*, 4:1 (Oct. 2013), pp. 603–610. DOI: [10.3762/bjnano.4.67](https://doi.org/10.3762/bjnano.4.67) (see pp. 18, 116).
- [95] MARTIN ESMANN: **Probing single metal nanoparticles with a novel adiabatic-nanofocusing scanning near-field optical microscope**. PhD thesis. University Oldenburg, 2016 (see pp. 19, 86, 164).
- [96] DIYAR SADIQ, JAVID SHIRDEL, JAE SUNG LEE, et al.: **Adiabatic Nanofocusing Scattering-Type Optical Nanoscopy of Individual Gold Nanoparticles**. In: *Nano Letters*, 11:4 (Apr. 2011), pp. 1609–1613. DOI: [10.1021/nl1045457](https://doi.org/10.1021/nl1045457) (see pp. 19, 84).
- [97] DIYAR SADIQ: **Scattering-type optical nanoscopy based on ultrafast adiabatic nanofocusing : A novel light source with 10 nm spatial and 10 fs temporal resolution**. PhD thesis. 2012 (see p. 19).
- [98] SLAWA SCHMIDT, BJÖRN PIGLOSIEWICZ, DIYAR SADIQ, et al.: **Adiabatic Nanofocusing on Ultrasooth Single-Crystalline Gold Tapers Creates a 10-nm-Sized Light Source with Few-Cycle Time Resolution**. In: *ACS Nano*, 6:7 (July 2012), pp. 6040–6048. DOI: [10.1021/nn301121h](https://doi.org/10.1021/nn301121h) (see pp. 19, 30, 82).
- [99] LEWIS GOMEZ, RENAUD BACHELOT, ALEXANDRE BOUHELIER, et al.: **Apertureless scanning near-field optical microscopy: a comparison between homodyne and heterodyne approaches**. In: *Journal of the Optical Society of America B*, 23:5 (2006), p. 823. DOI: [10.1364/JOSAB.23.000823](https://doi.org/10.1364/JOSAB.23.000823) (see p. 21).
- [100] NENAD OCELIC, ANDREAS HUBER, and RAINER HILLENBRAND: **Pseudoheterodyne detection for background-free near-field spectroscopy**. In: *Applied Physics Letters*, 89:10 (Sept. 2006), p. 101124. DOI: [10.1063/1.2348781](https://doi.org/10.1063/1.2348781) (see pp. 22–23).
- [101] M. VAEZ-IRAVANI and R. TOLEDO-CROW: **Phase contrast and amplitude pseudoheterodyne interference near field scanning optical microscopy**. In: *Applied Physics Letters*, 62:10 (1993), pp. 1044–1046. DOI: [10.1063/1.108789](https://doi.org/10.1063/1.108789) (see p. 23).
- [102] B DEUTSCH, R HILLENBRAND, and L NOVOTNY: **Near-field amplitude and phase recovery using phase-shifting interferometry**. In: *Optics express*, 16:2 (2008), pp. 494–501. DOI: [10.1364/OE.16.000494](https://doi.org/10.1364/OE.16.000494) (see pp. 23–24).
- [103] BRADLEY M. DEUTSCH: **Phase-shifting interferometry for near-field optical microscopy and nanoparticle detection**. PhD thesis. 2012, p. 173. URL: <http://hdl.handle.net/1802/19262> (see pp. 23, 25).
- [104] HORST SCHREIBER and JOHN H. BRUNING: **Phase Shifting Interferometry**. In: *Optical Shop Testing*. Vol. 36. 1. Hoboken, NJ, USA: John Wiley & Sons, Inc., 1990, pp. 547–666. DOI: [10.1002/9780470135976.ch14](https://doi.org/10.1002/9780470135976.ch14) (see p. 24).

- [105] P. SCOTT CARNEY, BRADLEY DEUTSCH, ALEXANDER A. GOVYADINOV, and RAINER HILLENBRAND: **Phase in nanooptics**. In: *ACS Nano*, **6**:1 (2012), pp. 8–12. DOI: [10.1021/nn205008y](https://doi.org/10.1021/nn205008y) (see p. 25).
- [106] M SCHNELL, P S CARNEY, and R HILLENBRAND: **Synthetic optical holography for rapid nanoimaging**. In: *Nature communications*, **5**: (2014), p. 3499. DOI: [10.1038/ncomms4499](https://doi.org/10.1038/ncomms4499) (see pp. 25–26).
- [107] BRADLEY DEUTSCH, MARTIN SCHNELL, RAINER HILLENBRAND, and P. SCOTT CARNEY: **Synthetic optical holography with nonlinear-phase reference**. In: *Optics Express*, **22**:22 (2014), p. 26621. DOI: [10.1364/OE.22.026621](https://doi.org/10.1364/OE.22.026621) (see pp. 25–26).
- [108] M. SCHNELL, M. J. PEREZ-ROLDAN, P. S. CARNEY, and R. HILLENBRAND: **Quantitative confocal phase imaging by synthetic optical holography**. In: *Optics Express*, **22**:12 (2014), p. 15267. DOI: [10.1364/OE.22.015267](https://doi.org/10.1364/OE.22.015267) (see p. 25).
- [109] JUE-MIN YI, VLADIMIR SMIRNOV, XIANJI PIAO, et al.: **Suppression of Radiative Damping and Enhancement of Second Harmonic Generation in Bull’s Eye Nanoresonators**. In: *ACS Nano*, **10**:1 (Jan. 2016), pp. 475–483. DOI: [10.1021/acsnano.5b05384](https://doi.org/10.1021/acsnano.5b05384) (see p. 33).
- [110] O. MAHBOUB, S. CARRETERO PALACIOS, C. GENET, et al.: **Optimization of bull’s eye structures for transmission enhancement**. In: *Optics Express*, **18**:11 (2010), p. 11292. DOI: [10.1364/oe.18.011292](https://doi.org/10.1364/oe.18.011292) (see p. 33).
- [111] S. CARRETERO-PALACIOS, O. MAHBOUB, F. J. GARCIA-VIDAL, et al.: **Mechanisms for extraordinary optical transmission through bull’s eye structures**. In: *Optics Express*, **19**:11 (2011), p. 10429. DOI: [10.1364/oe.19.010429](https://doi.org/10.1364/oe.19.010429) (see p. 33).
- [112] FABIAN MOOSHAMMER, MARKUS A. HUBER, FABIAN SANDNER, et al.: **Quantifying Nanoscale Electromagnetic Fields in Near-Field Microscopy by Fourier Demodulation Analysis**. In: *ACS Photonics*, (2020). DOI: [10.1021/acsp Photonics.9b01533](https://doi.org/10.1021/acsp Photonics.9b01533) (see p. 34).
- [113] R. CARMINATI, A. CAZÉ, D. CAO, et al.: **Electromagnetic density of states in complex plasmonic systems**. In: *Surface Science Reports*, **70**:1 (2015), pp. 1–41. DOI: [10.1016/j.surfrep.2014.11.001](https://doi.org/10.1016/j.surfrep.2014.11.001) (see p. 34).
- [114] KOHEI IMURA, TETSUHIKO NAGAHARA, and HIROMI OKAMOTO: **Imaging of surface plasmon and ultrafast dynamics in gold nanorods by near-field microscopy**. In: *Journal of Physical Chemistry B*, **108**:42 (2004), pp. 16344–16347. DOI: [10.1021/jp047950h](https://doi.org/10.1021/jp047950h) (see p. 34).
- [115] FERNANDO PUENTE LEÓN, UWE KIENCKE, and HOLGER JÄKEL: **Signale und Systeme**. 5. überarb. Oldenbourg, München, 2011 (see p. 37).

- [116] MARTIN ESMANN, ABBAS CHIMEH, ANKE KORTE, et al.: **Plasmonic nanofocusing spectral interferometry**. In: *Nanophotonics*, (2020). DOI: [10.1515/nanoph-2019-0397](https://doi.org/10.1515/nanoph-2019-0397) (see pp. 39, 44).
- [117] JINXIN ZHAN, WEI WANG, JENS BRAUER, et al.: **Spatial and spectral mode mapping of a dielectric nanodot by broadband interferometric homodyne scanning near-field spectroscopy**. In: *Advanced Photonics*, (submitted: (2020) (see pp. 44, 142).
- [118] STEFAN W KOCH HARTMUT HAUG: **Atoms in a Classical Light Field**. In: *Quantum Theory of the Optical and Electronic Properties of Semiconductors*. WORLD SCIENTIFIC, Jan. 2009, pp. 17–28. DOI: [10.1142/9789812838858\\_0002](https://doi.org/10.1142/9789812838858_0002) (see p. 51).
- [119] ROBERT W. BOYD: **Quantum-Mechanical Theory of the Nonlinear Optical Susceptibility**. In: *Nonlinear Optics*, (2008), pp. 135–206. DOI: [10.1016/B978-0-12-369470-6.00003-4](https://doi.org/10.1016/B978-0-12-369470-6.00003-4) (see p. 52).
- [120] JAN KRIEGER: **Theoretische Quantenmechanik und Anwendungen**. In: *Arbeit*, November (2007). URL: <http://www.jkrieger.de/download/quantenmechanik.pdf> (see p. 54).
- [121] MATHIJS DE JONG, LUIS SEIJO, ANDRIES MEIJERINK, and FREDDY T. RABOUW: **Resolving the ambiguity in the relation between Stokes shift and Huang–Rhys parameter**. In: *Physical Chemistry Chemical Physics*, 17:26 (2015), pp. 16959–16969. DOI: [10.1039/C5CP02093J](https://doi.org/10.1039/C5CP02093J) (see pp. 55–58).
- [122] ANDREI TOKMAKOFF: **5.74 Introductory Quantum Mechanics II**. In: *MIT Opencourseware*, (2009) (see pp. 56–58).
- [123] HEINZ MUSTROPH: **Potential-Energy Surfaces, the Born-Oppenheimer Approximations, and the Franck-Condon Principle: Back to the Roots**. In: *ChemPhysChem*, 17:17 (Sept. 2016), pp. 2616–2629. DOI: [10.1002/cphc.201600243](https://doi.org/10.1002/cphc.201600243) (see p. 56).
- [124] PETRA IMHOF: **Franck-Condon-Analyse der vibronischen Spektren einfacher Aromaten zur Untersuchung der Geometrieänderung nach elektronischer Anregung**. PhD thesis. University Düsseldorf, 2001 (see p. 56).
- [125] VOLKHARD MAY and OLIVER KÜHN: **Electronic and Vibrational Molecular States**. In: *Charge and Energy Transfer Dynamics in Molecular Systems*. Weinheim, Germany: Wiley-VCH Verlag GmbH & Co. KGaA, Feb. 2011. Chap. 2, pp. 9–66. DOI: [10.1002/9783527633791.ch2](https://doi.org/10.1002/9783527633791.ch2) (see p. 57).
- [126] WOLFGANG DEMTROEDER: **Experimentalphysik 2**. Springer-Lehrbuch. Berlin, Heidelberg: Springer Berlin Heidelberg, 2013. DOI: [10.1007/978-3-642-29944-5](https://doi.org/10.1007/978-3-642-29944-5) (see p. 58).
- [127] M.V. KLEIN and T.E. FURTAK: **Optics**. Wiley seri. Wiley, 1986 (see pp. 59–62, 66).

- [128] STEVEN J. BYRNES: **Multilayer optical calculations**. In: *arXiv:1603.02720*, (Mar. 2016), p. 21. arXiv: [1603.02720](https://arxiv.org/abs/1603.02720). URL: <http://arxiv.org/abs/1603.02720> (see p. 62).
- [129] ROBERT L. OLMON, BRIAN SLOVICK, TIMOTHY W. JOHNSON, et al.: **Optical dielectric function of gold**. In: *Physical Review B*, **86**:23 (Dec. 2012), p. 235147. DOI: [10.1103/PhysRevB.86.235147](https://doi.org/10.1103/PhysRevB.86.235147). arXiv: [0801.4433](https://arxiv.org/abs/0801.4433) (see pp. 62, 129).
- [130] CHARALAMBOS C. KATSIDIS and DIMITRIOS I. SIAPKAS: **General transfer-matrix method for optical multilayer systems with coherent, partially coherent, and incoherent interference**. In: *Applied Optics*, **41**:19 (July 2002), p. 3978. DOI: [10.1364/AO.41.003978](https://doi.org/10.1364/AO.41.003978) (see pp. 63–64).
- [131] BAHAA E A SALEH and MALVIN CARL TEICH: **Polarization and Crystal Optics**. In: *Fundamentals of Photonics*. Vol. 5. New York, USA: John Wiley & Sons, Inc., 1991, pp. 193–237. DOI: [10.1002/0471213748.ch6](https://doi.org/10.1002/0471213748.ch6) (see p. 65).
- [132] J. A. FLECK, JR. and M. D. FEIT: **Beam propagation in uniaxial anisotropic media**. In: *Journal of the Optical Society of America*, **73**:7 (1983), p. 920. DOI: [10.1364/JOSA.73.000920](https://doi.org/10.1364/JOSA.73.000920) (see p. 65).
- [133] POCHI YEH: **Optics of anisotropic layered media: A new  $4 \times 4$  matrix algebra**. In: *Surface Science*, **96**:1-3 (1980), pp. 41–53. DOI: [10.1016/0039-6028\(80\)90293-9](https://doi.org/10.1016/0039-6028(80)90293-9) (see p. 69).
- [134] POCHI YEH: **Electromagnetic propagation in birefringent layered media**. In: *Journal of the Optical Society of America*, **69**:5 (May 1979), p. 742. DOI: [10.1364/JOSA.69.000742](https://doi.org/10.1364/JOSA.69.000742) (see p. 69).
- [135] DWIGHT W BERREMAN: **Optics in Stratified and Anisotropic Media:  $4 \times 4$ -Matrix Formulation**. In: *Journal of the Optical Society of America*, **62**:4 (Apr. 1972), p. 502. DOI: [10.1364/JOSA.62.000502](https://doi.org/10.1364/JOSA.62.000502) (see p. 69).
- [136] I. ABDULHALIM: **Analytic propagation matrix method for linear optics of arbitrary biaxial layered media**. In: *Journal of Optics A: Pure and Applied Optics*, **1**:5 (1999), pp. 646–653. DOI: [10.1088/1464-4258/1/5/311](https://doi.org/10.1088/1464-4258/1/5/311) (see p. 69).
- [137] NIKOLAI CHRISTIAN PASSLER and ALEXANDER PAARMANN: **Generalized  $4 \times 4$  matrix formalism for light propagation in anisotropic stratified media: study of surface phonon polaritons in polar dielectric heterostructures**. In: *Journal of the Optical Society of America B*, **34**:10 (2017), p. 2128. DOI: [10.1364/JOSAB.34.002128](https://doi.org/10.1364/JOSAB.34.002128). arXiv: [1707.00462](https://arxiv.org/abs/1707.00462) (see p. 69).
- [138] BERNARD HOSTEN and MICHEL CASTAINGS: **Transfer matrix of multilayered absorbing and anisotropic media. Measurements and simulations of ultrasonic wave propagation through composite materials**. In: *The Journal of the Acoustical Society of America*, **94**:3 (1993), p. 1488. DOI: [10.1121/1.408152](https://doi.org/10.1121/1.408152) (see p. 69).

- [139] D. DEN ENGELSEN: **Ellipsometry of Anisotropic Films**. In: *Journal of the Optical Society of America*, **61**:11 (Nov. 1971), p. 1460. DOI: [10.1364/JOSA.61.001460](https://doi.org/10.1364/JOSA.61.001460) (see p. 70).
- [140] B. NOVOTNY, L. AND HECHT: **Principles of Nano-Optics**. 2006 (see pp. 70–71, 73, 76, 83, 93–94).
- [141] JIN SUN, P. SCOTT CARNEY, and JOHN C. SCHOTLAND: **Strong tip effects in near-field scanning optical tomography**. In: *Journal of Applied Physics*, **102**:10 (Nov. 2007), p. 103103. DOI: [10.1063/1.2812545](https://doi.org/10.1063/1.2812545) (see pp. 77–78).
- [142] BRADLEY DEUTSCH, RAINER HILLENBRAND, and LUKAS NOVOTNY: **Visualizing the optical interaction tensor of a gold nanoparticle pair**. In: *Nano Letters*, **10**:2 (2010), pp. 652–656. DOI: [10.1021/nl9037505](https://doi.org/10.1021/nl9037505) (see pp. 77–78).
- [143] AITZOL GARCÍA-ETXARRI, ISABEL ROMERO, F. JAVIER GARCÍA DE ABAJO, RAINER HILLENBRAND, and JAVIER AIZPURUA: **Influence of the tip in near-field imaging of nanoparticle plasmonic modes: Weak and strong coupling regimes**. In: *Physical Review B - Condensed Matter and Materials Physics*, **79**: (2009), pp. 1–5. DOI: [10.1103/PhysRevB.79.125439](https://doi.org/10.1103/PhysRevB.79.125439) (see pp. 78, 121).
- [144] M. SCHNELL, A. GARCIA-ETXARRI, J. ALKORTA, J. AIZPURUA, and R. HILLENBRAND: **Phase-Resolved Mapping of the Near-Field Vector and Polarization State in Nanoscale Antenna Gaps**. In: *Nano Letters*, **10**:9 (Sept. 2010), pp. 3524–3528. DOI: [10.1021/nl101693a](https://doi.org/10.1021/nl101693a) (see p. 78).
- [145] V. AMENDOLA, R. PILOT, M. FRASCONI, O.M. MARAGÒ, and M.A. IATÌ: **Surface plasmon resonance in gold nanoparticles: A review**. In: *Journal of Physics Condensed Matter*, **29**:20 (2017). DOI: [10.1088/1361-648X/aa60f3](https://doi.org/10.1088/1361-648X/aa60f3) (see p. 80).
- [146] MATTHEW PELTON, JAVIER AIZPURUA, and GARNETT BRYANT: **Metal-nanoparticle plasmonics**. In: *Laser and Photonics Reviews*, **2**:3 (2008), pp. 136–159. DOI: [10.1002/lpor.200810003](https://doi.org/10.1002/lpor.200810003) (see p. 80).
- [147] STEFAN A. MAIER: **Plasmonics: Fundamentals and Applications**. Vol. 677. 1. New York, NY: Springer US, Sept. 2007, pp. 3–18. DOI: [10.1007/0-387-37825-1](https://doi.org/10.1007/0-387-37825-1). arXiv: [0405528](https://arxiv.org/abs/0405528) [cond-mat] (see p. 80).
- [148] J. D. JACKSON: **Classical Electrodynamics**. 1999. DOI: [10.1119/1.19136](https://doi.org/10.1119/1.19136) (see p. 80).
- [149] RICARDO DÍEZ MUIÑO, EUGENE E KRASOVSKII, WOLFGANG SCHATTKÉ, CHRISTOPH LIENAU, and HRVOJE PETEK: **Electromagnetic Interactions with Solids**. In: *Dynamics at Solid State Surfaces and Interfaces*. Vol. 2. Weinheim, Germany: Wiley-VCH Verlag GmbH & Co. KGaA, Apr. 2012, pp. 181–237. DOI: [10.1002/9783527646463.ch5](https://doi.org/10.1002/9783527646463.ch5) (see p. 80).

- [150] ROBERT L. OLMON, BRIAN SLOVICK, TIMOTHY W. JOHNSON, et al.: **Optical dielectric function of gold (SUPPORTING MATERIAL)**. In: *Physical Review B*, **86**:23 (Dec. 2012), p. 235147. DOI: [10.1103/PhysRevB.86.235147](https://doi.org/10.1103/PhysRevB.86.235147) (see pp. [81](#), [131](#)).
- [151] MARKUS B. RASCHKE and CHRISTOPH LIENAU: **Apertureless near-field optical microscopy: Tip-sample coupling in elastic light scattering**. In: *Applied Physics Letters*, **83**:24 (Dec. 2003), pp. 5089–5091. DOI: [10.1063/1.1632023](https://doi.org/10.1063/1.1632023) (see pp. [80](#), [92](#), [107](#), [112](#)).
- [152] JAN RENGER, STEFAN GRAFSTRÖM, LUKAS M. ENG, and RAINER HILLENBRAND: **Resonant light scattering by near-field-induced phonon polaritons**. In: *Physical Review B - Condensed Matter and Materials Physics*, **71**:7 (2005), pp. 1–7. DOI: [10.1103/PhysRevB.71.075410](https://doi.org/10.1103/PhysRevB.71.075410) (see p. [80](#)).
- [153] WEIZHE CHEN, ALEXEY KIMEL, ANDREI KIRILYUK, and THEO RASING: **Apertureless SNOM study on gold nanoparticles: Experiments and simulations**. In: *Physica Status Solidi (B) Basic Research*, **247**:8 (2010), pp. 2047–2050. DOI: [10.1002/pssb.200983940](https://doi.org/10.1002/pssb.200983940) (see p. [80](#)).
- [154] SIMON F. BECKER, MARTIN ESMANN, KYUNGWAN YOO, et al.: **Gap-Plasmon-Enhanced Nanofocusing Near-Field Microscopy**. In: *ACS Photonics*, **3**:2 (Feb. 2016), pp. 223–232. DOI: [10.1021/acsp Photonics.5b00438](https://doi.org/10.1021/acsp Photonics.5b00438) (see pp. [80](#), [84](#), [139](#)).
- [155] VIKTOR MYROSHNYCHENKO, JESSICA RODRÍGUEZ-FERNÁNDEZ, ISABEL PASTORIZA-SANTOS, et al.: **Modelling the optical response of gold nanoparticles**. In: *Chemical Society Reviews*, **37**:9 (2008), p. 1792. DOI: [10.1039/b711486a](https://doi.org/10.1039/b711486a) (see p. [81](#)).
- [156] O. SQALLI, I. UTKE, P. HOFFMANN, and F. MARQUIS-WEIBLE: **Gold elliptical nanoantennas as probes for near field optical microscopy**. In: *Journal of Applied Physics*, **92**:2 (2002), pp. 1078–1083. DOI: [10.1063/1.1487918](https://doi.org/10.1063/1.1487918) (see p. [81](#)).
- [157] A HAIDARY, Y MIYAHARA, and P GRÜTTER: **Antenna and Plasmonic Properties of Scanning Probe Tips at Optical and Terahertz Regimes**. In: *Proceedings of the 2014 COMSOL Conference in Boston*, (2014), pp. 1–6 (see pp. [81](#), [92](#)).
- [158] C. SÖNNICHSEN, T. FRANZL, T. WILK, et al.: **Drastic reduction of plasmon damping in gold nanorods**. In: *Physical Review Letters*, **88**:7 (2002), pp. 774021–774024. DOI: [10.1103/PhysRevLett.88.077402](https://doi.org/10.1103/PhysRevLett.88.077402) (see p. [81](#)).
- [159] A CVITKOVIC, N OCELIC, and R HILLENBRAND: **Analytical model for quantitative prediction of material contrasts in scattering-type near-field optical microscopy**. In: *Optics express*, **15**:14 (2007), pp. 8550–65. DOI: [10.1364/OE.15.008550](https://doi.org/10.1364/OE.15.008550) (see p. [81](#)).
- [160] PETRA GROSS, MARTIN ESMANN, SIMON F. BECKER, et al.: **Plasmonic nanofocusing – grey holes for light**. In: *Advances in Physics: X*, **6149**:May (2016), pp. 1–34. DOI: [10.1080/23746149.2016.1177469](https://doi.org/10.1080/23746149.2016.1177469) (see p. [82](#)).

- [161] SAMUEL BERWEGER, JOANNA M. ATKIN, XIAOJI G. XU, ROBERT L. OLMON, and MARKUS B. RASCHKE: **Femtosecond Nanofocusing with Full Optical Waveform Control**. In: *Nano Letters*, **11**:10 (Oct. 2011), pp. 4309–4313. DOI: [10.1021/nl2023299](https://doi.org/10.1021/nl2023299). arXiv: [1106.1690](https://arxiv.org/abs/1106.1690) (see p. 82).
- [162] DOO JAE PARK, BJOERN PIGLOSIEWICZ, SLAWA SCHMIDT, et al.: **Strong Field Acceleration and Steering of Ultrafast Electron Pulses from a Sharp Metallic Nanotip**. In: *Physical Review Letters*, **109**:24 (Dec. 2012), p. 244803. DOI: [10.1103/PhysRevLett.109.244803](https://doi.org/10.1103/PhysRevLett.109.244803) (see p. 82).
- [163] M. KRÜGER, M. SCHENK, and P. HOMMELHOFF: **Strong-Field Effects and Attosecond Control of Electrons in Photoemission from a Nanoscale Metal Tip**. In: *Springer Proceedings in Physics*. Vol. 125. 2012, pp. 401–406. DOI: [10.1007/978-3-642-28948-4\\_66](https://doi.org/10.1007/978-3-642-28948-4_66). arXiv: [1107.1591](https://arxiv.org/abs/1107.1591) (see p. 82).
- [164] C. ROPERS, D. R. SOLLI, C. P. SCHULZ, C. LIENAU, and T. ELSAESSER: **Localized Multiphoton Emission of Femtosecond Electron Pulses from Metal Nanotips**. In: *Physical Review Letters*, **98**:4 (Jan. 2007), p. 043907. DOI: [10.1103/PhysRevLett.98.043907](https://doi.org/10.1103/PhysRevLett.98.043907) (see p. 82).
- [165] G. HERINK, D. R. SOLLI, M. GULDE, and C. ROPERS: **Field-driven photoemission from nanostructures quenches the quiver motion**. In: *Nature*, **483**:7388 (Mar. 2012), pp. 190–193. DOI: [10.1038/nature10878](https://doi.org/10.1038/nature10878) (see p. 82).
- [166] NAHID TALEBI, WILFRIED SIGLE, RALF VOGELGESANG, et al.: **Excitation of Mesoscopic Plasmonic Tapers by Relativistic Electrons: Phase Matching versus Eigenmode Resonances**. In: *ACS Nano*, **9**:7 (July 2015), pp. 7641–7648. DOI: [10.1021/acs.nano.5b03024](https://doi.org/10.1021/acs.nano.5b03024) (see p. 82).
- [167] SERGEY V. YALUNIN, BENJAMIN SCHRÖDER, and CLAUS ROPERS: **Theory of electron energy loss near plasmonic wires, nanorods, and cones**. In: *Physical Review B*, **93**:11 (Mar. 2016), p. 115408. DOI: [10.1103/PhysRevB.93.115408](https://doi.org/10.1103/PhysRevB.93.115408) (see p. 82).
- [168] SURONG GUO, NAHID TALEBI, WILFRIED SIGLE, et al.: **Reflection and Phase Matching in Plasmonic Gold Tapers**. In: *Nano Letters*, **16**:10 (2016), pp. 6137–6144. DOI: [10.1021/acs.nanolett.6b02353](https://doi.org/10.1021/acs.nanolett.6b02353) (see p. 82).
- [169] OLIVIER J. F. MARTIN, CHRISTIAN GIRARD, and ALAIN DEREUX: **Generalized Field Propagator for Electromagnetic Scattering and Light Confinement**. In: *Physical Review Letters*, **74**:4 (Jan. 1995), pp. 526–529. DOI: [10.1103/PhysRevLett.74.526](https://doi.org/10.1103/PhysRevLett.74.526) (see p. 83).

- [170] OLE KELLER, MUFEI XIAO, and SERGEY BOZHEVOLNYI: **Configurational resonances in optical near-field microscopy: a rigorous point-dipole approach.** In: *Surface Science*, **280**:1-2 (1993), pp. 217–230. DOI: [10.1016/0039-6028\(93\)90370-Y](https://doi.org/10.1016/0039-6028(93)90370-Y) (see p. 83).
- [171] LUKAS NOVOTNY: **Effective Wavelength Scaling for Optical Antennas.** In: *Physical Review Letters*, **98**:26 (June 2007), p. 266802. DOI: [10.1103/PhysRevLett.98.266802](https://doi.org/10.1103/PhysRevLett.98.266802) (see p. 85).
- [172] BJÖRN PIGLOSIWICZ, SLAWA SCHMIDT, DOO JAE PARK, et al.: **Carrier-envelope phase effects on the strong-field photoemission of electrons from metallic nanostructures.** In: *Nature Photonics*, **8**:1 (Jan. 2014), pp. 37–42. DOI: [10.1038/nphoton.2013.288](https://doi.org/10.1038/nphoton.2013.288) (see p. 91).
- [173] J. LAGOIS and B. FISCHER: **Experimental observation of surface exciton polaritons.** In: *Physical Review Letters*, **36**:12 (1976), pp. 680–683. DOI: [10.1103/PhysRevLett.36.680](https://doi.org/10.1103/PhysRevLett.36.680) (see p. 92).
- [174] S. SCHNEIDER, J. SEIDEL, S. GRAFSTRÖM, et al.: **Impact of optical in-plane anisotropy on near-field phonon polariton spectroscopy.** In: *Applied Physics Letters*, **90**:14 (Apr. 2007), p. 143101. DOI: [10.1063/1.2718489](https://doi.org/10.1063/1.2718489) (see p. 92).
- [175] S. C. KEHR, M. CEBULA, O. MIETH, et al.: **Anisotropy Contrast in Phonon-Enhanced Apertureless Near-Field Microscopy Using a Free-Electron Laser.** In: *Physical Review Letters*, **100**:25 (June 2008), p. 256403. DOI: [10.1103/PhysRevLett.100.256403](https://doi.org/10.1103/PhysRevLett.100.256403) (see p. 92).
- [176] A. SANDERS, R. W. BOWMAN, L. ZHANG, et al.: **Understanding the plasmonics of nanostructured atomic force microscopy tips.** In: *Applied Physics Letters*, **109**:15 (2016). DOI: [10.1063/1.4964601](https://doi.org/10.1063/1.4964601). arXiv: [1607.06591](https://arxiv.org/abs/1607.06591) (see p. 92).
- [177] I.V. LINDELL, A. VILJANEN, and K.I. NIKOSKINEN: **Electrostatic image method for the anisotropic half space.** In: *IEE Proceedings - Science, Measurement and Technology*, **144**:4 (July 1997), pp. 156–162. DOI: [10.1049/ip-smt:19971317](https://doi.org/10.1049/ip-smt:19971317) (see p. 98).
- [178] S. C. SCHNEIDER, S. GRAFSTRÖM, and L. M. ENG: **Scattering near-field optical microscopy of optically anisotropic systems.** In: *Physical Review B*, **71**:11 (Mar. 2005), p. 115418. DOI: [10.1103/PhysRevB.71.115418](https://doi.org/10.1103/PhysRevB.71.115418) (see p. 98).
- [179] PAOLO BIAGIONI, JER-SHING HUANG, and BERT HECHT: **Nanoantennas for visible and infrared radiation.** In: *Reports on Progress in Physics*, (Mar. 2011), p. 76. DOI: [10.1088/0034-4885/75/2/024402](https://doi.org/10.1088/0034-4885/75/2/024402). arXiv: [1103.1568](https://arxiv.org/abs/1103.1568) (see pp. 103, 162, 165).
- [180] A. G. CURTO, G. VOLPE, T. H. TAMINIAU, et al.: **Unidirectional Emission of a Quantum Dot Coupled to a Nanoantenna.** In: *Science*, **329**:5994 (Aug. 2010), pp. 930–933. DOI: [10.1126/science.1191922](https://doi.org/10.1126/science.1191922) (see p. 103).

- [181] AHMED ABBAS, MOSTAFA EL-SAID, and SAMIR F MAHMOUD: **Characteristics of an Optical Bowtie Nanoantenna**. In: (2013), pp. 1708–1711 (see p. 103).
- [182] LUKAS NOVOTNY and NIEK VAN HULST: **Antennas for light**. In: *Nature Photonics*, **5**:2 (2011), pp. 83–90. DOI: [10.1038/nphoton.2010.237](https://doi.org/10.1038/nphoton.2010.237). arXiv: [1305.0033](https://arxiv.org/abs/1305.0033) (see pp. 103, 162).
- [183] MICHAEL G. STANFORD, BRETT B. LEWIS, KYLE MAHADY, JASON D. FOWLKES, and PHILIP D. RACK: **Review Article: Advanced nanoscale patterning and material synthesis with gas field helium and neon ion beams**. In: *Journal of Vacuum Science & Technology B, Nanotechnology and Microelectronics: Materials, Processing, Measurement, and Phenomena*, **35**:3 (May 2017), p. 030802. DOI: [10.1116/1.4981016](https://doi.org/10.1116/1.4981016) (see p. 103).
- [184] KASPAR D. KO, ANIL KUMAR, KIN HUNG FUNG, et al.: **Nonlinear optical response from arrays of Au bowtie nanoantennas**. In: *Nano Letters*, **11**:1 (2011), pp. 61–65. DOI: [10.1021/nl102751m](https://doi.org/10.1021/nl102751m) (see p. 104).
- [185] PASCAL ANGER, PALASH BHARADWAJ, and LUKAS NOVOTNY: **Enhancement and quenching of single-molecule fluorescence**. In: *Physical Review Letters*, **96**:11 (2006), pp. 3–6. DOI: [10.1103/PhysRevLett.96.113002](https://doi.org/10.1103/PhysRevLett.96.113002) (see p. 120).
- [186] VYACHESLAV ROMANOV and GILBERT C. WALKER: **Infrared near-field detection of a narrow resonance due to molecular vibrations in a nanoparticle**. In: *Langmuir*, **23**:5 (2007), pp. 2829–2837. DOI: [10.1021/la0625594](https://doi.org/10.1021/la0625594) (see p. 121).
- [187] A. CVITKOVIC, N. OCELIC, J. AIZPURUA, R. GUCKENBERGER, and R. HILLENBRAND: **Infrared imaging of single nanoparticles via strong field enhancement in a scanning nanogap**. In: *Physical Review Letters*, **97**:6 (2006), pp. 1–4. DOI: [10.1103/PhysRevLett.97.060801](https://doi.org/10.1103/PhysRevLett.97.060801) (see p. 121).
- [188] K. M. SHAFEEKH, SURESH DAS, CRISTINA SISSA, and ANNA PAINELLI: **Asymmetric squaraine dyes: Spectroscopic and theoretical investigation**. In: *Journal of Physical Chemistry B*, **117**:28 (2013), pp. 8536–8546. DOI: [10.1021/jp401099g](https://doi.org/10.1021/jp401099g) (see p. 145).
- [189] S. BRÜCK, C. KRAUSE, R. TURRISI, et al.: **Structure–property relationship of anilino-squaraines in organic solar cells**. In: *Phys. Chem. Chem. Phys.*, **16**:3 (2014), pp. 1067–1077. DOI: [10.1039/C3CP54163K](https://doi.org/10.1039/C3CP54163K) (see p. 145).
- [190] MATTHIAS SCHULZ, MAJVOR MACK, OLIVER KOLLOGE, ARNE LÜTZEN, and MANUELA SCHIEK: **Organic photodiodes from homochiral L-proline derived squaraine compounds with strong circular dichroism**. In: *Physical Chemistry Chemical Physics*, **19**:10 (2017), pp. 6996–7008. DOI: [10.1039/C7CP00306D](https://doi.org/10.1039/C7CP00306D) (see p. 145).

- [191] FRANK BALZER, HEIKO KOLLMANN, MATTHIAS SCHULZ, et al.: **Spotlight on Excitonic Coupling in Polymorphic and Textured Anilino Squaraine Thin Films**. In: *Crystal Growth & Design*, **17**:12 (Dec. 2017), pp. 6455–6466. DOI: [10.1021/acs.cgd.7b01131](https://doi.org/10.1021/acs.cgd.7b01131) (see pp. 145–146, 148).
- [192] XIN XIAO, GUODAN WEI, SIYI WANG, et al.: **Small-molecule photovoltaics based on functionalized squaraine donor blends**. In: *Advanced Materials*, **24**:15 (2012), pp. 1956–1960. DOI: [10.1002/adma.201104261](https://doi.org/10.1002/adma.201104261) (see p. 145).
- [193] MATTHIAS SCHULZ, MAJVOR MACK, OLIVER KOLLOGE, ARNE LÜTZEN, and MANUELA SCHIEK: **Organic photodiodes from homochiral L-proline derived squaraine compounds with strong circular dichroism**. In: *Physical Chemistry Chemical Physics*, **19**:10 (2017), pp. 6996–7008. DOI: [10.1039/C7CP00306D](https://doi.org/10.1039/C7CP00306D) (see pp. 145, 154).
- [194] NINA BEROVA, LORENZO DI BARI, and GENNARO PESCIPELLI: **Application of electronic circular dichroism in configurational and conformational analysis of organic compounds**. In: *Chemical Society Reviews*, **36**:6 (2007), p. 914. DOI: [10.1039/b515476f](https://doi.org/10.1039/b515476f) (see pp. 145–146).
- [195] M. KASHA, H. R. RAWLS, and M. ASHRAF EL-BAYOUMI: **The exciton model in molecular spectroscopy**. In: *Pure Appl. Chem.*, **11**:3-4 (1965), pp. 371–392. DOI: [10.1351/pac196511030371](https://doi.org/10.1351/pac196511030371) (see p. 146).
- [196] S. SIDDIQUI and FRANK C. SPANO: **H- and J-aggregates of conjugated polymers and oligomers**. In: *Chemical Physics Letters*, **308**:1-2 (1999), pp. 99–105. DOI: [10.1016/S0009-2614\(99\)00577-1](https://doi.org/10.1016/S0009-2614(99)00577-1) (see p. 146).
- [197] VLADIMIR V SHELKOVNIKOV and ALEXANDER I PLEKHANOV: **Optical and Resonant Non-Linear Optical Properties of J-Aggregates of Pseudoisocyanine Derivatives in Thin Solid Films**. In: *Edited by Jamal Uddin*, 2001 (2012), p. 317 (see p. 146).
- [198] EDWINE E. JELLY: **Molecular, Nematic and Crystal States of I: I-Diethyl-Cyanine Chloride**. In: *Nature*, **139**:3519 (Apr. 1937), pp. 631–631. DOI: [10.1038/139631b0](https://doi.org/10.1038/139631b0) (see p. 146).
- [199] EDWINE E. JELLY: **Spectral Absorption and Fluorescence of Dyes in the Molecular State**. In: *Nature*, **138**:3502 (Dec. 1936), pp. 1009–1010. DOI: [10.1038/1381009a0](https://doi.org/10.1038/1381009a0) (see p. 146).
- [200] A. EISFELD and J.S. BRIGGS: **The J- and H-bands of organic dye aggregates**. In: *Chemical Physics*, **324**:2-3 (May 2006), pp. 376–384. DOI: [10.1016/j.chemphys.2005.11.015](https://doi.org/10.1016/j.chemphys.2005.11.015) (see p. 146).

- [201] FRANK WÜRTHNER, THEO E. KAISER, and CHANTU R. SAHA-MÖLLER: **J-Aggregates: From Serendipitous Discovery to Supramolecular Engineering of Functional Dye Materials**. In: *Angewandte Chemie International Edition*, **50**:15 (Apr. 2011), pp. 3376–3410. DOI: [10.1002/anie.201002307](https://doi.org/10.1002/anie.201002307) (see p. 146).
- [202] F. C. SPANO: **Optical microcavities enhance the exciton coherence length and eliminate vibronic coupling in J-aggregates**. In: *Journal of Chemical Physics*, **142**:18 (2015). DOI: [10.1063/1.4919348](https://doi.org/10.1063/1.4919348). arXiv: [1202.5712](https://arxiv.org/abs/1202.5712) (see p. 146).
- [203] NICHOLAS J. HESTAND, CHENYU ZHENG, ANIRUDH RAJU PENMETCHA, et al.: **Confirmation of the Origins of Panchromatic Spectra in Squaraine Thin Films Targeted for Organic Photovoltaic Devices**. In: *The Journal of Physical Chemistry C*, **119**:33 (Aug. 2015), pp. 18964–18974. DOI: [10.1021/acs.jpcc.5b05095](https://doi.org/10.1021/acs.jpcc.5b05095) (see pp. 146–147).
- [204] FRANK C. SPANO: **EXCITONS IN CONJUGATED OLIGOMER AGGREGATES, FILMS, AND CRYSTALS**. In: *Annual Review of Physical Chemistry*, **57**:1 (May 2006), pp. 217–243. DOI: [10.1146/annurev.physchem.57.032905.104557](https://doi.org/10.1146/annurev.physchem.57.032905.104557) (see p. 147).
- [205] DANIEL A. HIGGINS and PAUL F. BARBARA: **Excitonic transitions in J-aggregates probed by near-field scanning optical microscopy**. In: *The Journal of Physical Chemistry*, **99**:1 (Jan. 1995), pp. 3–7. DOI: [10.1021/j100001a002](https://doi.org/10.1021/j100001a002) (see p. 147).
- [206] KYOUNG-DUCK PARK and MARKUS B. RASCHKE: **Polarization control with plasmonic antenna-tips: A universal approach for optical nano-crystallography and vector-field imaging**. In: (2018), pp. 1–14. arXiv: [1801.03206](https://arxiv.org/abs/1801.03206). URL: <http://arxiv.org/abs/1801.03206> (see pp. 157, 190).
- [207] SEUNGCHUL KIM, JONGHAN JIN, YOUNG JIN KIM, et al.: **High-harmonic generation by resonant plasmon field enhancement**. In: *Nature*, **453**:7196 (2008), pp. 757–760. DOI: [10.1038/nature07012](https://doi.org/10.1038/nature07012) (see p. 162).
- [208] H. KOLLMANN, M. ESMANN, S. F. BECKER, et al.: **Ultrafast third-harmonic spectroscopy of single nanoantennas fabricated using helium-ion beam lithography**. In: ed. by GEORG VON FREYMAN, WINSTON V. SCHOENFELD, and RAYMOND C. RUMPF. March. Mar. 2016, p. 975908. DOI: [10.1117/12.2212689](https://doi.org/10.1117/12.2212689) (see p. 162).
- [209] ANIKA KINKHABWALA, ZONGFU YU, SHANHUI FAN, et al.: **Large single-molecule fluorescence enhancements produced by a bowtie nanoantenna**. In: *Nature Photonics*, **3**:11 (2009), pp. 654–657. DOI: [10.1038/nphoton.2009.187](https://doi.org/10.1038/nphoton.2009.187) (see p. 162).
- [210] T. H. TAMINIAU, F. D. STEFANI, F. B. SEGERINK, and N. F. VAN HULST: **Optical antennas direct single-molecule emission**. In: *Nature Photonics*, **2**:4 (Mar. 2008), pp. 234–237. DOI: [10.1038/nphoton.2008.32](https://doi.org/10.1038/nphoton.2008.32) (see p. 162).

- [211] NAHLA A. HATAB, CHUN HWAY HSUEH, ABIGAIL L. GADDIS, et al.: **Free-standing optical gold bowtie nanoantenna with variable gap size for enhanced Raman spectroscopy**. In: *Nano Letters*, **10**:12 (2010), pp. 4952–4955. DOI: [10.1021/nl102963g](https://doi.org/10.1021/nl102963g) (see p. 162).
- [212] MORITZ GITTINGER, KATJA HÖFLICH, VLADIMIR SMIRNOV, et al.: **Strongly coupled, high-quality plasmonic dimer antennas fabricated using a sketch-and-peel technique**. In: *Nanophotonics*, **9**:2 (2020), pp. 401–412. DOI: [10.1515/nanoph-2019-0379](https://doi.org/10.1515/nanoph-2019-0379) (see pp. 162, 165).
- [213] N. ROTENBERG and L. KUIPERS: **Mapping nanoscale light fields**. 2014. DOI: [10.1038/nphoton.2014.285](https://doi.org/10.1038/nphoton.2014.285) (see p. 162).
- [214] B. LE FEBER, J. E. SIPE, M. WULF, L. KUIPERS, and N. ROTENBERG: **A full vectorial mapping of nanophotonic light fields**. In: *Light: Science & Applications*, **8**:1 (Dec. 2019), p. 28. DOI: [10.1038/s41377-019-0124-3](https://doi.org/10.1038/s41377-019-0124-3). arXiv: [1803.10145](https://arxiv.org/abs/1803.10145) (see p. 163).
- [215] MORITZ ESSLINGER and RALF VOGELGESANG: **Reciprocity theory of apertureless scanning near-field optical microscopy with point-dipole probes**. In: *ACS Nano*, **6**:9 (2012), pp. 8173–8182. DOI: [10.1021/nn302864d](https://doi.org/10.1021/nn302864d) (see p. 163).
- [216] K. G. LEE, H. W. KIHM, J. E. KIHM, et al.: **Vector field microscopic imaging of light**. In: *Nature Photonics*, **1**:1 (2007), pp. 53–56. DOI: [10.1038/nphoton.2006.37](https://doi.org/10.1038/nphoton.2006.37) (see p. 163).
- [217] O. L. MUSKENS, V. GIANNINI, J. A. SÁNCHEZ-GIL, and J. GÓMEZ RIVAS: **Optical scattering resonances of single and coupled dimer plasmonic nanoantennas**. In: *Optics Express*, **15**:26 (2007), p. 17736. DOI: [10.1364/OE.15.017736](https://doi.org/10.1364/OE.15.017736). arXiv: [0612689](https://arxiv.org/abs/0612689) [cond-mat] (see p. 165).
- [218] MARTIN BRINKMANN, ERIC GONTHIER, STÉFAN BOGEN, et al.: **Segregated versus mixed interchain stacking in highly oriented films of naphthalene diimide bithiophene copolymers**. In: *ACS Nano*, **6**:11 (2012), pp. 10319–10326. DOI: [10.1021/nn304213h](https://doi.org/10.1021/nn304213h) (see p. 185).
- [219] SABINE LUDWIGS: **P3HT Revisited – From Molecular Scale to Solar Cell Devices**. Vol. 265. 2014. DOI: [10.1007/978-3-662-45145-8](https://doi.org/10.1007/978-3-662-45145-8). arXiv: [0808.2157](https://arxiv.org/abs/0808.2157) (see p. 185).
- [220] DANIEL TREFZ, YANNIC M. GROSS, CARSTEN DINGLER, et al.: **Tuning Orientational Order of Highly Aggregating P(NDI2OD-T2) by Solvent Vapor Annealing and Blade Coating**. In: *Macromolecules*, **52**:1 (2019), pp. 43–54. DOI: [10.1021/acs.macromol.8b02176](https://doi.org/10.1021/acs.macromol.8b02176) (see pp. 185–186).
- [221] ANTONIO FACCHETTI: **Organic semiconductors: Made to order**. In: *Nature Materials*, **12**:7 (June 2013), pp. 598–600. DOI: [10.1038/nmat3686](https://doi.org/10.1038/nmat3686) (see p. 187).



# Jens Brauer

Lebenslauf/Publikationen/Konferenzbeiträge

Max-Bill-Straße 6  
80807 München  
☎ 01512 / 7570184  
✉ jens-brauer@web.de  
🌐 www.jens-brauer.de

## Persönliches

Geboren 16.03.1989 in Emden  
Familienstand ledig

## Berufserfahrung

07/2018 - Softwareentwickler (C++/Python/Simulink) bei Bertrand Ingenieurbüro München  
jetzt  
Schwerpunktprojekt „Virtuelles Fahrerlebnis“ im BMW Forschungs- und Innovationszentrum

## Studium & Promotion

### Promotion im Fach „Physik“

11/2013 - vsl. Carl von Ossietzky University Oldenburg, Arbeitsgruppe „Ultraschnelle Nano-Optik“  
07/2020

Masterstudium für den M.Sc. Abschluss im Fach „Physik“, Note:1.12 (sehr gut)

10/2011 - Carl von Ossietzky Universität Oldenburg  
10/2013

Masterarbeit: *Adiabatische Nanofokussierung und Impulsraumabbildung*

**Betreuer: Prof. Dr. Christoph Lienau**

Bachelorstudium für den B.Sc. Abschluss im Fach „Physik“, Note:1.19 (sehr gut)

10/2008 - Carl von Ossietzky Universität Oldenburg  
09/2011

Bachelorarbeit: *Streuung und Reabsorption in Fluoreszenzkollektoren aus spektral- und winkelaufgelöster Emission*

**Betreuer: Prof. Dr. Gottfried Heinrich Bauer**

## Programmierkenntnisse + EDV

sehr gut Matlab, Python + pyQT, Simulink  
sehr gut L<sup>A</sup>T<sub>E</sub>X, Word, Powerpoint  
gut HTML, PHP, Javascript, jQuery, AngularJs etc.  
gut Maple, Mathematica  
sehr gut C, C++  
gut Git Versionskontrolle

## Publikationen

2020 Jinxin Zhan, Wei Wang, **Jens Brauer**, Lukas Schmidt-Mende, Christoph Lienau & Petra Groß. Spatial and spectral mode mapping of a dielectric nanodot by broadband interferometric homodyne scanning near-field spectroscopy. *Advanced Photonics*, (submitted)

- 2017 **Jens Brauer**, Jinxin Zhan, Abbas Chimeh, Anke Korte, Christoph Lienau und Petra Groß. In-line interferometer for broadband near-field scanning optical spectroscopy. *Optics Express*, 25(13):15504
- 2015 Jörg Robin, **Jens Brauer**, Stefan Sulmann, Valerio Marino, Daniele Dell'Orco, Christoph Lienau und Karl-Wilhelm Koch. Differential Nanosecond Protein Dynamics in Homologous Calcium Sensors. *ACS Chemical Biology*, 10(10):2344–2352
- 2013 Martin Esmann, Simon F. Becker, Bernhard B. da Cunha, **Jens Brauer**, Ralf Vogelgesang, Petra Groß und Christoph Lienau. k-space imaging of the eigenmodes of sharp gold tapers for scanning near-field optical microscopy. *Beilstein Journal of Nanotechnology*, 4(1):603–610

## Beiträge auf Konferenzen/Summer Schools

- 13/03/18 Frühjahrstagung der deutschen Physiker Gesellschaft (DPG) in Berlin  
**Poster** zum Thema „*Scanning near-field optical spectroscopy with an inline interferometer for probing local absorption*“
- 09/12/17 Iraqi-German Winter school on Nanophotonics in Delmenhorst  
**Vortrag** zum Thema „*Mapping the local angular distribution of squaraine dye molecules with broad-band SNOM spectroscopy*“
- 19/03/17 - Frühjahrstagung der deutschen Physiker Gesellschaft (DPG) in Dresden  
24/03/17 **Vortrag** zum Thema „*Scanning near-field optical microscopy with inline-homodyne detection*“
- 12/09/16- Summer School of the Research Group Nano Energy, Elstal (Berlin), **Vortrag und Poster**  
15/09/16 zum Thema „Polarization Sensitive Scanning Near-Field Optical Microscopy on Polymers“
- 06/03/16 - Frühjahrstagung der deutschen Physiker Gesellschaft (DPG) in Regensburg  
11/03/16 **Vortrag** zum Thema „*Polarization sensitive scanning near field optical microscope on polymer thin films*“
- 06/10/15 - International symposium Molecular Basis of Senses meets Quantum Biology Barcelona.  
10/10/2015 **Posterpräsentation** + internationaler Austausch
- 24/09/15 - Second Iraqi-German Summer School on Nanophotonics, HWK Delmenhorst  
25/09/15 **Vortrag** zum Thema „*Scanning near field optical microscopy on polymers*“
- 28/10/13- 3rd SPP 1391 „Ultrafast Nano-Optics“ Summer School, Mühlheim an der Ruhr,  
30/10/13 **Posterpräsentation** zum Thema „*Radiation Pattern Imaging of a Sharp Gold Taper for Near-field Scanning Optical Microscopy*“

## Lehre

- Betreuung Betreuung eines Bachelor-Studenten zum Thema „Realisierung und Charakterisierung eines spektral breitbandigen Mach-Zehnder-Interferometers für ein aperturloses Rasternahfeldmikroskop“
- Tutorium Leitung einer Übungsgruppe zur Vorlesung „Physik für Umweltwissenschaften“
- Praktikum Zwei Semester Betreuung für das fortgeschrittene Praktikum für Master Studenten der Physik zum Versuch „Weißlichterzeugung“

## Workshops + Softskills

### Workshops/Programme verschiedener externer Firmen

- Google Mehrmaliges Treffen mit einem Mitarbeiter von Google München im Rahmen eines Mentoring Programms
- Fielax Interface Science Workshop,  
Bremerhaven Kurs über Elektronik, serielle Schnittschnellen und Datenübertragung

Wefers und Junior Management Programm  
Coll Die eigene Rolle erkennen - Führungskraft entwickeln  
Leica Super-resolution Workshop on Light Microscopy  
Biovoxxel Imaging Workshop  
Tress&Tress How to publish in peer-reviewed journals  
Gbr  
Google Digital Workshop „Online Marketing“

---

## Besondere Leistungen + Stipendien

2011 Stipendium für herausragende Noten im Bachelor Studiengang  
2013 Stipendium für herausragende Noten im Master Studiengang  
11/2013 - DFG gefördertes Doktorandenstipendium im **Graduiertenkolleg „Molecular Basis of  
11/2014 **Sensory Biology**“**  
11/2014 - MWK gefördertes Doktorandenstipendium im **Landesgraduiertenkolleg „Nano-  
11/2017 **Energieforschung**“**

## Danksagung

Zum Schluss möchte ich mich bei allen bedanken, die mich auf dem Weg zur Fertigstellung dieser Arbeit unterstützt haben.

Dabei möchte ich mich ganz herzlich bei Herrn Prof. Dr. Christoph Lienau für die Chance bedanken, an einem so interessanten Projekt, und zudem mittels modernster Technik, arbeiten zu dürfen. Die Freiheit im Laserlabor neue Ideen ausprobieren zu können, sowie die Tatsache, dass es nie ein Problem war, fehlende Teile schnell nachzubeschaffen, haben die Arbeit nie langweilig werden lassen. Außerdem haben die Diskussionen über unsere Messdaten maßgeblich zum Verständnis beigetragen.

Herrn Prof. Dr. Erich Runge von der TU Ilmenau danke ich herzlich für seine schnelle Zusage, das Zweitgutachten meiner Dissertation anzufertigen.

Ein ganz besonderer Dank geht an Frau Dr. Petra Groß, die meine Promotion die ganzen Jahre über wissenschaftlich betreut hat und bei aufkommenden Fragen immer zur Stelle war. Selbst nach meiner Zeit an der Uni konnte in Skype Gsprächen noch über neue Auswertungen diskutiert werden. Die anregenden Diskussionen waren immer sehr hilfreich und haben mir sehr geholfen diese Arbeit zu verwirklichen.

Weiterhin bedanke ich mich bei Jinxin Zhan für die tolle Zusammenarbeit im Labor und die nachfolgenden Diskussionen über die Datenanalyse.

Meinen ehemaligen Bürokollegen Dr. Martin Esmann und Simon Becker, die mich bereits in meiner Masterarbeit auf dem Gebiet SNOM eingearbeitet haben und einige Tipps auf Lager hatten, möchte ich ebenfalls danken.

Der gesamten Arbeitsgruppe "Ultraschnelle Nano-Optik" danke ich für die nette Atmosphäre und die tolle Hilfsbereitschaft.

Zum Schluss möchte ich mich bei meiner Familie und meinen Freunden bedanken, die mich fortwährend unterstützt haben.

**Vielen Dank!**

# Selbstständigkeitserklärung

Hiermit versichere ich, dass ich die vorliegende Arbeit selbstständig verfasst und nur die angegebenen Hilfsmittel verwendet habe. Außerdem versichere ich, dass ich die allgemeinen Prinzipien wissenschaftlicher Arbeit und Veröffentlichung, wie sie in den Leitlinien guter wissenschaftlicher Praxis der Carl von Ossietzky Universität Oldenburg festgelegt sind, befolgt habe.

München, 01.07.2020

Ort, Datum

---

Jens Brauer